PHYSIK-DEPARTMENT
LEHRSTUHL FÜR FUNKTIONELLE MATERIALIEN E13
TECHNISCHE UNIVERSITÄT MÜNCHEN

Atomic order and its influence on functional properties of NiMn-based Heusler systems

Pascal Bruno Neibecker

Vollständiger Abdruck der von der Fakultät für Physik der Technischen Universität München
zur Erlangung des akademischen Grades eines Doktors der Naturwissenschaften
(Dr. rer. nat.) genehmigten Dissertation.

Vorsitzende/-r:	Prof. Dr. Frank Pollmann
Prüfende/-r der Dissertation:	1. Prof. Dr. Winfried Petry 2. Prof. Dr. Rudolf Gross 3. Prof. Dr. Ferdinand Haider

Die Dissertation wurde am 30.10.2017 bei der Technischen Universität München eingereicht
und durch die Fakultät für Physik am 18.6.2018 angenommen.

To Letícia

Acknowledgements

The research work presented in this thesis would not have been possible without the help, support and insights of many supervisors, co-workers, collaborators and friends.

First of all, I want to express my great appreciation to Michael Leitner who competently directed and supervised me at all smaller and larger scientific steps undertaken on the way to this thesis. Michael was really the best supervisor I could have imagined and I feel that I learned so much from him about Solid State Physics that it is painful to remember how little I knew at the beginning of this PhD project. Next, of course I want to thank Prof. Petry who gave me the freedom to pursue my own research ideas and the support to successfully accomplish them. At the same time, I would like to offer my special thanks to Prof. Kainuma of Tohoku University in Sendai, Japan who hosted me as a JSPS fellow in his group for six months. The support and the warm-hearted welcome from him and his entire research group were the cornerstone of many results presented in this thesis. At this point, I also want to express my gratitude to Xiao Xu who always had time for me and helped me with every possible aspect of my experimental work in Japan. Furthermore, I want to thank Emiko Kamakura without whom my time in Japan would have been so much more difficult as she constantly helped me with all administrative issues. In this respect, also the constant support in administrative issues by Elisabeth Jörg-Müller is gratefully acknowledged.

Besides my supervisors, my special thanks are extended to my colleagues at the FRM II, especially at the Positron group of Christoph Hugenschmidt where I was adopted as one of their own even though we were working on quite different scientific projects. My special thanks here are directed to Hubert Ceeh, Josef Weber and Josef Ketels who were the best office mates I could have asked for. Your understanding of Physics initiated many interesting and enriching discussions. Furthermore, and much more important, our friendship was the foundation of four fulfilling PhD years in Garching that made the good moments of my PhD work even better and carried me through the more difficult moments. Also, I want to thank Markus Reiner for many interesting discussions about football, Bavaria and the world. Further, I am grateful to Marcel Dickmann, Matthias Dodenhöft, Thomas Gigl, Eike Hecht, Johannes Mitteneder, Benjamin Rienäcker, Markus Singer and Samantha Zimnik for being such great colleagues. I would additionally like to offer my special thanks to Sebastian

Vohburger for all his assistance and help with manufacturing related issues in the work shop. Further, I want to express my thanks to Georg Zagler, Lucas Hollender and Rayi Pin-Yi Chiu for trusting me to co-supervise their thesis.

My time in Japan would have been so much less productive and so much less fun without the support and friendship of all members of the Kainuma group. Especially, I want to thank Aono-san, Takekawa-san, Inho-san, Kimura-san and Xu-san. Aono-san was a great help in carrying out X-ray diffraction experiments, Takekawa-san invested a lot of time into my projects and carried out the WDS measurements presented in this thesis and Kimura-san carried out very valuable TEM measurements for the Ni_2MnAl project for me. With Inho-san and Xu-san, I very much enjoyed the discussions about science and everything else and especially I will remember the night-time walks from the lab to the dorms. Also, I will always remember in the best possible way the Kainuma group getaways and Onsen visits.

I am particularly grateful for the assistance given by Anatoliy Senyshyn of the Heinz Maier-Leibnitz Zentrum (MLZ) concerning measurements at SPODI, neutron powder diffraction in general and especially Rietveld refinement. Also, I am thankful for the experimental support at SPODI by Martin Mühlbauer and Oleksandr Dolotko. Further, I want to express my gratitude to Melanie Kirkham and Ashfia Huq at Oak Ridge National Lab for their support during the measurements at SNS as well as to Florence Porcher at LLB for her support during our beam time at 3T2.

I would like to offer my special thanks to Markus Gruner of the University of Duisburg-Essen for his theoretical input and the great collaboration over the years. Also, I am very thankful for many insightful discussions about Heusler systems. Further, I am grateful for the assistance by Georg Benka and Andreas Bauer of chair E51 with sample preparation and for carrying out PPMS measurements. I enjoyed very much your insights in and our discussions about sample issues and experimental results. Besides that, I want to thank Matthias Opel of the Walther-Meißner-Institute at the Technische Universität München (TUM) for his support with SQUID measurements and the great collaboration in the $Ni_{2-x}Co_xMnAl$ project.

I further acknowledge the support of Armin Kriele of the Materials Science lab at the MLZ for all his support with lab related issues as well as with DSC and XRD measurements. Additionally, I wish to acknowledge the support provided by the Kristalllabor at the TUM in matters of sample preparation, specifically by Susanne Mayr and Michael Stanger.

Finally, I want to thank Prof. Nilges of the Chemistry department at the TUM and Prof. Busch of Saarland University for their support with sample preparation. Specifically, I am grateful to Simon Hechler and Maximilian Frey as well as to Maximilian Baumgartner and Thomas Wylezich who supported me with the experimental work in the respective laboratories.

My heartfelt thanks go out to my family and friends who always supported me and reminded me of the things that really matter in life. Most of all, I want to thank my wife Letícia for being the constant source of happiness and inspiration in my life.

Abstract

The state of atomic order in NiMn-based Heusler systems influences a variety of materials properties, e.g. magnetic properties and martensitic transformations, ultimately defining their functionality. In fact, besides the alloy composition, the state of atomic order is a further degree of freedom that can effectively be employed for tailoring the material's functionality to specific application scenarios. Hence, understanding first of all the emergence of the state of order in these materials as well as second the interdependencies between the state of order and certain materials properties is a necessity in order to unleash their potential.

In this thesis, the state of order in NiMn-based Heusler systems and certain derived properties are studied experimentally by means of calorimetry and magnetization measurements as well as via diffraction techniques which is further substantiated by theoretical considerations and computer simulations. Specifically, the emergence of $L2_1$ order in Ni_2MnZ alloys (explicitly Ni_2MnAl and $Ni_2MnAl_{0.5}Ga_{0.5}$) is investigated and a model description of magneto-structural interactions on the atomic as well as on the mesoscopic scale is developed. Furthermore, the composition dependence of these magneto-structural interactions is studied via manipulating the ferromagnetic exchange interactions in the system by substituting Co for Ni. Besides that, the interplay between the electronic structure and the state of atomic order in quaternary Heusler derivatives is examined. Finally, the knowledge is transferred from the full-Heusler systems to the related half-Heusler systems, specifically $Ni_{2-x}MnSb$, where the transition from the $C1_b$ to the $L2_1$ structure is studied as a function of composition and temperature.

The presented comprehensive and systematic investigation of the state of atomic order in NiMn-based Heusler systems and its influence on the magnetic, electronic and structural properties draws a detailed picture of the complex magneto-structural interdependencies in these materials and provides a rich palette of outcomes from basic functional mechanisms to detailed and case-specific sample preparation instructions. The insights provided in this thesis will ultimately help to improve the functionality of these materials in e.g. magnetocaloric, ferromagnetic shape memory and spintronics applications.

Der atomare Ordnungszustand in NiMn-basierten Heusler Systemen beeinflusst eine Reihe von Materialeigenschaften wie z.Bsp. die magnetischen Eigenschaften und martensitische Phasenübergänge und bestimmt als Folge dessen letztlich die Funktionalität dieser Materialien. Neben der Zusammensetzung ist der atomare Ordnungszustand ein weiterer Freiheitsgrad, der effizient dazu genutzt werden kann, die Funktionalität bezüglich spezieller Anwendungsszenarien maßzuschneidern. Folglich ist ein Verständnis der Entstehung dieser Ordnungszustände als auch die Abhängigkeiten einzelner Materialeigenschaften von dem zu Grunde liegenden Ordnungszustand eine Notwendigkeit um das volle Potenziale dieser Materialien auszuschöpfen.

Diese Arbeit befasst sich mit der experimentellen Untersuchung des atomaren Ordnungszustands in NiMn-basierten Heusler Systemen und daraus abgeleiteten Materialeigenschaften über kalorimetrische und magnetische Messungen sowie Streuexperimente. Die experimentellen Erkenntnisse werden darüber hinaus mit theoretischen Überlegungen und Computersimulationen unterfüttert. Im Speziellen untersucht diese Arbeit die Entstehung von $L2_1$ Ordnung in Ni_2MnZ Legierungen (explizit Ni_2MnAl und $Ni_2MnAl_{0.5}Ga_{0.5}$) und entwickelt ein Modell für die magnetostrukturellen Abhängigkeiten auf der atomaren wie auch auf der mesoskopischen Skala. Im Weiteren beleuchtet die Arbeit den Einfluss der Zusammensetzungen der Legierung auf die genannten magnetostrukturellen Abhängigkeiten, indem die ferromagnetische Interaktion im System durch das Ersetzen von Ni durch Co manipuliert wird. Darüber hinaus wird der Zusammenhang zwischen der atomaren Ordnung und der elektronischen Struktur in quartären Heusler Derivaten untersucht. Schlussendlich wird das Wissen über den Ordnungszustand in Voll-Heusler Systemen auf die verwandten Halb-Heusler Systeme, im Speziellen $Ni_{2-x}MnSb$, übertragen, wo der Übergang zwischen der $C1_b$ Struktur und der $L2_1$ Struktur als Funktion der Zusammensetzung und der Temperatur herausgearbeitet wird.

Die hier präsentierten, umfassenden und systematischen Untersuchungen zum atomaren Ordnungszustand in NiMn-basierten Heusler Systemen und dessen Einfluss auf magnetische, elektronische und strukturelle Eigenschaften zeichnen ein detailliertes Bild der komplexen magnetostrukturellen Abhängigkeiten in diesen Materialsystemen und liefert eine reiche Palette an Ergebnissen - vom Verständnis grundlegender Funktionsmechanismen bis zu detaillierten und fallspezifischen Probenpräparationsanleitungen. Die im Rahmen dieser Arbeit gewonnenen Einsichten werden letztendlich dabei helfen die Funktionalität dieser Materialien in beispielsweise magnetokalorischen, Formgedächtnis- und spintronischen Anwendungen zu verbessern.

Table of contents

Overview

This dissertation is primarily concerned with investigating effects of structural order on the functional properties of Ni_2MnZ Heusler compounds. Functionality here essentially refers to magnetic properties as for instance the bulk magnetization and the magnetic transition temperature, however, also implications for the electronic structure and martensitic phase transitions are discussed. Besides the degree of order, repeatedly also effects of composition will be taken into consideration.

While all chapters are related to this overall subject, every chapter has the aspiration to stand independently, solving a particular scientific problem. Clearly, the subtopics are partially related to each other and cross-references between the chapters are frequently made. At this point, a short overview about the chapters and their individual content is given.

- **Chapter 1 – Experimental methods and sample preparation** discusses the experimental methods employed throughout this thesis. Specifically, the measurement principles are elucidated and some particular aspects relevant for the discussion of the thesis work are outlined. Additionally, sample preparation and also pre-characterization is discussed. This refers mainly to measurements of sample composition and sample homogeneity that do not experience adequate discussion in the other chapters.

- **Chapter 2 – Magnetic properties of Ni_2MnZ Heusler compounds** deals with the experimental and theoretical investigation of bulk magnetic properties in Ni_2MnZ alloys. First, $Ni_2MnAl_{0.5}Ga_{0.5}$ is established as an ideal model material to study order dependent properties in Ni_2MnZ compounds. On this basis, the magnetic properties in $Ni_2MnAl_{0.5}Ga_{0.5}$ in the antiferromagnetic (AFM) B2 structure are investigated. Next, gradually $L2_1$ order is evoked via isothermal annealing treatments and its influence on the magnetic properties is studied. Eventually, two factors are identified that predominantly influence the magnetism in these Heusler compounds: the degree of (short range) order in the sample as well as the $L2_1$ antiphase domain (APD) structure. Furthermore, a direct connection between these quantities and two magnetic properties is made. Specifically, the magnetic transition temperature is demonstrated to probe foremost the state of short range order in the sample, while the spontaneous magnetization and the DC susceptibility are mainly coupled to the APD structure. This relationship is eventually used to decipher the pathway of $L2_1$ order emergence. Applying the same analysis to the case of ternary Ni_2MnAl compounds shows the kinetic limitations of this alloy system with respect to its ordering capability. Additionally, it is demonstrated via Monte Carlo simulations that magneto-structural coupling leads to the observed magnetic properties. Specifically, it is shown that magnetic domains inherently coincide with structural APDs. While within a structural domain, due to lattice site occupancies, ferromagnetic (FM) interactions prevail, across APD boundaries, due to a nearest neighbor AFM Mn-Mn interaction, AFM interactions dominate. As a consequence, entire $L2_1$ APDs behave magnetically as supermoments which are coupled to each other in an AFM fashion. The presented magneto-structural model, taking into account a simple well-accepted magnetic Hamiltonian for the system as well as simulated atomic configurations, perfectly reproduces the experimentally observed magnetic properties.

- **Chapter 3 – Ordering kinetics in Ni_2MnZ Heusler compounds** reports on the kinetics of the $L2_1$ ordering process in $Ni_2MnAl_{0.5}Ga_{0.5}$, Ni_2MnAl and $Ni_2Mn_{1.12}Al_{0.88}$ compounds via monitoring the processes identified in the Chapter 2, namely the formation of (short range) order and the growth of the antiphase domain structure. On this basis, time-temperature-transformation (*TTT*) diagrams are constructed using a kinetic model that contains the full two-dimensional information of the parameter space composed of annealing temperature and annealing time for isothermal annealing procedures. The indirect measurements via calorimetry and magnetometry are supplemented by neutron powder diffraction and electron diffraction measurements which allow to probe the increase in the state of order as well as the APD growth directly during the annealing process. Furthermore, the influence of quenched-in vacancies on the ordering kinetics is investigated. Specifically, vacancy concentrations are adjusted via quenching from a variety of temperatures in the B2-stable regime, while the ordering process is studied via annealing at a variety of temperatures in the $L2_1$-stable regime. Additionally, cooling rate dependent experiments are developed in order to study a different regime of order formation where the degree of order is solely dependent on the cooling rate rather than the quenching temperature. From the various experiments, activation energies for order formation and vacancy formation are deduced.

- **Chapter 4 – Neutron diffraction study of magnetic antiphase domain coupling in Ni_2MnZ compounds** deals with the APD structure and its influence on the local magnetic properties of Ni_2MnAl and $Ni_2MnAl_{0.5}Ga_{0.5}$ compounds. As a complement to the bulk measurements in Chapter 2, in this chapter, neutron powder diffraction measurements are presented covering a wide parameter range of degrees of order, APD structures and temperatures. Specifically, the nuclear and magnetic structure is determined from the intensity and width of the magnetic and nuclear reflections. While the growth of the $L2_1$ APD structure is revealed as a function of annealing time by sharpening nuclear superstructure peaks, the magnetic peaks stay constant in intensity and shape despite the drastic changes in the underlying nuclear structure. Considering the postulation of AFM coupled APD, a model for describing the magnetic and nuclear scattering intensity is developed and compared to the experimental observations. For the first time, a direct proof for the existence of AFM coupled APD is established. Furthermore, the appearance of a pre-martensitic phase is observed in $Ni_2MnAl_{0.5}Ga_{0.5}$ compounds that is highly sensitive on the degree of order in the austenite parent phase.

- **Chapter 5 – Magnetic structure of B2-ordered $Ni_{2-x}Co_x$MnAl compounds** investigates the effect of substituting Co for Ni in B2-ordered $Ni_{2-x}Co_xMnAl$ alloys. After having carefully studied the order dependency of the magnetic properties in Ni_2MnZ alloys in the previous chapters, revealing an AFM structure in predominantly B2-ordered compounds and an evolution of FM properties with increasing $L2_1$ order, structurally related Co_2MnZ alloys show FM properties in all states of atomic order. The reason for this can be found in the stronger FM interaction of Co in comparison to Ni, while it is unclear how the transition from the AFM to the FM regime in B2-ordered $Ni_{2-x}Co_xMnZ$ systems occurs. This question is addressed via investigating the magnetic structure of B2-ordered $Ni_{2-x}Co_xMnAl$ compounds employing bulk magnetization measurements and neutron powder diffraction measurements for a variety of compositions and temperatures. The presented results suggest a magnetic structure composed of canted Mn moments with the canting angle of neighboring Mn spins being dependent on the Co content. Above a certain Co content, the canting angle reaches zero degrees and the compounds show ideal FM properties, independent of the nuclear structure.

- **Chapter 6 – Ordering tendencies and electronic properties in quaternary Heusler derivatives** explores the interplay of electronic properties and the atomic structure in NiCoMnZ quaternary Heusler compounds. In the pertinent literature, NiCoMnGa and NiCoMnAl have been identified as candidates for half-metallic materials in their fully ordered Y structure. However, the actual nuclear structure in these alloy systems has never been systematically investigated and also the influence of the atomic order on the electronic structure was not thoroughly studied. In this chapter, comprehensive experimental studies on the ordering tendencies in NiCoMnAl and NiCoMnGa are presented using bulk magnetization measurements, calorimetric measurements as well as in-situ neutron powder diffraction. The experimental results give a clear picture of the ordering tendencies in the systems, showing a tendency for B2 order in NiCoMnAl and a tendency for $L2_1$ order in NiCoMnGa. These results have additionally been supported by density functional theory (DFT) calculations. Based on the DFT results, a new tetragonal thermodynamic ground state structure is postulated for both compounds that is however, due to a low phase transition temperature, kinetically not accessible on experimental time scales. Also, the electronic density of states (DOS) was calculated for a variety of nuclear structures. The results show a strong order dependency of the electronic DOS with the formation of a pseudo-gap in the minority channel of the fully ordered Y structure. Yet, this pseudo-gap results from a distinct Ni-Co order on the 4a and 4b sites of the cubic Y structure and is hence absent in the tetragonal and disordered structures.

- **Chapter 7 – Half- to full-Heusler transition in $Ni_{2-x}MnSb$** reports on the half- to full-Heusler transition in $Ni_{2-x}MnSb$ compounds as function of composition and temperature. While stoichiometric NiMnSb adopts the $C1_b$ half-Heusler structure, stoichiometric Ni_2MnSb adopts the $L2_1$ full-Heusler structure. The $Ni_{2-x}MnSb$ system with variable Ni content shows a $C1_b$-$L2_1$ transition both as function of x at a selected temperature, as well as as function of temperature at a selected composition. A microscopic understanding of this interesting phase transition with respect to the ordering of structural vacancies however is missing. This question is approached via in-situ neutron powder diffraction measurements giving access simultaneously to the structure factor as well as to the lattice constant which eventually allows to investigate the mechanism of the ordering process from the $C1_b$ to the $L2_1$ phase. The neutron diffraction measurements are complemented by high temperature calorimetry as well as room temperature X-ray powder diffraction and low temperature magnetization measurements. The comprehensive experimental data set gives insights into the ordering of structural vacancies at the phase transition. Specifically, besides simple Ni/vacancy ordering, the annihilation of structural vacancies is postulated.

Crystal structures in Heusler derived systems

Throughout this thesis, a variety of crystal structures typical for Heusler systems as well as the phase transitions between them are discussed. The complexity of the considered structures reaches from one to four inequivalent lattice sites hosting up to four different constituents. While most structures are cubic, also tetragonal derivatives of the cubic structures are considered. In this section, these crystal structures are introduced and the nomenclature used to describe them in this thesis is presented. The figure below gives an overview over all crystal structures taking the NiCoMnZ system as an example. In the figure, brackets indicate a state of mixing. Consequently, e.g. (NiCo)MnZ represents the situation where Ni and Co occupy their respective sublattices randomly and hence this quaternary compound can be considered to be pseudo-ternary. The here presented discussion of crystal structures in Heusler systems is an extended version of the discussion in a recently published article by the author of this work (Neibecker et al., 2017) as presented in Chapter 6 of this thesis.

The original Heusler structure as introduced by Heusler (1903, 1904); Heusler et al. (1903) are ternary compounds of composition X_2YZ displaying $L2_1$ order. This $L2_1$ order is defined in Hahn (2005) by the space group 225 ($Fm\bar{3}m$) with inequivalent occupancies of the Wyckoff positions 4a, 4b and 8c and Cu_2MnAl as the prototypical representative. Typically, according to Graf et al. (2011) the 8c position is occupied by X which usually is a late transition metal, while the other two sites are occupied by Y (usually an early transition metal) and Z (usually a main-group metal).

This thesis is primarily concerned with Ni_2MnZ alloys and their derivatives, with Ni_2MnGa, due to its remarkable ferromagnetic shape memory properties (see for instance Ullakko et al., 1996), being the prototype. In the following, the occurring structures in Ni_2MnZ compounds are described using the case of Ni_2MnGa and Ni_2MnAl as examples. Ni_2MnGa displays a stable $L2_1$ phase above 260 K (Webster et al., 1984; Zheludev et al., 1995) while it undergoes a pre-martensitic and later martensitic transition at lower temperatures. As reported by Sánchez-Alarcos et al. (2007), at around 1053 K Ni_2MnGa shows a second-order

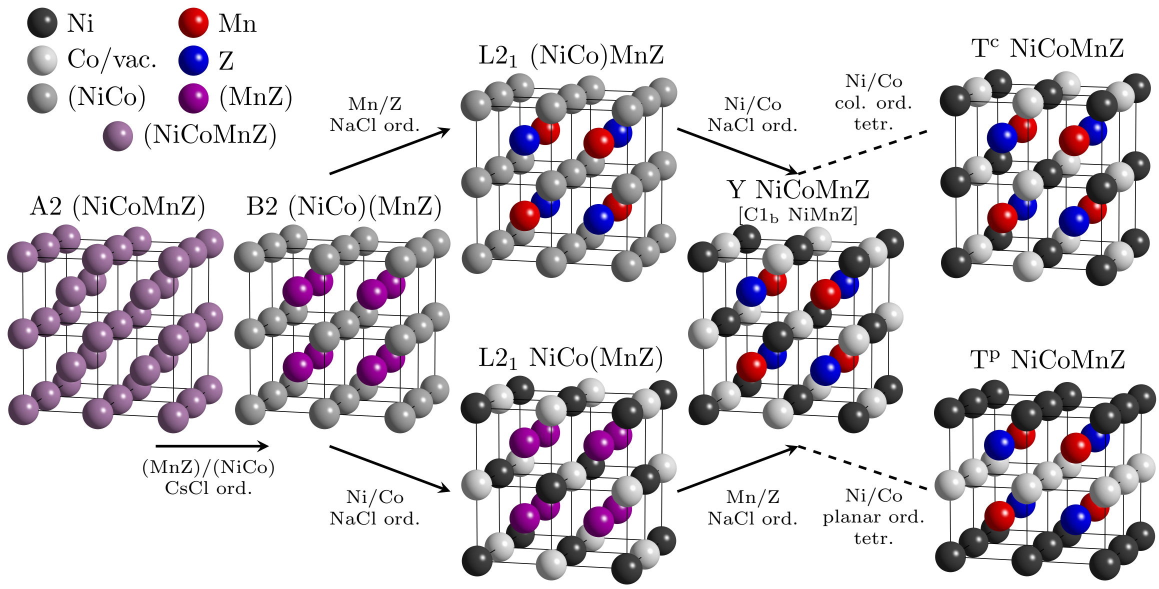

Schematic depiction of crystal structures occurring in Heusler derived systems. As an example, the quaternary NiCoMnZ system is considered while disordering processes on the various sublattices describe also the related ternary, binary and unary structures.

phase transition to the B2 structure, corresponding to a state of disorder between Mn and Ga. The resulting structure is described by space group 221 (Pm$\bar{3}$m) with Wyckoff position 1a being occupied preferentially by Ni, while Mn and Ga randomly occupy 1b. This partial disordering can be understood by the ordering between Ni and Mn/Ga being stabilized by nearest neighbor (NN) interactions on the common bcc lattice, while the ordering between Mn and Ga corresponding to full $L2_1$ order is accounted for by the presumably weaker next nearest neighbor (NNN) interactions. Whether $L2_1$ order can be realized depends foremost on the transition temperature and hence the atomic mobility at the transition. In Ni_2MnAl for instance, the B2-$L2_1$ transition temperature is significantly lower than in Ni_2MnGa and consequently only the B2 state (Acet et al., 2002; Ziebeck and Webster, 1975) or very early stages of $L2_1$ order can experimentally be observed. In both Ni_2MnGa and Ni_2MnAl, the B2 state is stable up to the melting temperature, and hence, there is no transition to the fully disordered bcc A2 structure defined by space group 229 (Im$\bar{3}$m). As discussed by Webster (1971), Co_2MnZ systems behave similarly, with well-developed $L2_1$ order in Co_2MnGa and only B2 order in Co_2MnAl.

Quaternary Heusler derivatives are in many cases related to their ternary parent compounds. This thesis is primarily concerned with NiCoMnZ-type systems where Ni is partially substituted by Co. As discussed above, both Ni- and Co-based ternary systems adopt the B2 structure at high temperatures. Consequently, it is reasonable to assume that this is also the case for NiCoMnZ compounds. This particular B2 order can be understood as site 1a being shared by Ni and Co and site 1b by Mn and Z. As introduced above this is denoted as (NiCo)(MnZ), where brackets imply mixing between the elements. Note, other B2 possibilities such as (NiMn)(CoZ) and (NiZ)(CoMn) do realistically not occur in these compounds.

As the temperature is decreased, in quaternary compounds transitions to higher ordered phases are expected. With respect to the Mn-Z sublattice, a NaCl-like ordering of Mn and Z is likely to occur. Potentially, a similar ordering could also be realized on the Ni-Co sublattice. Which structures occur in reality depends on the interaction strengths: for dominating Mn-Z interactions, the B2 phase would transform into a L2$_1$ structure of type (NiCo)MnZ, where Ni and Co are randomly occupying the 8c sites. If Ni-Co interacts stronger, a NiCo(MnZ) with Mn/Z on 8c would be expected. In both cases, the ordering of the other sublattice at even lower temperature would transform the system to the so-called Y structure (Bacon and Plant, 1971; Pauly et al., 1968) of prototype LiMgPdSn as described by Eberz et al. (1980) with space group 216 (F$\bar{4}$3m) and Wyckoff positions 4a, 4b, 4c, and 4d being occupied by Ni, Co, Mn and Z, respectively. Note that ternary Heusler compounds that develop structural vacancies, i.e. one of the sublattices is partially unoccupied, can be understood as pseudo-quaternary compounds. For instance, Ni$_{2-x}$MnSb adopts for a wide range of x the so-called half-Heusler structure with space group F$\bar{4}$3m. This is in principle the Y structure with either Wyckoff position 4a or 4b being (partially) unoccupied. Yet, given that Ni$_{2-x}$MnSb is a ternary compound, this structure is not referred to as Y structure but as C1$_\mathrm{b}$ structure.

In the case of quaternary Heusler derivatives, besides the cubic Y structure, also other fully ordered compounds need to be considered as thermodynamic ground states. In this thesis, specifically two tetragonal, fully ordered variants are presented, denoted as T$^\mathrm{c}$ and T$^\mathrm{p}$. T$^\mathrm{c}$ refers to a structure of alternating columns of Ni and Co and is described by the space group 131 (P4$_2$/mmc), with Ni on Wyckoff position 2e, Co on 2f, Mn on 2c, and Z on 2d. T$^\mathrm{p}$ refers to a structure of alternating Ni and Co planes and is described by the space group 129 (P4/nmm) with Ni on 2a, Co on 2b and Mn and Z on two inequivalent 2c positions. The T$_p$ structure was previously introduced by Johnson and Jeitschko (1974) for the prototypical compound ZrCuSiAs. Both tetragonal structures possess a 4-atomic primitive unit cell and are hence, a priori equally probable as the Y structure.

Chapter 1

Experimental methods and sample preparation

In this chapter, the experimental methods employed in this thesis are discussed and measurement principles are elucidated. Those concepts will be supported by exemplary measurements from this thesis that will be discussed in detail in the different chapters. Also, sample preparation and pre-characterization procedures are outlined.

1.1 Neutron powder diffraction

In order to study the nuclear and magnetic structure of intermetallic compounds, neutron powder diffraction measurements have been performed. These experiments were carried out at three different instruments: the SPODI high resolution neutron powder diffractometer at the Forschungsreaktor München II (FRM II) in Garching, Germany, the 3T2 powder diffractometer at the Laboratoire Léon Brillouin (LLB) in Saclay, France and the POWGEN powder diffractometer at the Spallation Neutron Source (SNS), Oak Ridge, USA. In principle, neutron powder diffractometers can be divided into two distinct types, i.e. diffractometers using a monochromatic neutron beam usually built at nuclear reactors and diffractometers using a pulsed neutron beam usually built at spallation sources (for an overview, see Willis and Carlile, 2009). The type of instrument imposes certain specifications for powder diffraction measurements. While both SPODI and 3T2 use a monochromatic neutron beam, POWGEN employs a pulsed beam.

In the following, as an example for powder diffractometers at nuclear reactors, the SPODI diffractometer will be described. A sketch of a powder diffractometer using a monochromatic neutron beam is shown in Fig. 1.1. At SPODI, an incoming white neutron beam from the

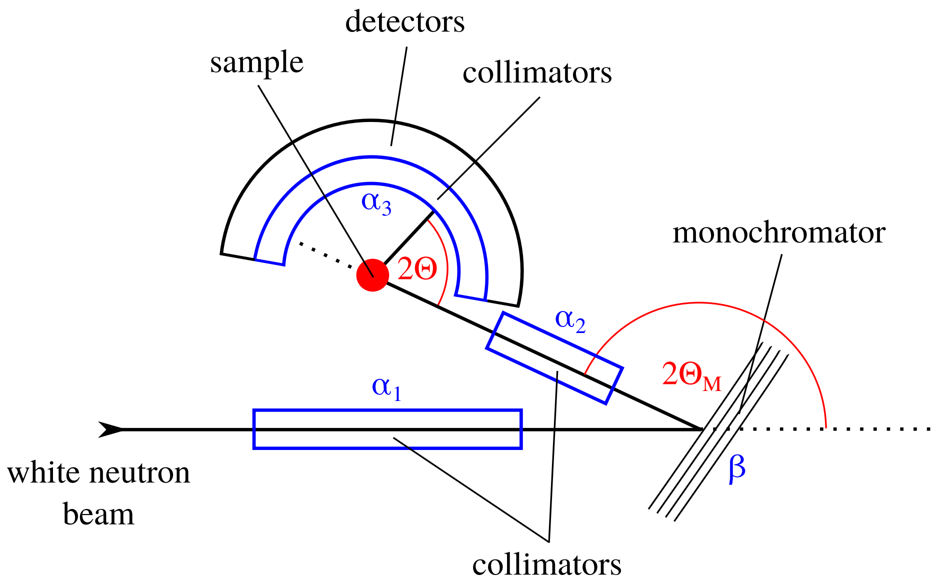

Fig. 1.1 Sketch of an angle-dispersive, monochromatic neutron powder diffractometer at a nuclear reactor in parallel configuration.

reactor passes through a collimator and arrives at a monochromator crystal where a fixed wavelength is selected by Bragg scattering. Specifically, all SPODI measurements presented in this thesis were carried out using a Ge-(551) monochromator that produces neutrons with a wavelength of 1.5482 Å (Hoelzel et al., 2012). SPODI makes use of an extremely large take-off angle $2\Theta_\mathrm{M}$ of 155°. The monochromatic neutron beam then hits a polycrystalline or powder sample with a sample volume of approximately $1\,\mathrm{cm}^3$.

SPODI and most other neutron powder diffractometers operate in a so-called parallel configuration meaning that the twice reflected neutron beam experiences a focusing effect that reduces the full width at half maximum s of the reflections (Willis and Carlile, 2009). The resolution of a monochromatic powder diffractometer was derived by Caglioti et al. (1958) who considered essentially 4 parameters, namely the mosaicity of the monochromator (β), the horizontal beam divergence between source and monochromator (denoted as α_1), the horizontal beam divergence between monochromator and sample (denoted as α_2) and the horizontal beam divergence between sample and detector (denoted as α_3). With these parameters, s is calculated as

$$s = \sqrt{U\tan^2\Theta + V\tan\Theta + W} \tag{1.1}$$

with

$$U = \frac{4(\alpha_1^2\alpha_2^2 + \alpha_1^2\beta^2 + \alpha_2^2\beta^2)}{\tan^2\Theta_M(\alpha_1^2 + \alpha_2^2 + 4\beta^2)} \tag{1.2}$$

$$V = -\frac{4\alpha_2^2(\alpha_1^2 + 2\beta^2)}{\tan\Theta_M(\alpha_1^2 + \alpha_2^2 + 4\beta^2)} \tag{1.3}$$

$$W = \frac{\alpha_1^2\alpha_2^2 + \alpha_1^2\alpha_3^2 + \alpha_2^2\alpha_3^2 + 4\beta^2(\alpha_2^2 + \alpha_3^2)}{\alpha_1^2 + \alpha_2^2 + 4\beta^2} \tag{1.4}$$

According to Hoelzel et al. (2012), at SPODI the crystal mosaicities are 20’ and 11’ in horizontal and vertical direction, and the beam is collimated to horizontal beam divergences of $\alpha_1 = 20'$, $\alpha_2 = 25'$ and $\alpha_3 = 10'$. This results in s values $<$ 0.325° for 15° $<$ 2Θ $<$ 110°.

SPODI makes use of 80 ^{3}He detector tubes with fixed Soller collimators that cover an angular range of 160° (Hoelzel et al., 2012). The employed ^{3}He tubes are 2D detectors with a vertical resolution of approximately 3 mm. Diffractograms are recorded by stepwise scanning the entire angular range (0 to 160°) with a step width of $\Delta(2\Theta) = 0.05$ for the high-resolution diffractograms in this thesis and with a step width of $\Delta(2\Theta) = 0.1$ for the in-situ diffractograms employing a constant heating ramp. Additionally, in order to increase the data reliability, in the high-resolution diffractograms every angular step was recorded by more than 1 (usually 4) detectors, which was however omitted in the in-situ measurements in order to obtain a better temperature resolution.

At a pulsed instrument, the measurement principle is different. Here, a pulsed white neutron beam is produced via high energy protons hitting e.g. a liquid mercury target (Willis and Carlile, 2009). At the SNS, the pulse frequency is 60 Hz. The created neutron pulses are then directed via a thin moderator onto the sample. In the white neutron beam, a distribution of wavelengths is contained that travels the distance from source to detector in different times. The faster neutrons with a shorter wavelength need less time than the slower neutrons with a longer wavelength. The detectors are fixed in place and the entire diffraction pattern is recorded as a function of the time-of-flight which encodes the wavelength of a particular neutron detected. The boundary condition of this procedure is to ensure that every detected neutron originates from the same pulse, meaning that so-called frame overlap has to be avoided. This is usually done using wavelength choppers in the incident beam. Clearly, the wavelength band that can be recorded without frame overlap depends on the distance between source and detector L as well as the pulse frequency of the source f and can be calculated according to Willis and Carlile (2009) via

$$\Delta\lambda = \frac{h}{m_N} = \frac{3956\frac{\text{Å}m}{s}}{L \cdot f} \tag{1.5}$$

with h being the Planck constant and m_N being the mass of the neutron. At POWGEN, f = 60 Hz and L = 62.5–64.5 m depending on the detector bank (Huq et al., 2011). Hence, POWGEN has a bandwidth of approximately 1 Å. For larger wavelength bands, the choppers

cw (Å)	λ_{min} (Å)	λ_{max} (Å)	q_{min} (Å^{-1})	q_{max} (Å^{-1})
1.333	0.8	1.866	1.0239	15.1700
2.665	2.132	3.198	0.5975	5.6923

Table 1.1 Wavelengths bands used at POWGEN for the measurements presented in this thesis. The accessible 2Θ range of the instrument is 17.5° to 150°.

have to rotate at lower frequency basically removing every other pulse completely. Using choppers with 60 Hz, several wavelength bands can be selected. In this thesis, measurements were performed using 2 distinct wavelengths bands covering different Q-ranges which are referred to with respect to their center wavelength *cw*. Those 2 wavelengths bands including their respective specifications are given in Tab. 1.1.

While the peak shape of instruments using a monochromatic neutron beam as SPODI is a simple Gaussian (Hoelzel et al., 2012), peak shapes of time-of-flight instruments are more complicated. As pointed out by Von Dreele et al. (1982), the peak shape at such instruments arises from a convolution of two exponential functions describing the neutron pulse and a Gaussian instrumental contribution. The instrument resolution for time-of-flight instruments is given by the following expression (Willis and Carlile, 2009)

$$\frac{\Delta Q}{Q} = -\frac{\Delta t}{t} + \frac{\Delta L}{L} + \cot(\Theta)\Delta\Theta \tag{1.6}$$

where $\frac{\Delta t}{t}$ is the relative uncertainty in flight time, $\frac{\Delta L}{L}$ is the relative uncertainty in length between the moderator and the detector and $\Delta\Theta$ is the uncertainty in the (half) scattering angle. In the Rietveld refinements of the time-of-flight powder diffraction data, a back-to-back exponential function multiplied with a pseudo-Voigt function was employed using parameters provided by the instrument scientists as obtained from measuring standard samples.

Intensity distribution in neutron powder diffraction measurements

The intensity distribution in neutron powder diffraction measurements is composed of four parts, i.e. elastic and inelastic scattering with a coherent and incoherent contribution, respectively. The sharp, δ-like peaks known from diffraction experiments on crystalline materials result from the coherent elastic contribution while incoherent elastic scattering and inelastic scattering do not result in sharp peaks. However, due to a finite instrument resolution, it is necessary to model the background and subtract it from the diffraction pattern in order to obtain the (integrated) intensity of the Bragg peak. The intensity distribution of the Bragg peaks in reciprocal space which is the main quantity of interest in powder diffraction experiments can in turn be derived from the differential cross section for coherent elastic scattering $\frac{\mathrm{d}\sigma}{\mathrm{d}\Omega}$. For Bravais crystals according to Squires (2012), this differential cross section $\frac{\mathrm{d}\sigma}{\mathrm{d}\Omega}$ is given as

$$\left(\frac{\mathrm{d}\sigma}{\mathrm{d}\Omega}\right)_{\text{coherent, elastic}} = \frac{\sigma_{\text{coherent}}}{4\pi} N \frac{(2\pi)^3}{v_0} \exp(-2W) \sum_{\boldsymbol{\tau}} \delta(\mathbf{Q} - \boldsymbol{\tau}) \tag{1.7}$$

with $\sigma_{\text{coherent}} = 4\pi(\bar{b})^2$ being the coherent scattering cross section and $\bar{b}$ being the average scattering length in the one atomic Bravais unit cell, N being the number of unit cells in the crystal, v_0 being the volume of the unit cell, $\exp(-2W)$ being the so-called Debye-Waller factor and $\sum_{\boldsymbol{\tau}} \delta(\boldsymbol{Q} - \boldsymbol{\tau})$ describing the scattering condition. Here, $\boldsymbol{\tau}$ denotes a reciprocal lattice vector while $\boldsymbol{Q} = \boldsymbol{k} - \boldsymbol{k}'$ is the scattering vector with $\boldsymbol{k}$ being the wave vector of the incoming neutron and $\boldsymbol{k'}$ being the wave vector of the scattered neutron. It is apparent that this cross-section for coherent elastic scattering is only non-zero when the scattering vector equals a reciprocal lattice vector which is well known as Bragg's law.

Furthermore, this expression can be determined for non-Bravais lattices with more than one atom in the unit cell, which defines the situation for almost all scenarios of interest within in the scope of this thesis. Also according to Squires (2012), this differential cross-section can be written as

$$\left(\frac{\mathrm{d}\sigma}{\mathrm{d}\Omega}\right)_{\text{coherent, elastic}} = N \frac{(2\pi)^3}{v_0} \sum_{\boldsymbol{\tau}} \delta(\mathbf{Q} - \boldsymbol{\tau}) |F_N(\boldsymbol{Q})|^2 \tag{1.8}$$

where an additional term $|F_N(\boldsymbol{Q})|^2$ appears in the sum that already contains the slightly modified Debye-Waller factor. Specifically, $F_N(\boldsymbol{Q})$ is the so-called nuclear unit cell structure factor given as (Squires, 2012)

$$F_N(\mathbf{Q}) = \sum_{\boldsymbol{d}} \bar{b}_d \exp(\mathrm{i}\mathbf{Q} \cdot \boldsymbol{d}) \sqrt{\exp(-2W_d)} \tag{1.9}$$

with a sum over all unit cell positions d, $\bar{b}_d$ being the average scattering length at position $\boldsymbol{d}$ and $\exp(-2W_d)$ being the Debye-Waller factor at position $\boldsymbol{d}$ in the unit cell.

The Debye-Waller factor thereby accounts for the average displacement of atoms from their equilibrium position in the crystal and can, according to Squires (2012), in the case of cubic crystals be written as

$$2W = \frac{1}{3}\mathbf{Q}^2 \langle \boldsymbol{u}^2 \rangle \tag{1.10}$$

Here the average displacement $\langle \boldsymbol{u}^2 \rangle$ is generally composed of a static contribution due to disorder or strain in the sample and a temperature dependent contribution due to oscillatory movements which are basically contained in the phonon density of states.

Furthermore, also for magnetic scattering, the cross-section for elastic scattering can be derived. According to Squires (2012) the cross-section for a multiple domain ferromagnet on a Bravais lattice where the magnetic peaks are superimposed on the nuclear peaks takes on the form

$$\left(\frac{\mathrm{d}\sigma}{\mathrm{d}\Omega}\right)_{\text{elastic}} = (\gamma r_0)^2 N \frac{(2\pi)^3}{v_0} \langle \boldsymbol{S^\eta} \rangle^2 \sum_{\boldsymbol{\tau}} \big(\frac{1}{2} g F(\boldsymbol{\tau})\big)^2 \exp(-2W) \big(1 - (\hat{\boldsymbol{\tau}} \cdot \hat{\boldsymbol{\eta}})^2_{\text{average}}\big) \delta(\boldsymbol{Q} - \boldsymbol{\tau}) \tag{1.11}$$

with γ being the half of the Landé factor of the neutron with a value of -1.91, r_0 being the classical radius of the electron with a value of $2.818 \cdot 10^{-15}$ m, N being the number of unit cells, v_0 being the volume of the unit cell, $\langle \boldsymbol{S^\eta} \rangle$ being the mean value of the spin in the direction of $\boldsymbol{\eta}$ for each domain, g being the Landé factor of the neutron, $F(\boldsymbol{\tau})$ being the magnetic form factor, $\exp(-2\mathrm{W})$ again being the Debye-Waller factor, the term $\big(1 - (\hat{\boldsymbol{\tau}} \cdot \hat{\boldsymbol{\eta}})^2_{\text{average}}\big)$ taking into account the orientation of the spins with respect to the scattering vector (note, in case that all directions are equally likely, this term takes on a value of $2/3$) and $\delta(\boldsymbol{Q} - \boldsymbol{\tau})$ again being related to the Bragg condition. Note, r_0 is in the same order of magnitude as typical values for the nuclear scattering length b and hence magnetic scattering is as a rule of thumb comparable in intensity to nuclear scattering in neutron diffraction.

Similarly, according to Squires (2012) the cross-section can be rewritten for antiferromagnetic (AFM) structures on the same lattice and takes on the form

$$\begin{aligned}\left(\frac{\mathrm{d}\sigma}{\mathrm{d}\Omega}\right)_{\text{elastic}} = (\gamma r_0)^2 N_m \frac{(2\pi)^3}{v_{0m}} \sum_{\boldsymbol{\tau_m}} \left(\left|\frac{1}{2} \langle \boldsymbol{S^\eta} \rangle g F(\boldsymbol{\tau_m}) \sum_{\boldsymbol{d}} \sigma_d \exp(\mathrm{i} \boldsymbol{\tau_m} \cdot \boldsymbol{d})\right|\right)^2 \\ \cdot \exp(-2W) \big(1 - (\hat{\boldsymbol{\tau}}_m \cdot \hat{\boldsymbol{\eta}})^2_{\text{average}}\big) \delta(\boldsymbol{Q} - \boldsymbol{\tau_m})\end{aligned} \tag{1.12}$$

In (1.12), due to the AFM spin alignment, the magnetic unit cell is doubled in size with respect to the nuclear unit cell. τ_m is a magnetic reciprocal lattice vector, N_m is the number of magnetic unit cells, v_{0m} is the volume of the magnetic unit cell and $\langle \boldsymbol{S^\eta} \rangle$ is the *staggered* mean spin referring to all ions in one sublattice. Also, a more complicated expression for the magnetic structure factor is contained given the non-equal occupancy of the lattice sites with up and down spins. Hence,

$$F_M(\tau_m) = \frac{1}{2} \langle \boldsymbol{S^\eta} \rangle g F(\boldsymbol{\tau_m}) \sum_{\boldsymbol{d}} \sigma_d \exp(\mathrm{i} \boldsymbol{\tau_m} \cdot \boldsymbol{d}) \cdot \sqrt{\exp(-2W) \big(1 - (\hat{\boldsymbol{\tau}}_m \cdot \hat{\boldsymbol{\eta}})^2_{\text{av.}}\big)} \tag{1.13}$$

is a sum over all ions in the magnetic unit cell where σ_d takes on values of ± 1. In a similar fashion, an elastic magnetic scattering cross-section can be denoted for any magnetic structure on a regular lattice.

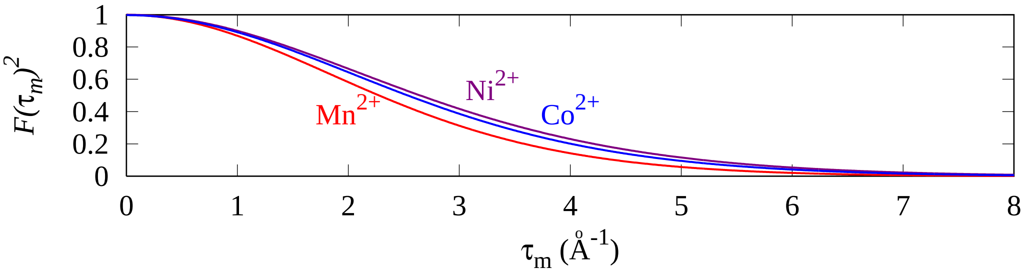

Fig. 1.2 Magnetic form factors for Mn^{2+}, Ni^{2+} and Co^{2+} in the dipole approximation as given in Brown (2003).

The magnetic form factor $F(\boldsymbol{\tau_m})$ is very important for scattering experiments since it describes the rapid decay of the magnetic intensity towards higher scattering angles. This thesis is primarily concerned with magnetic structures formed by the transition metals Mn, Ni and Co. For 3-d transition metals, spin-orbit coupling can be neglected and the magnetic form factor in the dipole approximation can be calculated based on empirical analytical expressions as tabulated by Brown (2003). Respective form factors for Mn^{2+}, Ni^{2+} and Co^{2+} are depicted in Fig. 1.2.

The differential cross-sections as described above are finally not the experimentally probed quantity. Rather, in diffraction experiments, the cross section of a Bragg peak, i.e. the integral of the differential cross-section over certain directions, is measured. In the case of powder diffraction, the total cross sections of Debye-Scherrer cones are of interest whose intensity/peak area can according to Squires (2012) be calculated via

$$A = \Phi \frac{V}{v_0^2} \frac{d\lambda^3}{8\pi r \sin\Theta \sin 2\Theta} \sum_{\boldsymbol{\tau}} |F_{N/M}(\boldsymbol{\tau})|^2 \tag{1.14}$$

where Φ is the neutron flux, $V = N v_0$ represents the volume of the crystal, λ is the neutron wavelength, d is th effective diameter of the neutron detector which is placed at a distance r from the target and $\sum_{\boldsymbol{\tau}}$ is the sum over all $\boldsymbol{\tau}$ with the same value of $|\boldsymbol{\tau}|$. In simple terms, the intensity of a peak is hence given by the square of the absolute structure factor, the multiplicity of the individual peak taking into account the statistical probability to find a crystallite oriented in a way to fulfill the Bragg condition for a particular lattice plane, the Lorentz factor given as $1/(\sin\Theta \sin 2\Theta)$ taking into account geometrical considerations, the Debye-Waller factor taking into account the intensity decay towards higher angles due to atomic displacements from the equilibrium position and, trivially, the sample size and neutron flux.

As originally introduced by Rietveld (1969), structure factor determination of powder diffraction data usually involves so-called Rietveld refinement, i.e. the calculation of the entire diffractogram assuming a certain structural/magnetic model and comparing the resulting pattern with the experimentally observed pattern. In a further step, the parameters of the model are adjusted by a least-squares minimization algorithm in order to minimize the difference between the calculated and observed diffractogram. Finally, the initial model has been refined to match the observed pattern as good as possible and the model parameters such as e.g. sublattice occupancies, lattice constants, Debye-Waller factors, magnetic moments, strain and size broadening as well as peak shape parameters can be extracted. Such a Rietveld refinement process has been performed for most powder diffractograms recorded in this thesis using the FullProf suite (Rodriguez-Carvajal, 1990, 1993; Rodriguez-Carvajal and Roisnel, 1998; Roisnel and Rodriguez-Carvajal, 2000).

1.2 X-ray powder diffraction

In this thesis, X-ray powder diffraction has been employed on the one hand as a complement to the neutron powder diffraction measurements and on the other hand as pre-characterization method to confirm sample quality. While the general principles of powder diffraction elucidated above for the case of neutron diffraction also apply to X-ray diffraction, there are some important differences. Mainly, the atomic form factor for X-ray scattering is in opposition to the atomic form factor for neutron scattering not a constant. The reason for this is that X-rays scatter at the electron density $\rho(\boldsymbol{r})$ instead of the nuclear potential. The atomic form factor is the Fourier transform of this electron density which has a significant spatial extension. As a consequence, the X-ray atomic form factor decays as a function of $\boldsymbol{Q}$. Specifically, the atomic form factor for X-ray scattering can be calculated according to Fultz and Howe (2012) as

$$f(\boldsymbol{Q}) = \frac{e^2}{mc^2} \int_{\mathbb{R}} \rho(\boldsymbol{r}) \exp\left(-\mathrm{i}\boldsymbol{Q} \cdot \boldsymbol{r}\right) d^3\boldsymbol{r} \tag{1.15}$$

with e being the charge of the electron, m being the mass of the electron and c being the speed of light. Due to the dependency on the integral of the electron density, the X-ray atomic form factor is proportional to the atomic number Z. This imposes an interesting implication as the scattering contrast in X-ray diffraction is very different from the neutron scattering contrast. Consequently, in many cases, the combination of X-ray and neutron scattering allows to obtain independent information necessary to solve for example the question of site occupancies in a compound.

The X-ray powder diffractograms presented in this thesis have been measured on a laboratory Rigaku SmartLab diffractometer at Tohoku University, Japan using Cu-K_α radiation and a Bragg-Brentano geometry. Samples for X-ray diffraction have been ground manually to grain sizes $< 32\,\mu$m. Similar to the neutron diffractograms, also the X-ray diffractograms presented in this thesis have been Rietveld refined using the FullProf suite.

1.3 Electron diffraction

Besides neutron and X-ray diffraction, specifically for the Ni_2MnAl system, also electron diffraction has been employed within the scope of this thesis in order to decipher the nuclear structure of these compounds. While X-rays scatter at the electron density, electrons interact with a Coulomb like potential and are as a consequence as elucidated in Fultz and Howe (2012) scattered much more strongly than X-rays. Electron diffraction in this thesis was performed using a Transmission Electron Microscope (TEM) on very thin polycrystalline samples. Due to the small thickness of the samples, usually only a single grain is imaged and hence electron diffraction is in principle a single crystal diffraction method. In the TEM, the measurement background for electron diffraction experiments is usually low. This is of advantage especially when broad and low intensity superstructure peaks stemming from incipient ordering processes are investigated, as it is the case for Ni_2MnAl. However, in contrast to X-ray and neutron diffraction, in electron diffraction, due to the strong interaction, the kinematic scattering theory does not always apply and hence, a quantitative analysis of electron diffraction images is usually not easily possible.

The set-up of a TEM is complex, consisting of a series of lens systems to enable a variety of imaging modes. This thesis is only concerned with the diffraction mode. Here, a electron gun produces a continuous ray of electrons which are accelerated using high acceleration voltages of several hundred kV. An illumination lens system ensures that the electrons travel straight and parallel to the optical axis when they hit the sample. A so-called objective lens is positioned right behind the sample with the sample being located in its object plane. The objective lens images the sample in the image plane while the diffraction pattern is formed in its back focal plane. An intermediate lens is focused on this back focal plane and projects the diffraction pattern onto a screen, an image plate or a CCD camera. By using an intermediate aperture in the image plane, it is further possible to extract the diffraction pattern of certain areas of the sample. This operation mode is then called Selected Area Diffraction (SAD), yet it was not prominently used in this thesis. For a detailed overview about TEM methods, please resort to Fultz and Howe (2012).

Electron diffraction experiments for this thesis have been performed in collaboration with Yuta Kimura in the group of Ryosuke Kainuma at Tohoku University, Japan using a JEOL JEM-2100 (HC) microscope operating at an acceleration voltage of 200 kV. Samples have been prepared by cutting thin sheets from the bulk ingots using a low speed diamond saw followed by grinding the sheets to thicknesses of approximately 60 μm. After punching disc shaped specimens from the sheets, the discs have been jet-polished using a solution of 20 % perchloric acid in methanol.

1.4 Magnetization measurements

Magnetization measurements for this thesis have been performed using magnetic induction methods, specifically Vibrating Sample Magnetometry (VSM) and Superconducting Quantum Interference Device (SQUID) magnetometry.

VSM is based on the Faraday law of electromagnetic induction (Jiles, 2015) which states that the electromotive force induced in a coil/closed circuit is proportional to the negative flux change rate through the coil. Hence, by moving a magnetic sample through an arrangement of detection coils, the magnetization of the sample can be determined. The measurement principle of the VSM was proposed by Foner (1956, 1959) as an evolution of the Vibrating Coil Magnetometer. In the common set-up, large field coils provide an external magnetic field while the sample is oscillated perpendicular to this field (Foner, 1959). This oscillation of the magnetic sample induces a voltage in the detection coils. In order to make sure that the extracted signal is independent of the exact sample position, the sample position is adjusted between the coils to evoke a minimal signal in direction of the detection coils and a maximal signal in the direction orthogonal to them. The VSM measurements for this thesis have been performed using a TOEI VSM covering a temperature range from 77 K to 690 K and providing external magnetic fields up to 1.6 T. To calibrate the instrument, a Ni standard sample was used. Sample preparation for VSM samples was performed by cutting or breaking small approximately rectangular pieces from the bulk ingots with masses of 20–60 mg depending on the materials' saturation magnetizations.

SQUID magnetometers provide nowadays the best resolution for field measurements (Jiles, 2015). They are based on the concept of a so-called Josephson junctions, i.e. thin barrier layers (e.g. insulators) in a superconducting material. Specifically, a SQUID is composed of a superconducting ring with one (RF-SQUID) or two (DC-SQUID) barrier layers called “weak links”. Changes of the magnetic flux threading the ring result in a periodic change of the critical current of the junctions while the period corresponds to a flux quantum (Jiles, 2015). As a consequence, upon flux change, the voltage-current characteristic oscillates in a sinusoidal fashion. The device acts as a flux-to-voltage converter and can be used to detect smallest changes in magnetic flux. For a detailed review on SQUID technology and systems, see John and Alex (2004).

In this thesis, $M(T)$ and $M(H)$ SQUID measurements were performed using a Magnetic Property Measurement System (MPMS) by Quantum Design, Inc. Specifically, SQUID measurements were partially performed in collaboration with Xiao Xu at the Center for Low Temperature Science, Institute for Materials Research at Tohoku University, Japan and partially in collaboration with Matthias Opel at the Walther-Meißner-Institute for Low Temperature Research of the Bavarian Academy of Sciences and Humanities, Germany in a temperature range from 5 K to 350 K and in a field range up to 7 T. In most cases, the SQUID was operated in the so-called RSO (reciprocating sample oscillation) mode where the sample oscillates continuously. However, in samples with large absolute magnetizations, the DC mode was applied where the sample is moved through the pick-up coils in discrete steps.

1.5 Calorimetric measurements

Calorimetric measurements for this thesis have been performed employing Differential Scanning Calorimetry (DSC). Differential Scanning Calorimeters are based on the concept of measuring the heat flow between a sample and a reference that undergo a common controlled temperature treatment. Due to the difference principle, external factors (e.g. external temperature variations) affecting both the sample and the reference in the same way do not influence the signal which is a tremendous advantage in comparison to the design of conventional calorimeters. In general, two measurement principles need to be distinguished: heat flux DSCs and power compensation DSCs (for an overview see Höhne et al., 2013). In heat flux DSCs, the difference in heat flow to a sample and a reference both located in the same furnace is measured upon heating the furnace usually with a constant heating ramp (Höhne et al., 2013). As long as sample and reference behave identically, the signal is zero. However, as soon as the sample undergoes a phase transition, latent heat needs to be provided or is released. As a consequence, the heat flow to the sample is different from the heat flow to the reference which is expressed in a peak in the differential heat flow signal. In power compensation DSCs, two identical furnace set-ups, one containing the reference and the other one containing the sample, are heated with the same heating ramp while the heating power provided to either furnace is monitored. The signal is the difference in heating power that has to be provided to the furnaces in order to follow the pre-set temperature program. If the sample undergoes a phase transition, the power that needs to be provided to the sample

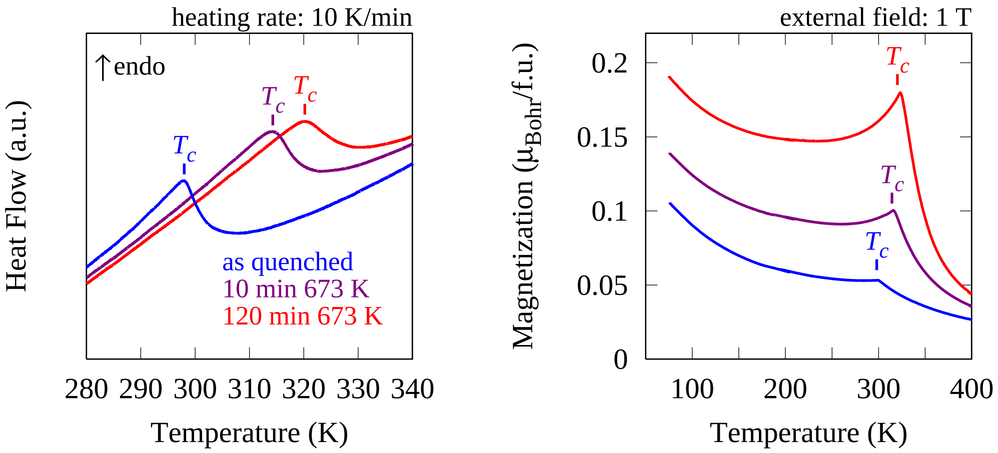

Fig. 1.3 DSC (left panel) and VSM (right panel) measurements on $Ni_2Mn_{1.12}Al_{0.88}$ samples in different annealing conditions. In the calorimetric measurements and in the $M(T)$ measurements, the evolution of $L2_1$ order with increased annealing time can clearly be followed with the magnetic transition temperature being increased upon annealing.

furnace is different from the powder that needs to be provided to the reference furnace which is again visible as a peak in the signal.

In this thesis, calorimetry was mainly used to follow the $L2_1$ ordering kinetics in Heusler system by means of tracking the magnetic transition temperature T_c as a function of isothermal annealing time at various annealing temperatures. In order to apply a consistent method for determination of T_c, the calorimetric signal of the magnetic transition has been modeled by two continuously joint second-degree polynomials convolved with a centered Gaussian kernel. Fig. 1.3 shows as an example DSC curves (left panel) and $M(T)$ curves measured in a VSM (right panel) of $Ni_2Mn_{1.12}Al_{0.88}$ samples quenched from 1273 K (B2-stable regime) with subsequent annealing at 673 K ($L2_1$-stable regime). With increased annealing time, clearly a shift in the magnetic transition temperature, as well as an overall increase in the bulk magnetization is observed. The T_c values obtained from fitting the calorimetric signal are indicated above the curves. Evidently, the transition temperatures determined from DSC coincide with the cusps in the $M(T)$ curves.

DSC measurements in this thesis have been performed on 3 different instruments. Low temperature DSC measurements between approximately 200 K and 850 K were carried out with a Seiko SII Exstar 6200 DSC and a Perkin Elmer DSC 8500 using Cu and Al sample pans. High temperature DSC measurements have been performed using a Netzsch DSC 404 C Pegasus in a temperature range from room temperature to 1500 K. Before the measurement, all samples have been carefully polished to ensure a good thermal contact between the sample and the pan. All DSCs have been temperature and heat flow calibrated over the entire measurement range.

1.6 Sample preparation

Samples for this thesis have been prepared by induction melting and tilt or suction casting of high-purity elements under Argon atmosphere. After casting, all samples have been subject to a solution annealing treatment at 1173–1273 K for 48–72 h depending on the alloy system in order to remove segregation effects from casting. In the case of the NiCoMnGa and NiCoMnAl polycrystalline bulk neutron diffraction samples, shorter solution annealing treatments have been applied in order to restrict grain growth. After solution annealing, samples have been quenched in room temperature or iced water. All additional heat treatments and sample preparation procedures were performed on the solution annealed and quenched bulk ingots as outlined in the individual chapters.

All ingots have been checked for their actual composition using Wavelength-Dispersive X-Ray Spectroscopy (WDS) or Energy-Dispersive X-Ray Spectroscopy (EDS). WDS measurements have been performed in collaboration with the group of Ryosuke Kainuma at Tohoku University, Japan. EDS measurements have been performed at the Staatliche Materialprüfamt für den Maschinenbau at Technische Universität München, Germany. For EDS and WDS analysis, thin plates have been cut from the solution annealed ingots that have been mirror-polished in order to provide an adequate surface quality for the measurements. The measured compositions for all samples prepared and used in this thesis is given in Tab. 1.2. The values given are averaged over 8 randomly selected measurements points on the sample in the case of WDS analysis and 5 randomly selected measurements points in the case of EDS analysis.

Additionally, all samples have been checked for homogeneity, i.e. the absence of phase decomposition, using Scanning Electron Microscopy. Also, as standard characterization procedure, samples have been subject to calorimetric measurements in order to retrieve magnetic and structural transition temperatures as a comparison to values reported in the literature.

As pointed out in Chapter 5, bulk ingots for the $\mathrm{Ni}_{2-x}\mathrm{Co}_x\mathrm{MnAl}$ system have been partially obtained from the group of Ryosuke Kainuma at Tohoku University, Japan. Yet, also for those samples, solution heat treatment and sample pre-characterization has been performed by the author of this thesis in order to apply the same preparation protocol to all samples used in the scope of this thesis.

Chapter 2,Chapter 3

Compound	Ni (at. %)	Mn (at. %)	Ga (at. %)	Al (at. %)
$Ni_2MnAl_{0.5}Ga_{0.5}$	50.45(26)	25.87(20)	11.97(14)	11.74(20)
Ni_2MnAl	51.03(22)	24.91(27)	24.06(17)	
$^aNi_2Mn_{1.12}Al_{0.88}$	50.46(19)	28.25(10)	-	21.29(20)
$^bNi_2Mn_{1.12}Al_{0.88}$	50.63(17)	28.37(22)	-	21.00(24)
$^cNi_2Mn_{1.12}Al_{0.88}$	49.85(13)	29.15(38)	-	21.01(26)

Chapter 4

Compound	Ni* (at. %)	Mn* (at. %)	Ga* (at. %)	Al* (at. %)
$^aNi_2MnAl_{0.5}Ga_{0.5}$	50.97(16)	26.29(13)	11.23(14)	11.50(14)
$^bNi_2MnAl_{0.5}Ga_{0.5}$	51.19(27)	25.69(18)	11.15(16)	11.97(46)
$^aNi_2MnAl$	49.74(18)	25.61(11)	24.65(13)	
$^bNi_2MnAl$	48.84(19)	25.56(14)	25.59(15)	

Chapter 5

Compound	Ni (at. %)	Co (at. %)	Mn (at. %)	Al (at. %)
$Ni_{50}Co_0MnAl$	51.03(22)	-	24.91(27)	24.06(17)
$Ni_{49}Co_1MnAl$	49.51(10)	1.04(03)	24.24(49)	25.22(54)
$Ni_{47}Co_3MnAl$	47.33(16)	3.21(03)	24.51(42)	24.95(50)
$Ni_{45}Co_5MnAl$	45.06(16)	5.14(04)	25.32(48)	24.47(41)
$Ni_{43}Co_7MnAl$	43.04(10)	7.17(06)	25.59(53)	24.20(51)
$Ni_{40}Co_{10}MnAl$	40.01(19)	10.35(14)	25.96(26)	23.68(38)
$Ni_{35}Co_{15}MnAl$	35.48(33)	15.52(09)	24.31(48)	24.69(16)

Chapter 6

Compound	Ni (at. %)	Co (at. %)	Mn (at. %)	Ga/Al (at. %)
NiCoMnGa	25.56(16)	23.41(09)	26.06(15)	24.97(21)
NiCoMnAl	25.06(10)	25.47(14)	25.69(48)	23.78(50)

Chapter 7

Compound	Ni (at. %)	Mn (at. %)	Sb (at. %)	-
$Ni_{1.05}MnSb$	34.02(25)	33.62(19)	32.36(27)	
$Ni_{1.25}MnSb$	38.15(27)	31.70(11)	30.15(25)	
$Ni_{1.50}MnSb$	42.53(23)	29.19(18)	28.29(18)	
$Ni_{1.60}MnSb$	44.16(19)	27.93(11)	27.91(14)	
$Ni_{1.75}MnSb$	46.50(57)	27.01(50)	26.50(21)	

Table 1.2 Sample compositions as determined by WDS/EDS*.

Chapter 2

Magnetic properties of Ni_2MnZ Heusler compounds

2.1 Introduction

Order-dependent functionality

Heusler alloys are a class of materials introduced by Heusler (1903, 1904); Heusler et al. (1903) that show a number of interesting properties and functionalities (Graf et al., 2011). With the discovery of the ferromagnetic shape memory effect (FSME) by Murray et al. (2000); Ullakko et al. (1996) and later the magnetocaloric effect (MCE) by Hu et al. (2000), specifically the subfamily of Ni_2MnZ Heusler alloys has drawn considerable attention in recent decades. Both the shape memory and the magnetocaloric effect rely on the transformation of a high temperature austenite phase into a low temperature martensite phase that evolves from the $L2_1$-ordered austenite parent phase via a diffusionless phase transition. The FSME is then a results of a magnetic field-induced reorientation of martensitic variants leading to a strain in the material (James and Wuttig, 1998; Likhachev and Ullakko, 2000). The MCE is based on the entropy change upon application of a magnetic field which initiates a martensitic transition that is coupled to a change in magnetic properties (Krenke et al., 2005; Liu et al., 2012). Needless to say, the magnitude of the MCE is very sensitive to the structural and magnetic transition temperatures as well as to the magnetic properties of the austenite and martensite phases. Understanding the magnetic properties of Ni_2MnZ alloys is thus a necessity in order to tailor the functionality of these materials.

While the martensite phase in Ni_2MnZ compounds has a non-cubic (tetragonal, monoclinic or orthorhombic) modulated or unmodulated structure (see for instance Brown et al., 2002; Martynov and Kokorin, 1992; Pons et al., 2000; Sozinov et al., 2002), the austenite phase adopts the cubic full-Heusler $L2_1$ structure with space group 225 ($Fm\bar{3}m$)[1] (see for example Webster et al., 1984). This structure is characterized by the inequivalent occupancies of the Wyckoff positions 8c, 4a and 4b by Ni, Mn and Z, respectively, with Z usually being a post-transition metal such as e.g. Al, Ga, In, Sn, Sb, etc. In most Ni_2MnZ alloys, the $L2_1$ structure transforms at high temperatures into the B2 (CsCl) structure (Webster and Ziebeck, 1988) of space group 221 ($Pm\bar{3}m$) with Wyckoff positions 1a and 1b – 1a being preferentially occupied by Ni and 1b being randomly occupied by Mn and Z. The B2-$L2_1$ transition is a second order phase transition, resulting in intermediate degrees of $L2_1$ order being present in many Ni_2MnZ compounds under realistic conditions. Clearly, the degree of $L2_1$ order in the austenite parent phase is imprinted onto the martensitic structure since the diffusionless transition does not allow for a reconfiguration of atoms. Interestingly, the degree of $L2_1$ order was observed to have a profound influence on the martensitic transformation temperature and also the crystal structure of the low temperature martensite phase (Kainuma et al., 2000) and hence, it is of tremendous importance to fundamentally understand the ordering process from B2 to $L2_1$.

The prototypical Ni_2MnZ alloy showing the FSME is Ni_2MnGa. However, with Ni_2MnGa being inherently brittle, the search for more ductile and cost-effective alloys is ongoing. The closely related Ni_2MnAl system was in this respect identified as a promising candidate (Fujita et al., 2000; Gejima et al., 1999; Kainuma et al., 2000). Yet, the low ordering tendency observed in the Ni_2MnAl system restricts its functionality. The difficulty in preparing fully $L2_1$-ordered samples presumably results from a significantly lower B2-$L2_1$ transition temperature in comparison to Ni_2MnGa (Acet et al., 2002; Mañosa et al., 2004). With kinetics being drastically slowed down at the transition temperature, the adjustment of long-range order requires often impractically long annealing times, making it eventually impossible to obtain perfect $L2_1$ order in these compounds. However, as recently proposed by the author of this thesis (see Neibecker et al., 2014), elaborate annealing treatments taking advantage of quenched-in excess vacancies can be used in order to evoke relatively large degrees of $L2_1$ order even in Ni_2MnAl compounds.

Order-dependent magnetic properties

Besides influencing the martensitic transition, also the magnetic properties of Ni_2MnZ compounds are directly coupled to the nuclear structure of the austenite phase. This is the result of essentially two dominant exchange interactions present in the system which is expressed by the following Hamiltonian

---

[1] Space groups and Wyckoff positions as tabulated by Hahn (2005).

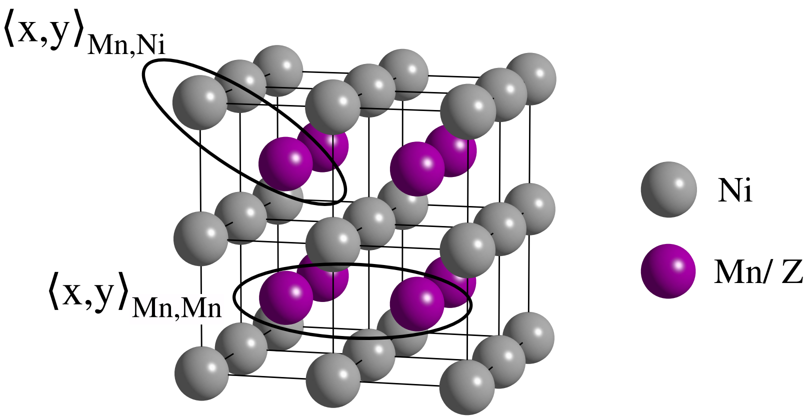

Fig. 2.1 Illustration of Mn neighbors in the disordered B2 structure in line with the notation of (2.1), (2.2).

$$H = -J_1 \sum_{\langle x,y\rangle_{\mathrm{Mn,Mn}}} \vec{\sigma}_x \vec{\sigma}_y - J_2 \sum_{\langle x,y\rangle_{\mathrm{Mn,Ni}}} \vec{\sigma}_x \vec{\sigma}_y \tag{2.1}$$

with sums over nearest Mn-Mn and nearest Ni-Mn neighbors (NN). NN Mn-Mn pairs here specifically refer to site-antisite pairs in the $L2_1$ structure (NN Mn-Mn pairs in the B2 structure) as illustrated in Fig. 2.1. Note that Ni magnetic moments in the stated Hamiltonian are assumed to be induced by their surrounding Mn moments (Ležaić et al., 2013; Simon et al., 2015) as described by

$$\vec{\sigma}^{\mathrm{Ni}} = \tfrac{1}{4} \sum_{\langle x\rangle_{\mathrm{Mn}}} \vec{\sigma}_x . \tag{2.2}$$

In (2.1), $J_1 < 0$ represents an antiferromagnetic (AFM) Mn-Mn NN interaction and $J_2 > 0$ represents a Ni-Mn ferromagnetic (FM) interaction. In the fully ordered $L2_1$ structure, no direct Mn-Mn pairs are present. Hence, the AFM interaction is absent and the magnetic exchange is reduced to the FM Ni-Mn interaction giving $L2_1$-ordered Ni_2MnZ compounds FM properties. However, in the disordered B2 structure, Mn and Z are randomly occupying the 1b position and hence direct Mn-Mn neighbor pairs that couple in an AFM fashion are present in the system. Furthermore, due to the Mn-Z disorder, the induced Ni moments are zero giving B2 ordered Ni_2MnZ compounds AFM properties (Acet et al., 2002). Note that due to the nuclear disorder, competition between FM and AFM exchange interactions is present in Ni_2MnZ systems and locally, non-collinear magnetic structures can exist. These competing interactions also lead to complicated magnetic properties in intermediate states of $L2_1$ order with a non-trivial transition between the AFM properties of the B2 structure and the FM properties of the $L2_1$ structure.

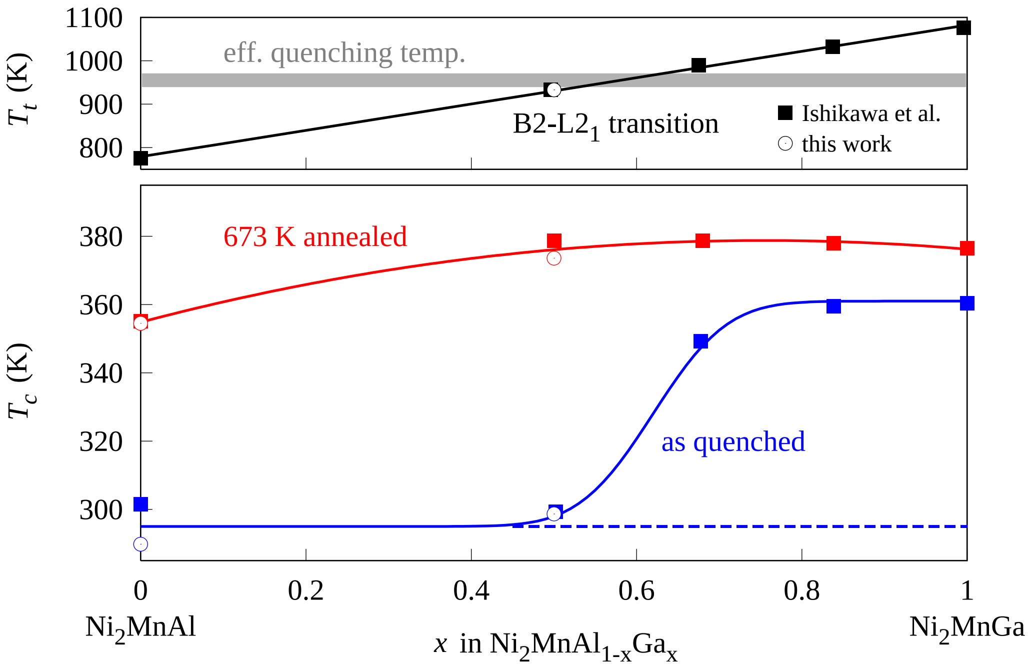

Fig. 2.2 Structural and magnetic phase diagram of $Ni_2MnAl_{1-x}Ga_x$ based on data measured in this thesis work and data reported by Ishikawa et al. (2008).

Recent results by Ishikawa et al. (2008); Umetsu et al. (2011) revealed that the local state of order alone is insufficient for explaining the magnetic properties of Ni_2MnZ alloys. Instead, also the microstructure was observed to play a vital role. Specifically, Ishikawa et al. (2008) demonstrated for the model alloy $Ni_2MnAl_{0.5}Ga_{0.5}$ that the L2$_1$ antiphase domain (APD) structure is inherently connected to the compound's magnetic properties. Due to the fact that in density functional theory (DFT) calculations, the size of the employed simulation cells rarely evoked the consideration of APD structures in the evaluation of magnetic properties, it is not very well understood so far by what mechanism the structural APDs influence the magnetism in these alloys. It was conjectured that at the antiphase domain boundary (APB) a disordered boundary phase is formed which is in its properties comparable to the AFM B2 phase (Murakami et al., 2013; Umetsu et al., 2011). Recent High-Resolution Scanning Transmission Electron Microscopy (HRSTEM) results by Murakami et al. (2013) seem to support this idea which is also in line with the two-phase state of B2 and L2$_1$ order postulated for related ternary compounds such as Ni_2MnAl (Acet et al., 2002). Furthermore, in off-stoichiometric Ni_2MnZ alloys, chemical segregation effects at APBs were recently observed by Niitsu et al. (2017) which demonstrates that APBs are able to provoke a phase decomposition under certain circumstances.

$Ni_2MnAl_{0.5}Ga_{0.5}$

The results in this chapter are inspired by numerous studies on the magnetic properties of $Ni_2MnAl_{0.5}Ga_{0.5}$ compounds (e.g. Ishikawa et al., 2008; Murakami et al., 2013, 2011; Park et al., 2012; Umetsu et al., 2011) and make use of the particular kinetic accessibility of states of order in this compound. As demonstrated by Ishikawa et al. (2008), $Ni_2MnAl_{0.5}Ga_{0.5}$ samples quenched from elevated temperatures show B2 order and AFM properties (comparable to Ni_2MnAl) while a special two-stage annealing treatment evokes $L2_1$ order and textbook FM properties (similar to Ni_2MnGa). This behavior can be understood based on the pseudo-binary $Ni_2MnAl_{1-x}Ga_x$ phase diagram presented in Fig. 2.2. Here, the magnetic transition temperatures T_c and the structural phase transition temperature T_t are presented as function of the composition x depicting data from Ishikawa et al. (2008) and from this work. First of all, it is quite evident that the T_t-x relation can well be described by a linear dependency as T_t monotonously increases with Ga content from Ni_2MnAl to Ni_2MnGa. At the same time, T_c in B2-quenched samples is rather constant at a value of $\approx$ 295 K on the Al rich side of the phase diagram, goes through a transition at just above 50 at. $\%$ Ga and is constant again above 75 at. $\%$ Ga at a value of $\approx$ 360 K. Isothermal annealing in the $L2_1$-stable regime (here at 673 K) equates T_c across the phase diagram at values between 360 and 380 K.

These observations can be explained with the help of an effective quenching temperature as indicated in the upper part of Fig. 2.2. The possibility to quench-in B2 order in $Ni_2MnAl_{0.5}Ga_{0.5}$ compounds indicates that upon quenching, the sample falls out of equilibrium above the B2-$L2_1$ transition temperature of 933 K. However, increasing the Ga content just moderately to 68 % drastically increases T_c of the as-quenched state. In fact, even though T_t increases just by $\approx$ 60 K, it appears that the sample falls out of equilibrium well in the $L2_1$-ordered regime. Assuming that the diffusion kinetics are comparable across the phase diagram, a claim well justifiable considering the similarity of Ni_2MnAl and Ni_2MnGa alloys, the temperature at which the samples fall out of equilibrium upon quenching can be confined to the narrow range of 940-980 K. As a consequence, compounds on the Ga rich side of the phase diagram fall out of equilibrium in the $L2_1$-stable regime and only allow to access very late stages of the $L2_1$ ordering process. Compounds on the Al rich side of the phase diagram fall out of equilibrium in the B2-stable regime and $L2_1$ order needs to be adjusted via secondary annealing treatments. Indeed, isothermal annealing at $T_a = 673$ K results in relatively constant T_c values across the phase diagram with slightly lower T_c values being observed on the Al rich side. This is however not surprising considering that the homologous annealing temperature T_a/T_t is higher in Ni_2MnAl than in Ni_2MnGa and the equilibrium T_c value at a given T_a accordingly lower. Therefore, it is plausible that the equilibrium magnetic properties of all $Ni_2MnAl_{1-x}Ga_x$ compounds are similar while the differences observed are presumably not of thermodynamic origin but rather a result of altered diffusion kinetics at the respective annealing temperatures.

As a consequence of the structural transition temperatures, the magnetic properties in $Ni_2MnAl_{0.5}Ga_{0.5}$ can be studied in practically all possible stages of order formation. Hence, this material is the ideal model material for investigating magnetic properties in disordered Ni_2MnZ compounds which is the main topic of this chapter. Furthermore, the acquired knowledge will be transferred to ternary Ni_2MnAl alloys where, as discussed, due to kinetics, only certain regimes of order formation are accessible. It is demonstrated that magnetic properties in Ni_2MnAl resemble the magnetic properties observed in $Ni_2MnAl_{0.5}Ga_{0.5}$ in very early stages of order formation.

2.2 Experimental results

2.2.1 $Ni_2MnAl_{0.5}Ga_{0.5}$

Order-dependent magnetic properties

Fig. 2.3a-d depict a series of $M(T)$ curves of $Ni_2MnAl_{0.5}Ga_{0.5}$ samples initially water-quenched from the B2-stable regime (1073 K) and subsequently annealed in the $L2_1$-stable regime at T_a = a) 573 K, b) 623 K, c) 673 K and d) 773 K in order to evoke $L2_1$ order in the samples. Magnetic transition temperatures for all depicted $M(T)$ curves have been obtained by Differential Scanning Calorimetry (DSC) and are given in Tab. 2.1 together with the corresponding annealing times. As can be seen, after quenching from the B2 regime, the samples show typical AFM behavior with a very low bulk magnetization M and a small cusp at the Néel temperature T_N. Upon isothermal annealing at low temperatures (e.g. T_a = 573 K, Fig. 2.3a), a consistent increase in T_N is observed together with an increase in M. Note that due to reasons of conciseness, in the following, the magnetic transition temperatures will be denoted as critical temperature T_c for all annealing conditions given that the magnetic properties in the compounds change from AFM to FM as function of the atomic order. Interestingly, with annealing, a pronounced cusp develops at T_c which in the early stages increases in size with increasing annealing time. Comparing isothermal annealing at 573 K to annealing treatments at higher temperatures (T_a = 623 K, 673 K, 773 K, Fig. 2.3b–d) reveals that initially the magnetization curves follow the same evolution pathway at all T_a. However, at elevated temperatures higher degrees of $L2_1$ order are kinetically accessible resulting in stronger FM properties. Note in this respect the different y-axis scales in Fig. 2.3a–f. With

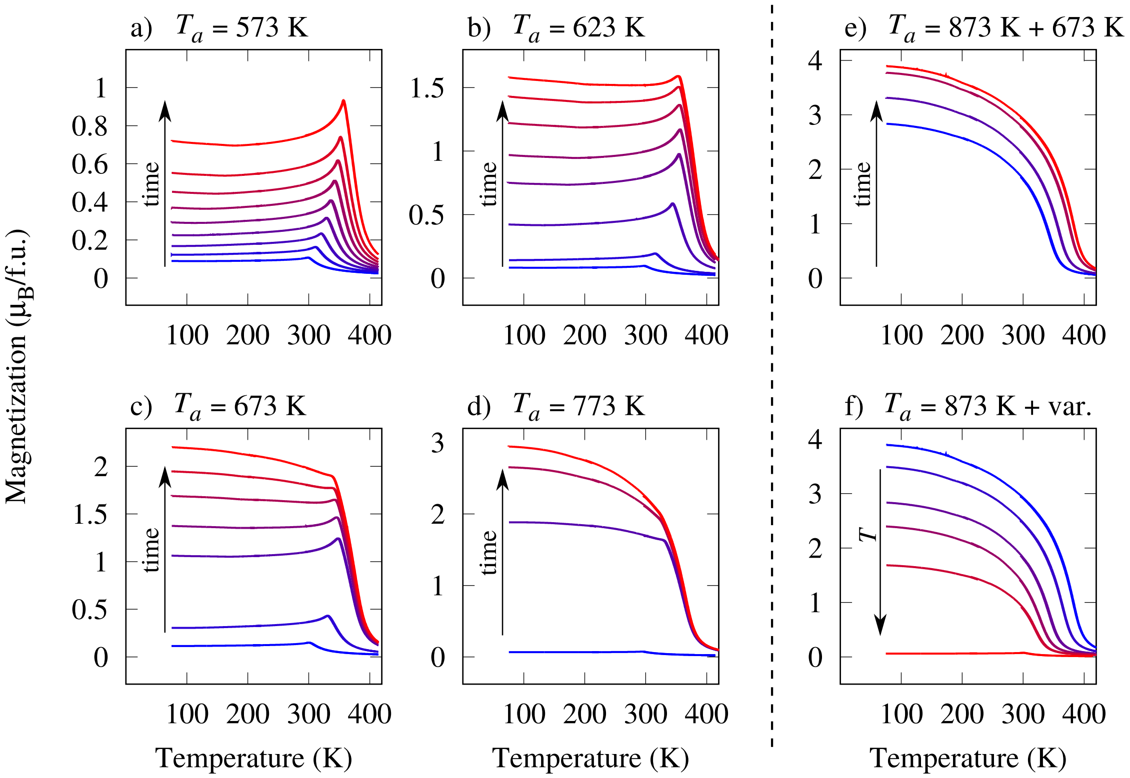

Fig. 2.3 Evolution of $M(T)$ curves upon annealing B2-ordered $Ni_2MnAl_{0.5}Ga_{0.5}$ samples at a) 573 K, b) 623 K, c) 673 K and d) 773 K. Measurements have been performed under an external magnetic field of 10 kOe. Magnetic transition temperatures for every depicted $M(T)$ curve have been determined by DSC measurements and are given in Tab. 2.1 together with the corresponding annealing times. e) depicts the evolution of the $M(T)$ curves in 24 h at 873 K annealed, quenched and subsequently at 673 K annealed samples while the different curves represent different annealing times at 673 K as given in Tab. 2.1. f) shows $M(T)$ curves for samples annealed for 24 h at 873 K followed by a 24 h annealing treatment at various lower temperatures. These temperatures are also given in Tab. 2.1. All $M(T)$ curves depicted here are directly related to the $M(H)$ curves presented in Fig. 2.4 and Fig. 2.5.

increasing $L2_1$ order, the cusp below T_c decreases again and is only slightly noticeable after isothermal annealing for 1440 min at 773 K.

Ishikawa et al. (2008) already reported these peculiar $M(T)$ curves for quenched samples and also presented a method to evoke textbook FM properties in $Ni_2MnAl_{0.5}Ga_{0.5}$ compounds via a two-stage annealing treatment of first 24 h at 873 K followed by additional annealing at lower annealing temperatures. Following this procedure and applying annealing treatments of 24 h at 873 K with additional annealing for 24 h at various lower temperatures yields the curves presented in Fig. 2.3f. Again, the corresponding annealing temperatures can be found in Tab. 2.1. Obviously, in the two-step annealed samples the cusp completely

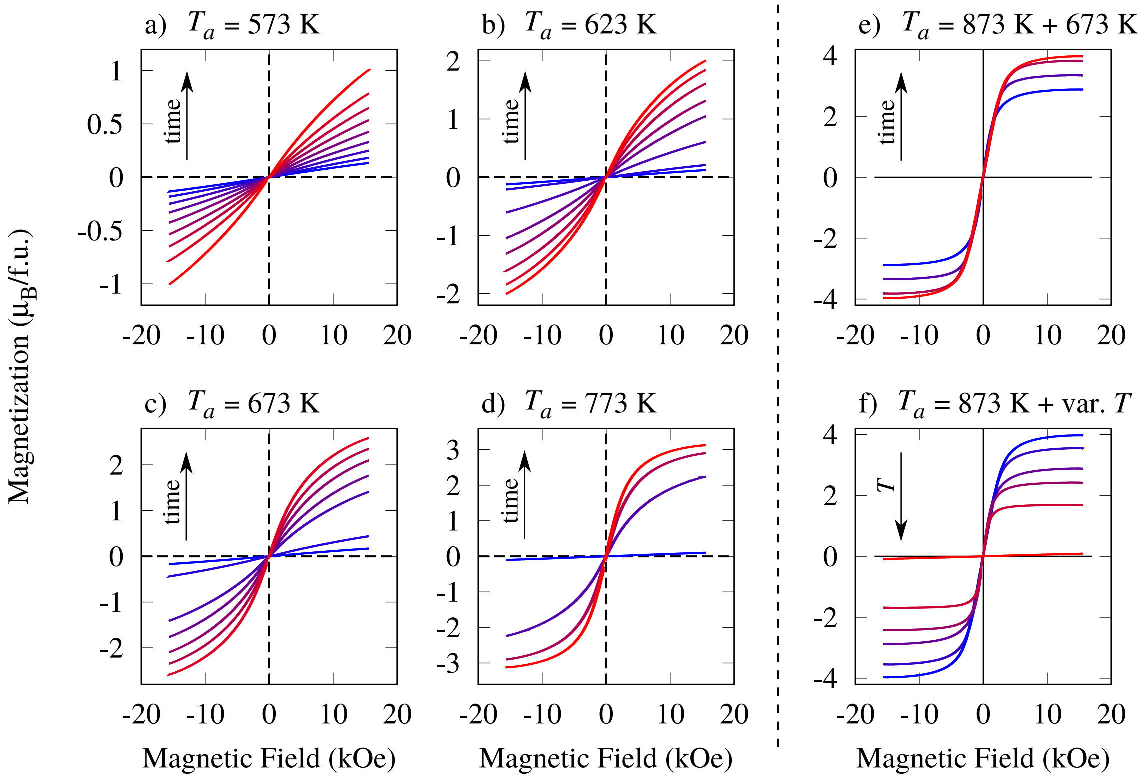

Fig. 2.4 Evolution of $M(H)$ curves upon annealing B2 ordered $Ni_2MnAl_{0.5}Ga_{0.5}$ samples at a) 573 K, b) 623 K, c) 673 K and d) 773 K. Measurements have been performed at 77 K. Magnetic transition temperatures for all annealing state are given in Tab. 2.1 together with the corresponding annealing times. e) depicts the evolution of the $M(H)$ curves in 24 h at 873 K annealed, quenched and subsequently at 673 K annealed samples while the different curves represent different annealing times at 673 K given in Tab. 2.1. f) shows $M(H)$ curves for samples annealed for 24 h at 873 K followed by a 24 h annealing treatment at various lower temperatures. These temperatures together with the corresponding T_c values are given in Tab. 2.1. All $M(H)$ curves depicted here are directly related to the $M(T)$ and $M(H)$ curves presented in Fig. 2.3 and Fig. 2.5.

disappeared. Comparing the 773 K annealed samples in d and f shows that after an annealing time of 1440 min at 773 K, even though the cusp is hardly visible, still a significantly reduced bulk magnetization is observed, with the two-step annealed sample in f showing a bulk magnetization at low temperatures that is 0.43 μ_B/f.u. higher. Note, however, that both samples in d and f have almost the same T_c with 361.8 K and 363.0 K, respectively.

In analogy to Fig. 2.3, Fig. 2.4 and Fig. 2.5 show $M(H)$ curves for a variety of annealing conditions. a–d refer to isothermal annealing of initially B2 quenched samples while e–f refer to two-step annealed samples, first for 24 h at 873 K followed by isothermal annealing at 673 K for different annealing times in e and followed by isothermal annealing for 24 h

time (min.)	T_c (K)	$M^{77\,\mathrm{K}}_{15kOe}$ (μ_B/f.u.)	$M^{295\,\mathrm{K}}_{15kOe}$ (μ_B/f.u.)	$\chi^{77\,\mathrm{K}}$ (μ_B/f.u. kOe)	time (min.)	T_c (K)	$M^{77\,\mathrm{K}}_{15kOe}$ (μ_B/f.u.)	$M^{295\,\mathrm{K}}_{15kOe}$ (μ_B/f.u.)	$\chi^{77\,\mathrm{K}}$ (μ_B/f.u. kOe)
a) T_a = 573 K					b) T_a = 623 K				
0	299.8	0.13	0.15	0.0079(0006)	0	299.2	0.12	0.13	0.0066(0005)
30	311.8	0.18	0.21	0.0107(0008)	5	316.2	0.20	0.24	0.0114(0008)
120	321.6	0.24	0.28	0.0133(0010)	120	349.8	0.59	0.63	0.0388(0025)
300	330.2	0.32	0.37	0.0171(0013)	480	366.0	1.02	1.03	0.0746(0050)
600	338.3	0.41	0.46	0.0231(0018)	960	372.2	1.29	1.26	0.1041(073)
1050	346.0	0.52	0.56	0.0327(0022)	1770	375.9	1.58	1.51	0.1423(0100)
1700	352.0	0.63	0.66	0.0439(0030)	2770	379.2	1.81	1.70	0.1792(0127)
2770	358.8	0.76	0.78	0.0518(0035)	3770	380.4	1.97	1.82	0.2118(0160)
5650	367.0	0.98	0.98	0.0742(0054)	-	-	-	-	-
c) T_a = 673 K					d) T_a = 773 K				
0	301.0	0.16	0.20	0.0097(0008)	0	294.7	0.10	0.11	0.0056(0005)
1	333.9	0.43	0.49	0.0250(0017)	20	359.1	2.22	1.91	0.3139(0329)
90	365.5	1.38	1.37	0.1221(0086)	120	361.4	2.89	2.25	0.5691(0923)
210	369.2	1.73	1.66	0.1762(0109)	1440	361.8	3.12	2.35	0.7133(1178)
450	371.7	2.07	1.91	0.2420(0203)	-	-	-	-	-
930	372.8	2.32	2.07	0.3034(0306)	-	-	-	-	-
2130	373.6	2.56	2.22	0.3713(0452)	-	-	-	-	-
e) T_a = 873 K (24 h) + 673 K					f) T_a = 873 K (24 h) + var. T_a (24 h)				
					T_a (K)				
0	339.3	2.88	1.95	1.4115(0893)	973	300.8	0.09	0.10	0.0058(0005)
10	354.5	3.35	2.37	1.1905(0965)	933	316.5	1.69	0.99	1.3696(0704)
120	373.0	3.82	2.86	1.0794(0839)	898	325.3	2.42	1.48	1.4400(1053)
1440	380.5	3.97	3.04	1.1112(0654)	873	339.3	2.88	1.95	1.4115(0896)
-	-	-	-	-	773	363.0	3.55	2.56	1.1964(0738)
-	-	-	-	-	673	380.5	3.97	3.04	1.1112(0654)

Table 2.1 Annealing times and corresponding magnetic transition temperatures T_c, bulk magnetizations M at 15 kOe and 77 K as well as 295 K and DC susceptibilities at zero field and 77 K of $\mathrm{Ni_2MnAl_{0.5}Ga_{0.5}}$ samples in various annealing conditions. The data refers to the magnetization curves depicted in Figs. 2.3, 2.4 and 2.5.

at different annealing temperatures T_a in f. Again, the respective annealing times and temperatures together with the magnetic transition temperatures, the bulk magnetizations at an external field of 15 kOe at 77 K and 295 K as well as the DC susceptibilities at 77 K and zero field can be found in Tab. 2.1. As the $M(T)$ curves, also the $M(H)$ curves show a characteristic evolution of magnetic properties upon isothermal annealing, starting with a typical AFM curve shape with a low susceptibility and low magnetization. With increasing annealing time, the susceptibility increases and, in the accessible field range, the theoretically predicted magnetization values for Ni_2MnZ compounds (Entel et al., 2006) of around 4 μ_B/f.u. are eventually approached. The $M(H)$ curve after 1440 min annealing at 773 K in Fig. 2.4d already exhibits quite ideal FM properties. Comparing with the two-step annealed samples in e–f however clearly shows that also the 773 K annealed samples in d still show some compensation of the bulk magnetization.

Fig. 2.5 shows $M(H)$ curves of the same annealing states as in Fig. 2.4 however at 295 K. As visible in Tab. 2.1, 295 K is just below T_c for the B2 quenched samples. However, due to the unusually flat $M(T)$ curves between 77 K and 295 K for samples showing the characteristic cusp in the $M(T)$ curves, the $M(H)$ curves are quite similar at 77 K and 295 K. In opposition to that, the two-step annealed samples (Fig. 2.5e–f) and also the final states of annealing at 773 K (Fig. 2.5d) show a clear decrease of bulk magnetization M upon approaching T_c as expected for a ferromagnet. When comparing the bulk magnetizations at 77 K and 295 K as tabulated in Tab. 2.1, it is evident that for early stages of isothermal annealing they are almost identical, while in the later stages, the values at 77 K are around 1 μ_B/f.u. higher than at 295 K. These observations further demonstrate the magnetic compensation in the early stages of annealing.

Interpretation of the experimental results

After having described the characteristic features of the bulk magnetization curves in various annealing conditions, the underlying processes for the observed behavior shall be elucidated. Ishikawa et al. (2008); Umetsu et al. (2011) were able to link the peculiar magnetic properties observed in $Ni_2MnAl_{0.5}Ga_{0.5}$ to the size of the $L2_1$ APD structure by comparing the domain size observed by dark field TEM to magnetization measurements. Specifically, they revealed that the cusp close to T_c and the compensation of the bulk magnetization in early stages of ordering are inherently linked to the APD dimensions, without however giving a convincing mechanism for this dependency. Also, Ishikawa et al. (2008) already disclosed that despite very different bulk magnetizations, apparently two-step 873 K, 673 K and one-step 673 K annealed samples show comparable T_c values despite very different bulk magnetization values. At the same time, the pathway of $L2_1$ ordering in Heusler alloys was previously

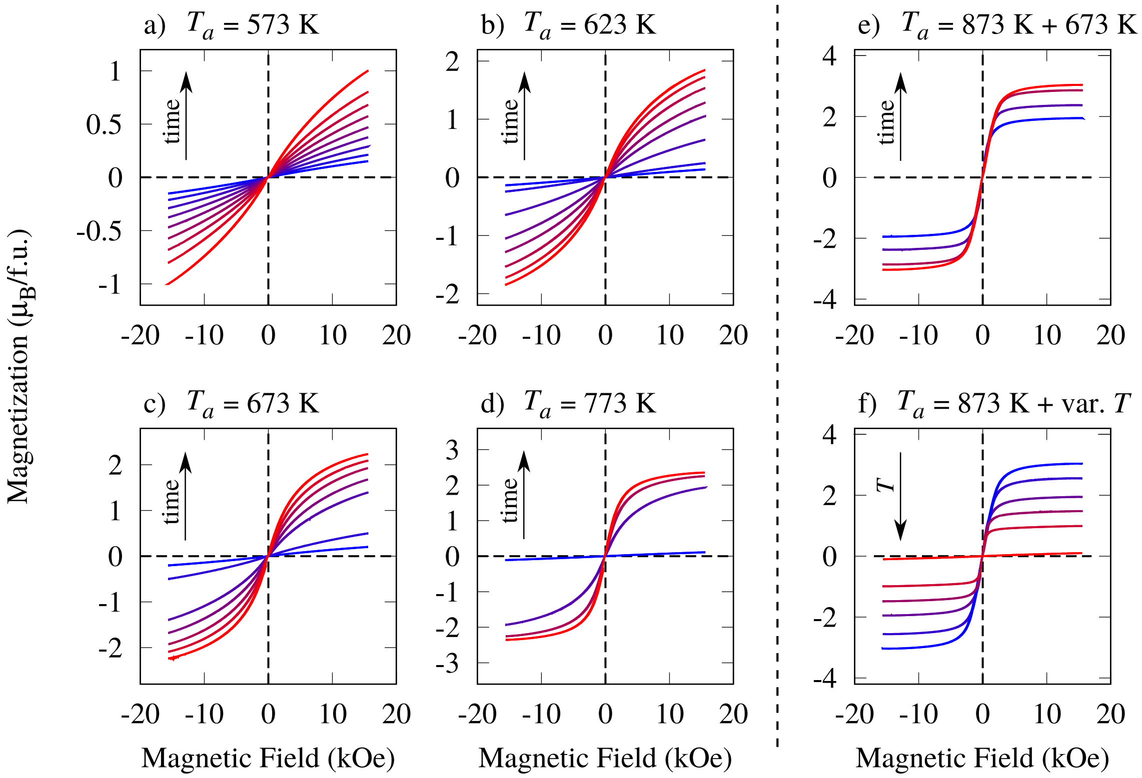

Fig. 2.5 Evolution of $M(H)$ curves upon annealing B2 ordered $Ni_2MnAl_{0.5}Ga_{0.5}$ samples at a) 573 K, b) 623 K, c) 673 K and d) 773 K. Measurements have been performed at 295 K. Magnetic transition temperatures for any annealing state are given in Tab. 2.1 together with the corresponding annealing times. e) depicts the evolution of the $M(H)$ curves in 24 h at 873 K annealed, quenched and subsequently at 673 K annealed samples while the different curves represent different annealing times at 673 K given in Tab. 2.1. f) shows $M(H)$ curves for samples annealed for 24 h at 873 K followed by a 24 h annealing treatment at various lower temperatures. These temperatures together with the corresponding T_c are given in Tab. 2.1. All $M(H)$ curves depicted here are directly related to the $M(T)$ curves presented in Fig. 2.3 and Fig. 2.5.

shown by Murakami et al. (1980a,b) to be composed of essentially two processes, namely the formation of (local) order and the growth of the APD structure. This observation is reasonable given that the non-equilibrium process of order formation is mediated via short range energetic interactions. As a consequence, the atomic order on the local, short range scale equilibrates quickly after few atomic jumps, while initially, the density of APD is high. The growth of the APD structure however needs significantly more time since the correlations over larger distances are not mediated via direct energetic interactions. Comparing these findings to the magnetization measurements shown in Figs. 2.3, 2.4, and 2.5 allows to infer

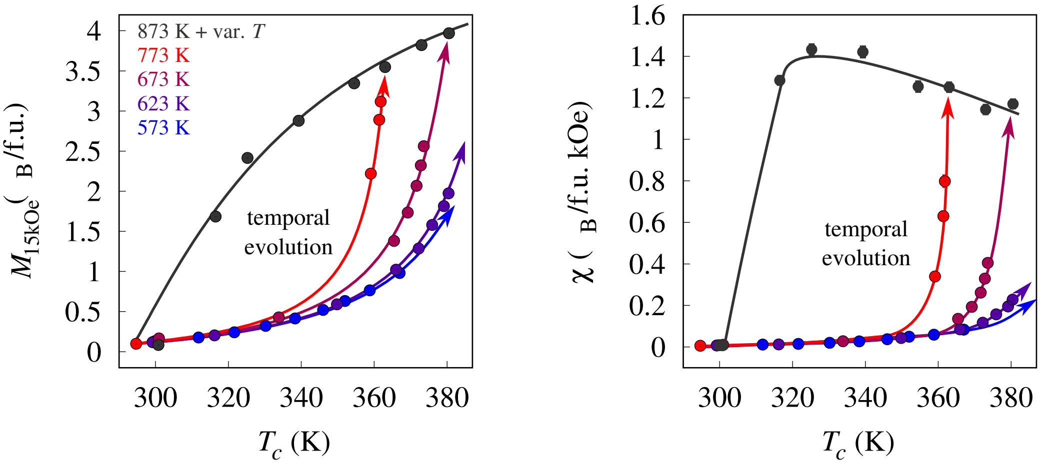

Fig. 2.6 Evolution pathway of L2_1 ordering in $Ni_2MnAl_{0.5}Ga_{0.5}$ in the 2D parameter space composed of T_c-M at 77 K (left) and T_c-χ at 77 K (right).

that both processes, i.e. short-range order formation and APD growth, can be linked with specific magnetic properties that predominantly depend on them.

Following this assumption, it appears that T_c evolves much faster during isothermal annealing treatments than M. Considering e.g. annealing at 673 K (see Tab. 2.1), it is observed that T_c after 2130 min annealing time is with a value of 373.6 K close to the presumed equilibrium value for annealing at 673 K of 380.5 K ($\approx$ 90 %) of that value while the magnetization at 77 K and 15 kOe is with a value of 2.56 μ_B/f.u. significantly lower than the presumed equilibrium value of 3.97 μ_B/f.u. ($\approx$ 65 %). Even more pronounced is the difference in DC susceptibilities χ that were determined by linearly fitting the $M(H)$ curves around zero field. Here, in the 2130 min annealed sample, a value of 0.37 μ_B/f.u. kOe is found while the presumed equilibrium state shows a value of 1.11 μ_B/f.u. kOe ($\approx$ 33 %). Hence, different magnetic properties seem to depend differently on the state of order in the sample and can consequently be used to track the underlying processes independently.

Specifically, it is the intention to understand the evolution of L2_1 order in the 2D parameter spaces $T_c - M$ and $T_c - \chi$ for the entire data set presented in Tab. 2.1. These parameter spaces are composed of the magnetic transition temperature T_c and the bulk magnetization at 15 kOe and 77 K $M_{15\mathrm{kOe}}$ as well as of T_c and the DC susceptibility at zero field and 77 K χ, respectively. This evolution is presented in Fig. 2.6, with $T_c - M$ being depicted in the left panel and $T_c - \chi$ being depicted in the right panel. The as-quenched, B2-ordered state is found in the lower left corner of both plots, being characterized by a T_c of $\approx$ 300 K and a very low M and χ value. Isothermal annealing brings first about an increase in T_c while clearly M and especially χ initially remain at a low value. It should be pointed out that starting from the lower left corner, upon isothermal annealing at various temperatures initially the same pathway is followed at all annealing temperatures. Upon further annealing, T_c approaches the equilibrium value and the ordering pathway evolves vertically in the 2D parameter space, while T_c increases only incrementally. Note that the equilibrium T_c and M values differ for annealing at different temperatures due to the second order nature of the B2-L2_1 transition. This explains, why the curves take a slightly different pathway depending on the annealing temperature T_a. Higher T_a correspond to a lower equilibrium state of order and hence a lower T_c and M value. The presumed equilibrium values under the boundary condition of a large APD structure are also depicted in Fig. 2.6. Specifically, the dark gray data points resemble all two-step annealed states. Since the two-step annealed states do show quasi prototypical FM behavior, it is assumed that in fact the APD structure under these annealing conditions is large enough not to influence the magnetic properties anymore. Hence, in the two-step annealed samples, the degree of long-range order is the only parameter influencing the magnetic properties. Clearly, annealing at higher temperatures yields a lower degree of L2_1 order meaning that an increased number of Mn and Al/Ga atoms change their positions which leads to a compensation of the bulk magnetization via Mn-Mn nearest neighbor pairs coupling in an AFM fashion. This is of course to distinguish from the existence of a small scale APD structure that evolves kinetically upon annealing a disordered sample in the L2_1-stable regime.

Since a similar pathway in the 2D parameter spaces is followed at all T_a, the altered kinetics at different T_a allows to access different regimes of the evolution path. While at 573 K, essentially the initial evolution of T_c can be followed and the later evolution of M/X is kinetically inaccessible, upon annealing at 773 K kinetics is so fast that early stages of the ordering process are difficult to grasp. The comprehensive data set recorded in this thesis allows for the first time to describe the entire ordering process for $Ni_2MnAl_{0.5}Ga_{0.5}$ in the 2D parameter spaces from the very early to the very late stages.

2.2.2 The Ni_2MnAl system

Order-dependent magnetic properties

In the following, the insights gained from the model compound $Ni_2MnAl_{0.5}Ga_{0.5}$ with respect to the L2_1 ordering process and its influence on the magnetic properties of these materials is transfered to the ternary Ni_2MnAl system. Ni_2MnAl is a sought-after Heusler material with interesting properties such as a relatively high ductility and higher cost efficiency than e.g. Ni_2MnGa. Yet, Ni_2MnAl tends to adopt a low degree of L2_1 order which impedes the material to live up to its expectations. Having demonstrated that across the $Ni_2MnAl_{1-x}Ga_x$

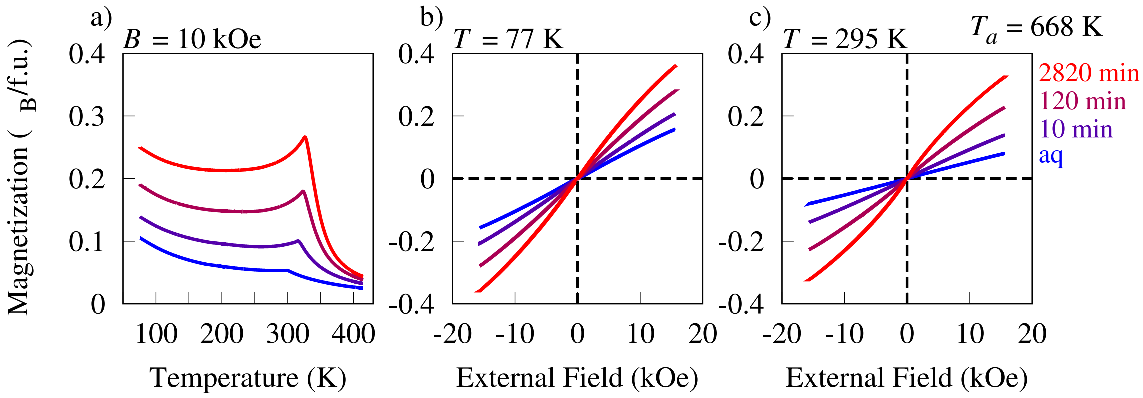

Fig. 2.7 a) $M(T)$ and b–c) $M(H)$ curves for $Ni_2Mn_{1.12}Al_{0.88}$ in different annealing conditions. Initially, samples have been quenched from 1273 K, followed by isothermal annealing at 668 K for the annealing times indicated. $M(T)$ measurements have been performed in an external magnetic field of 10kOe. $M(H)$ were measured at 77 K b) and 295 K c).

system similar magnetic properties are observed, it is appealing to compare Ni_2MnAl with a limited kinetic accessibility of $L2_1$ order to the model system $Ni_2MnAl_{0.5}Ga_{0.5}$. Specifically, this comparison will be made for a Mn-rich off-stoichiometric Ni_2MnAl compound whose composition resembles technically relevant alloys. For a detailed introduction to the Ni_2MnAl system please refer to Chapter 3.

Fig. 2.7 depicts $M(T)$ and $M(H)$ curves of $Ni_2Mn_{1.12}Al_{0.88}$ samples initially quenched from the B2-stable regime at 1273 K and subsequently annealed at 668 K in the $L2_1$-stable regime. As can be seen, the evolution of magnetic properties of $Ni_2Mn_{1.12}Al_{0.88}$ mimics respective evolution in $Ni_2MnAl_{0.5}Ga_{0.5}$. The B2-quenched state is AFM in nature with a low bulk magnetization M and a low DC susceptibility χ. Upon annealing, the compound develops stronger FM properties with a cusp emerging close to the magnetic transition temperature T_c. Simultaneously, T_c increases as function of annealing time. Tab. 2.2a summarizes the magnetic properties for $Ni_2Mn_{1.12}Al_{0.88}$ upon isothermal annealing at 668 K. Specifically, T_c as determined by DSC, M at 77 K and 295 K under an external field of 15 kOe as well as the DC susceptibility χ at zero field and 77 K are tabulated together with the corresponding annealing times.

Comparing the magnetic properties of $Ni_2Mn_{1.12}Al_{0.88}$ to $Ni_2MnAl_{0.5}Ga_{0.5}$ reveals that the B2-quenched state, even though adopting comparable properties in both compounds, shows in $Ni_2Mn_{1.12}Al_{0.88}$ a decrease in magnetization between 77 K and approximately 300 K that is not found in $Ni_2MnAl_{0.5}Ga_{0.5}$. Interestingly, it appears that upon annealing, this feature persists and the developing FM properties together with the cusp are superimposed on the declining $M(T)$ curves of the as-quenched state. Similar $M(T)$ curves have been

time (min.)	T_c (K)	$M^{77\,\mathrm{K}}_{15kOe}$ (μ_B/f.u.)	$M^{295\,\mathrm{K}}_{15kOe}$ (μ_B/f.u.)	$\chi^{77\,\mathrm{K}}$ (μ_B/f.u. kOe)
a) T_q = 1273 K, T_a = 668 K				
0	298.2	0.15	0.08	0.0100(1)
10	314.4	0.20	0.13	0.0136(1)
120	320.0	0.27	0.22	0.0191(2)
2820	327.6	0.35	0.32	0.0272(2)
b) T_q = 1073 K, T_a = 668 K				
0	295.6	0.16	0.08	0.0127(1)
30	307.1	-	0.13	-
240	326.3	0.31	0.27	0.0247(2)
2820	345.2	0.99	0.96	0.1236(7)
6220	347.6	1.19	1.11	0.1778(7)
T_q (K)	T_c (K)	$M^{77\,\mathrm{K}}_{15kOe}$ (μ_B/f.u.)	$M^{295\,\mathrm{K}}_{15kOe}$ (μ_B/f.u.)	$\chi^{77\,\mathrm{K}}$ (μ_B/f.u. kOe)
c) as-quenched from T_q				
1273	298.2	0.16	0.08	0.0100(1)
1173	297.5	0.14	0.07	0.0095(1)
1073	295.6	0.16	0.08	0.0127(1)
973	295.7	0.15	0.07	0.0125(1)
873	298.2	0.16	0.08	0.0123(1)
d) as-quenched from T_q, 2880 min annealed at 668 K				
1273	327.6	0.35	0.32	0.0272(2)
1173	331.7	0.43	0.42	0.0350(3)
1073	345.2	0.99	0.96	0.1236(7)
973	333.6	0.44	0.44	0.0359(3)
873	317.6	0.22	0.16	0.0168(1)

Table 2.2 Magnetic transition temperatures as determined by DSC, bulk magnetization values at 15 kOe and 77 K/295 K and DC susceptibilities for samples annealed for different annealing times at various annealing temperatures. The data given here refers to the measurements depicted in Figures 2.7, 2.8 and 2.9.

reported by e.g. Ishikawa et al. (2008) for stoichiometric Ni_2MnAl in the B2-quenched state, yet, so far, no explanation has been given explaining this peculiar feature.

The influence of the quenching temperature on the atomic order and the magnetic properties

Primarily to study the kinetics of the $L2_1$ ordering process (see Section 3.4), $Ni_2Mn_{1.12}Al_{0.88}$ samples have been quenched from various quenching temperatures T_q followed by subsequent isothermal annealing at T_a = 668 K. The primary goal of this experiment was to confirm

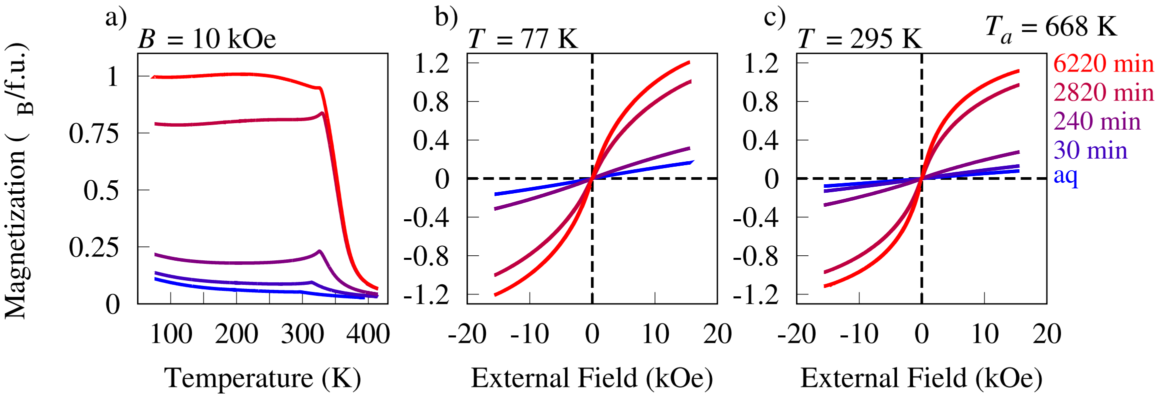

Fig. 2.8 (a) $M(T)$ and (b–c) $M(H)$ curves for $Ni_2Mn_{1.12}Al_{0.88}$ in different annealing conditions. Initially, samples have been quenched from 1073 K, followed by isothermal annealing at 668 K for the annealing times indicated. $M(T)$ measurements have been performed in an external magnetic field of 10kOe. $M(H)$ were measured at 77 K (b) and 295 K (c).

the hypothesis that a higher quenching temperature leads to a larger amount of quenched-in excess vacancies which again influences the ordering/diffusion kinetics. Clearly, the equilibrium state of order at a given annealing temperature T_a should by no means be affected by T_q. Surprisingly, a highly counterintuitive behavior was consistently observed. Fig. 2.8 shows $M(T)$ and $M(H)$ curves for $Ni_2Mn_{1.12}Al_{0.88}$ quenched from 1073 K followed by subsequent annealing at 668 K in close analogy to the measurements shown in Fig. 2.7. Characteristic magnetic properties retrieved from the measurements are again tabulated in Tab. 2.2. As can be seen, even though the initial as-quenched state shows identical magnetic properties when quenched from 1273 K and 1073 K, the evolution of magnetic properties upon low temperature annealing is quite different. While the early stages of annealing in both annealing conditions agree well, at later stages, the samples quenched from 1073 K show more pronounced FM properties. For instance, samples annealed for 2820 min at 668 K, show in case of quenching from 1273 K a T_c value of 327.6 K and a $M^{77K}_{15\text{kOe}}$ value of 0.35 μ_B/f.u. while they exhibit in the case of quenching from 1073 K a T_c value of 345.2 K and a $M^{77K}_{15\text{kOe}}$ value of 0.99 μ_B/f.u..

After consistently observing this effect for T_q = 1273 K and T_q = 1073 K, a comprehensive investigation on the dependency of the state of order and the magnetic properties from the quenching temperature T_q was performed. Fig. 2.9 shows $M(T)$ and $M(H)$ curves for samples quenched from various T_q in the as-quenched state as well as in the 2880 min at 668 K annealed state. As can be seen, the as-quenched states show identical magnetic properties with differences only being observed in the $M(T)$ curves at 500 Oe. It should however be noted that at low fields the sample demagnetization influenced by the sample shape comes into play and in the presented experiments, sample shape could not actively

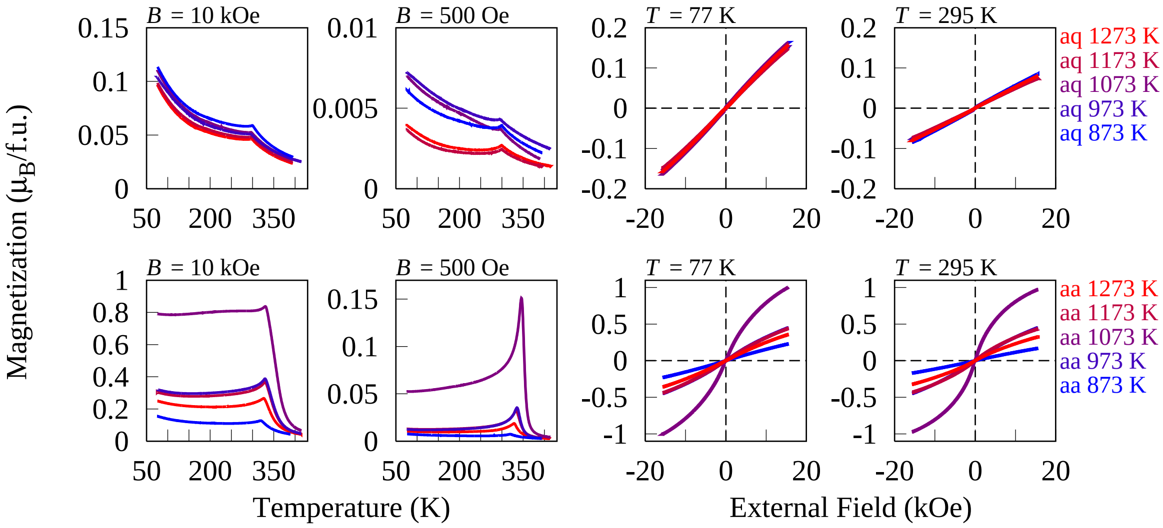

Fig. 2.9 $M(T)$ curves at 10 kOe and 500 Oe as well as $M(H)$ curves at 77 K and 295 K for $\mathrm{Ni_2Mn_{1.12}Al_{0.88}}$ samples in different annealing conditions. The top row refers to samples quenched from different temperatures T_q in the B2-stable regime. The bottom row refers to sample quenched from the indicated temperatures followed by a 2880 min annealing treatment in the $L2_1$-stable regime at 668 K.

be controlled since samples tend to break along grain boundaries. Despite these deviations in the $M(T)$ curves at 500 Oe, the magnetic properties in all as-quenched states are similar, indicating that the state of order after quenching is indeed the same. Annealing at 668 K for 2880 min brings about FM properties, yet, as visible in Fig. 2.9 and Tab. 2.2, the FM properties in the 1073 K quenched sample are more pronounced than in the samples quenched from lower or higher temperatures. This behavior is reflected in all monitored magnetic properties, specifically T_c, M and χ. While, as already discussed, the slower ordering process after quenching from lower temperatures is well explainable by a decreased amount of excess vacancies present in the sample, this argument does not explain why quenching from higher temperatures also leads apparently to lower degrees of $L2_1$ order after similar annealing times.

In order to study the nature of the ordering process, in analogy to Fig. 2.6, the ordering pathway in the 2D parameter space composed of M/χ and T_c can be evaluated for all measured states of annealing. Fig. 2.10 shows the results of this analysis. As can be seen, the data points are composed of the three distinct experimental series, the isothermal annealing series as given in Tab. 2.2a–b, the series of annealing states as-quenched from a variety of T_q in the B2-stable regime as given in Tab. 2.2c, as well as the samples quenched from different T_q and subsequently 2880 min annealed at 668 K as given in Tab. 2.2d. Evidently, all annealing states follow the same trajectory in the 2D parameter space composed of T_c-M

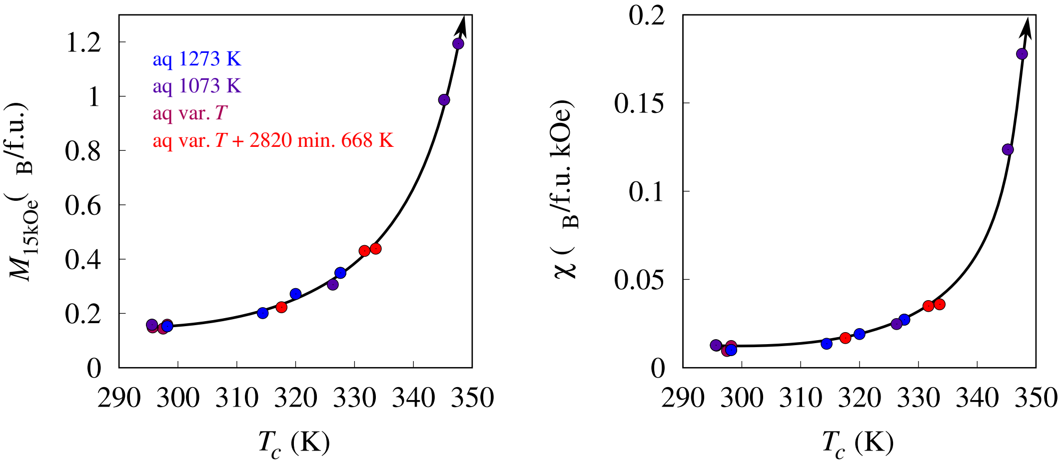

Fig. 2.10 Evolution pathway of $L2_1$ ordering in $Ni_2Mn_{1.12}Al_{0.88}$ in the 2D parameter space composed of T_c-M at 77 K (left) and T_c-X at 77 K (right).

(left) and T_c-X (right). Comparing Fig. 2.10 to Fig. 2.6 shows a convincing agreement of the pathway between $Ni_2Mn_{1.12}Al_{0.88}$ and $Ni_2MnAl_{0.5}Ga_{0.5}$ with a primary movement along the T_c axis, while M and especially X start to increase as soon as T_c is close to the equilibrium value. Note that the values for M and X are significantly lower than for $Ni_2MnAl_{0.5}Ga_{0.5}$ indicating that 2820 min annealing at 668 K corresponds still to a highly compensated magnetic state with presumably a large density of APDs. Nonetheless, the common trajectory of the $Ni_2Mn_{1.12}Al_{0.88}$ data points from all experimental series is a good indication that in fact the same ordering pathway is followed in all cases and that the same ordering mechanism is active in all samples. Hence, the observed differences in order formation after quenching from different temperature T_q can presumably be ascribed to diffusion kinetics rather than thermodynamics while the reason for this is still unclear.

2.3 Monte Carlo simulations of order-dependent magnetic properties

2.3.1 Introduction

In order to understand the observed magnetic properties of Ni_2MnZ Heusler compounds and specifically the influence of the mesoscale nuclear structure, computer simulations are a viable support of the experimental work. They have the tremendous advantage that selected parameters can be studied independently which is often not possible under experimental conditions. Hence, in this section, Monte Carlo simulations are employed in order to understand the microscopic origin of the observed macroscopic magnetic properties.

In the introductory remarks, for the studied Ni_2MnZ alloys, a Heisenberg Hamiltonian for classical spins was presented as

$$H = -J_1 \sum_{\langle i,j \rangle_{\mathrm{Mn,Mn}}} \vec{\sigma}_i \vec{\sigma}_j - J_2 \sum_{\langle i,j \rangle_{\mathrm{Mn,Ni}}} \vec{\sigma}_i \vec{\sigma}_j \tag{2.3}$$

taking into account a weak nearest neighbor (NN) FM Ni-Mn interaction (J_2) and a strong NN Mn-Mn interaction that is AFM in nature (J_1). In the following, J_1 shall be fixed to -1. The sums in the Hamiltonian are sums over nearest neighbors counting every pair once. Note, NN Mn-Mn pairs specifically refer to Mn site-antisite pairs in the $L2_1$ structure. Consequently, a Mn on a Mn site interacts antiferromagnetically with a Mn on a Z site.

Additionally, it was already introduced that the moments on Ni are induced by the Mn spins on the 8 surrounding lattice sites as expressed via

$$\vec{\sigma}^{\mathrm{Ni}} = \tfrac{1}{4} \sum_{\langle i \rangle_{\mathrm{Mn}}} \vec{\sigma}_i . \tag{2.4}$$

Hence, in the B2 structure, with disorder between the Mn and Z sublattice, due to the AFM coupling, on average the sum of the neighboring Mn spins is zero. As a result, the induced moment on Ni in B2 ordered Ni_2MnZ compounds is also zero and the material shows perfect AFM properties. In the perfectly ordered $L2_1$ structure, NN Mn-Mn pairs do not exist and hence only the FM Ni-Mn interactions are active in the system. As a result, all Mn moments point in the same direction and the induced moment on Ni takes on a maximal value. These boundary cases have previously been studied for Ni_2MnAl by DFT calculations where the magnetic moment on Ni was determined to be 0.32 μ_B/f.u. in the $L2_1$ structure and zero in the B2 structure (Simon et al., 2015). Simon et al. (2015) also found that the calculated moment on Ni in Ni_2MnAl decreases linearly with the Mn occupancy on the Al lattice.

Given the induced non-rigid moments on Ni, the Heisenberg Hamiltonian of the system can be renormalized to an effective Hamiltonian taking into account only the rigid Mn moments as demonstrated by Ležaić et al. (2013). The resulting effective Hamiltonian can hence be written as

$$H = C - (-1 + J_2) \sum_{\langle i,j \rangle_{100}} \vec{\sigma}_i \vec{\sigma}_j - \frac{J_2}{2} \sum_{\langle i,j \rangle_{110}} \vec{\sigma}_i \vec{\sigma}_j - \frac{J_2}{4} \sum_{\langle i,j \rangle_{111}} \vec{\sigma}_i \vec{\sigma}_j - B_z \sum_i \sigma_i \tag{2.5}$$

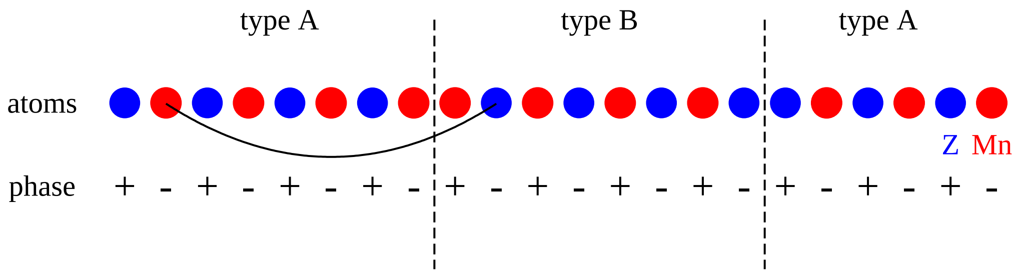

Fig. 2.11 Schematic depiction of the $L2_1$ APD types in Ni_2MnZ compounds. Shown is a proposed MC move that preserves the proportion of APD types.

where the Ni-Mn interaction is renormalized to an effective Mn-Mn interaction in $\langle 100 \rangle$, $\langle 110 \rangle$ and $\langle 111 \rangle$ direction. This renormalized Hamiltonian is much easier to deal with and has significant advantages in terms of computational costs in Monte Carlo (MC) simulations of the magnetic properties. Note that a term describing the effect of an external magnetic field B_z was added to the renormalized Hamiltonian as it is needed for the simulation of magnetic properties presented below. B_z in above notation refers to an external magnetic field which is strictly applied in z-direction. Again, the sums refer to NN sums in which any given pair is counted once.

2.3.2 Simulation of atomic structures

In order to decipher the magnetic interactions across APBs and consequently study the effect of the mesoscale nuclear structure on the magnetic properties, in a first step, a realistic APD structure has to be composed. Considering that the APD structure is crystallographically highly complex, such a structure cannot be artificially tailored but needs to be simulated in order to mimic reality. This can conveniently be done using an Ising model on a simple cubic lattice. Specifically, a Metropolis algorithm (Metropolis et al., 1953) was employed to simulate the sublattice occupancies on the 3D simple cubic Mn-Z sublattice of Ni_2MnZ Heusler compounds under conservation of mass (which is identical to the 3D antiferromagnetic Ising model on a simple cubic lattice). Further, equal proportions of the two possible APD types were required. Fig. 2.11 shows a 1D representation of the problem. Depicted is a chain of Mn and Z atoms with two APBs. Drawing the phase information below the atoms shows that in fact only two types of APD exist, one where Mn are on $+$ positions and Z are on $-$ positions and one where it is the other way around. When now atoms are exclusively exchanged between APD of different types, the overall proportion of APD types remains constant. Hence, in the employed algorithm, a random lattice site in domain A is selected and

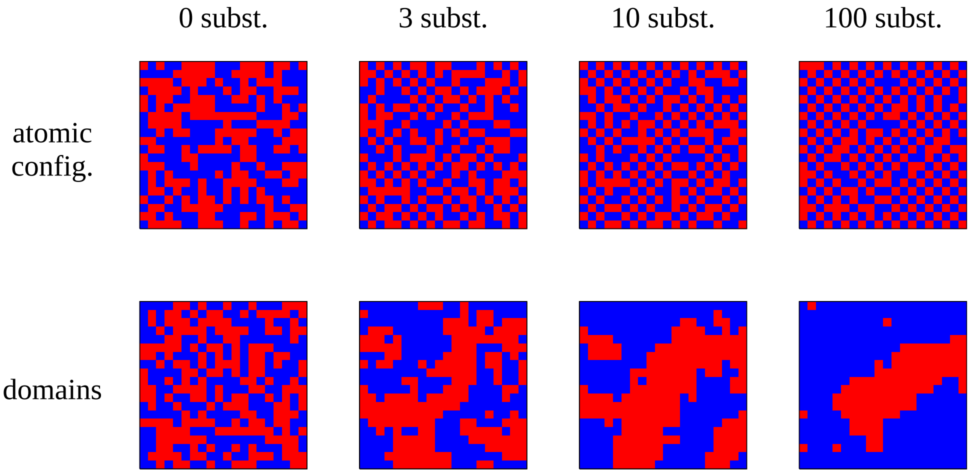

Fig. 2.12 MC simulations of the L2_1 APD structure with red and blue representing Mn and Z, respectively. The upper row shows the retrieved atomic configurations while the lower row shows the phase of the ordered domains. From left to right, the proposed substitutions per lattice site increase from 0 on the left to 100 on the right. Simulations were performed on a 64×64×64 lattice with periodic boundary conditions while here only a 20×20 section is depicted.

the atomic species (either Mn or Z) is determined. Next, random lattice sites in domain B are chosen until one is found that is occupied with the other species. The atoms on the randomly selected lattice sites are then exchanged with the probability $\min\left(1, \exp(-\frac{E_f - E_i}{k_B T})\right)$ where E_i is the energy of the configuration before the move and E_f is the energy of the configuration after the move. The energy is calculated as

$$E = -J \sum_{\langle i,j \rangle} \sigma_i \sigma_j \tag{2.6}$$

with a sum over all pairs of neighbors counted once and parameter J being negative. Here, J is set equal to -1. On the simple cubic lattice, any lattice site has 6 neighbors and $\sigma_{i,j}$ in a Ising sense can take on values of $\{\pm 1\}$ for Mn and Z, respectively. Consequently, a Mn/Z surrounded by 6 Z/Mn has the lowest possible energy of -6 while a Mn/Z surrounded by 6 Mn/Z has a energy of $+6$.

In other words, according to the acceptance probability, a move is accepted if the resulting configuration is energetically favorable while it is accepted with a probability of $\exp(-\frac{E_f - E_i}{k_B T})$ in case it is unfavorable, meaning that E_f is larger than E_i. If the temperature T is low, the acceptance probability of an unfavorable move is close to zero and the algorithm will create fully ordered configurations. On the other hand, if T is high, the acceptance probability also for energetically unfavored configurations is high which results in a disordered configuration. The transition between the ordered and the disordered phase is a second order phase transition as is in reality the B2-$L2_1$ transition.

In order to simulate realistic APD structures, a random occupancy of Mn and Z is created on a $64{\times}64{\times}64$ lattice with periodic boundary conditions as a starting point and the simulation is run at a temperature where Mn-Z order is stable (here, simulations were run at $0.44T_t$ with T_t being the phase transition temperature). Non-equilibrium states of order with APBs are then sampled via proposing MC moves. The amount of MC moves/proposed substitutions is basically equivalent to annealing time in an isothermal annealing experiment. Fig. 2.12 shows the result of this computer simulation. For reasons of readability, only $20{\times}20$ sections of the simulated configurations are depicted. The picture of zero proposed substitutions per lattice site represent the random starting configuration. With an increased number of proposed substitutions per lattice site, first the emergence of local order can be observed, while initially a high density of APBs exists. Clearly, as the first few proposed substitutions per atom already establish the local order inside a domain, after a low number of substitutions the growth of the APD structure becomes the dominating characteristic of the simulations. The observed features, namely the initial emergence of local order followed by the growth of the APD structure, nicely agree with the interpretation of the experimental data presented in the first part of this chapter. Note that the simulated configurations depend strictly on the temperature of the simulation which was chosen in order to yield a state of high order. At higher temperatures, the order inside a given domain will be lower and also the APB might show a different appearance. Yet, studying these effects systematically is outside the scope of this thesis. Due to the requirement that the proportion of domain types remains constant, the obtainable size of the APD structure in the employed simulations is restricted by the size of the lattice. At maximum, the atomic configuration can be divided into two large domains, one of type A and one of type B, that are divided by two smooth interfaces.

2.3.3 Simulation of magnetic properties

In a further step, a simulated APD structure was fed into a magnetic simulation based on the renormalized Hamiltonian presented in (2.5). To simulate spin configurations on the Mn-Z lattice, a Heisenberg heat bath algorithm similar to the Ising heat bath algorithm described in Krauth (2006) in combination with a cluster algorithm similar to Wolff (1989) was employed.

In principle, the degrees of freedom in the magnetic simulations are, with J_1 being fixed, J_2 representing the strength of the FM interaction in the system, the temperature and the external magnetic field B_z. To understand the general effect of APBs in the system, a progressed state of APD formation (approximately 50 proposed substitutions per lattice site) was used to study the magnetic ground state configurations under a low magnetic field and at low temperature. Fig. 2.13 shows a 2D section of such ground state configurations for different J_2. The white lines in the figure show the APBs, the arrows represent the 2D orientation of the spins, while the color also depicts the directional information. First of all, it is apparent that on the left hand side, with the lowest J_2 value, the APDs and the magnetic domains coincide while across the APB an AFM coupling is present. Hence, for low J_2 values, the magnetic domain walls are quasi exclusively 180° walls. Upon increasing the ferromagnetic interaction J_2 in the system, first the coupling angle across the APB decreases and from a certain point on, the entire configuration becomes FM despite the presence of APBs. The results of the computer simulations for low J_2 values reproduce the experimental results by Park et al. (2012) where using Lorentz-TEM, a coincidence of structural and magnetic domain walls was observed in $Ni_2MnAl_{0.5}Ga_{0.5}$ with unusually narrow magnetic domain walls. Further, Park et al. (2012) reported that most magnetic domain walls were 180° walls.

To quantify the coupling behavior as a function of J_2, the coupling angle between the average magnetization vector $\bar{\sigma}_A$ in all domains of type A and the magnetization vector $\bar{\sigma}_B$ in all domains of type B is shown in Fig. 2.14. For low J_2 values, the coupling between APDs is perfectly AFM with an angle Θ of 180° while in the regime of $0.58 < J_2 < 0.68$, a transition to the FM state with $\Theta = 0°$ is observed. Interestingly, the transition from AFM to FM coupling is gradual with a variety of transition states where the coupling angle Θ takes

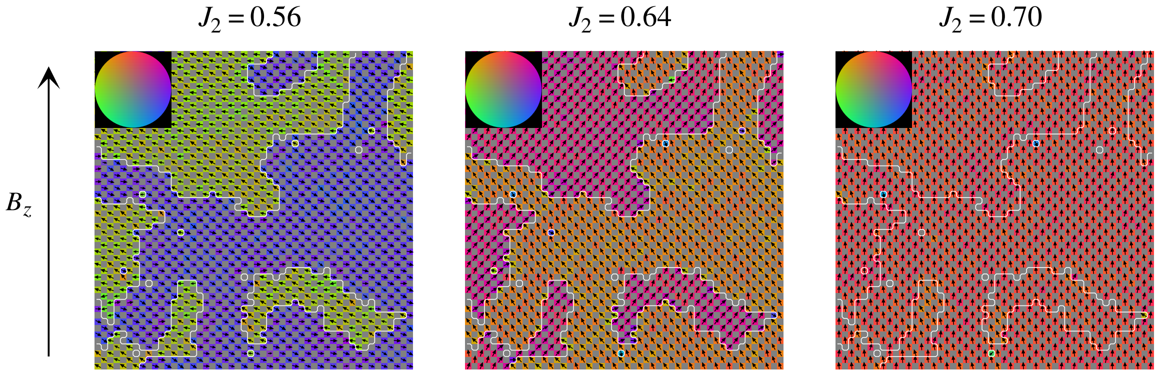

Fig. 2.13 Simulated ground state configurations for a progressed state of a simulated APD structure and different interaction parameters J_2. On the left hand side, where J_2 is small, a clear AFM coupling across structural antiphase domains is seen. On the right hand side, where J_2 is large, a fully FM configuration is observed.

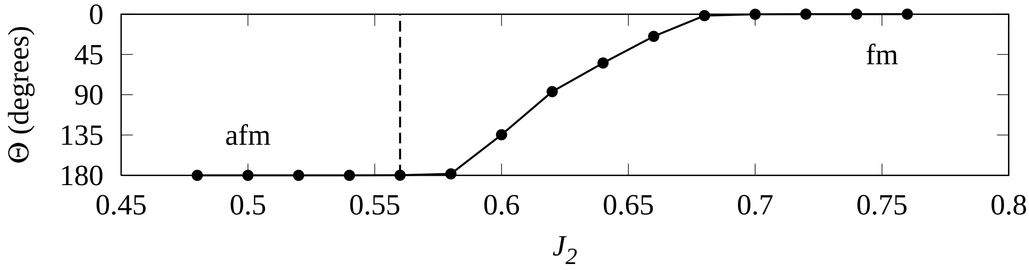

Fig. 2.14 Magnetic phase diagram for a Ni_2MnZ compound with progressed APD structure as a function of the FM exchange interaction J_2. Depicted is the angle Θ between the mean magnetization vector in domain type A and domain type B. The dashed line represents the J_2 value selected for $M(T)$ and $M(H)$ simulations.

on intermediate values. For the further simulation of $M(T)$ and $M(H)$ curves, J_2 has been fixed in the AFM regime at a value of 0.56.

In order to simulate $M(T)$ and $M(H)$ curves as a function of the domain size, a series of realistic APD structures has been created in the fashion described above. Next, $M(T)$ curves have been simulated on cooling and heating under the presence of a constant external magnetic field $B_z = 0.01$. The $M(T)$ curves are shown in the left panel of Fig. 2.15 while the growth state of the APD structure is encoded in the number of proposed substitutions per atom. In this respect, $M(T)$ curves for random occupancy (0 subst./atom), 1, 2, 3, 10, 30, 50 and 100 subst./atom are shown together with the $M(T)$ curve of a single domain $L2_1$-ordered configuration. The y-axis of the plot shows the relative Mn magnetization, hence a value of 1 stands for a perfect alignment of all Mn moments with the external magnetic field. All simulations were performed on a 64×64×64 lattice with periodic boundary conditions.

The results show that with random Mn-Z occupancy (B2 order), the overall magnetization is low and AFM properties are observed. Increasing $L2_1$ order leads to the emergence of a characteristic cusp close to the magnetic transition temperature T_c that grows in size as the state of order progresses. Furthermore, with an increased number of proposed MC moves, T_c as well as the bulk magnetization M gradually increase. Hence, the simulations convincingly reproduce the main features of the experimentally obtained $M(T)$ curves presented in Fig 2.3.

Simulated $M(H)$ curves for the same structural configurations as in the left panel are depicted in the right panel of Fig. 2.15. Those simulations have been performed at a k_BT value of 0.1. It is found that the initial random Mn-Z configuration shows a very low magnetization M together with a low DC susceptibility. With increased $L2_1$ order, the susceptibility as well as the bulk magnetization increase. The single domain $L2_1$ structure

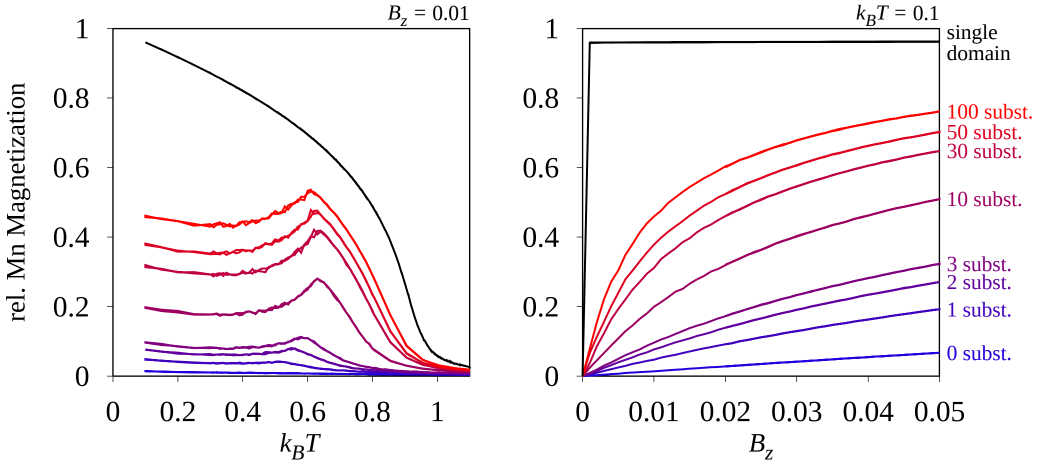

Fig. 2.15 Simulated $M(T)$ (left) and $M(H)$ curves (right) as a function of the domain size in a Ni_2MnZ compound. The domain structure is encoded as proposed substitutions per atom in the above described simulation of the APD structure. $M(T)$ curves have been simulated in an external magnetic field B_z of 0.01 and $M(H)$ curves were simulated at a temperature k_BT of 0.1.

then yields perfect ferromagnetic properties at all fields since sample demagnetization is not accounted for in the simulations. Again, the results perfectly agree with the qualitative behavior observed experimentally (see Fig. 2.4).

The ideal $\{100\}$-APB

Having demonstrated a convincing agreement between experiment and simulation for the simulated APD structures, in the following, the mechanism of the observed magnetic coupling across APBs is investigated. Assuming an atomically sharp APB, this coupling is in its elementary features easy to understand and was already proposed for MnAl in the 1960s by Zijlstra and Haanstra (1966) and later for the prototypical Heusler compound Cu_2MnAl in the 1970s by Lapworth and Jakubovics (1974). At certain APBs, Mn atoms are in NN positions and hence couple in an AFM fashion. At the same time, due to a high degree of local $L2_1$ order, the domains themselves show FM properties. Hence, any APB induces an orientation change of the local magnetization direction of the entire domain with respect to the neighboring domain and consequently, entire domains behave as supermoments that couple in an AFM fashion. However, the magnetization distribution in a magnetically coupled APD structure and its influence on the magnetic properties has so far not been convincingly described. Due to their complexity, also the magnetization distribution in the simulated APD structures are not suited to solve this problem. For this reason, in this section, artificial APBs

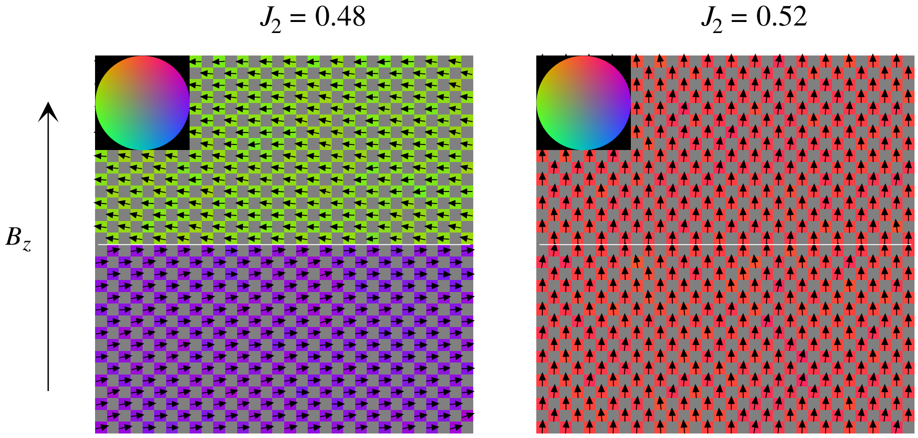

Fig. 2.16 Simulated ground state configurations for a {100}-APB with different interaction parameters J_2. On the left hand side, J_2 is small and a clear AFM coupling of structural antiphase domains is observed. On the right hand side, where J_2 is large, a fully FM configuration is found.

with a simple crystallographic orientation are investigated. In principle, an APB can have an arbitrary crystallographic orientation. Here, exemplarily, a {100}-APB is studied.

The magnetic ground state configurations for two values of J_2 under a small magnetic field and at low temperature are presented in Fig. 2.16. Also for {100}-APBs, at low J_2 an AFM-like coupling between domains is observed. As known from antiferromagnets, under the presence of an external magnetic field, the spins align orthogonal to the field direction – a behavior also observed at the AFM coupled APB. At larger J_2 values the magnetic exchange across the APB changes and the entire configuration shows FM properties where all spins are aligned in parallel.

Analyzing the spin configuration as a function of the FM exchange interaction J_2 yields the results presented in Fig. 2.17. In contrast to the observed behavior in simulated APD structures, the coupling at the {100}-APB switches abruptly from AFM to FM coupling at J_2 values just above 0.5. This value is considerably lower than the transition observed in the simulated structure (see Fig. 2.14) where J_2 values of 0.58 still show perfect AFM coupling.

Using {100}-APD structures of different size, magnetization curves were simulated in order to confirm the overall agreement of the magnetic coupling across {100}-APBs with respect to the simulated APD structures. Fig. 2.18 shows the implementation of different domain sizes for the {100}-APD structures. All magnetic simulations were executed on 128×32×32 lattices with periodic boundary conditions while different APD sizes were realized via introducing APBs every 8, 16, 32 and 64 atoms. Note that due to the periodic boundary conditions, the extension of the APD structure in the other two dimensions is quasi

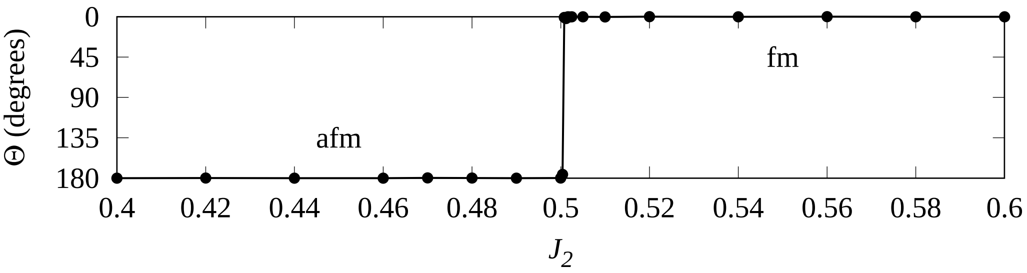

Fig. 2.17 Magnetic phase diagram for a {100}-APB structure on a 32×32×32 lattice with periodic boundary conditions as a function of the FM exchange interaction J_2. Depicted is the angle Θ between the mean magnetization vector in domain type A and domain type B. Different to the simulated APD structure, at the {100}-APB the transition from the AFM to the FM regime seems to be abrupt at values just above $J_2 = 0.5$.

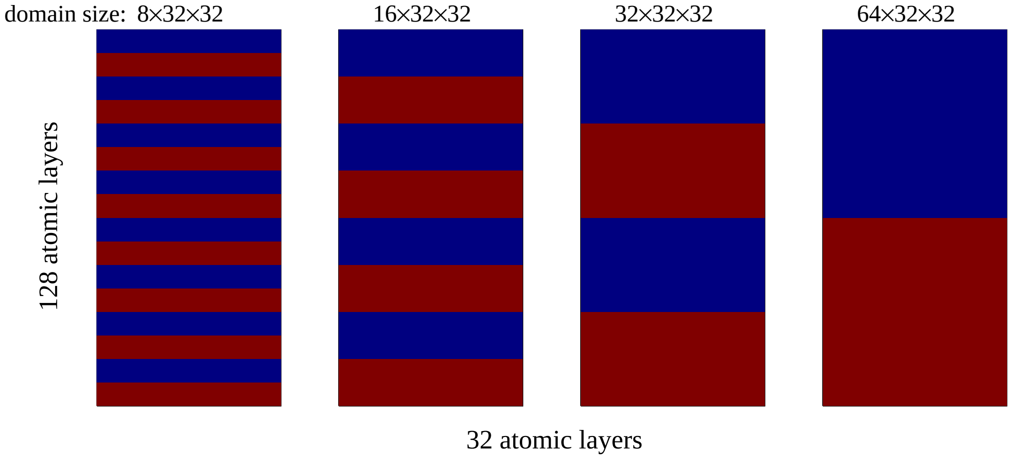

Fig. 2.18 Depiction of structural {100}-APD with varying APB densities as used for the simulation of magnetization curves.

infinite. In order to ensure AFM coupling across the APBs in the ground state, all simulations have been performed with a J_2 value of 0.4, well in the regime of AFM coupling.

Fig. 2.19 shows $M(T)$ (left) and $M(H)$ curves (right) simulated on the {100}-APD structures presented above. The characteristic features of the magnetization curves for the simulated APD structures (see Fig. 2.15) are nicely recovered also for the {100}-APD structures. Clearly, at high APB densities a cusp close to the transition in the $M(T)$ curves is observed. Interestingly, due to the possibility to realize larger APD sizes with respect to the simulated structures on a 64×64×64 lattice, the disappearance of the cusp towards larger APD dimensions is observed in the $M(T)$ curves of the {100}-APD structures. Furthermore, a comparison between the simulations and the experimental data in Fig. 2.3d reveals an

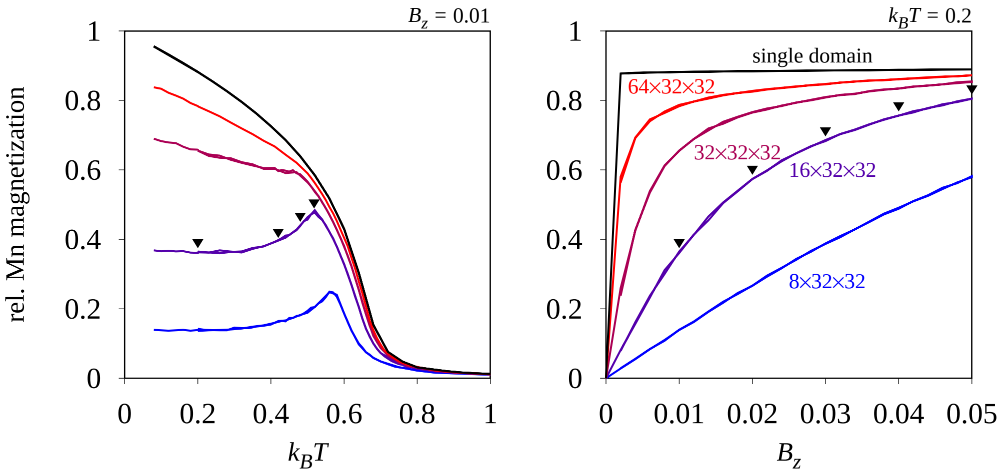

Fig. 2.19 Simulated $M(T)$ and $M(H)$ curves on the $\{100\}$-APD structures as depicted in Fig. 2.18. Simulations were performed on 128×32×32 lattices with periodic boundary conditions. The y-axis shows the relative Mn magnetization, meaning that a value of 1 corresponds to the situation where all Mn spins are completely aligned with the external magnetic field B_z. Black triangles indicate configurations analyzed in detail below and presented in Fig. 2.21. $M(T)$ curves were simulated on heating and cooling. $M(H)$ curves were simulated under increasing field and decreasing field.

excellent agreement with the $M(T)$ curves of samples annealed at 773 K. Note that the shift of the $M(T)$ curves towards lower temperatures (and hence the lower magnetic transition temperature T_c) with respect to the $M(T)$ curves presented in Fig. 2.15 results from the lower FM J_2 interaction parameter. Yet, the qualitative curve shape in both cases is identical. Furthermore, the $M(H)$ curves in the right panel of Fig. 2.19 show a convincing agreement to the experimental results and as well to the $M(H)$ curves for the simulated APD structures. Specifically, the increase in DC susceptibility together with the increasingly FM curve shape with increased APD size is clearly observed. For the $M(H)$ curves, it is evident that the progress towards ideal FM properties is more advanced in the $\{100\}$-APD structures than in the simulated ones presented in Fig. 2.15. The black triangles in Fig. 2.19 indicate the configurations that will be analyzed more thoroughly on the following pages in order to understand the emergence of the cusp and the effect of an external magnetic field on the spin configurations on a microscopic level.

To understand the magnetization distribution as function of the distance to the APB, the magnetization along the external magnetic field B_z is evaluated in planes parallel to the APB. Fig. 2.20 shows this average magnetization per lattice plane along the 128 atoms sized z-direction for domain sizes of 8×32×32, 16×32×32, 32×32×32 and 64×32×32, respectively, at an external magnetic field B_z of 0.01 and a temperature k_BT of 0.2. APBs in

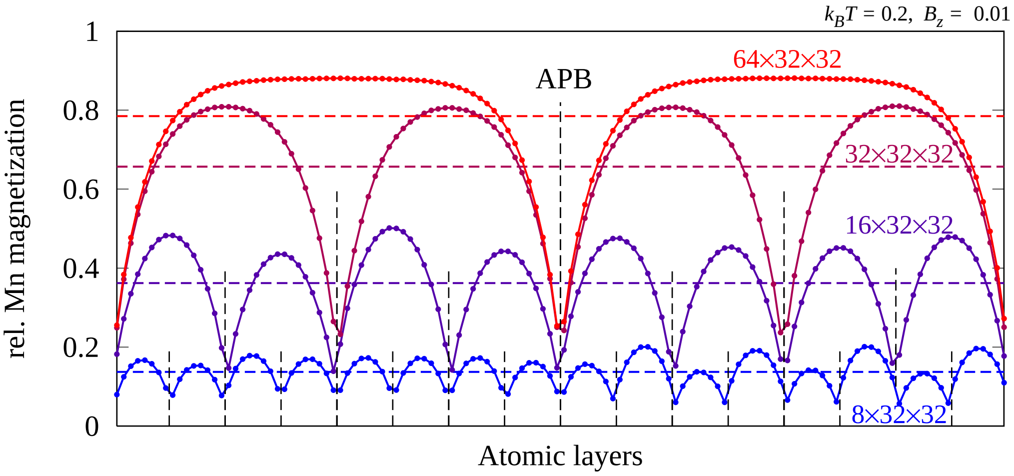

Fig. 2.20 Average magnetization parallel to APBs in $\{100\}$-APD structures as function of APD size. Vertical dashed lines depict APBs. Horizontal dashed lines show the average magnetization of the configurations. Simulations were performed on 128×32×32 lattices with periodic boundary conditions as averaged over 60 configurations per parameter set.

the different configurations are illustrated by vertical dashed lines. What is striking is the fact that the magnetization in the center of an APD is significantly higher than at the APB. The reason are the NN Mn-Mn spins at the APB which arrange in an AFM fashion orthogonal to the applied field. Consequently the magnetization in B_z direction is small. However, with increasing distance from the APB, the effect of the AFM interaction at the APB becomes smaller and the magnetic moments turn in order to align with B_z. Interestingly, with an external magnetic field being present, the angle of the spins at the APB is not 180° anymore but lower. Hence, the magnetization has a contribution in B_z direction also at the boundary. Increasing the APD size now results in two things: First of all, the angle between the spins at both sides of the APB decreases. Consequently the magnetization along B_z increases. Second, due to the larger APD size, the spins in the center of the domain are less influenced by the APB which results in a higher magnetization in the center of the domain. Clearly, due to both effects, the average magnetization $\bar{M}_z$ of the entire configuration increases with APD size.

Up to this point, it has not been elucidated how the external magnetic field and temperature interact with a given spin structure. Specifically, the emergence of the characteristic cusp close to T_c has not been addressed. To resolve this issue, simulations have been performed on the $\{100\}$-APD structure with domain size 16×32×32 at different external magnetic fields B_z and constant temperature as well as at different temperatures and constant B_z. The results are depicted in Fig. 2.21 and refer to the parameter sets indicated by the black triangles in Fig. 2.19. The left panel of Fig. 2.21 shows the magnetization in z-direction averaged

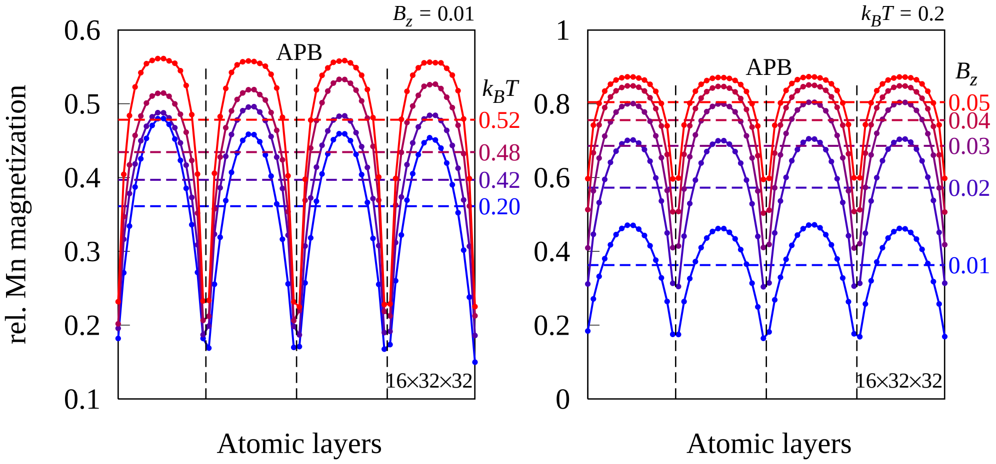

Fig. 2.21 Average magnetization in planes parallel to APBs in $\{100\}$-APD structures as function of temperature (left) and as function of the external magnetic field (right). The depicted parameter sets correspond to the black triangles in Fig. 2.19. Vertical dashed lines show APBs. Horizontal dashed lines show the average magnetization of the configurations. Simulations were performed on $128\times32\times32$ lattices with periodic boundary conditions and domain sizes of $16\times32\times32$. Depicted are 64 atomic layers sections of the configurations. Magnetization values are averaged over 60 configurations.

over lattice planes parallel to the APB as a function of temperature k_BT and the right panel shows the average magnetization in z-direction as a function of B_z. In the left panel, the increase in magnetization approaching the cusp is clearly revealed. When increasing the temperature, essentially two effects are observed. First of all, the angle between spins in neighboring domains decreases meaning that the magnetic moments align stronger with the external magnetic field. At the same time, the magnetic stiffness decreases which leads to a decoupling of the spins. This in turn implies an increased tendency of the magnetic moments to align with the external magnetic field as function of distance to the APB.

The response to an external magnetic field B_z is even more pronounced than the k_BT dependency (note the different y-axis scales in Fig. 2.21). Both effects described for the temperature dependent average magnetization distributions are also valid for the field dependent curves. With increasing field, both the angle between adjacent spins at the APB decreases and, at least initially, also the magnetic moments far away from the APB align faster with the external magnetic field. However, upon approaching higher fields, the local magnetization in the middle of the domains starts saturating and the average magnetization curves flatten in between APBs.

The presented computer simulations establish a comprehensive picture of the mechanisms leading to the experimentally observed magnetization curves. A schematic drawing

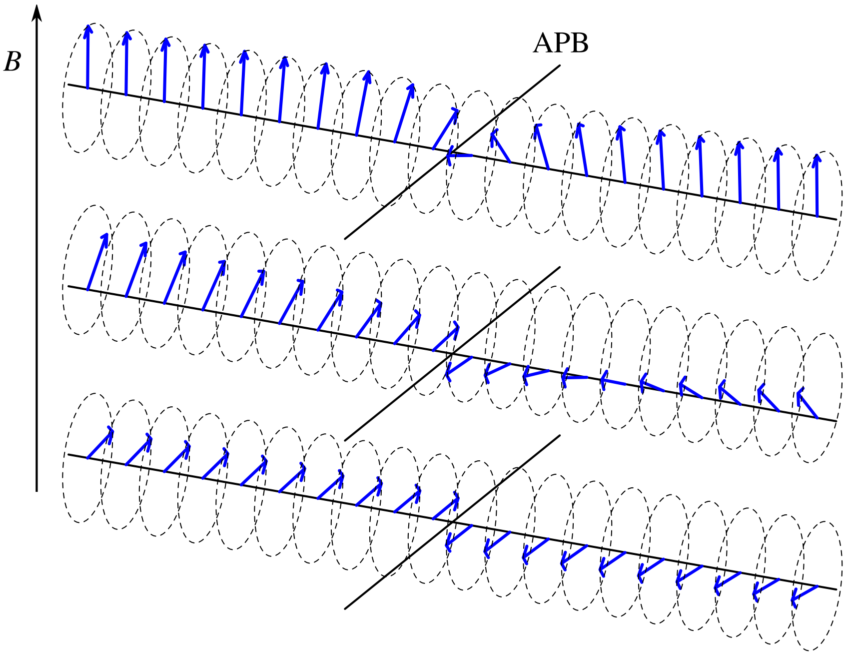

Fig. 2.22 Schematic drawing of the spin orientation at APBs in the AFM coupling regime as a function of the external magnetic field B.

summarizing the established view of the spin alignments in the vicinity of APBs is shown in Fig. 2.22. At the APB, under the presence of low magnetic fields, the spins align in an AFM fashion while they are oriented orthogonally to the external magnetic field. When increasing the field (similar for temperature and domain size), the magnetic moments in the center of the domains which are less affected by the APB rotate to align with the external magnetic field while at the boundary the angle between the spins in adjacent domains decreases. The schematic drawing in Fig. 2.22 visualizes the spin alignments in a 1D representation.

2.4 Remarks on APBs

In the presented simulations, a simplistic model for APBs was assumed emerging from an Ising Hamiltonian with only NN interactions and low simulation temperatures. As a result, the APBs are atomically sharp which in turn allows for a NN Mn-Mn coupling over the interface. In reality, the description of APBs in intermetallic systems is substantially more complex and as a function of temperature, so called wetting of APBs by a disordered phase is expected (see for instance Schmid and Binder, 1992). Schmid and Binder (1992) determined the critical temperature of the roughening/APB wetting transition as 1/3 of the transition temperature. Hence, APB wetting is possible to occur also in the annealing treatments applied in this work.

APBs can experimentally be investigated by Transmission Electron Microscopy (TEM) or High Angle Annular Dark-Field Scanning Transmission Electron Microscopy (HAADF-STEM) as demonstrated for $Ni_2MnAl_{0.5}Ga_{0.5}$ by Ishikawa et al. (2008); Murakami et al. (2013, 2011); Umetsu et al. (2011). In Murakami et al. (2013), the APB width was determined to extend over 2-3 nm. Yet, as the authors point out, slight tilting of the specimen with respect to the electron beam make these values inherently error-prone. In fact, the stated values have to be taken as an upper limit of the APB width. For instance, experimental investigations of APB roughening in the $L1_2$ compound Cu-Pd was observed only close to the transition temperature while below, the APB was proven to be sharp (Ricolleau et al., 1992). Since the annealing treatments in the presented experiments were predominantly performed hundreds of degrees below the transition temperature, the assumption of a relatively sharp interface is presumably reasonable. As an additional complication, phase decomposition effects can arise at APBs. Recently, Niitsu et al. (2017) convincingly reported the segregation of specific constituents at the APBs in off-stoichiometric Ni_2MnIn alloys. Such segregation effects were also not considered in the presented simulations.

In the light of this criticism, the results of this chapter shall again be reviewed regarding the question which implications more complicated APB structures would have for the investigated magnetic APD coupling. Here, it should be pointed out that the mentioned objections leave the main message of the simulation part of this chapter, i.e. the magnetic coupling across APBs in Ni_2MnZ Heusler alloys, untouched. There is no reason to believe that segregation or wetting should destroy the magnetic coupling *per se*. In fact, independent of the size of the APB, the magnetic coupling is only dependent on the sublattices on which Mn atoms are situated. Consequently, the coupling effect would persist also for extended APBs. Furthermore, there is experimental evidence for the existence of a magnetic APD coupling in the investigated alloy system as reported by (see Murakami et al., 2013, 2011; Park et al., 2012). The striking part of the presented results is that the peculiar features of the magnetization curves directly result from the magneto-structural interplay at the APB emerging from a simple well-accepted Hamiltonian. As a consequence, there is strong evidence that the coupling itself is the primary feature explaining the magnetic properties of partially ordered Ni_2MnZ alloys. Segregation at the APBs or possible wetting/roughening effects at the APB potentially lead to a local alteration of the nuclear structure along with an altered distribution of Mn-Mn NN pairs at the interface. Consequently, it is thinkable that the coupling across an APB is different in strength from e.g. the coupling inside the domain. Hence, it would be plausible that AFM coupling persists or is absent in reality while exchange parameters and coupling regimes retrieved from e.g. DFT calculations would predict otherwise. Yet, the overall concept of the magnetic APD coupling does not lose its general validity as a consequence of a more complex APB structure.

2.5 Conclusions

In this chapter, the evolution of magnetic properties in Ni_2MnZ compounds was investigated as function of the atomic order, specifically during the emergence of $L2_1$ order starting with a disordered B2 structure. It was observed that the magnetic transition temperature increases much faster with increasing order than the bulk magnetization or the DC susceptibility. This phenomenon was phenomenologically ascribed to the presence of $L2_1$ APBs in the early stages of $L2_1$ ordering. Furthermore, it was inferred that the magnetic transition temperature primarily probes the local state of order, i.e. the short-range order in the sample, while the bulk magnetization and DC susceptibility mainly depend on the APD structure. As a consequence, in the 2D parameter space of magnetic transition temperature and bulk magnetization/DC susceptibility, a clear trajectory first along the magnetic transition temperature axis and then along the bulk magnetization/DC susceptibility axis was found.

In the second part of this chapter, computer simulations have been used to reveal the origins of this unusual dependency of the magnetic properties on the mesoscale nuclear structure. Using a well-accepted Heisenberg Hamiltonian for classical spins with nearest neighbor interactions, it was found that magnetic domains coincide naturally with structural APD in Ni_2MnZ compounds. The reason for this is an AFM exchange interaction of Mn atoms across structural APBs while inside the $L2_1$-ordered domain FM interactions prevail. As a consequence, entire APDs behave as supermoments that couple AFM with each other. Simulating $M(H)$ and $M(T)$ curves for the simulated APD structures showed convincing agreement to the experimental observations reproducing all characteristic features of the measurements. Consequently, the presented results make a strong case for magnetically coupled APDs in Ni_2MnZ Heusler compounds.

Chapter 3

Ordering kinetics in Ni_2MnZ Heusler compounds

3.1 Introduction

In Chapter 2, $Ni_2MnAl_{0.5}Ga_{0.5}$ was introduced as an ideal model material to study the ordering process in Ni_2MnZ Heusler alloys. In opposition to ternary Ni_2MnAl and Ni_2MnGa where the ordering kinetics and transformation temperatures restrict the accessible range of the ordering process to either the very early (Acet et al., 2002) or the very late stages (Sánchez-Alarcos et al., 2010; Sánchez-Alarcos et al., 2007), in $Ni_2MnAl_{0.5}Ga_{0.5}$, the entire ordering process can be accessed. In this compound, on the one hand, as in Ni_2MnAl, B2 order can be quenched-in. On the other hand, as in Ni_2MnGa, perfect $L2_1$ order with large antiphase domains (APDs) can be adjusted via the appropriate annealing treatment. Hence, this model material enables to study the B2-$L2_1$ transition in Ni_2MnZ alloys in detail over its entire formation process.

The pathway of this ordering process was qualitatively described in Chapter 2 by its evolution in the two-dimensional parameter space composed of the magnetic transition temperature T_c and the bulk magnetization M/DC susceptibility χ. Specifically, it was demonstrated that the ordering process evolves first along the T_c-axis and later, when T_c is quasi in saturation, along the M/χ-axis. This was ascribed to first the evolution of (short-range) order and second the growth of the $L2_1$ APD structure. To fully understand the $L2_1$ ordering process, the evolution of characteristic properties such as T_c and M, and by that the evolution of the underlying processes, has not only to be described qualitatively but also a quantitative description of the kinetics of the process is needed.

Ordering kinetics in intermetallic compounds have been a research interest for decades. In the binary Fe_3Al system for instance, Feder and Cahn (1960) investigated the DO_3 ordering process by means of electrical resistivity measurements. Later, in-situ X-ray diffraction studies by Lawley and Cahn (1961); Oki et al. (1973) revealed that the B2-DO_3 transformation can be characterized via a fast evolution of the DO_3 peak intensities, related to (short-range) order formation, while the peak width evolution, related to APD growth, was observed to be initially slower than the intensity evolution and still ongoing when the intensity evolution curve already saturated. The first investigations of the kinetics of the $L2_1$ ordering process have been performed in $AuAgZn_2$ by Murakami (1985); Murakami et al. (1980a,b). Using X-ray diffraction, Murakami et al. (1980a) studied the evolution of $L2_1$ order and described the temperature dependence of the process quantitatively using standard rate equations as previously introduced by Feder and Cahn (1960). Via the width of the superstructure peaks, Murakami et al. (1980a) also investigated and quantitatively described the growth of the $L2_1$ APD structure.

In Ni_2MnGa, various investigations have been performed on the interdependencies of the degree of order in the austenite phase and magnetic properties as well as martensitic transitions (Kreissl et al., 2003; Sánchez-Alarcos et al., 2008, 2010; Sánchez-Alarcos et al., 2007; Seguí, 2014; Seguí and Cesari, 2011, 2012; Seguí et al., 2007). Specifically, Sánchez-Alarcos et al. (2010) could demonstrate via neutron diffraction and bulk characterization methods that there is a linear dependency between the degree of $L2_1$ order and the magnetic transition temperature of the austenite phase as well as the martensite transformation temperature. This general relationship could also be confirmed for $Ni_{2-x}Co_xMnGa$ alloys by Seguí and Cesari (2012). Furthermore, Seguí et al. (2007) showed that elaborate annealing treatments can be used to effectively influence the transformation sequence of magnetic and structural transitions in $Ni_{2-x}Co_xMnGa$ alloys, a feature highly relevant for magnetocaloric applications where respective transformation sequences can significantly influence the materials functionality.

Quantitative investigations of the ordering kinetics in Ni_2MnGa were reported by Sánchez-Alarcos et al. (2010) where the calorimetric $L2_1$ disordering peak was analyzed by Differential Scanning Calorimetry (DSC) using different heating rates. In this study, the activation energy of the disordering process was determined as 1.49 eV employing the Kissinger method. The experimental method employed throughout this chapter, namely monitoring the $L2_1$ ordering kinetics indirectly via the magnetic transition temperature, was previously used by Seguí (2014). Specifically, via annealing at different annealing temperatures, Seguí (2014) determined an activation energy of 1.46 eV for the $L2_1$ ordering process in $Ni_{2-x}Co_xMnGa$.

For the Ni_2MnAl system, the trends observed in Ni_2MnGa-related alloys were confirmed. Specifically, a dependency of the martensite transformation temperature from the annealing condition and hence the degree of $L2_1$ order was observed by Kainuma et al. (2000); Mehaddene et al. (2008). However, neither for Ni_2MnAl nor for the model compound $Ni_2MnAl_{0.5}Ga_{0.5}$, a comprehensive analysis of the $L2_1$ ordering kinetics has been performed up to this point.

In this chapter, the temporal evolution of $L2_1$ order in $Ni_2MnAl_{0.5}Ga_{0.5}$, stoichiometric Ni_2MnAl and off-stoichiometric Ni_2MnAl is studied in initially B2-ordered samples, mainly via tracking the two previously introduced magnetic properties, i.e. the magnetic transition temperature T_c and the bulk magnetization M, as function of annealing time during isothermal annealing treatments. On the basis of these measurements, the activation energies of the ordering processes are determined and time temperature transformation (*TTT*) diagrams are constructed. Furthermore, the dependency of the ordering process in off-stoichiometric Ni_2MnAl compounds from quenched-in excess vacancies is demonstrated and the vacancy formation energy is determined. Eventually, the indirect measurements of order formation are compared to neutron powder diffraction measurement and electron diffraction measurements that allow to deduce directly the degree of $L2_1$ order and the correlation lengths of the ordered $L2_1$ domains. The data presented in this chapter was partially published in Neibecker et al. (2014).

3.2 Results – $Ni_2MnAl_{0.5}Ga_{0.5}$

3.2.1 Isothermal annealing experiments in $Ni_2MnAl_{0.5}Ga_{0.5}$

In the following, the kinetics of the B2-$L2_1$ transformation process in $Ni_2MnAl_{0.5}Ga_{0.5}$ are discussed based on the evolution of the magnetic transition temperature T_c as determined by calorimetry. The calorimetric measurements as well as the isothermal annealing treatments have been performed by DSC as outlined in Chapter 1, heating to and cooling from the annealing temperature with a heating rate of 10 K/min. Additionally, the growth of the APD structure was followed via the bulk magnetization M, specifically, the value of M in an external magnetic field of 15 kOe at a temperature of 77 K as introduced in Chapter 2. Concerning this matter, it should be noted that the exact relation between M and the APD size is a priori not known. While it is quite evident that initially, the increase in M is strongly coupled to the dimensions of the APD structure (see Chapter 2), it is unclear how this dependency evolves at larger APD sizes.

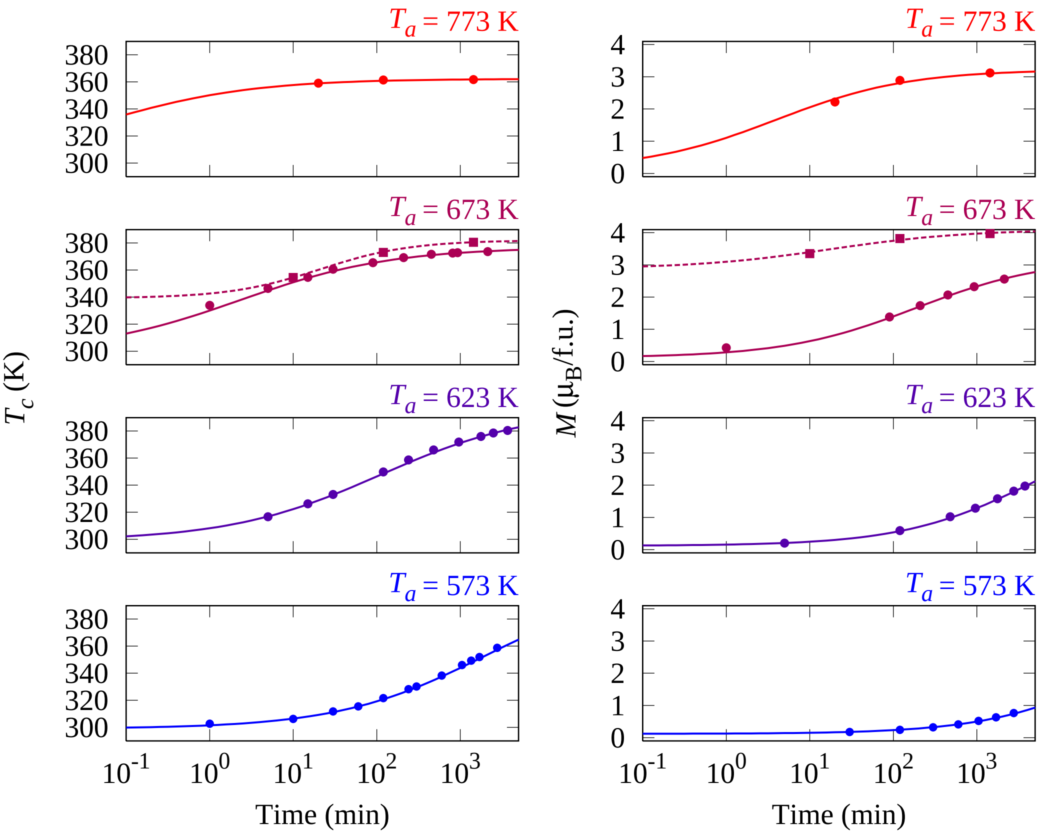

Fig. 3.1 T_c (left) and M (right) evolution as a function of isothermal annealing time at various annealing temperatures T_a in $Ni_2MnAl_{0.5}Ga_{0.5}$ samples quenched from 1073 K (points) and 873 K (squares). T_c refers to the magnetic transition temperature determined by calorimetry and M refers to the bulk magnetization at 15 kOe and 77 K. The lines are a guide to the eye and represent a phenomenological curve fit.

Fig. 3.1 shows the T_c and M evolution upon isothermal annealing of initially 1073 K-quenched samples at 4 different annealing temperatures (T_a = 573 K, 623 K, 673 K and 773 K). Evidently, both T_c and M increase with increased annealing time and hence with an increased degree of $L2_1$ order. At the same time, the evolution kinetics of both T_c and M increase with increased T_a, as it is expected for a process relying on the constituents' atomic mobility. Annealing at different temperatures T_a hence probes directly this mentioned mobility. Assuming a similar curve shape for the T_c and M evolution at all T_a, roughly an increase in the ordering kinetics of three orders of magnitudes can be estimated between isothermal annealing at 573 K and 773 K. Furthermore, it can be observed that the evolution of T_c is faster than the evolution M, as it was already qualitatively discussed in the previous chapter.

For one temperature series, i.e. isothermal annealing at 673 K, a second measurement series was recorded for samples quenched from the $L2_1$-stable regime at 873 K. The results are also depicted in Fig. 3.1. Evidently, due to the increased equilibrium degree of $L2_1$ order at 873 K, the as-quenched values for T_c and M are significantly higher than for the samples quenched from 1073 K. It is observed that the T_c evolution follows qualitatively the same pathway while the M evolution shows pronounced differences in both series. This observation can be ascribed to the growth of the APD structure upon annealing at 873 K prior to quenching. As a consequence, both sample series adopt a different APD structure, expressed in different M evolution curves. Yet the degree of (short-range) order, especially in the late stages of annealing, is similar in both series. Consequently, the T_c evolution curves coincide at long annealing times. Furthermore, as clearly observed for the T_c evolution, the kinetics of order adjustment at 673 K is similar in both sample series.

Different from the pertinent literature where usually standard rate equations as described by Feder and Cahn (1960) are employed to analyze ordering kinetics, in this chapter, a straightforward approach to study quantitatively the kinetics of the $L2_1$ ordering process is outlined. The presented approach is based on the assumption that all isothermal annealing curves for the T_c and M evolution can be described by a common master curve onto which all data points can be shifted via stretching their time axes with T_a-dependent stretching factors ϵ and via normalizing them with respect to the T_a-dependent equilibrium T_c/M values.

In order to construct such a master curve, in a first step, the equilibrium T_c-T_a and M-T_a dependency has to be determined. As described in Chapter 2, the equilibrium degree of order under the boundary condition of a large APD structure is accessible in $Ni_2MnAl_{0.5}Ga_{0.5}$ via a two step isothermal annealing treatment first at 873 K followed by annealing at the target temperature and finally quenching to room temperature. With respect to M, the equilibrium value refers to the spontaneous magnetization M_s as determined by extrapolating the linear part of the ferromagnetic $M(H)$ curves at 77 K to zero external field. T_c-T_a and M_s-T_a curves are presented in Fig. 3.2 together with an empirical curve description. As can be seen, the second-order B2-$L2_1$ transition is retrieved in both the temperature-dependent T_c and M_s values while clearly the respective curve shapes differ. Specifically, the T_c-T_a transition is broad and T_c does not approach the B2 (1073 K-quenched) value immediately at the transition temperature but rather continues to converge slowly towards the equilibrium value also above the transition temperature. Hence, it can be inferred that T_c is not only dependent on the degree of long-range order in the sample but that it is additionally sensitive to short-range order in the sample. In contrast to this, M_s approaches the zero bulk magnetization of the B2

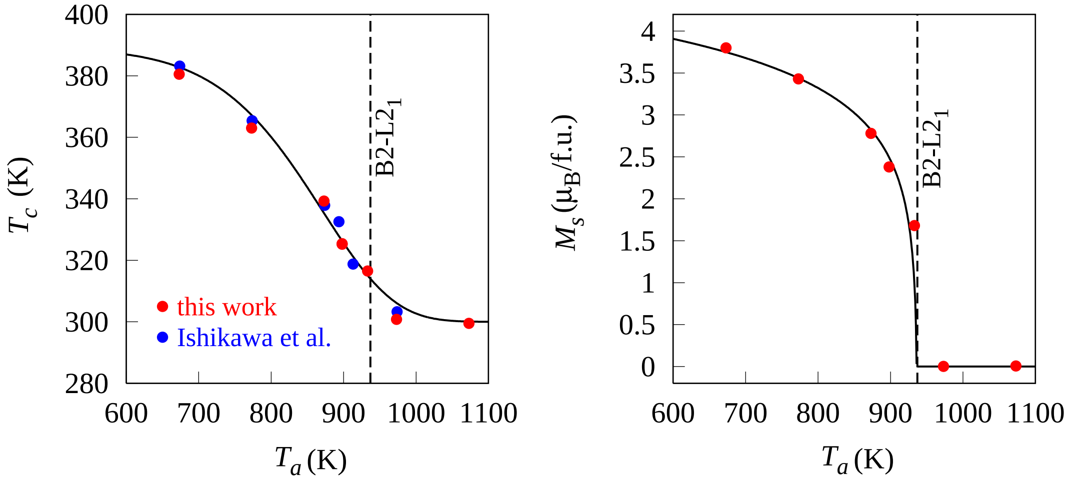

Fig. 3.2 Magnetic transition temperature T_c (left) and spontaneous magnetization M_s (right) as function of annealing temperature T_a measured in $Ni_2MnAl_{0.5}Ga_{0.5}$ samples initially quenched from 1073 K that were subsequently annealed for 24 h at the respective temperature T_a followed by quenching in ice water. The solid lines represent phenomenological curve descriptions. The dashed line refers to the B2-L2$_1$ transition temperature as reported by Ishikawa et al. (2008).

state abruptly at the transition temperature and shows a sharp transition. It should be noted that the measurements performed within the scope of this thesis perfectly agree with the independent data set reported by Ishikawa et al. (2008) for the T_c-T_a dependency (blue points in Fig. 3.2). Furthermore, the estimated B2-L2$_1$ transition temperature from the temperature dependent M_s measurements agrees well with the phase transition temperature determined by calorimetric measurements as reported by Ishikawa et al. (2008) (dashed line in Fig. 3.2).

Making use of the equilibrium T_c and M_s values, a master curve for the temporal evolution of T_c and M is created. For this purpose, the kinetics curves are first normalized to the equilibrium T_c/M_s values at any T_a and second, T_a dependent stretching factors ϵ are applied in order to shift all data points onto a common curve. The resulting master curve then evolves in relative units from 0 to 1 and is depicted in Fig. 3.3. Note, the time axis is normalized to the 573 K measurement. This means that the stretching factor of the 573 K data set is 1, while all other stretching factors express the acceleration of the temporal evolution on the master curve at the elevated T_a. As can be seen, for both T_c and M, the description of all data sets with a common master curve is satisfying.

The determined T_a-dependent stretching factors ϵ are further used to estimate activation energies of both processes, namely the (short-range) order formation and the APD growth. Fig. 3.4 shows the stretching factors ϵ as a function of T_a^{-1} on a semilogarithmic scale.

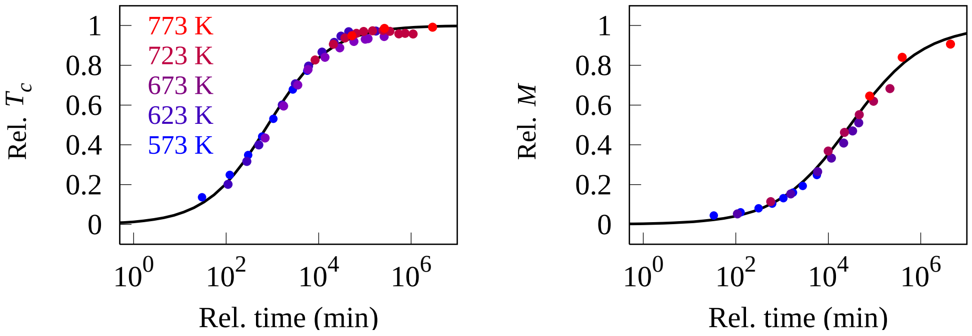

Fig. 3.3 Master curve for the temporal evolution of T_c (left) and M (right) in $Ni_2MnAl_{0.5}Ga_{0.5}$ samples quenched from 1073 K. The x-axis shows the time relative to the 573 K measurement.

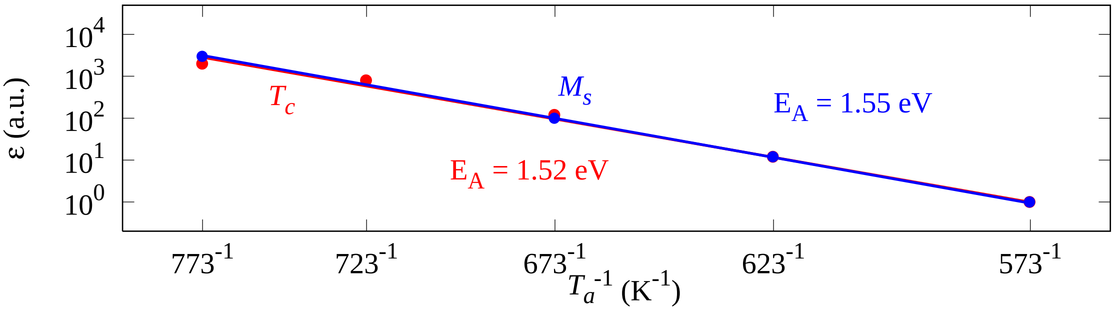

Fig. 3.4 Temperature dependent stretching factors ϵ for the estimation of the activation energies of the $L2_1$ ordering process for $Ni_2MnAl_{0.5}Ga_{0.5}$ samples quenched from 1073 K. The red points and line refer to the T_c evolution while the blue points and line refer to the M evolution.

Clearly, the stretching factors can be described with an exponential dependency of the form

$$\epsilon(T_a) = \exp\big(-\frac{E_A}{k_B}(\frac{1}{T_a} - \frac{1}{T_0})\big). \tag{3.1}$$

with T_0 = 573 K, E_A being the activation energy of the ordering process and k_B being the Boltzmann constant. For the evolution of T_c and M, activation energies of 1.52 eV and 1.55 eV were determined, respectively. These values perfectly agree with the activation energies for the $L2_1$ order formation of 1.46 eV and 1.49 eV previously reported by Sánchez-Alarcos et al. (2010) and Seguí (2014) for Ni_2MnGa and $Ni_{2-x}Co_xMnGa$.

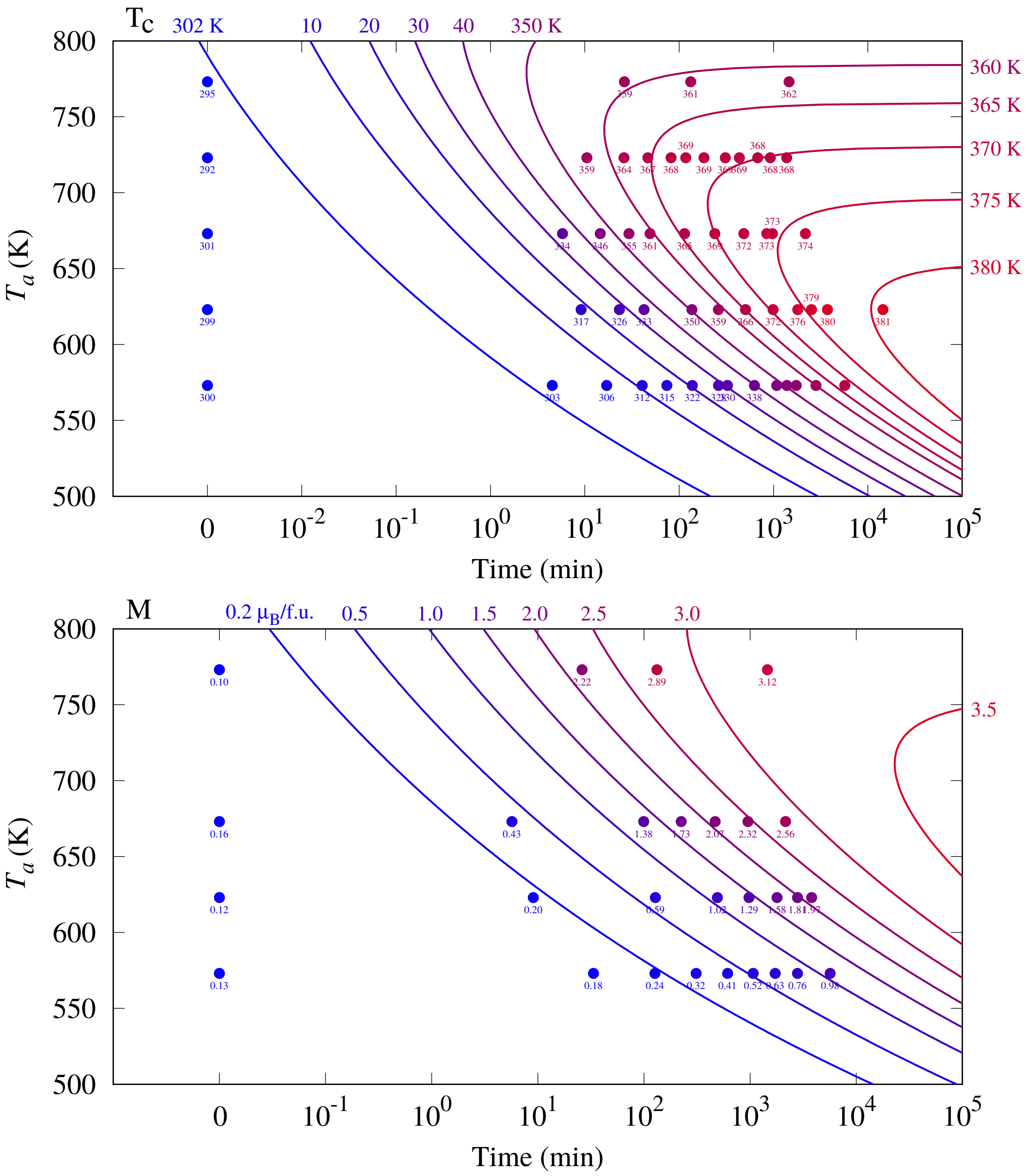

Fig. 3.5 *TTT* diagram for the evolution of T_c (top) and M (bottom) in $Ni_2MnAl_{0.5}Ga_{0.5}$ samples initially quenched from 1073 K. Depicted are iso-T_c lines as calculated with the model described in the text, while the points represent time-corrected T_c/M values as obtained in isothermal annealing experiments (see Fig. 3.1). The numbers at the points show the measured T_c values in K and M values in μ_B/f.u. The data points on the left refer to the quenched samples and correspond to time zero.

3.2.2 *TTT* diagrams for T_c and M evolution

The determined T_c-T_a and M_s-T_a dependencies together with the stretching factors ϵ can be used to construct time temperature transformation (*TTT*) diagrams for both the T_c and the

M evolution. Such *TTT* diagrams were originally developed to describe the transformation of the austenite phase in steels upon isothermal annealing (Davenport and Bain, 1930) or to describe crystallization processes for example in metallic glass forming systems (Kim et al., 1996). Yet, they can easily be transferred to the $L2_1$ ordering process.

Specifically, in this thesis, T_a-dependent T_c-time and M-time curves for isothermal annealing processes were calculated via adapting the master curve for any given annealing temperature. This was done via scaling the y-axis with respect to the equilibrium T_c/M value at that annealing temperature while the x-axis was scaled with the respective stretching factor. As a result, iso-T_c and iso-M lines can be drawn as a function of isothermal annealing time in the T_c/M-time space.

TTT diagrams for T_c evolution and M evolution are depicted in Fig. 3.5. The data points represent the measured data including a time correction taking into account the annealing effect evoked by heating to and cooling from T_a with a constant heating rate of 10 K/min in the DSC measurements. It is evident that the iso-T_c lines calculated with the model describe the measured data reasonably well with small deviations being observed in the equilibrium T_c values as function of T_a. The iso-T_c lines show a characteristic nose in the T_a-time space which shifts to lower T_a values and larger annealing times with increasing T_c. The reason for this lies in the second order nature of the underlying phase transition with an increased degree of equilibrium order at lower temperatures and, at the same time, temperature-dependent atomic mobilities which are higher at elevated temperatures. Hence, the equilibrium values reachable at lower T_a are higher while the convergence to these equilibrium values is slower.

For the M evolution, the constructed *TTT* diagram shows the same qualitative features as the *TTT* diagram for the T_c evolution with the difference that the convergence to the final M values takes significantly more time. This is expressed in the iso-M curves being shifted to the right with respect to the *TTT* diagram for the evolution of T_c. In this respect, it should be noted that as shown in Fig. 3.2, the equilibrium M value at low temperatures is approximately $4\,\mu_B$/f.u.

It needs to be pointed out that M in the depicted *TTT* diagrams refers to the bulk magnetization in an external field of 15 kOe at a temperature of 77 K which is rather a technical parameter than a meaningful physical property. However, taking into account that the magnetic properties show only in the very final stages of the ordering process an ideal ferromagnetic $M(H)$ curve shape, the better suited spontaneous magnetization is not easily accessible over the entire ordering process. Additionally, it needs to be considered that similar *TTT* diagrams can easily be constructed for any external field which practically gives a protocol to tailor materials properties for explicit application scenarios. For instance, it is well thinkable that a magnetocaloric device operates under certain boundary conditions,

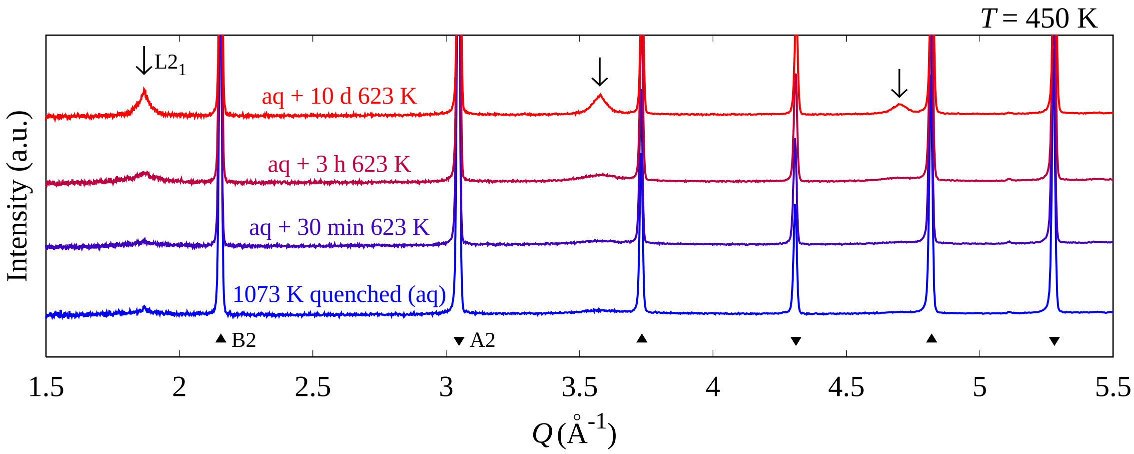

Fig. 3.6 Neutron powder diffraction patterns of $Ni_2MnAl_{0.5}Ga_{0.5}$ upon annealing at 623 K in samples initially quenched from 1073 K. Symbols below and above the diffractograms indicate the 3 distinct peak families present in the L2$_1$ structure, i.e. A2, B2 and L2$_1$ peaks. The patterns have been recorded at 450 K in the paramagnetic regime.

namely in a certain external magnetic field and at a specified temperature. As a consequence, it would be required to design a material with a well defined set of magnetic properties such as a specific magnetic transition temperature and a certain bulk magnetization under the given conditions. *TTT* diagrams providing an exact protocol for adjusting the intended materials properties can consequently be composed following the introduced procedure outlined in this thesis.

3.2.3 Comparison to neutron powder diffraction measurements

In order to provide a direct method for order determination in support of the indirect bulk measurements presented above, neutron powder diffraction measurements have been performed on $Ni_2MnAl_{0.5}Ga_{0.5}$ samples in different annealing conditions. The results of this broader neutron diffraction study are presented in detail in Chapter 4. At this point, the evolution of the L2$_1$ peak intensity and the correlation length of the ordered domains upon isothermal annealing is discussed.

Fig. 3.6 shows neutron powder diffraction patterns recorded at the POWGEN time-of-flight powder diffractometer at the Spallation Neutron Source (SNS), USA. Diffraction patterns were measured using two wavelengths bands with center wavelengths *cw* of 1.333 Å and 2.665 Å. In Fig. 3.6, exemplarily the 2.665 Å measurements are depicted. Shown are 4 different annealing conditions: quenched from the B2-stable regime at 1073 K as well as quenched plus 0.5 h, 3 h and 10 d isothermally annealed at 623 K. Below and above the

$Ni_2MnAl_{0.5}Ga_{0.5}$				
Observable	aq	0.5 h	3 h	10 d
T_c (K)	314.5	330.8	342.6	387.1
$\eta_{\mathrm{L2_1}}$	0.75	0.73	0.93	1.05
correlation length (Å)	8.2	10.5	12.1	30.0

Table 3.1 Magnetic transition temperature T_c, degree of L2_1 order $\eta_{\mathrm{L2_1}}$ and correlation length of the L2_1 domains measured as function of annealing time at 623 K in $Ni_2MnAl_{0.5}Ga_{0.5}$ powder samples quenched from 1073 K.

diffraction patterns, the different peak families are indicated. Since the L2_1 structure is a superstructure of the B2 structure which again is a superstructure of the A2 structure, every peak in the diffractogram can be assigned to either the A2, B2 or L2_1 family. Specifically, the A2 structure factor results from all lattice sites contributing in phase, consequently the structure factor of the A2 reflections is only dependent on the alloy composition. The B2 structure factor result in this case from a diffraction contrast between the 1a site (occupied by Ni) and 1b site (randomly occupied by Mn, Al and Ga) of the B2 (Pm$\bar{3}$m) structure. Finally, the L2_1 structure factor results from the diffraction contrast between the 4a (occupied my Mn) and 4b site (randomly occupied by Al and Ga) of the L2_1 (Fm$\bar{3}$m) structure.

Clearly, the B2-L2_1 phase transition is visible in the diffractograms upon isothermal annealing in the L2_1-stable regime. Specifically, the B2 and A2 peaks are similar in intensity and shape in all annealing states. In contrast to that, the L2_1 peaks are extremely broad and weak in the as-quenched state and grow in intensity as well as sharpness with increased annealing time. Note that in the 1073 K-quenched sample, the L2_1 peaks should be completely absent. The reason for a weak intensity in these samples is the incapability of achieving the same quenching efficiency in the powder samples as in the bulk samples which hence evokes a slightly progressed state of ordering in the powder samples. This lack of quenching efficiency is not only visible in the diffraction patterns but was also confirmed in the magnetic transition temperature of the powder samples which are given in Tab. 3.1. As can be seen, the as-quenched T_c is with a value of 314.5 K approximately 20 K higher than the as-quenched T_c of the bulk samples while overall the response to isothermal annealing and also the final T_c values are in good conformity for the bulk and powder samples. Interestingly, even after 10 d of annealing at 623 K, the L2_1 peaks are significantly broader than the B2 and A2 peaks. This indicates that the L2_1 peak width is up to the largest annealing times not only dependent on the instrument resolution and binning but also on the correlation length of the L2_1 APD structure which increases during the ordering process.

Both the intensity evolution and the correlation length can also be investigated quantitatively. For this purpose, the diffractograms shown in Fig. 3.6 were Rietveld-refined. In the refinement, the occupancy of Mn and Al/Ga on the 4a and 4b Wyckoff positions of the L2$_1$ structure were free parameters. From the retrieved sublattice occupancies, the degree of L2$_1$ order $\eta_{\mathrm{L2_1}}$ was calculated. The L2$_1$ structure factor is defined as

$$F_{\mathrm{L2_1}} = \left(\bar{b}_{\mathrm{4a}} - \bar{b}_{\mathrm{4b}}\right) = \left(\left[\eta_{\mathrm{L2_1}} b_{\mathrm{Mn}} + (1-\eta_{\mathrm{L2_1}})\frac{b_{\mathrm{Al}} + b_{\mathrm{Ga}}}{2}\right] - \left[(1-\eta_{\mathrm{L2_1}}) b_{\mathrm{Mn}} + \eta_{\mathrm{L2_1}}\frac{b_{\mathrm{Al}} + b_{\mathrm{Ga}}}{2}\right]\right). \tag{3.2}$$

where $\bar{b}_{\mathrm{4a}}$ and $\bar{b}_{\mathrm{4b}}$ are the average coherent neutron scattering lengths on the Wyckoff sites 4a and 4b while b_{Ga}, b_{Al} b_{Mn} are the coherent neutron scattering lengths for Ga, Al and Mn, respectively. In order to model the effect of APDs, an hkl-dependent size broadening with condition $\mathrm{h} + \mathrm{k} + \mathrm{l} = 2n + 1$ with $n \in \mathbb{N}$ was considered. As described by Fultz and Howe (2012), the correlation length or crystallite size L can be calculated as $L = 0.443/\Gamma$, with Γ being the half width at half maximum (HWHM) of a Lorentzian fit of the individual peaks corrected for the instrument resolution. The size parameters obtained by Rietveld refinement were converted to match the stated definition by Fultz and Howe (2012). The refined values for $\eta_{\mathrm{L2_1}}$ and the determined correlation lengths are given in Table 3.1. Furthermore, their temporal evolution is shown in Fig. 3.7. As can be seen, the degree of L2$_1$ order gradually increases from 0.75 in the as-quenched state to approximately 1 in the 10 days annealed state. As pointed out above, the existence of a broad, weak L2$_1$ intensity in the as-quenched state is due to an insufficient quenching rate for the powder samples. Hence, the starting point depicted with square symbols in Fig. 3.7 in reality represents an already progressed state of L2$_1$ ordering and in principle would have to be shifted on the time axis in order to grasp the real evolution curve. However, since the peaks are that broad, the definition of the background plays an important role especially in the early stages of ordering with a very diffuse L2$_1$ intensity. Hence, inherent errors in the determination of $\eta_{\mathrm{L2_1}}$ are immanent. In Fig. 3.7, also the evolution of the APD structure is depicted. As can bee seen, initially, the correlation length of the ordered domain increases slowly while it continues to increase when $\eta_{\mathrm{L2_1}}$ is already in saturation.

Comparing the neutron diffraction results to the evolution of magnetic properties shows a good conformity to the previous observations. The evolution of T_c as well as the evolution of $\eta_{\mathrm{L2_1}}$ are relatively fast processes preceding the temporal evolution of M as well as the growth of correlation length. However, in-situ neutron diffraction experiments during isothermal annealing treatments would be beneficial in order to further investigate the exact dependencies between short-range order and correlation length as well as between structural and magnetic properties in the L2$_1$ ordering process.

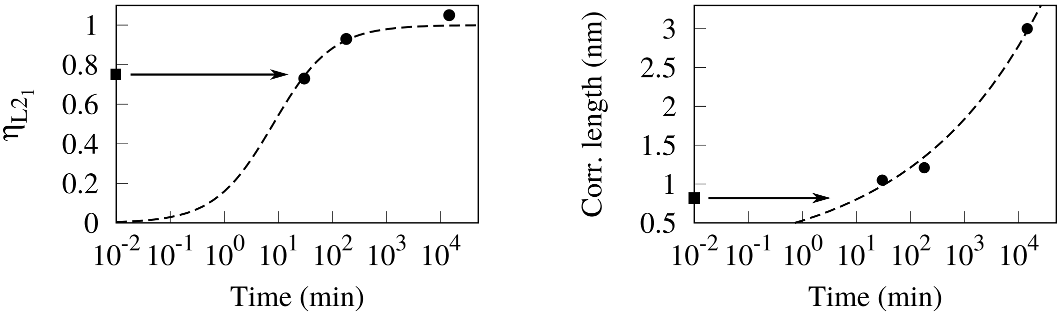

Fig. 3.7 Degree of $L2_1$ order η_{L2_1} (left) and correlation length estimation (right) as function of annealing time at 623 K in $Ni_2MnAl_{0.5}Ga_{0.5}$ samples initially quenched from 1073 K. The arrows indicate an effectively progressed state of order in the as-quenched samples due to a less effective quenching process observed for powder samples.

3.3 Results – Ni_2MnAl

As discussed in the introduction of this chapter, in Ni_2MnAl, in general a low $L2_1$ ordering tendency is observed (see, for instance Acet et al., 2002; Ziebeck and Webster, 1975). In order to reveal the origin of this low ordering tendency, the ordering kinetics in Ni_2MnAl has been investigated and is in the following compared to the previously presented ordering kinetics in the model system $Ni_2MnAl_{0.5}Ga_{0.5}$. For this purpose, polycrystalline samples were quenched from the B2-stable regime at 1073 K in room temperature water. Subsequently, the samples have been isothermally annealed at a variety of annealing temperatures T_a. The magnetic transition temperature T_c has again been monitored as an indirect fingerprint of the state of (short-range) order in the sample. The evolution of T_c as a function of time and isothermal annealing temperature is presented in Fig. 3.8 for T_a = 573 K, 623 K, 673 K and 723 K. Additionally, Fig. 3.8 shows as a comparison the T_c evolution curves of $Ni_2MnAl_{0.5}Ga_{0.5}$ as previously presented in Fig. 3.1.

Evidently, the T_c evolution in Ni_2MnAl shows qualitative conformity to the one in $Ni_2MnAl_{0.5}Ga_{0.5}$. Specifically, an increase of T_c is observed with increased annealing time and consequently with an increased degree of $L2_1$ order. Furthermore, the ordering kinetics increase as function of T_a, as also found for $Ni_2MnAl_{0.5}Ga_{0.5}$. Yet, quantitatively, drastic differences are observed. The T_c evolution in Ni_2MnAl is after a comparable sample preparation, i.e. quenching from 1073 K, approximately two orders of magnitude slower than in $Ni_2MnAl_{0.5}Ga_{0.5}$. Clearly, when comparing the ordering kinetics in both compounds at the same T_a, the higher B2-$L2_1$ transition temperature of $Ni_2MnAl_{0.5}Ga_{0.5}$ (933 K) with respect to Ni_2MnAl (775 K) has to be taken into account. Assuming that the T_c-T_a dependency for equilibrium order is qualitatively the same in both compounds, the homologous annealing

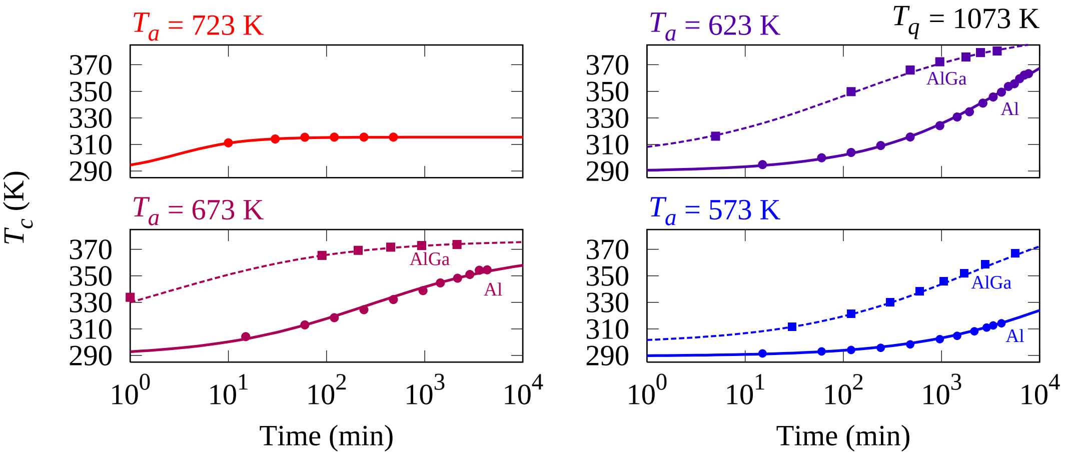

Fig. 3.8 Evolution of the magnetic transition temperature T_c as a function of annealing temperature T_a in Ni_2MnAl samples quenched from 1073 K. The solid lines represent a phenomenological curve fit to be understood as guide to the eye. The circles correspond to Ni_2MnAl and the squares correspond to $Ni_2MnAl_{0.5}Ga_{0.5}$.

temperature can be calculated for any T_a (note, the homologous annealing temperature is defined as T_a divided by the B2-L2$_1$ transition temperature). Clearly, a lower B2-L2$_1$ transition temperature leads to a higher homologous temperature and hence a lower equilibrium degree of order at the same T_a. This lower equilibrium degree of order results in a lower driving force for order adjustment and hence, potentially, a reduced ordering kinetics. Yet, estimating the equilibrium degree of order as a function of homologous temperature for both compounds from e.g. in-situ structure factor determinations presented by Sánchez-Alarcos et al. (2007) yields at the relevant temperatures an equilibrium degree of order difference in the order of only 10 %. This small difference cannot explain the drastic differences in the ordering kinetics. Hence, the nature of the lower ordering tendency in Ni_2MnAl compounds can be attributed to kinetic rather than thermodynamic reasons.

As for $Ni_2MnAl_{0.5}Ga_{0.5}$, also for Ni_2MnAl, a *TTT* diagram for the T_c evolution can be constructed. Again, first the equilibrium T_c-T_a dependency needs to be established. The dependency as retrieved from ballistic cooling, i.e. cooling with the maximal achievable cooling rate of samples in the DSC (see also the following discussion on cooling rate sensitive experiments in $Ni_2Mn_{1.12}Al_{0.88}$), from different annealing temperatures T_a as well as from isothermal annealing experiments is depicted in Fig. 3.9. The low temperature data points specifically refer to the T_c values measured in samples long time isothermally annealed at the indicated temperatures. As can be seen, the curve shape of the T_c-T_a dependency is comparable to the one observed for $Ni_2MnAl_{0.5}Ga_{0.5}$ and the second order B2-L2$_1$ transition is clearly resolved. At 573 K, even the longest applied annealing treatments were due to

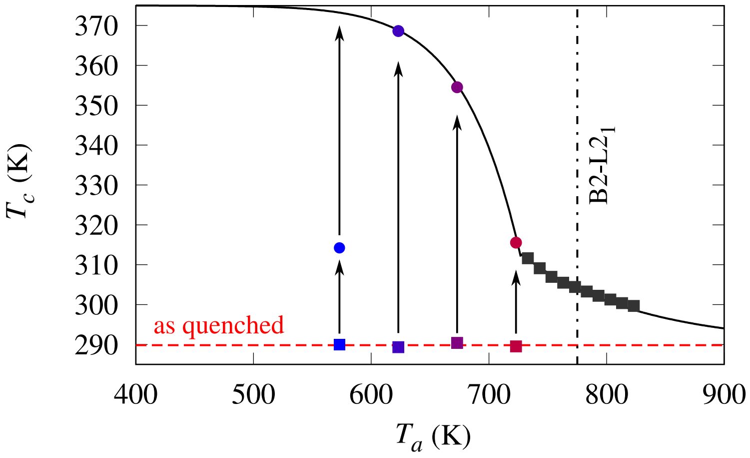

Fig. 3.9 Magnetic transition temperature T_c as function of annealing temperature T_a measured in samples quenched from 1073 K (see Fig. 3.8) and in samples cooled ballistically from different equilibrium annealing temperatures T_q in the DSC.

slow kinetics insufficient for adjusting the equilibrium degree of order. Interestingly, ballistic cooling from temperatures around the previously reported B2-L2$_1$ transition temperature of 775 K (Kainuma et al., 2000) resulted in T_c values around 10 K higher than the ones obtained when quenching from 1073 K. This again indicates that T_c is highly sensitive to the short-range order in the sample. With the T_c-T_a dependency and the isothermal T_c curves, also for Ni_2MnAl, a common master curve can be created. Following the procedure introduced for $Ni_2MnAl_{0.5}Ga_{0.5}$, temperature dependent stretching factors were retrieved. Furthermore, the stretching factors were used to determine the activation energy of the ordering process. For Ni_2MnAl, an activation energy for the ordering process of ≈ 1.65 eV was found which is slightly higher than the activation energy determined for $Ni_2MnAl_{0.5}Ga_{0.5}$.

With this information, a *TTT* diagram was constructed which is presented in Fig. 3.10. Depicted is again the corrected measurement data together with the calculated iso-T_c lines. Evidently, the simple model assuming an Arrhenius dependency of the ordering kinetics describes the data qualitatively well. Specifically, at low annealing times, the iso-T_c lines calculated with the kinetic model show a good agreement to the measured data. Yet, towards large annealing times and high annealing temperatures the measured data is less well described by the model. Presumably, especially close to the phase transition temperature, the simple kinetic model has inherent limitations. The characteristic nose that was already described for $Ni_2MnAl_{0.5}Ga_{0.5}$ is also visible in the *TTT* diagram for Ni_2MnAl. As described above, it shifts with increasing T_c to larger annealing times and lower T_a values.

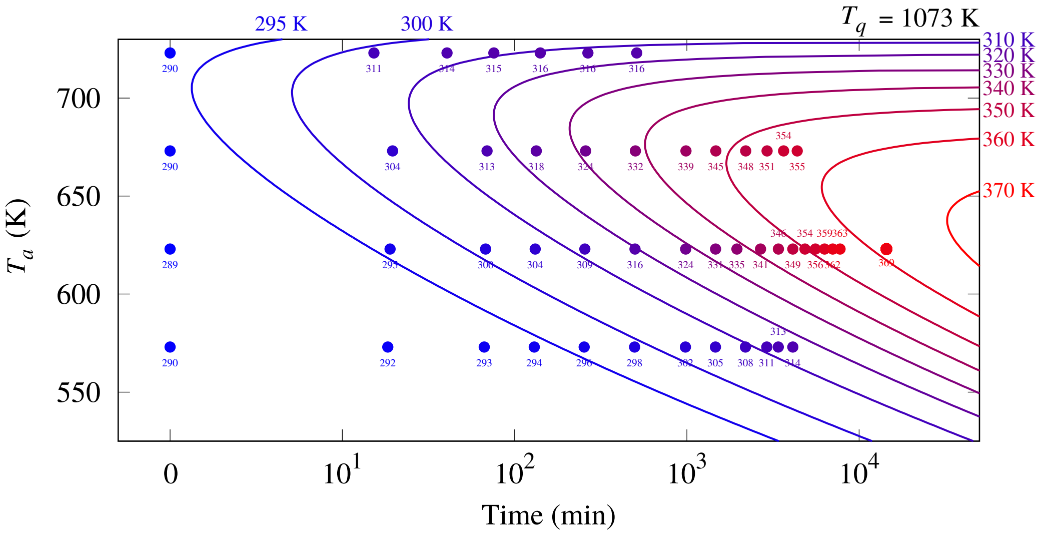

Fig. 3.10 *TTT* diagram for the evolution of T_c upon isothermal annealing of Ni$_2$MnAl samples quenched from 1073 K. The lines show iso-T_c lines as calculated with the introduced model while the points represent time-corrected measurement data as obtained by isothermal annealing experiments (see Fig. 3.8). The numbers at the points show the measured T_c values in K. The data points on the left refer to the quenched samples and correspond to time zero.

3.4 Results – Off-stoichiometric Ni$_2$Mn$_{1.12}$Al$_{0.88}$

3.4.1 The Ni$_2$Mn$_{1+x}$Al$_{1-x}$ system

In the Ni$_2$MnAl system, martensitic transformations are only observed in off-stoichiometric compounds while stoichiometric Ni$_2$MnAl shows stability of the L2$_1$ phase to zero temperature (Ziebeck and Webster, 1975). Hence, for technical applications, off-stoichiometric compounds are of special interest. According to Kainuma et al. (2000), the martensitic phase is thermodynamically stable either under Ni excess or, in the case of a stoichiometric Ni composition, under Mn excess. The work presented in this thesis focuses on alloys with Mn excess. The pseudo-binary Ni$_2$Mn$_{1+x}$Al$_{1-x}$ phase diagram reproduced with data from Kainuma et al. (2000) is shown in Fig. 3.11. Here, the first occurrence of a martensite phase is reported for the compound Ni$_2$Mn$_{1.20}$Al$_{0.80}$ with a martensite start temperature of 276 K. Compounds with lower Mn contents are not reported to show a martensitic transition.

After having studied the ordering kinetics in Ni$_2$MnAl$_{0.5}$Ga$_{0.5}$ and stoichiometric Ni$_2$MnAl, the methodology is transferred to the off-stoichiometric compound Ni$_2$Mn$_{1.12}$Al$_{0.88}$. A priori it is not at all certain that the L2$_1$ ordering process shows similar characteristics for different off-stoichiometric compositions, given that diffusion mechanisms can change in different regimes of constituents' excess and deficiency (for a detailed study in B2 compounds, see

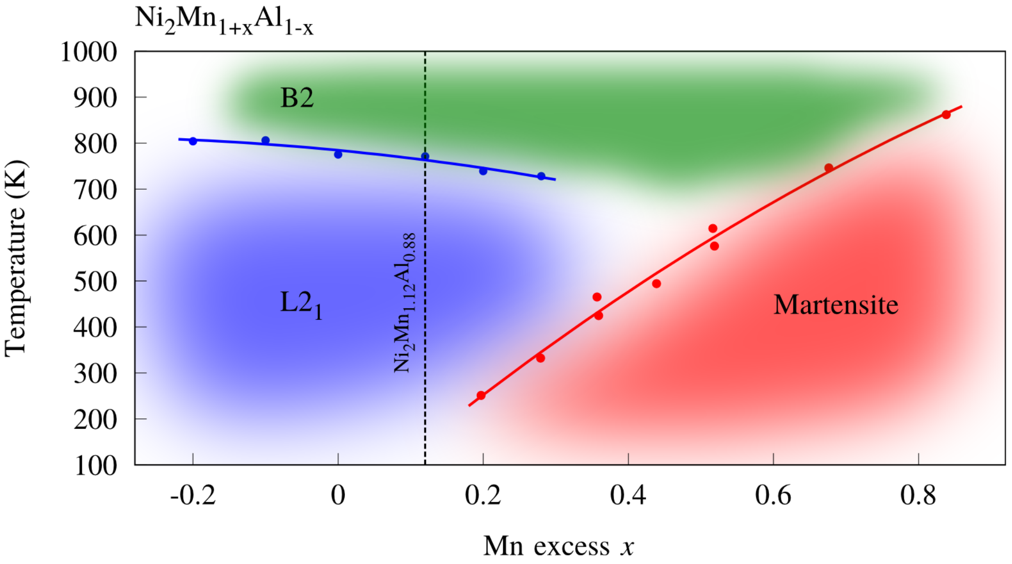

Fig. 3.11 Pseudobinary $Ni_2Mn_{1+x}Al_{1-x}$ phase diagram reproduced with data from Kainuma et al. (2000). The blue line shows the B2-$L2_1$ phase transition temperature, the red line shows the martensite start temperature M_S and the dashed line shows the composition investigated in this study.

Leitner, 2015). To obtain meaningful results for the $L2_1$ ordering kinetics, it is thus important that the selected composition is located in the same compositional regime as the technical relevant alloys (here: Ni stoichiometric, Mn excess, Al deficiency). Simultaneously, as it was the intention to study the ordering process of the $L2_1$ austenite phase and its effect on the magnetic properties down to cryogenic temperatures, a composition adopting a low-temperature martensite phase needed to be carefully avoided. Hence, the investigated compound $Ni_2Mn_{1.12}Al_{0.88}$ is located right outside the area of martensite stability. The here presented kinetics study relates to the previously presented investigation of the bulk magnetic properties of this compound as discussed in Section 2.2.2.

3.4.2 Isothermal annealing experiments in $Ni_2Mn_{1.12}Al_{0.88}$

In order to study the $L2_1$ ordering kinetics in $Ni_2Mn_{1.12}Al_{0.88}$, the magnetic transition temperature T_c was followed as function of annealing time at a variety of annealing temperatures T_a. Fig. 3.12 shows the T_c-time curves for 4 different annealing temperatures (T_a = 573 K, 623 K, 673 K and 723 K) for samples quenched from 1273 K in room temperature water.

The temporal evolution of $L2_1$ order can well be followed in the presented data, starting with a T_c value of approximately 298 K in the as-quenched samples. As discussed before, with

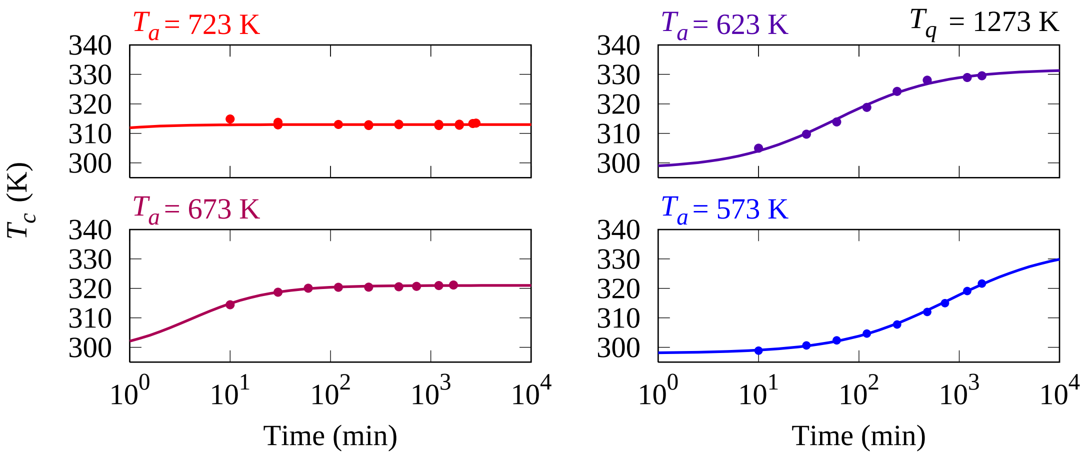

Fig. 3.12 Evolution of the magnetic transition temperature T_c as a function of annealing temperature T_a in samples quenched from 1273 K. The lines represent a phenomenological curve fit to be understood as guide to the eye.

increased annealing temperature, the kinetics of the ordering process is accelerated, the reason of which is the higher mobility of vacancies and atoms at higher temperatures. Assuming that the curve shape in the T_c-time diagram is the same at all annealing temperatures, an increase in ordering kinetics of three orders of magnitudes can be estimated between isothermal annealing at 573 K and 723 K. At the same time, the equilibrium state of order decreases as T_a approaches the B2-L2$_1$ transition temperature since the corresponding structural phase transition is a second order transition. Specifically, the sample annealed at 723 K (according to Fig. 3.11 approximately 50 K below the B2-L2$_1$ transition of the compound) reaches a plateau T_c value of 313.5 K while annealing at 673 K for instance yields a value of 321.1 K. It should be noted that the kinetics at 573 K is again so slow that equilibrium states of order cannot be reached on practical time scales even though the equilibrium T_c value at that temperature would be higher than the one at higher annealing temperatures.

3.4.3 Cooling rate sensitivity of the ordering process

While in the case of low-T annealing, T_c depends primarily on the annealing temperature and the annealing time, in a different regime of annealing temperatures, T_c is affected foremost by the cooling rate applied in the cooling process from the annealing/quenching temperature T_q to room temperature. To investigate latter regime, the following experimental set-up was developed: In the DSC, samples were equilibrium annealed at a temperature T_q, meaning that the annealing treatment was long enough to ensure that both the degree of order as well as the vacancy concentration were in thermodynamic equilibrium at this temperature. This being

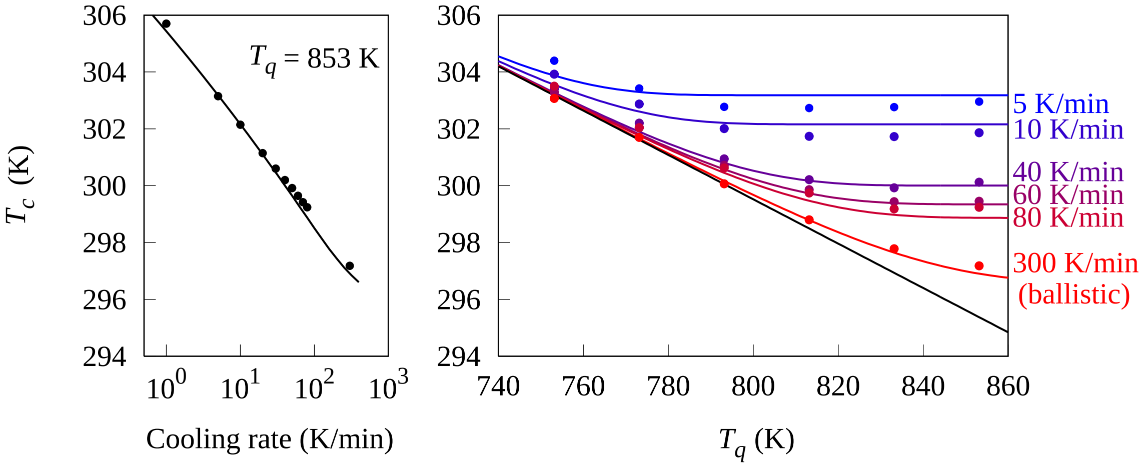

Fig. 3.13 Magnetic transition temperature T_c as function of cooling rate after equilibrium annealing at 853 K (left) and T_c as function of cooling rate and equilibrium annealing/quenching temperature T_q (right). The lines show cooling curves calculated with the model described in the text.

ensured, after the equilibrium annealing treatment, the sample had lost all thermal history. From T_q, the sample was cooled to room temperature with different, well defined, cooling rates. The result of the described experiment for $Ni_2Mn_{1.12}Al_{0.88}$ is presented in the left panel of Fig. 3.13. Here, samples were annealed at $T_q = 853$ K for 60 minutes prior to cooling the specimens with various cooling rates between 1 K/min and approximately 300 K/min to room temperature. Subsequently, the magnetic transition temperature was determined for every annealing treatment/cooling rate. As can be seen, on a logarithmic x-scale, the T_c-cooling rate curve is roughly linear with low cooling rates leading to high T_c values and high cooling rates leading to low T_c values.

The cooling rate sensitivity of T_c can be understood in terms of relaxation times at and below the second order B2-L2$_1$ phase transition. At high temperatures where atomic mobility is high, the sample is in thermodynamic equilibrium. Upon cooling, the atoms need to rearrange constantly to adjust the state of equilibrium order at the respective temperature. As long as the atomic relaxation is faster than the available time defined by the cooling ramp, the sample stays in equilibrium. However, at some point there is a transition to a regime where the atomic relaxation cannot follow the equilibrium state of order in the given time window. Consequently, the sample falls out of equilibrium and the state of order (and consequently T_c) at that specific temperature freezes. Needless to say, the temperature at which the sample falls out of equilibrium depends on the cooling rate and hence, when cooling from 853 K with different rates, a range of T_c values from 297.2 K (cooling rate approximately 300 K/min) to 305.7 K (cooling rate 1 K/min) is observed.

Described experiment can be extended by choosing not one but a variety of quenching temperatures T_q for cooling the sample to room temperature applying different cooling rates. A graph as presented in the left panel of Fig. 3.13 can then be constructed for any T_q and the obtained results are presented in a slightly different fashion in the right panel of Fig. 3.13. Here, the x-axis shows T_q, the y-axis depicts T_c and every point in the graph represents the obtained T_c value when cooling the sample with the specified cooling rate from the respective T_q. This experiment has been performed for 6 T_q values applying 6 cooling rates each. From Fig. 3.13, the temperature at which the sample falls out of equilibrium upon cooling with a given rate can be determined. For example, upon cooling with 5 K/min, there is no significant difference in T_c for T_q values between 793 K and 853 K ($T_c \approx 302.80$ K). However, cooling from 773 K yields a higher T_c value of 303.4 K. This observation means, that a sample cooled with 5 K/min falls out of equilibrium between 773 K and 793 K. Annealing at lower T_q values and cooling with 5 K/min hence preserves the equilibrium state of order at this specific T_q since the sample falls out of equilibrium immediately upon cooling. At the same time, annealing at higher temperatures does not result in different T_c values since T_c is solely dependent on the cooling rate. Consequently, the sample falls out of equilibrium at exactly the same temperature independent on the selected T_q. Increasing the cooling rate means that the temperature at which the sample falls out of thermodynamic equilibrium increases. For 80 K/min for instance, this temperature is between 813 K and 833 K.

The obtained results can well be described employing a kinetic model that assumes the degree of order η in the sample to be proportional to T_c and further the equilibrium degree of order η_{eq} to be linearly dependent on T in the relevant temperature range. Specifically, it assumes

$$\eta_{\text{eq}} = \eta_0 + \kappa(T - T_0) \tag{3.3}$$

with η_0, κ and T_0 being constant. The time derivative of η can then expressed by the following differential equation

$$\dot{\eta}(t) = \Big(\eta_{\text{eq}}(T) - \eta(t)\Big)\Big(1 - \exp(-\frac{t}{\tau})\Big) \tag{3.4}$$

where τ is a relaxation parameter defined as

$$\tau = \tau_0 \exp(-\frac{E_A}{k_B T}). \tag{3.5}$$

Here, E_A is the activation energy of the ordering process, k_B is the Boltzmann constant and τ_0 is a constant pre-factor.

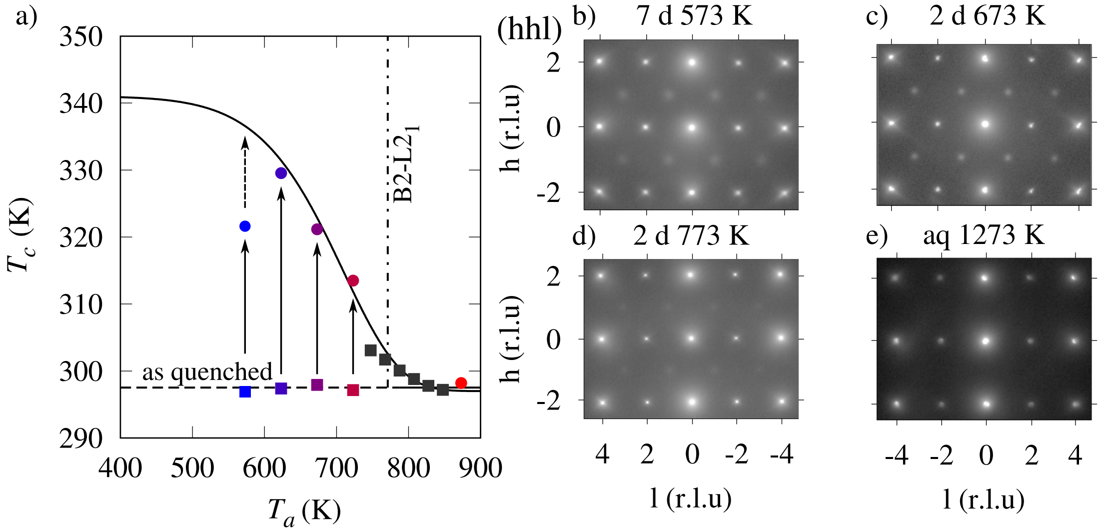

Fig. 3.14 Magnetic transition temperature T_c (a) as function of annealing temperature T_a measured in samples quenched from 1273 K (see Fig. 3.12, colored points/squares) and in samples cooled ballistically from different equilibrium annealing temperatures T_q (see Fig. 3.13, gray squares). The colored circles represent the most progressed T_c values upon annealing at the respective annealing temperature T_a (see Fig. 3.12) while the colored squares represent the initial, as-quenched T_c values for the samples quenched from 1273 K. The dotted line representing the B2-L2$_1$ transition is drawn according to DSC measurements reported by Kainuma et al. (2000). Electron diffraction results (b-e) for samples quenched from 1273 K with subsequent annealing for specified annealing times at 573 K, 673 K and 773 K.

Fitting the model to the data yields the solid lines in Fig. 3.13 while specifically the black line in the right panel shows the assumed T_c values for equilibrium order. As can be seen, qualitatively the model describes the measured data well with the exception that the model predicts a faster convergence of the different cooling rate curves at low T_q. Employing this model, the activation energy of the ordering process was determined as 2.5 eV.

3.4.4 *TTT* diagram for T_c evolution

From the data presented in Fig. 3.12 and Fig. 3.13, temperature dependent T_c values for equilibrium degrees of order can be extracted. The results are shown in Fig. 3.14a. The measured data was described phenomenologically by the black solid line. The equilibrium state of order at low temperatures is kinetically inaccessible and hence the final T_c value in the 573 K annealing series represents an intermediate state of order. While in a second order phase transition, the degree of long-range order approaches zero with an infinite slope at the transition temperature, the T_c-temperature dependency shows a slow convergence towards

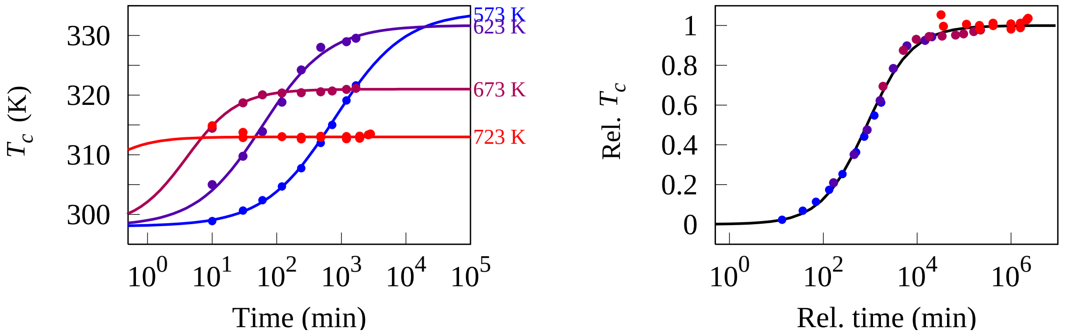

Fig. 3.15 T_c evolution upon isothermal annealing at different temperatures T_a (left, reproduced from Fig. 3.12) and master curve for the temporal evolution of T_c at different T_a (right). The x-axis in the right panel shows the time relative to the 573 K measurement.

the B2 T_c value even above the transition temperature. This behavior is qualitatively the same as in stoichiometric Ni_2MnAl and $Ni_2MnAl_{0.5}Ga_{0.5}$. Presumably, instead of depending only on the degree of long-range $L2_1$ order, T_c strongly depends on the short-range order in the sample and consequently does not show a sharp transition.

In order to determine the state of order directly, electron diffraction measurements have been performed on samples quenched from different annealing temperatures as depicted in Fig. 3.14b-e. Clearly, the 1273 K-quenched sample shows only B2 reflections, while the subsequent annealing treatments for 2 d at 773 K and 673 K as well as for 7 d at 573 K evoke the appearance of $L2_1$ superstructure reflections. Interestingly, these superstructure reflections are in general much broader than the B2 and A2 reflections, indicating a small correlation length of the ordered domains, i.e. a small scale $L2_1$ APD structure. The $L2_1$ superstructure peaks in the 773 K annealed samples are extremely weak and broad corresponding rather to a state of $L2_1$ short-range order. Considering that 773 K is right at the transition temperature, the degree of long range $L2_1$ order should indeed be close to zero. Annealing at 673 K evokes the most pronounced $L2_1$ superstructure reflections, being in line with a high equilibrium degree of order and fast kinetics, while as pointed out before, annealing at 573 K is so slow that presumably the adjustment of highly progressed states of $L2_1$ order is not possible. Hence, the superstructure peaks at 573 K are clearly broader than the ones at 673 K. In general, the electron diffraction results perfectly confirm the calorimetric measurements. Further they clearly reveal the described direct relationship between the magnetic transition temperature and the state of order in the sample.

From the presented measurements, a time temperature transformation (*TTT*) diagram for the T_c evolution in $Ni_2Mn_{1.12}Al_{0.88}$ can be constructed. For this purpose, first a common master curve is created that describes the temporal evolution of T_c upon isothermal annealing

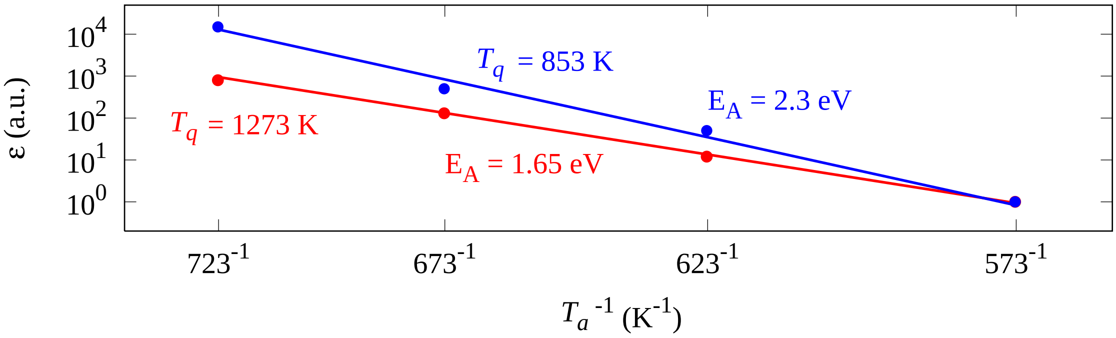

Fig. 3.16 Temperature dependent stretching factors ϵ for the determination of the activation energies of the ordering process for samples quenched from 1273 K (red) and for samples cooled with 80 K/min from 853 K (blue, see the following section).

at all annealing temperatures T_a. The left panel of Fig. 3.15 reproduces the T_c-time curves from Fig. 3.12 while the right panel shows the master curve created by stretching the time axis for different annealing temperatures with a temperature dependent factor ϵ and by normalizing the curves to the equilibrium T_c value at the respective T_a. Hence, the x-axis portrays the time relative to the 573 K annealing treatment. As can be seen, all curves can reasonably well be represented by a common master curve and the temporal evolution on this curve is then only characterized by an Arrhenius dependency describing the kinetics of the ordering process.

From the stretching factors ϵ, the activation energy of the ordering process can be determined as previously described. The stretching factors as function of the inverse annealing temperature for two sets of samples (quenched from 1273 K and slow cooled from 853 K) are presented in Fig. 3.16. In the case of the 1273 K-quenched samples, E_A was determined as 1.65 eV. Note that this value is in excellent agreement to the activation energies of 1.65 eV and 1.52 eV found for Ni_2MnAl and $Ni_2MnAl_{0.5}Ga_{0.5}$, respectively.

Using the retrieved activation energy, the data as depicted in the right panel of Fig. 3.15 was corrected for unintended annealing effects of the samples during the measurement, i.e. during heating to and cooling from the annealing temperature T_a with a heating/cooling rate of 10 K/min. This effect was iteratively corrected using the T_a-dependent equilibrium T_c values as given in Fig. 3.14 together with a simple Arrhenius description of the ordering kinetics making use of the determined activation energy of the ordering process.

Given the T_c-T_a dependency and the stretching factors ϵ, the T_c evolution at any temperature T_a was calculated with the described model. This information can be condensed into a *TTT* diagram as given in Fig. 3.17 where iso-T_c lines are drawn as function of annealing temperature T_a and isothermal annealing time. Evidently, the calculated iso-T_c lines agree well with the measured data. The decrease of the degree of equilibrium order with increased

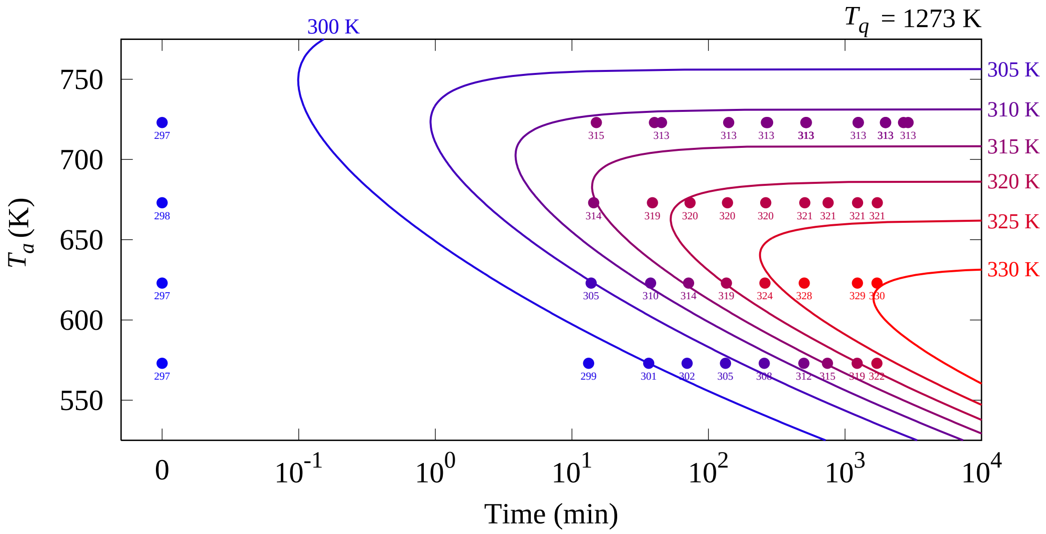

Fig. 3.17 *TTT* diagram for $Ni_2Mn_{1.12}Al_{0.88}$ samples quenched from 1273 K. The lines show iso-T_c lines as calculated with the described model, while the points represent time-corrected measurement data as obtained by isothermal annealing experiments (see Fig. 3.12). The numbers at the points show the measured T_c values in K. The data points on the left refer to the quenched samples and correspond to time zero.

annealing temperature leads to a shift of the characteristic nose in the *TTT* diagram to lower T_a values with increased T_c. As a consequence, when the equilibrium T_c value is reached, the iso-T_c line gets horizontal. As for any *TTT* diagram, the presented diagrams are only valid for a specified composition and, as an additional constraint, a specific thermal history of the sample. In this case, samples have been solution annealed for 48 h at 1273 K and were subsequently quenched in room temperature water. Both the solution treatment and the quenching procedure have a significant influence on the *TTT* diagram given that the vacancy concentration and presumably also the concentration of vacancy sinks are adjusted by these thermal treatments.

3.5 The role of excess vacancies in the ordering process

So far, the ordering kinetics have been studied as a function of annealing temperature T_a for a set of samples with an identical thermal history prior to the experiment. In a next step, the influence of the thermal history of a sample on the ordering kinetics is investigated. Specifically, the kinetics of the 1273 K-quenched $Ni_2Mn_{1.12}Al_{0.88}$ samples are compared to $Ni_2Mn_{1.12}Al_{0.88}$ samples slowly cooled from the B2-stable regime.

For this purpose, samples have been equilibrium annealed in the DSC for 60 minutes at 853 K and were subsequently cooled with a cooling rate of 80 K/min to room temperature.

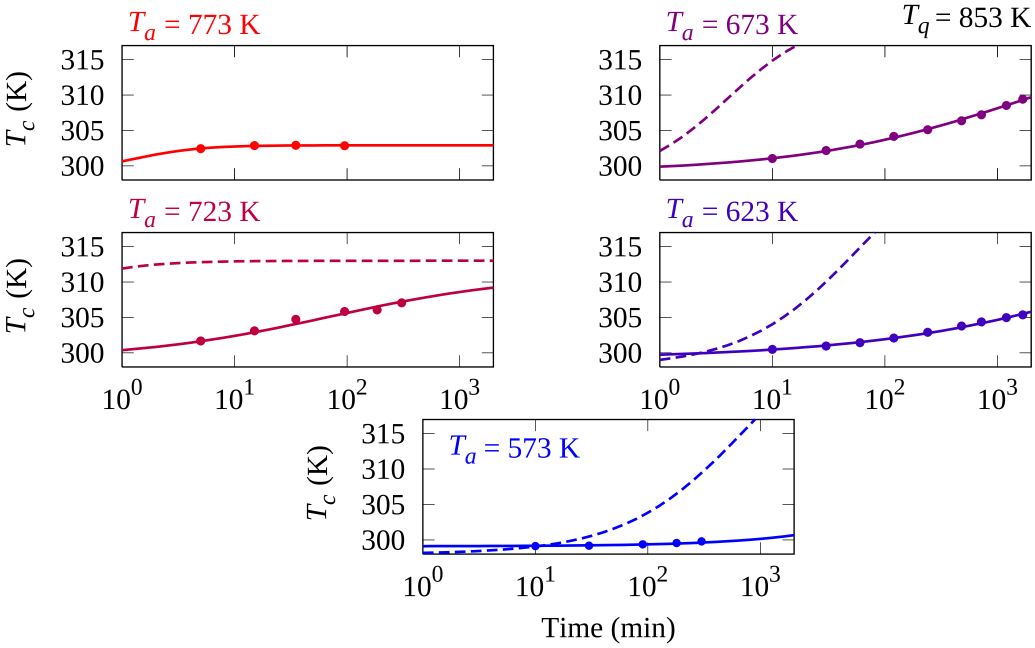

Fig. 3.18 $L2_1$ ordering kinetics as a function of annealing temperature in $Ni_2Mn_{1.12}Al_{0.88}$ samples cooled with 80 K/min from 853 K. The solid lines portray a phenomenological curve fit to be understood as guide to the eye. The dashed lines reproduce the kinetics curves for samples quenched from 1273 K as depicted in Fig. 3.12.

Next, isothermal annealing curves were recorded. Specifically, ordering kinetics have been measured at 5 annealing temperatures (T_a = 573 K, 623 K, 673 K, 723 K and 773 K). Fig. 3.18 depicts the evolution of T_c as a function of the annealing time. The dashed lines show the T_c-time curves of the 1273 K-quenched samples as presented in Fig. 3.12. Clearly, the ordering kinetics in the slow-cooled samples is pronouncedly slower than in the 1273 K-quenched samples. Quantitatively comparing the ordering kinetics of the quenched and slow-cooled samples yields a retardation of approximately two orders of magnitude in the 853 K-cooled samples. Interestingly, the initial T_c values of the 1273 K-quenched and slow-cooled samples shows only a minor difference of approximately 2-3 K, a phenomenon explained in detail in the discussion of Fig. 3.13.

Presumably, the observed slowdown in ordering kinetics results from the ordering process in $Ni_2Mn_{1.12}Al_{0.88}$ relying largely on quenched-in excess vacancies. While samples quenched from high temperatures have a higher concentration of quenched-in vacancies, the vacancy concentration in the slow-cooled samples is low. Interestingly, the state of order is less sensitive to the quenching temperature and cooling rate than the kinetics. Therefore, it can be concluded that vacancies fall out of equilibrium pronouncedly above the B2-$L2_1$ phase

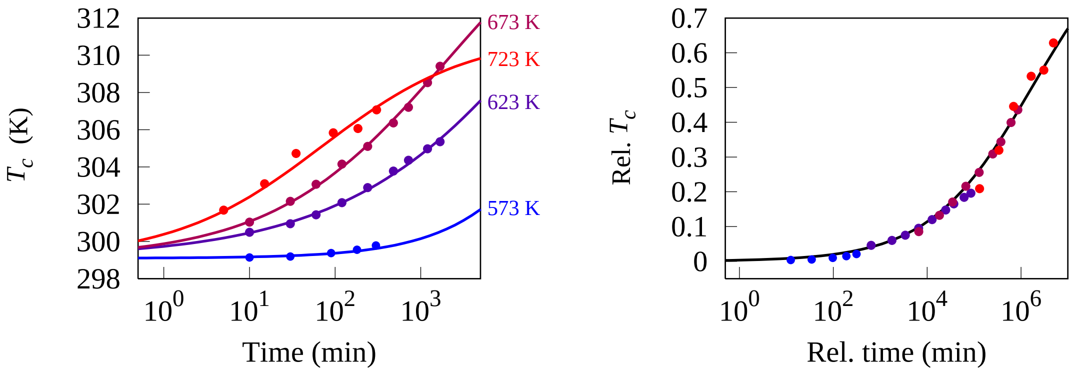

Fig. 3.19 T_c evolution upon isothermal annealing at different temperatures T_a (left) reproduced from Fig. 3.12 and master curve for the temporal evolution of T_c at different T_a (right). The x-axis in the right panel shows the time relative to the 573 K measurement.

transition temperature. Consequently, the kinetics of the ordering process is dominantly determined by the quenched-in vacancy concentration on the one hand and the annihilation rate of the excess vacancies on the other hand. Assuming that the concentration of vacancy sinks (e.g. grain boundaries and dislocations) is a sample specific parameter determined mainly by the initial sample preparation and solution annealing treatment and is hence similar in the 1273 K-quenched and slow-cooled samples, the only difference between the two sample families is the quenched-in vacancy concentration. Further assuming that vacancies do not interact with each other, i.e. do not form vacancy clusters when colliding with each other by chance in their diffusion process, the vacancy concentration should be directly proportional to the kinetics of the ordering process. Consequently, a factor of two orders of magnitude in ordering kinetics between the 1273 K-quenched and slow-cooled samples corresponds to a similar factor in the vacancy concentrations.

As for the 1273 K-quenched samples, also for the 853 K-cooled samples, a master curve for the temporal evolution of T_c can be created using temperature-dependent stretching coefficients ϵ. The corresponding master curve is depicted in Fig. 3.19. In Fig. 3.19, the 773 K series has been omitted since 773 K is above the B2-L2_1 transition temperature of the compound and the observed ordering process refers mainly to short-range ordering with presumably a quite different kinetics than the evolution of long-range L2_1 order. Comparing the master curve of the 853 K-cooled samples to the 1273 K-quenched samples, it is apparent that for the 853 K-cooled samples, at none of the annealing temperatures the equilibrium T_c value is reached but only intermediate states of order are accessible on experimental time scales.

Employing the T_c-T_a relationship presented in Fig. 3.14, a *TTT* diagram for the T_c evolution in 853 K-cooled samples can be composed. As for the 1273 K-quenched samples, also

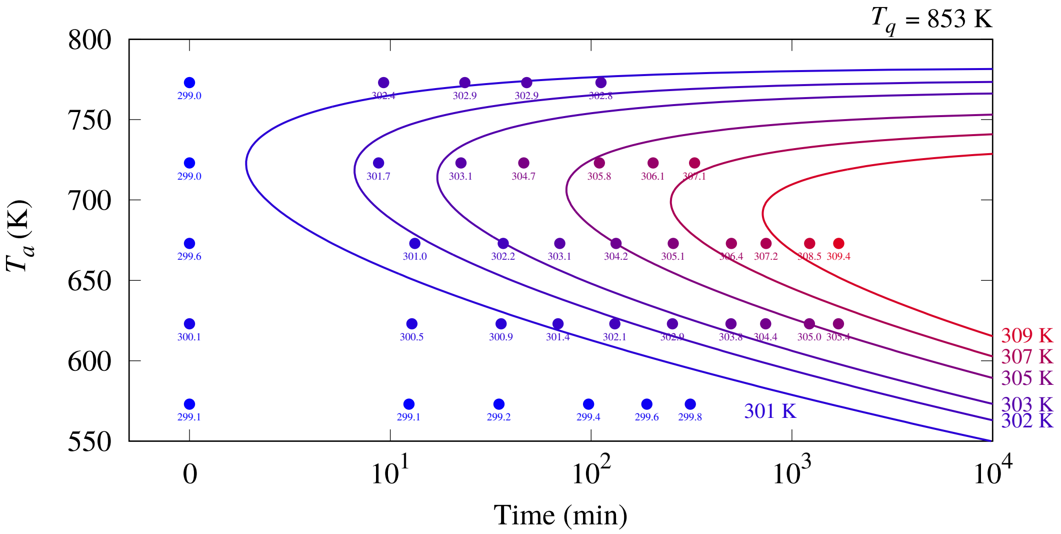

Fig. 3.20 *TTT* diagram for $Ni_2Mn_{1.12}Al_{0.88}$ samples quenched from 853 K. Shown are iso-T_c lines as calculated with the model, while the points represent time-corrected measurement data as obtained by isothermal annealing experiments (see Fig. 3.18). The values at the points show the measured T_c values in K. The data points on the left refer to the quenched samples and correspond to time zero.

for the 853 K-cooled samples, the activation energy of the ordering process was determined. The stretching factors ϵ together with the exponential fit are presented in Fig. 3.16 and the activation energy has been retrieved as 2.3 eV, a value in good conformity to the 2.5 eV previously found for the description of the cooling rates experiments.

The *TTT* diagram for the 853 K-cooled samples in analogy to the previously presented *TTT* diagrams is presented in Fig. 3.20. Evidently, the model describes the experimental data well with some deficiencies especially at elevated temperatures close to the transition temperature where the ordering kinetics is faster than predicted by the model.

3.5.1 Vacancy annihilation studied via ordering kinetics

The influence of excess vacancies on the ordering process can be investigated by a temperature change experiment. Specifically, 1273 K-quenched samples were sufficiently long isothermally annealed at T_a = 673 K to adjust the equilibrium T_c value at this temperature. Then, T_a was reduced to 623 K where the sample was again annealed for a specified time. Naturally, due to the altered T_a, the equilibrium T_c value increases and the T_c value of the sample evolves towards this equilibrium value. In the following, T_a was sequentially switched between 673 K and 623 K and the oscillation of T_c between the two equilibrium values was monitored.

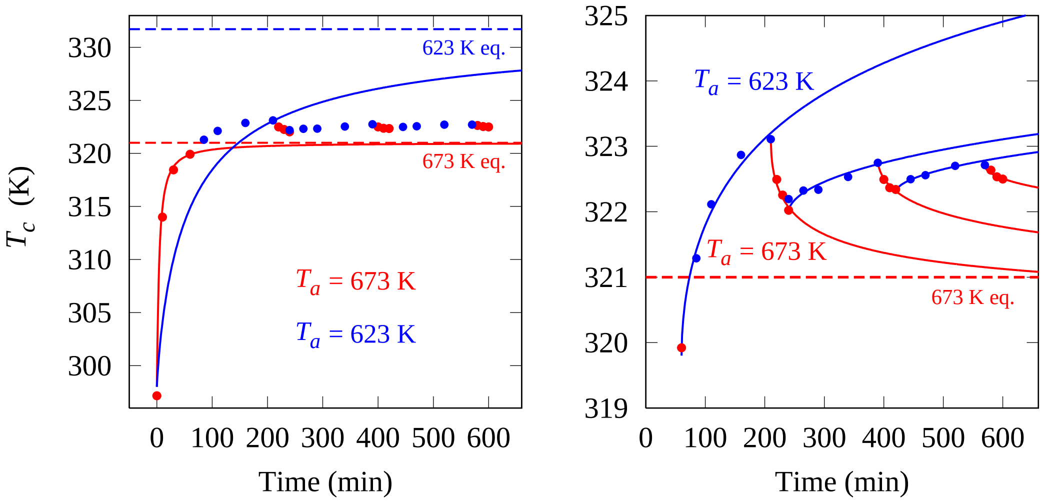

Fig. 3.21 T_c evolution as function of annealing time at changing isothermal annealing temperatures of 673 K and 623 K showing a slow down of the ordering kinetics with increased annealing time. Solid red lines and points refer to annealing at 673 K while blue lines and blue points refer to annealing at 623 K. The dashed lines refer to the respective equilibrium T_c values at 673 K (red) and 623 K (blue). The left panel shows the entire T_c evolution curve while the right panel emphasizes the late stages of the experiment where kinetics is slow and the T_c change less pronounced.

Fig. 3.21 shows the results of the discussed experiment. As can be seen, when switching the isothermal annealing temperature to 623 K after the equilibrium value at 673 K is almost reached, T_c continues evolving towards the equilibrium value at 623 K. Evidently, the kinetics of the T_c evolution is drastically reduced the longer the annealing process continues which is especially well visible in the consecutive temperature changes. Even though the driving force, i.e. the temperature difference to the equilibrium T_c value is hardly changed, the kinetics is significantly slowed down from annealing step to annealing step. This observation is a strong indication for the existence of quenched-in excess vacancies in the 1273 K-quenched samples that annihilate during the ordering process. With increased annealing time, vacancies migrate to vacancy sinks such as grain boundaries where they annihilate until the annealing-temperature-specific equilibrium vacancy concentration is reached. As a consequence, the amount of vacancies available for atomic diffusion processes is reduced and the kinetics slows down during the ordering process. Contrarily, in the case of a constant supply of vacancies carrying the ordering process, the kinetics of the T_c evolution would be roughly constant between the cycles. Interestingly, $Ni_2MnAl_{0.5}Ga_{0.5}$, as previously discussed, does not show a pronounced T_q dependency of the ordering kinetics indicating that the ordering process in this compound is less dependent on excess vacancies.

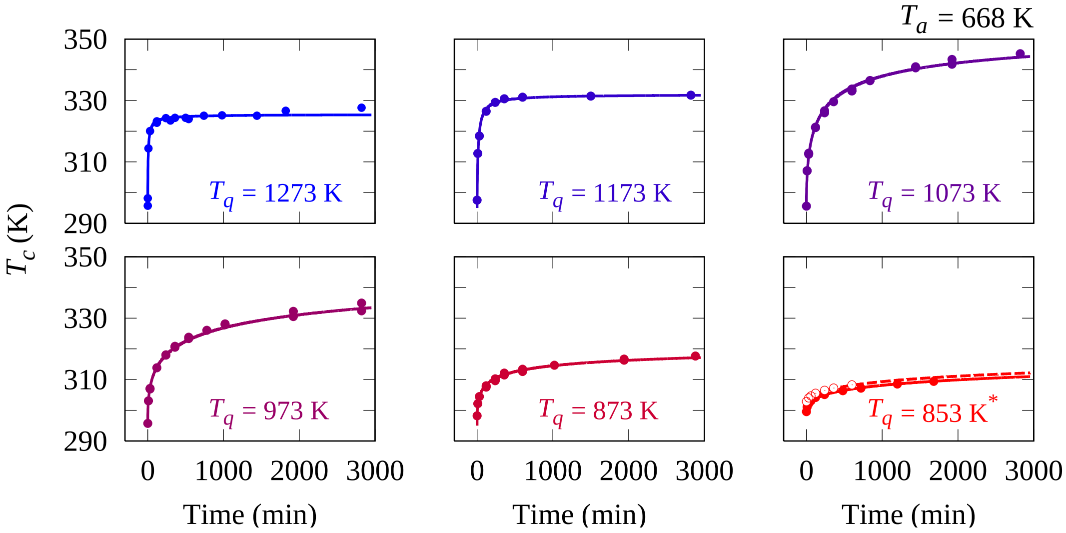

Fig. 3.22 T_c evolution upon isothermal annealing at 668 K for various quenching temperatures T_q. The lines are phenomenological curve fits to be understood as guides to the eye. The 853 K curves refer to samples cooled in the DSC with 80 K/min (full symbols) and 10 K/min (open symbols) starting at a temperature of 853 K.

3.5.2 T_q dependency of the ordering process

After having demonstrated the role of quenched-in excess vacancies in the ordering process, a method to tailor the excess vacancy concentration is presented. For this purpose, samples were equilibrium annealed at a variety of quenching temperatures T_q in the B2-stable regime. Subsequently, samples were quenched in order to conserve, if kinetically feasible, the vacancy concentration at T_q to room temperature. Afterwards, the kinetics of the ordering process at a selected annealing temperature T_a in the L2$_1$-stable regime was measured. Clearly, the amount of excess vacancies should directly influence the ordering kinetics and hence the evolution of T_c as a function of annealing time.

Fig. 3.22 shows the results of the described experiments for annealing at T_a = 668 K after quenching from 6 different temperatures (T_q = 853 K, 873 K, 973 K, 1073 K, 1173 K, 1273 K). As expected, the kinetics of the T_c evolution is strictly related to the quenching temperature with the sample quenched from 1273 K showing a 2 − 3 orders of magnitude faster kinetics than the sample slow-cooled from 853 K.

Interestingly, samples quenched from different T_q do not converge to the same equilibrium T_c value. Keeping in mind that thermodynamically the equilibrium state of order is only a function of the annealing temperature T_a, in theory, the quenching temperature should not have any influence on the equilibrium T_c value adjusted upon isothermal annealing at T_a. Consequently, much effort was put into confirming this unexpected behavior. First of all, in order to exclude the possibility of a progressing effect as e.g. an unknown precipitation formation that is not reverted upon equilibrium annealing at T_q, measurements have been repeated for the same sample several times and the order of T_q has been randomly chosen. In these experiments, the observed behavior was perfectly reproducible. Second of all, the entire set of parameters potentially influencing the results was carefully taken into account. A second batch of samples was produced from different raw materials using a different induction melting apparatus for sample preparation, a different sample size and, due to non-controllable experimental parameters, a slightly different composition. All of these efforts resulted in the same qualitative result. When quenched from different T_q, the initial ordering kinetics increased with increasing T_q while the final T_c value was unexpectedly also dependent on T_q.

While this observation is very interesting and not compliant to the current understanding of the second order B2-$L2_1$ phase transition, at this point no conclusive reasoning for this effect can be given. The only feasible explanation to the author's point of view can be an argumentation based on kinetics of the ordering process while a T_q-dependency of the equilibrium degree of order appears highly unlikely. Possibly, with larger excess vacancy concentrations, the abundance of excess vacancies leads to the formation of stable vacancy clusters upon random diffusion of the vacancies through the material. These vacancy clusters would then serve as vacancy sinks in the ongoing ordering process. Such a mechanism would explain why the kinetics is initially related to the quenching temperature in a sense that high quenching temperatures lead to fast ordering kinetics while later in the process, the kinetics rapidly slow down in exactly those samples that show the fastest initial kinetics. Yet, providing experimental evidence for this speculative argument is not possible based on the presented results and also preliminary Positron Annihilation Lifetime Spectroscopy (PALS) measurements do not allow to draw a clear conclusion.

Assuming that in fact the initial kinetics of the ordering process is directly proportional to the quenched-in vacancy concentration, the T_c evolution curves can be used to estimate the vacancy formation energy. For this purpose, again the T_c evolution curves are stretched to construct a common master curve (see Fig. 3.23). Yet, in contrast to the procedure applied in the previous sections, no y-scaling has been applied since the thermodynamic equilibrium T_c value has to be the same for all T_q values. Hence, the points follow the common master curve only initially, while at later stages the data points diverge from the master curve at a point which is related to T_q.

With the obtained stretching factors, again the activation energy of the ordering process can be determined. Fig. 3.24 shows the stretching factors ϵ as a function of the inverse quenching temperature on a logarithmic y-scale. As can be seen, the stretching factors follow

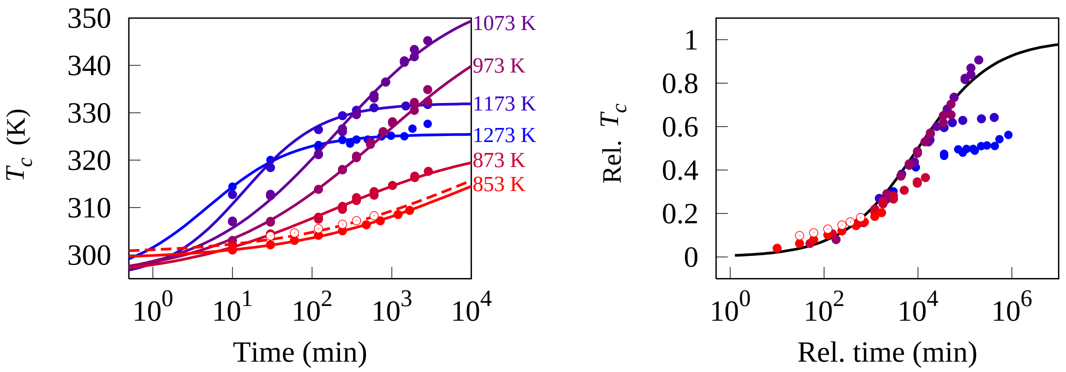

Fig. 3.23 T_c evolution upon isothermal annealing at 668 K for samples quenched from various quenching temperatures T_q (left) reproduced from Fig. 3.12 and the master curve for the temporal evolution of T_c at 668 K for various T_q (right). The x-axis in the right panel shows the time relative to the 573 K measurement.

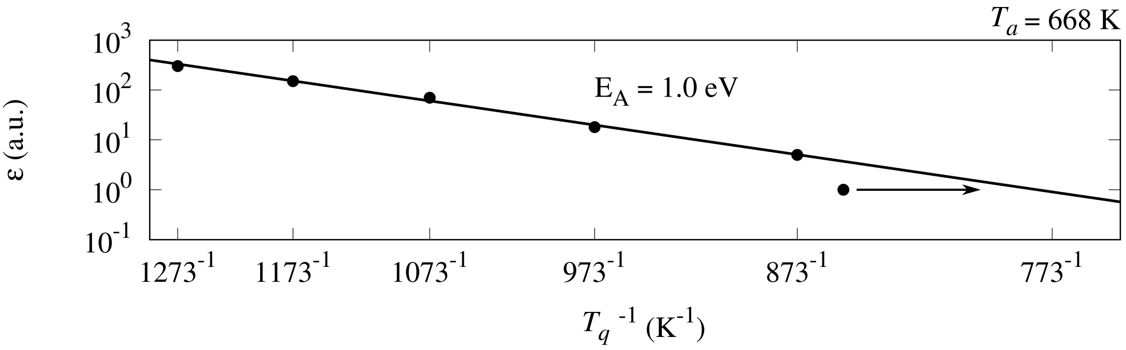

Fig. 3.24 Temperature dependent stretching factors ϵ for isothermal annealing of $Ni_2Mn_{1.12}Al_{0.88}$ samples at 668 K quenched from various temperatures T_q. The 853 K data point refers to a slow-cooled sample. The arrow indicates that the effective quenching temperature of the 853 K sample was estimated as $\approx$ 780 K.

an exponential T_q^{-1} dependency that can be described by an Arrhenius relation with an activation energy of $\approx$ 1.0 eV. This activation energy for vacancy formation is in very good agreement to the 0.95-1.02 eV reported by Merida et al. (2014, 2015) for the closely related Ni_2MnGa system.

Evidently, the data point for the 853 K-quenched sample in Fig. 3.24 does not follow the Arrhenius dependency of the other data points. Considering that the 853 K data point does not refer to water-quenched but slow-cooled samples (see Fig. 3.22), this indicates that the vacancy concentration effectively falls out of equilibrium at lower temperatures upon slow cooling. In fact, it can be estimated that the vacancy concentration in the slow-cooled samples equals the equilibrium vacancy concentration of $\approx$ 780 K. This temperature is in good agreement to the temperature range at which the order falls out of equilibrium in cooling rate dependent measurements employing cooling rates between 10 K/min and 80 K/min (see Fig. 3.13).

3.6 Remarks on activation energies

Throughout the course of this chapter, several activation energies have been determined by means of following the ordering kinetics of the $L2_1$ ordering process in Ni_2MnZ Heusler compounds. Specifically, via annealing $Ni_2MnAl_{0.5}Ga_{0.5}$, Ni_2MnAl and $Ni_2Mn_{1.12}Al_{0.88}$ samples initially quenched from high temperatures at different annealing temperatures T_a, the activation energy of the ordering process under the presence of quenched-in excess vacancies was determined. Here, values of 1.52-1.55 eV, 1.65 eV and 1.65 eV were found for $Ni_2MnAl_{0.5}Ga_{0.5}$, Ni_2MnAl and $Ni_2Mn_{1.12}Al_{0.88}$, respectively. Via following the state of $L2_1$ order as a function of cooling rate, as well as via annealing slow-cooled samples at various T_a, additionally the activation energy for the ordering process without the presence of excess vacancies was investigated. For $Ni_2Mn_{1.12}Al_{0.88}$, values of 2.3-2.5 eV were obtained. Finally, by quenching samples from different quenching temperatures T_q and following the ordering process upon isothermal annealing at a constant annealing temperature T_a, additionally the activation energy for vacancy formation in $Ni_2Mn_{1.12}Al_{0.88}$ was determined as 1.0 eV.

Clearly, the activation energies for the ordering process under the presence of excess vacancies are with a value of $\approx$ 1.6 eV similar in all studied compounds while the activation energy for the ordering process under equilibrium vacancy concentration is $\approx$ 0.7-0.9 eV larger. Relying on quenched-in excess vacancies, the activation energy of the ordering process under presence of excess vacancies is lacking the term for vacancy formation. Consequently, the observed difference should be equal to the vacancy formation energy in these compounds. Indeed, comparing the retrieved 0.7-0.9 eV to the experimentally observed 1.0 eV vacancy formation energy supports this conclusion.

Comparing the obtained activation energies to literature data draws the following picture: Seguí (2014) studied directly the activation energy of the $L2_1$ ordering process in quenched $Ni_{2-x}Co_xMnGa$ samples and report a value of 1.46 eV similar to the values determined in this thesis. Furthermore, self diffusion energies determined for Ni_2MnZ Heusler systems can partially be used to estimate the activation energy of the ordering process. Considering the correlated jump mechanism in B2 compounds in which all constituents show approximately the same activation energy for self diffusion (Mehrer, 1996; Wever, 1992), these activation energies should be a good estimation for the activation energy of the B2-$L2_1$ ordering process. Erdélyi et al. (2007) determined self diffusion coefficients and activation energies for Ni_2MnGa in the B2 phase and found values of 2.45 eV, 2.45 eV and 2.79 eV for ^{63}Ni,

^{54}Mn and ^{67}Ga, respectively. These values, probing the self diffusion under equilibrium vacancy concentration, agree well with the 2.3-2.5 eV found in the experiments reported in this work for $Ni_2Mn_{1.12}Al_{0.88}$. Furthermore, the vacancy formation energy for Ni_2MnGa was determined by Merida et al. (2014, 2015) by means of Positron Annihilation Lifetime Spectroscopy as 0.9-1.02 eV, also in good conformity to the values reported in this thesis for $Ni_2Mn_{1.12}Al_{0.88}$.

3.7 Conclusions

In this chapter, the kinetics of the $L2_1$ ordering process in Ni_2MnZ Heusler systems, explicitly in the model compound $Ni_2MnAl_{0.5}Ga_{0.5}$ as well as in the ternary compounds Ni_2MnAl and $Ni_2Mn_{1.12}Al_{0.88}$, was investigated by means of calorimetric and magnetization measurements. Specifically, the evolution of selected magnetic properties were tracked as function of the applied annealing treatment. Employing this method, isothermal evolution curves for the magnetic transition temperature as well as the bulk magnetization were recorded at various annealing temperatures. Based on these curves, time temperature transformation diagrams for the $L2_1$ ordering process during isothermal annealing treatments were created and activation energies of the ordering processes were determined. Furthermore, the strong influence of quenched-in excess vacancies on the ordering process in the Ni_2MnAl system was demonstrated. Concerning this matter, activation energies for the $L2_1$ ordering process for samples quenched from elevated temperatures with a large concentration of excess vacancies were determined as 1.52-1.55 eV, 1.65 eV and 1.65 eV for $Ni_2MnAl_{0.5}Ga_{0.5}$, Ni_2MnAl and $Ni_2Mn_{1.12}Al_{0.88}$, respectively. At the same time, for slow-cooled $Ni_2Mn_{1.12}Al_{0.88}$ samples with presumably equilibrium vacancy concentrations, significantly larger activation energies for $L2_1$ ordering of 2.3-2.5 eV were found. The difference of the activation energies between quenched and slow-cooled samples was attributed to the vacancy formation energy which was hence estimated as 0.7-0.9 eV. Via quenching samples from different quenching temperatures and comparing the kinetics of the ordering process, the activation energy for vacancy formation in $Ni_2Mn_{1.12}Al_{0.88}$ was indirectly measured, yielding a value of 1.0 eV in good conformity to the presented estimation.

Chapter 4

Neutron diffraction study of magnetic antiphase domain coupling in Ni_2MnZ compounds

4.1 Introduction

In Chapter 2, based on bulk magnetization measurements and Heisenberg Monte Carlo simulations, the existence of a magnetic coupling across $L2_1$ antiphase domains (APDs) in Ni_2MnZ Heusler alloys was postulated. This postulation was based on the great conformity between the magnetic simulations investigating the implications of mentioned coupling and the experimental bulk magnetization curves. Yet, a direct experimental proof for the postulated coupling is lacking.

In the pertinent literature, the most prominently employed method to study the orientation dependence of the local magnetization at antiphase boundaries (APBs) is Lorentz Transmission Electron Microscopy (Lorentz-TEM) where extremely small sample thicknesses restrict the magnetization field into the plane normal to the incoming electron beam. Within this plane, the orientation dependence of the magnetization field can then be studied and for Ni_2MnZ systems, a superposition of nuclear and magnetic domains together with a high frequency of 180° domain walls was observed (Murakami et al., 2013, 2011; Park et al., 2012; Venkateswaran et al., 2007; Yano et al., 2007). However, Lorentz-TEM investigations are subject to inherent limitations. First of all, the small sample size in one direction and associated with that the 2D character of the probed sample region might show different properties than the 3D bulk sample which is of primary interest. Second of all, the low number of

APDs/APBs in a TEM micrograph and hence the low statistical quantity potentially amplifies experimental anomalies over representative observations.

Needless to say, an experimental method probing the bulk and averaging over a large number of APDs would be desirable in order to contribute to the open question of interdependencies and coupling of magnetic domains and APDs in Ni_2MnZ Heusler alloys. While neutron scattering fulfills both mentioned criteria, it is by no means obvious how a neutron diffraction experiment would resolve the raised questions. Concerning this matter, it is necessary to understand the evolution of the nuclear structure upon $L2_1$ ordering an initially B2-ordered sample, the order-dependent magnetic structures and their mutual implications for neutron scattering. Then, on this basis, a meaningful experimental design can be proposed that proofs or rejects the hypothesis of magnetically coupled APDs.

The evolution of $L2_1$ order was discussed in detail in the previous chapters. Specifically, it was demonstrated that the ordering process can be roughly divided into two sub-processes that occur simultaneously but on different timescales. While upon annealing a B2-ordered sample in the $L2_1$-stable regime, first (short-range) order emerges, this order is initially disrupted by a large number of APDs – and hence APBs – which grow in size as the ordering process continues. Both sub-processes were shown to be probed primarily by different magnetic properties, namely the magnetic transition temperature T_c (short-range order) and the bulk magnetization M or DC susceptibility χ (APD growth). This dependency was used in Chapter 3 to follow the kinetic evolution of both short-range order and APD size – a knowledge that will be employed in this chapter for preparing meaningful sample sets.

It is well accepted that, under B2 order, Ni_2MnZ compounds show, due to an antiferromagnetic (AFM) exchange coupling of Mn atoms on nearest neighbor (NN) sites, AFM properties (Acet et al., 2002; Ishikawa et al., 2008; Ziebeck and Webster, 1975). This AFM coupling is nicely resolved using neutron powder diffraction (see, for example Ziebeck and Webster, 1975) where the AFM structure increases the size of the unit cell which leads to a magnetic superstructure that is visible in the neutron diffractograms via additional purely magnetic peaks that are spatially isolated from the nuclear peaks in reciprocal space.

Upon $L2_1$ ordering, besides the magnetic superstructure, an additional nuclear superstructure emerges at the Q values of the AFM superstructure peaks. The intensity of these nuclear superstructure peaks results from the contrast between the 4a and 4b Wyckoff positions of the $L2_1$ $Fm\bar{3}m$ structure, which in the case of Ni_2MnZ is given by the relative occupancies of Mn and Z on the two lattice sites. The width of the superstructure peak is in general dependent on the instrument resolution and, decisive in this case, the correlation length of the ordered domains. In the case of a small scale APD structure, the nuclear superstructure peaks can be significantly broadened with respect to the B2 and A2 peaks. Concerning the magnetic properties, it is well accepted e.g. from density functional theory (DFT) calculations that with increased $L2_1$ order, the magnetic properties of an individual domain become increasingly ferromagnetic (FM) (see, for instance Ayuela et al., 1999). The important question is how the mesoscale microstructure, i.e. the APDs/APBs, influences the magnetic structure. Here, in principle, three independent scenarios are thinkable.

In the first scenario, the APBs have no influence on the magnetic properties. Assuming long-range exchange interactions, the coupling of spins would simply persist through adjacent domains and the magnetic properties of a bulk sample would, as the magnetic properties of a single domain, be FM in nature. For the neutron diffractogram, this scenario would simply imply a decoration of the nuclear scattering length of the Mn sites with a magnetic contribution that would ultimately change the peak intensities of peaks at low Q values yet leave the peak width, as determined by the size of the ordered domains, unchanged. Hence, in this scenario, under a small scale APD structure the diffuse nuclear intensity would have a diffuse magnetic contribution which decreases in intensity with increasing Q.

The second scenario represents the superparamagnetic case with isolated FM APDs. In this case, the exchange interactions in the system would be short range and no exchange coupling across APBs would be possible. Here, up to a certain APD size, each APD would correspond to an isolated magnetic domain that can be regarded as a magnetic super moment. Due to the missing coupling between these super moments, the super moments would behave in a paramagnetic fashion. For the neutron diffractograms, this would imply similar consequences as in the first scenario. Also here, a diffuse magnetic intensity would be expected with the difference that the correlation length of the magnetic structure might even be smaller than the correlation length of the nuclear structure. Yet, these effects are expected to be small and probably not resolvable in an experiment.

The third scenario is the most interesting one since it represents the situation postulated in Chapter 2. Here, the FM domains would couple across the APBs in an AFM fashion. This scenario could in analogy to superparamagnetism be labeled superantiferromagnetism, yet this name has been attributed in the pertinent literature to other, unrelated phenomena and, in order to avoid confusion, it will be rather referred to as AFM coupling of APDs. The implications of this AFM-like coupling of APDs for neutron powder diffractograms are quite different from the first two scenarios and will be derived on the following pages. In order to simplify the problem, only the Mn and Z sublattices are considered (the 4a and 4b Wyckoff positions of the $L2_1$ structure) neglecting the Ni sublattice (8c position) which is anyway unaffected by the B2-$L2_1$ transition.

In order to describe the problem mathematically, first, the NaCl symmetry of the Mn-Z lattice needs to be described. For this purpose, a function $f(\mathbf{r})$ is introduced that takes on the

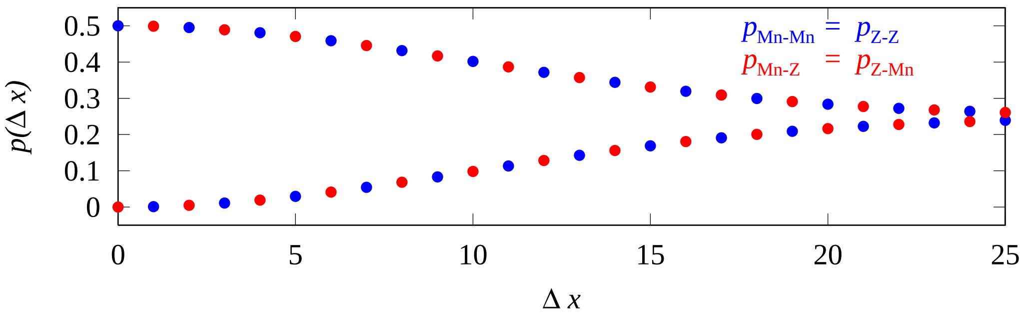

Fig. 4.1 One-dimensional pair probability functions for the Mn-Z sublattice under the presence of APDs.

form

$$f(\mathbf{r}) = (-1)^{\mathbf{r}} = (-1)^x \cdot (-1)^y \cdot (-1)^z \tag{4.1}$$

where $x, y, z \in \mathbb{Z}$ and $\mathbf{r} = (x, y, z)$. On this lattice, the effect of structural APDs is modeled which effectively leads to a spatial decay of the occupational correlation of the lattice that can be described with a Gaussian distribution. On this basis, pair probabilities $p_{\text{a-b}}(\mathbf{r}, \Delta\mathbf{r})$ can be defined that give the probability to find simultaneously an atom of type a at position $\mathbf{r}$ and an atom type b at position $\mathbf{r} + \Delta\mathbf{r}$. In total, there are 4 such probabilities, namely $p_{\text{Mn-Mn}}$, $p_{\text{Mn-Z}}$, $p_{\text{Z-Mn}}$ and $p_{\text{Z-Z}}$ that add up to 1 and that are defined as follows

$$p_{\text{Mn-Mn}}(\mathbf{r}, \Delta\mathbf{r}) = \frac{1}{4}\big(1 + f(\Delta\mathbf{r}) \cdot \exp(-\frac{\Delta\mathbf{r}^2}{2s^2})\big) = p_{\text{Z-Z}} \tag{4.2}$$

$$p_{\text{Mn-Z}}(\mathbf{r}, \Delta\mathbf{r}) = \frac{1}{4}\big(1 - f(\Delta\mathbf{r}) \cdot \exp(-\frac{\Delta\mathbf{r}^2}{2s^2})\big) = p_{\text{Z-Mn}} \tag{4.3}$$

where s denotes the standard deviation of the Gaussian distribution. For the 1-dimensional case, these pair probabilities with an arbitrary choice of s are depicted in Fig. 4.1. Considering the stoichiometric case, $p_{\text{Mn-Mn}}$ takes on a value of 0.5 at $\Delta x = 0$ while simultaneously, $p_{\text{Mn-Al}}$ is zero. Due to the presence of APDs and hence the increasing loss of occupational correlation with increasing Δx, both $p_{\text{Mn-Mn}}$ and $p_{\text{Mn-Al}}$ converge to a value of 0.25 for large Δx.

The scattering amplitude $A(\mathbf{Q})$ for neutron scattering is defined as

$$A(\mathbf{Q}) = \sum_{\mathbf{r}} b(\mathbf{r}) \exp(\mathrm{i}\mathbf{Q}\mathbf{r}) \tag{4.4}$$

where b is the neutron scattering length at position $\mathbf{r}$ and $\mathbf{Q}$ is the reciprocal scattering vector. The scattering intensity $I(\mathbf{Q})$ is then given as

$$I(\mathbf{Q}) = \langle (AA^*)(\mathbf{Q}) \rangle = \langle \sum_{\mathbf{r},\mathbf{r}+\Delta\mathbf{r}} b(\mathbf{r}) b^*(\mathbf{r}+\Delta\mathbf{r}) \exp\big(\mathbf{i}\mathbf{Q}\big((\mathbf{r}+\Delta\mathbf{r}) - \mathbf{r}\big)\big) \rangle. \tag{4.5}$$

which can be simplified to

$$I(\mathbf{Q}) = \langle \sum_{\mathbf{r},\mathbf{r}+\Delta\mathbf{r}} b(\mathbf{r}) b^*(\mathbf{r}+\Delta\mathbf{r}) \exp(\mathbf{i}\mathbf{Q}\Delta\mathbf{r}) \rangle = \mathscr{F}(\langle b(\mathbf{r}) b^*(\mathbf{r}+\Delta\mathbf{r}) \rangle). \tag{4.6}$$

with $\mathscr{F}(\langle b(\mathbf{r}) b^*(\mathbf{r}+\Delta\mathbf{r}) \rangle)$ being the Fourier transform of the expectation value of the product of the scattering lengths at positions $\mathbf{r}$ and $\mathbf{r}+\Delta\mathbf{r}$. For simplification, in the following, the neutron scattering lengths are assumed to be purely real.

In the Mn-Z system, a scattering length at position $\mathbf{r}$ is in general composed of a nuclear and a magnetic part. Specifically, the coherent nuclear scattering lengths of Mn and Z as well as an Ising-type magnetic moment μ strictly confined to the Mn positions are considered. This yields the following general expression for $b(\mathbf{r})$:

$$b(\mathbf{r}) = \sigma(\mathbf{r}) b_{\mathrm{Mn}} + \big(1 - \sigma(\mathbf{r})\big) b_Z + \sigma(\mathbf{r}) f(\mathbf{r}) \mu \tag{4.7}$$

with $\sigma(\mathbf{r})$ being a random variable defining the occupancy of lattice sites. Specifically, $\sigma(\mathbf{r}) = 1$ in the case of $\mathbf{r}$ being occupied by Mn and $\sigma(\mathbf{r}) = 0$ in the case of $\mathbf{r}$ being occupied by Z. As given in (4.6), the scattering intensity is the Fourier transform of the expectation value of the product of the scattering lengths at positions $\mathbf{r}$ and $\mathbf{r}+\Delta\mathbf{r}$. It is noted that, in order to be formally correct, the nuclear and magnetic scattering lengths cannot simply be added as done in (4.7) given that the scattering lengths depend on the neutron spin. However, for the case of unpolarized neutrons (the scenario discussed here), the cross terms cancel and the final result is indeed the simple addition of the nuclear and magnetic scattering intensity. Consequently, with (4.7), the expectation value can be calculated as

$$\begin{aligned} \langle b(\mathbf{r}) b(\mathbf{r}+\Delta\mathbf{r}) \rangle = p_{\text{Mn-Mn}} \frac{1}{2} [(b_{\mathrm{Mn}} + f(\mathbf{r})\mu)(b_{\mathrm{Mn}} + f(\mathbf{r}+\Delta\mathbf{r})\mu) + \\ (b_{\mathrm{Mn}} - f(\mathbf{r})\mu)(b_{\mathrm{Mn}} - f(\mathbf{r}+\Delta\mathbf{r})\mu)] + p_{\text{Z-Mn}} b_{\mathrm{Z}} b_{\mathrm{Mn}} + p_{\text{Mn-Z}} b_{\mathrm{Mn}} b_{\mathrm{Z}} + p_{\text{Z-Z}} b_{\mathrm{Z}}^2 \end{aligned} \tag{4.8}$$

Clearly, in all mixed Mn/Z terms, the magnetic contribution of the Mn scattering length cancels as the sum over all $\mathbf{r}$ contains as many Mn with up as Mn with down spins.

From (4.1) follows $f(\mathbf{r}+\Delta\mathbf{r})f(\mathbf{r}) = f(\Delta\mathbf{r})$. Together with $p_{\text{Mn-Mn}} = p_{\text{Z-Z}} = 1-p_{\text{Mn-Z}} = 1-p_{\text{Z-Mn}}$, (4.8) can be simplified to an expression of only $p_{\text{Mn-Mn}}$

$$\langle b(\mathbf{r})b(\mathbf{r}+\Delta\mathbf{r})\rangle = p_{\text{Mn-Mn}}\big((b_{\text{Mn}}-b_{\text{Z}})^2+\mu^2 f(\Delta\mathbf{r})\big)+2b_{\text{Z}}b_{\text{Mn}} \tag{4.9}$$

Hence, the scattering intensity can be calculated as

$$I(\mathbf{Q}) = 2b_{\text{Z}}b_{\text{Mn}}\mathscr{F}(1)+\mathscr{F}(p_{\text{Mn-Mn}})(\mathbf{Q})\big((b_{\text{Mn}}-b_{\text{Z}})^2\big)+\mathscr{F}(p_{\text{Mn-Mn}}\cdot f)(\mathbf{Q})(\mu^2) \tag{4.10}$$

where the Fourier transforms take on the form

$$\mathscr{F}(p_{\text{Mn-Mn}}) = \frac{1}{2}\mathscr{F}(1)+\frac{1}{2}\mathscr{F}(f)*\mathscr{F}\big(\exp(\frac{-\mathbf{r}^2}{2s^2})\big) \tag{4.11}$$

and

$$\mathscr{F}(p_{\text{Mn-Mn}}\cdot f) = \frac{1}{2}\mathscr{F}(f)+\frac{1}{2}\mathscr{F}\big(\exp(\frac{-\mathbf{r}^2}{2s^2})\big)*\mathscr{F}(1) \tag{4.12}$$

with $\mathscr{F}\big(\exp(\frac{-\mathbf{r}^2}{2s^2})\big) = \exp(-\frac{\mathbf{Q}^2s^2}{2})$. Note that $\mathscr{F}(1)$ is to be understood as the Fourier transform of discrete lattice positions in real space which yields a lattice of δ functions in reciprocal space. Consequently, $\mathscr{F}(1)$ corresponds to the fundamental reflections of the lattice, i.e. sites 4a and 4b being in phase, which in this case yields reflection at the B2 positions in reciprocal space. Similarly, $\mathscr{F}(f)$ results in peaks at the L2$_1$ positions in reciprocal space. Hence, $\mathscr{F}(p_{\text{Mn-Mn}})$ yields sharp peaks at B2 positions in reciprocal space and diffuse peaks at $L2_1$ positions while $\mathscr{F}(p_{\text{Mn-Mn}}\cdot f)$ yields diffuse peaks at B2 positions and sharp peaks at $L2_1$ positions. From (4.10), the nuclear and magnetic scattering intensities can directly be deduced with the correct pre-factors:

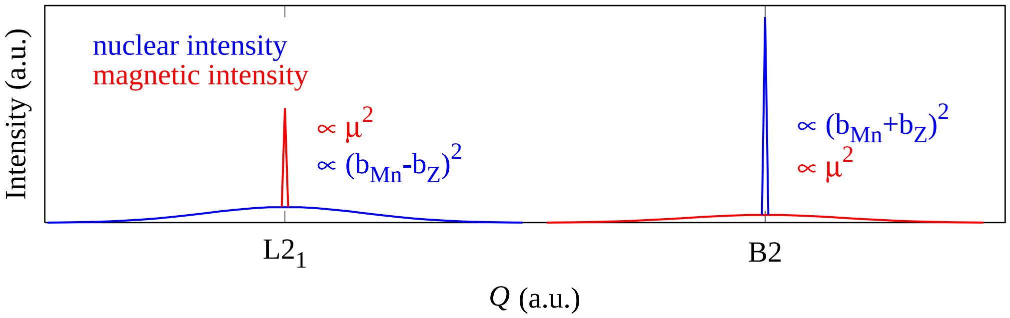

Fig. 4.2 Schematic drawing for the nuclear and magnetic scattering intensity for AFM coupled APDs as derived in the text.

$$I_{\text{nuclear}}(\mathbf{Q}) = \underbrace{\frac{1}{2}(b_{\text{Mn}} + b_{\text{Z}})^2 \mathscr{F}(1)}_{\text{sharp peaks at B2 pos.}} + \underbrace{\frac{1}{2}(b_{\text{Mn}} - b_{\text{Z}})^2 \mathscr{F}(f) * \mathscr{F}\big(\exp(\frac{-\mathbf{r}^2}{2s^2})\big)}_{\text{diffuse peaks at L2}_1\text{ pos.}} \tag{4.13}$$

$$I_{\text{magnetic}}(\mathbf{Q}) = \underbrace{\frac{1}{2}\mu^2 \mathscr{F}(f)}_{\text{sharp peaks at L2}_1\text{ pos.}} + \underbrace{\frac{1}{2}\mu^2 \mathscr{F}\big(\exp(\frac{-\mathbf{r}^2}{2s^2})\big) * \mathscr{F}(1)}_{\text{diffuse peaks at B2 pos.}} \tag{4.14}$$

Further contributions to the scattering intensity such as the magnetic form factor and the Debye-Waller factor have not been considered in this derivation. Fig. 4.2 shows a schematic drawing of the nuclear and magnetic scattering intensity under the presence of AFM coupled magnetic domains that coincide with the APDs.

The scenario of AFM coupled APDs on an atomic level is summarized in Fig. 4.3. Shown is a 1D representation of the 3D Mn-Z lattice with 2 Mn-Mn APBs. As in the derivation above, an Ising-type magnetic structure with up and down spins is assumed. The nuclear structure is composed of the Mn and Z coherent neutron scattering lengths and the magnetic structure is composed of the magnetic moments μ. While in one domain all spins point upwards, in the neighboring domain all spins point downwards. The resulting magnetic structure can further be understood as the superposition of an AFM-type superstructure and a mesoscale structure. While the superstructure results in sharp magnetic peaks at the L2$_1$ positions in reciprocal space, the mesoscale magnetic structure is responsible for a magnetic small angle signal. This model will in the following be compared to the experimental observations in order to confirm or reject the hypothesis of AFM-coupled APDs. For the experiments, the Ni$_2$MnZ systems Ni$_2$MnAl$_{0.5}$Ga$_{0.5}$ and Ni$_2$MnAl were selected, mainly because of the previously discussed possibility to access a wide range of states of order.

4.2 Sample preparation

Ni$_2$MnAl$_{0.5}$Ga$_{0.5}$ and Ni$_2$MnAl powder samples for neutron powder diffraction measurements were prepared from the bulk master alloys whose preparation is described in Chapter 1. Each master ingot was divided into two differently heat treated samples with masses of 6-9 g. Concerning this matter, the solution-annealed ingots were first crushed into smaller pieces and then manually ground to powders of diameter $< 125\,\mu$m. In order to remove mechanical stresses and strains introduced during the powder preparation, the powders have been sealed under vacuum in quartz ampules. Inside the quartz ampules, the powders were subject to a recovery annealing treatment for 4 h in the B2-stable regime at 1073 K followed by quenching in room temperature water. Afterwards, different states of L2$_1$ order/APD size were prepared by annealing the powders in the L2$_1$-stable regime for different annealing times. Specifically,

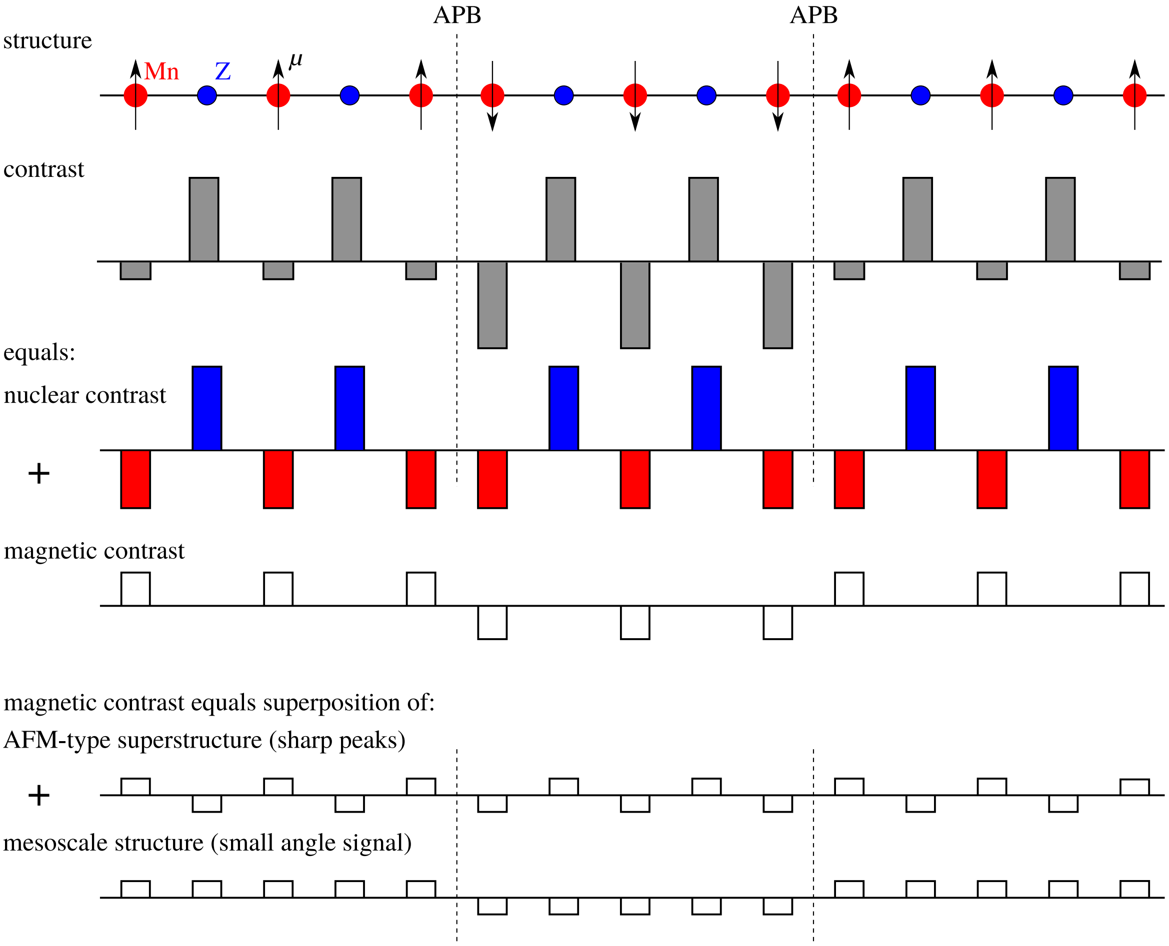

Fig. 4.3 Illustration of the nuclear and magnetic structure on the Mn-Z sublattice in a 1D representation. The magnetic structure is assumed to be Ising-type. While all moment within a domain are FM coupled and thus point in the same direction, across APBs, an AFM coupling exists. Hence, magnetic moments in neighboring domains point in opposite directions. The resulting magnetic structure can further be decomposed into an AFM-like superstructure responsible for sharp superstructure peaks in neutron diffraction and a mesoscale structure responsible for a small angle signal in neutron diffraction.

4 different annealing states have been prepared per system, with annealing times of 0 h, 0.5 h, 3 h and 10 d at 623 K in the case of $Ni_2MnAl_{0.5}Ga_{0.5}$ and annealing times of 0 h, 4 h, 24 h and 10 d at 623 K in the case of Ni_2MnAl. The annealing times for two systems were selected according to the previously presented bulk measurements with the objective to cover a wide range of states of order from ideal B2 order to $L2_1$ order with large APD sizes.

After the annealing treatment, the magnetic transition temperatures T_c of the powder samples have been determined using Differential Scanning Calorimetry (DSC). The results of these measurements are shown in Fig. 4.4. The retrieved T_c values are tabulated in

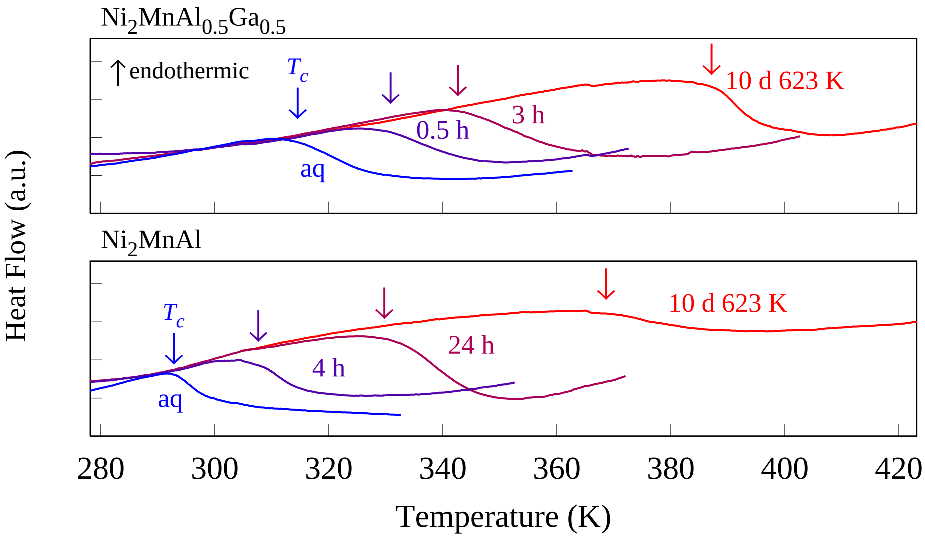

Fig. 4.4 DSC measurements of the magnetic transition in $Ni_2MnAl_{0.5}Ga_{0.5}$ (top) and Ni_2MnAl (bottom) in a variety of annealing conditions. Measurements have been performed on heating using a heating rate of 10 K/min. T_c has been determined as described in Chapter 1.

Tab. 4.1. Evidently, with increased annealing time, an increase of the magnetic transition temperature is observed. The annealing response and ordering kinetics of the powder samples are in good agreement to the previously discussed bulk measurements. While for Ni_2MnAl the agreement between the powder and bulk samples is excellent for the entire evolution curve, for $Ni_2MnAl_{0.5}Ga_{0.5}$, the as-quenched state shows with a T_c value 20 K higher than the one measured in the as-quenched bulk samples. This observation indicates that the quenching of the sealed powder samples is less effective than the quenching of the bulk samples. Consequently, a progressed state of order is preserved in the as-quenched powder samples.

4.3 Results

4.3.1 Magnetic antiphase domain coupling

Neutron powder diffraction measurements of $Ni_2MnAl_{0.5}Ga_{0.5}$ and Ni_2MnAl samples in various annealing conditions have been performed at the POWGEN diffractometer at the Spallation Neutron Source (SNS), USA. In the course of the experiment, two different wavelengths bands were used, characterized by their center wavelengths *cw* of 1.333 Å and 2.665 Å. For every annealing state prepared, several isothermal measurements have been performed at temperatures between 10 K and 450 K. Fig. 4.5 shows neutron powder diffractograms of $Ni_2MnAl_{0.5}Ga_{0.5}$ samples in the 4 annealing states specified above recorded at 20 K using

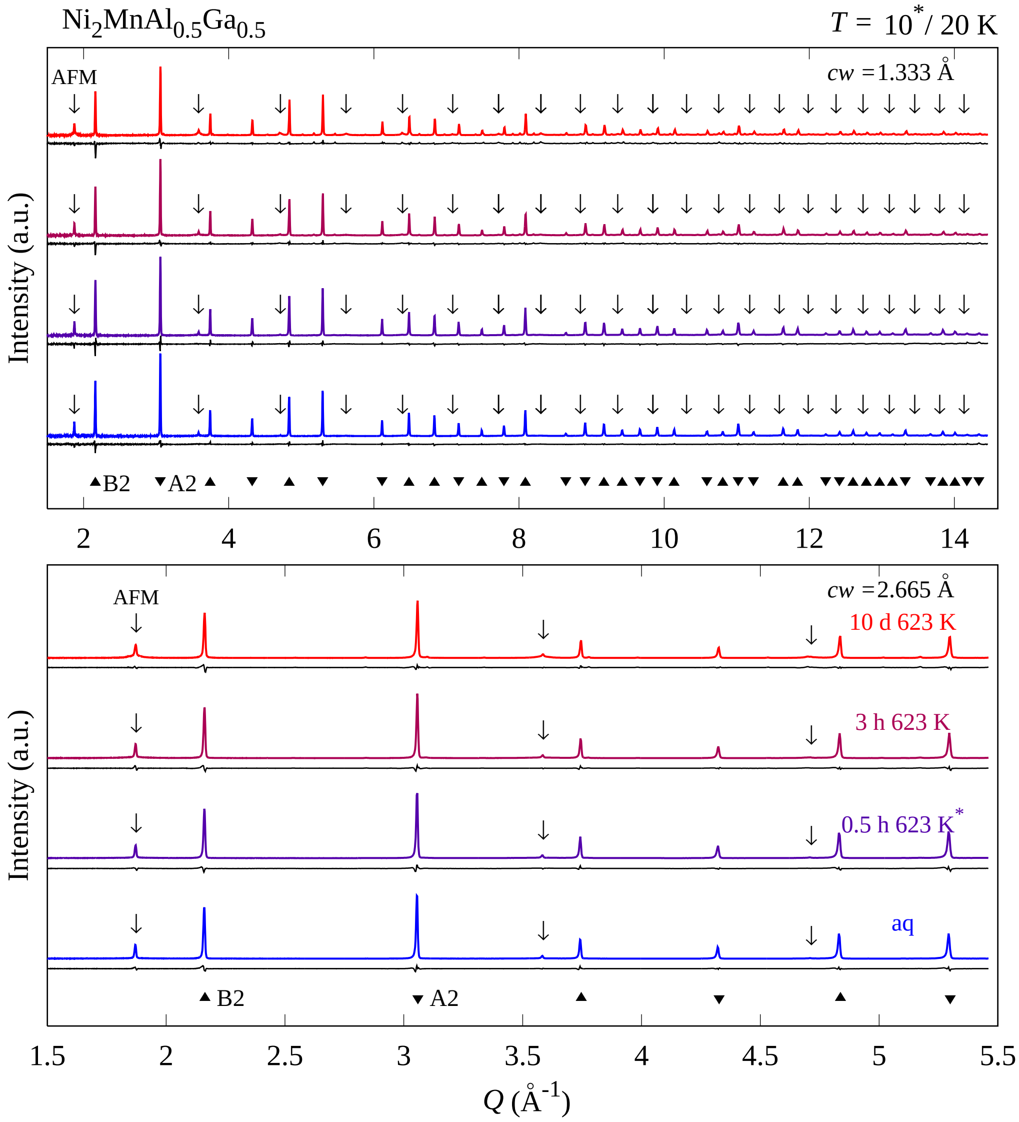

Fig. 4.5 Neutron powder diffractograms of $Ni_2MnAl_{0.5}Ga_{0.5}$ in 4 different annealing conditions recorded at 10*/20 K using two wavelengths bands with center wavelengths of 1.333 Å (top) and 2.665 Å (bottom). Depicted is as colored line the measured intensity, while the black line shows the residues of the Rietveld refinement. The nuclear peak families of the A2 and B2 contrast are indicated below the diffractograms while the position of the AFM superstructure peaks (and also of the nuclear $L2_1$ superstructure peaks) is indicated by arrows above the respective diffractogram. The annealing time increases from the bottom to the top.

both wavelengths bands. With the selection of wavelengths bands, a very large Q-range up to approximately 15 $Å^{-1}$ is covered. All diffractograms have been Rietveld-refined using the FullProf suite (Rodriguez-Carvajal, 1990, 1993; Rodriguez-Carvajal and Roisnel, 1998) and the residues of the refinement are depicted below the respective diffractograms. The peak positions for the nuclear and magnetic peaks are indicated via symbols below and above the diffractograms. Clearly, all annealing states show a pronounced magnetic superstructure marked by the black arrows while below the sharp magnetic peaks, with increased annealing time, broad/diffuse nuclear superstructure peaks develop (see also Fig. 3.6). The magnetic and nuclear contribution can easily be separated since the diffuse intensity persists to large Q values while the intensity of the sharp superstructure peaks decays quickly with Q and has nearly vanished at Q values of approximately 4.7 Å^{-1}. Already a qualitative inspection of the diffractograms at this point allows to assess a relatively constant intensity and shape of the sharp magnetic superstructure reflections across all annealing states.

Fig. 4.6 shows, in analogy to to Fig. 4.5, diffractograms for the $\mathrm{Ni_2MnAl}$ system in the 4 annealing states. Similar to $\mathrm{Ni_2MnAl_{0.5}Ga_{0.5}}$, also for $\mathrm{Ni_2MnAl}$, a magnetic superstructure is visible throughout all annealing states. Again, the diffractograms have been Rietveld-refined with the residues of the refinement shown below the diffractograms. With respect to $\mathrm{Ni_2MnAl_{0.5}Ga_{0.5}}$, the emerging diffuse nuclear $\mathrm{L2_1}$ intensity in $\mathrm{Ni_2MnAl}$ is apparently less pronounced, the reason of which can be either the retarded ordering kinetics and hence smaller APD dimensions after similar annealing times and/or the smaller scattering contrast between Al and Mn in comparison to Al/Ga and Mn.

Fig. 4.7 depicts temperature dependent diffractograms for $\mathrm{Ni_2MnAl_{0.5}Ga_{0.5}}$ and $\mathrm{Ni_2MnAl}$ in intermediate annealing states showing the strong temperature dependence of the magnetic superstructure peaks. For reasons of conciseness, this figure shows only measurements with a *cw* of 2.665 Å which is the wavelengths band best resolving the magnetic superstructure. Evidently, for both systems, the diffractograms recorded in the paramagnetic regime at 450 K show, as expected, no magnetic contribution. For Rietveld refinement of the nuclear structure, the measurements at 450 K were used, thereby determining the degree of $\mathrm{L2_1}$ order and estimating the correlation length of the ordered domains.

Rietveld refinement has been performed in the time-of-flight domain using the FullProf suite and making use of previously determined instrument resolution functions and instrument specific zero-shift values. First, the nuclear structure was refined in the 450 K measurements assuming the $\mathrm{L2_1}$ $\mathrm{Fm\bar{3}m}$ crystal structure as depicted in Fig. 4.8. In this refinement, site occupancies were determined and consequently the degree of $\mathrm{L2_1}$ order η_{L2_1} was calculated. In order to describe the broadened $\mathrm{L2_1}$ nuclear superstructure peaks, an hkl-dependent size broadening was considered obeying the condition $\mathrm{h} + \mathrm{k} + \mathrm{l} = 2n + 1$ with $n \in \mathbb{N}$. For every annealing condition, a size parameter proportional to the correlation length of the ordered domains was refined. The refined value was converted to concur with the description by Fultz and Howe (2012) where the correlation length or crystallite size is calculated as $0.443/\Gamma$,

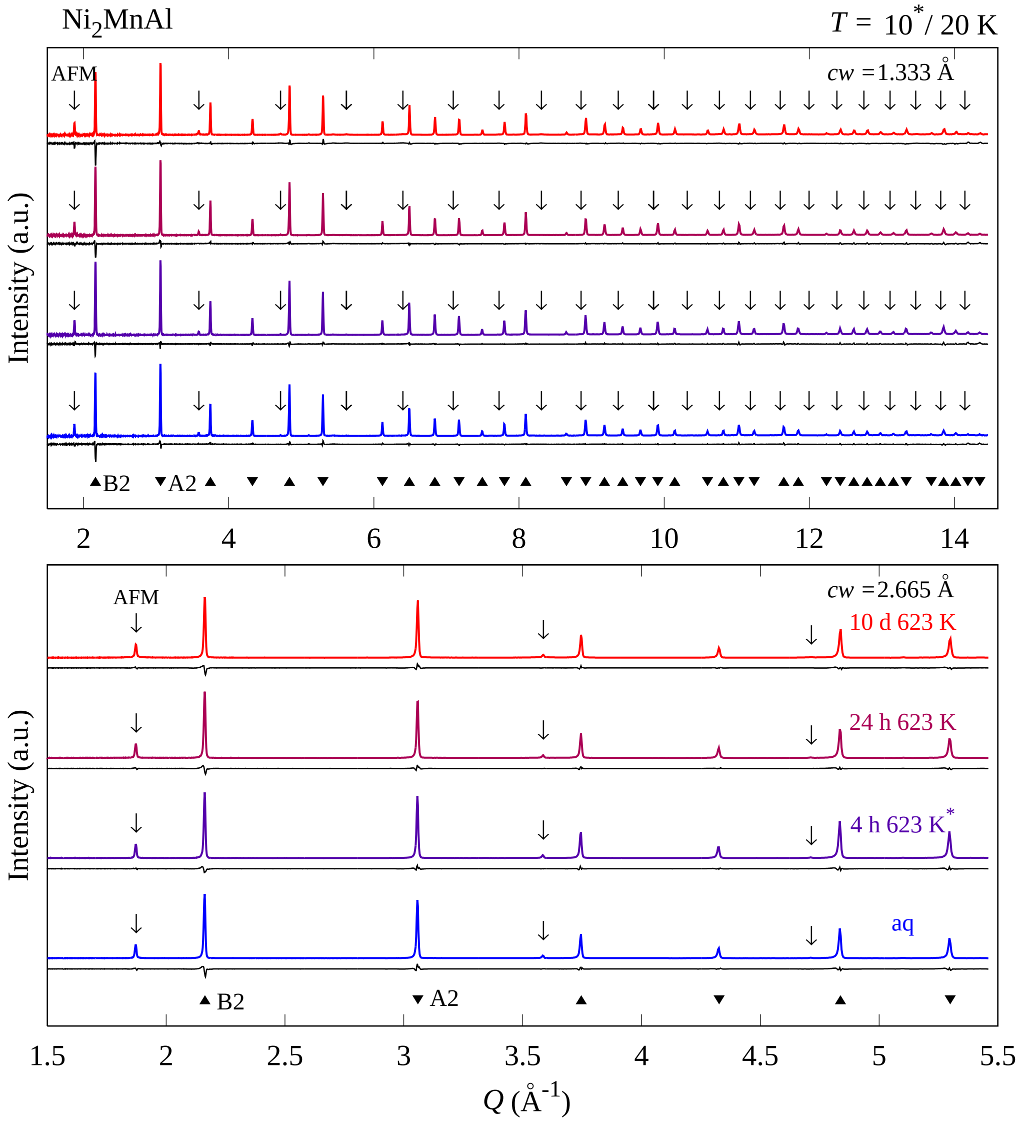

Fig. 4.6 Neutron powder diffractograms of Ni_2MnAl in 4 different annealing conditions recorded at 10*/20 K using two wavelengths bands with center wavelengths of 1.333 Å (top) and 2.665 Å (bottom). Depicted as colored line is the measured intensity, while the black line shows the residues of the Rietveld refinement. The peak positions of the nuclear peak families of the A2 and B2 contrast are indicated by black triangles below the diffractograms while the position of the AFM superstructure peaks (and also of the nuclear $L2_1$ superstructure peaks) is indicated by arrows above the diffractograms. The annealing time increases from the bottom to the top.

with Γ being the half width at half maximum (HWHM) of a Lorentzian fit of the individual peaks. The retrieved structural parameters together with the calorimetrically determined T_c

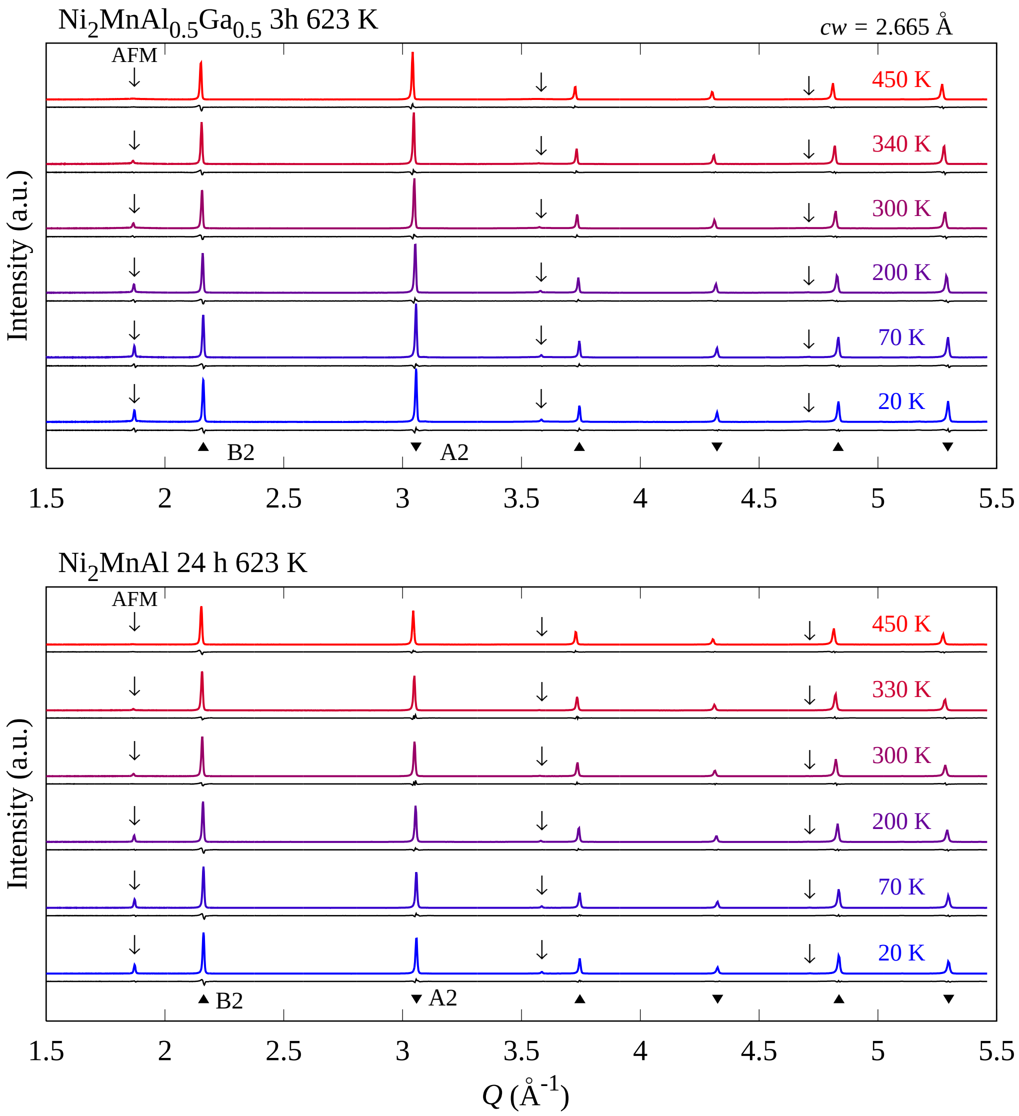

Fig. 4.7 Temperature dependent neutron powder diffractograms for $Ni_2MnAl_{0.5}Ga_{0.5}$ (top) and Ni_2MnAl (bottom) in an intermediate annealing state. Depicted is as colored line the measured intensity, while the black line shows the residues of the Rietveld refinement. The nuclear peak families of the A2 and B2 contrast are indicated below the diffractograms while the position of the AFM superstructure peaks (and also of the nuclear $L2_1$ superstructure peaks) is indicated by arrows above the respective diffractogram. The refined magnetic moments are given in Tab. 4.2.

values are given in Tab. 4.1 where the values for η_{L2_1} and the correlation lengths are averaged over the two wavelengths bands measured.

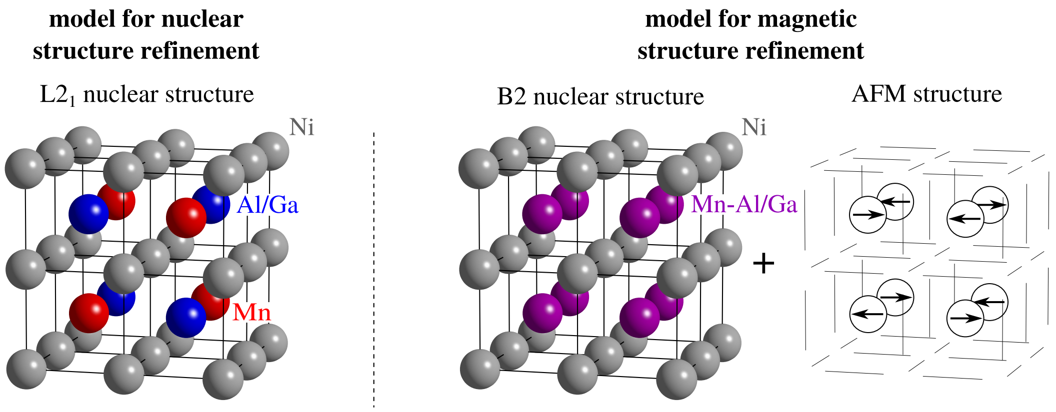

Fig. 4.8 Illustration of the structural models employed to refine the nuclear (left) and magnetic structures (right). Details on the refinement and the refined models is given in the text.

The refinements quantitatively confirm the qualitative observation that with increased annealing time, the diffuse $L2_1$ intensity as well as the correlation length of the ordered domains increases. For both $Ni_2MnAl_{0.5}Ga_{0.5}$ and Ni_2MnAl even the as-quenched state shows a significant diffuse intensity at the $L2_1$ peak positions with, initially a very low correlation length in the magnitude of the lattice constant. Intuitively this might be a surprise, yet considering the finite cooling rate during quenching, it is plausible that the atomic mobility at and below the B2-$L2_1$ transition is sufficient to accommodate initial ordering processes/the emergence of a short-range $L2_1$ order. Nonetheless, the very weak and broad intensity makes the refined values strongly dependent on the background description and thus inherently error-prone. In the advanced states of ordering, for both compounds clearly a pronounced diffuse intensity can be observed. For $Ni_2MnAl_{0.5}Ga_{0.5}$, the refined η_{L2_1} for the 10 d annealed condition yields a value of approximately 1 while the correlation length is estimated as 3 nm. For Ni_2MnAl the slower ordering kinetics already found in the bulk measurements is also observed in the powder diffraction and the 10 d annealed sample shows a η_{L2_1} value of 0.82 and a correlation length of only 1.6 nm.

For diffractograms at various temperatures, lattice constants have been refined which are given in Tab. 4.2. The transition from B2 to $L2_1$ with increased annealing time is also resolved in the lattice constant as previously demonstrated by Ishikawa et al. (2008). At 450 K, the lattice constant decreases from the as-quenched (B2-ordered) to the 10 d at 623 K annealed ($L2_1$ ordered) state by 0.15 % in the case of $Ni_2MnAl_{0.5}Ga_{0.5}$ and by 0.06 % in the case of Ni_2MnAl. The values for $Ni_2MnAl_{0.5}Ga_{0.5}$ are in perfect relative agreement to the work by Ishikawa et al. (2008) where a decrease between the B2 and $L2_1$ structure of 0.17 % was observed.

$Ni_2MnAl_{0.5}Ga_{0.5}$				
Observable	aq	0.5 h	3 h	10 d
T_c (K)	314.5	330.8	342.6	387.1
η_{L2_1}	0.75	0.73	0.93	1.05
correlation length (Å)	8.2	10.5	12.1	30.0
Ni_2MnAl				
Observable	aq	4 h	24 h	10 d
T_c (K)	292.8	307.6	329.7	368.6
η_{L2_1}	0.62	-	0.71	0.82
correlation length (Å)	4.6	-	5.2	16.8

Table 4.1 Degree of $L2_1$ order η_{L2_1} and correlation length of ordered domains for $Ni_2MnAl_{0.5}Ga_{0.5}$ and Ni_2MnAl samples obtained from Rietveld refinement of neutron powder diffraction data measured at 450 K as averaged over two measurements with different wavelengths bands. T_c values refer to the magnetic transition temperatures obtained from DSC measurements.

In order to provide a consistent model able to describe the magnetic structure throughout all annealing stages, the low temperature diffractograms were refined assuming the B2 Pm$\bar{3}$m nuclear structure together with an AFM structure on the Mn sublattice, leading to a magnetic unit cell identical to the $L2_1$ unit cell. As elucidated in the theoretical derivation in the beginning of this chapter, magnetically coupled APDs lead to sharp magnetic superstructure peaks at the $L2_1$ peak positions in reciprocal space, identical to an ideal AFM structure. In size and shape, these magnetic superstructure peaks should thus remain constant throughout the annealing stages as long as mentioned coupling persists, despite the emerging diffuse nuclear signal at the same positions. Hence, for refining the magnetic structure, the approach was taken to define the diffuse nuclear $L2_1$ peaks as background and describe the B2- and A2-type nuclear peaks together with the AFM-type magnetic superstructure peaks with the mentioned model schematically illustrated in Fig. 4.8. Applying this procedure, the magnetic moments on Mn together with the lattice constants were refined for all annealing states and a variety of temperatures. The results of these refinements are given in Tab. 4.2. The normal fonts refer to the refinement of measurements with *cw* = 1.333 Å while the italic fonts refer to the refinement of measurements with *cw* = 2.665 Å. In general, due to the better resolution in the relevant Q range, the background description of the *cw* = 2.665 Å is more accurate and consequently the refined magnetic moments more reliable.

At 20 K, for both $Ni_2MnAl_{0.5}Ga_{0.5}$ and Ni_2MnAl the refined moments on Mn scatter around 3.9 μ_B/f.u. in all annealing conditions. Comparing this to previous neutron diffraction results for Ni_2MnAl as reported by Ziebeck and Webster (1975) shows good agreement, with Ziebeck and Webster (1975) stating the AFM moment of Mn as 4.2 ± 0.2 μ_B/f.u. Interestingly,

		$Ni_2MnAl_{0.5}Ga_{0.5}$				Ni_2MnAl			
Observable	$T(K)$	aq	0.5 h	3 h	10 d	aq	4 h	24 h	10 d
σ_{AFM} (μ_B/f.u.)	10*/20	4.05(6)	4.10(10)*	3.84(11)	3.70(19)	3.54(8)	3.77(6)*	3.76(6)	3.97(10)
		3.97(4)	*4.11(7)**	*3.87(6)*	*3.96(6)*	*3.85(5)*	*3.93(4)**	*3.91(5)*	*3.86(5)*
	70	-	-	3.64(5)	-	-	-	3.53(11)	-
		-	-	*3.83(6)*	-	-	-	*3.83(5)*	-
	200	3.52(8)	-	3.58(11)	3.57(13)	3.17(7)	-	3.35(7)	3.54(8)
		3.33(5)	-	*3.37(7)*	*3.53(8)*	*3.14(5)*	-	*3.30(5)*	*3.42(7)*
	300	1.83(11)	1.82(12)	2.74(9)	2.70(11)	1.45(9)	2.15(8)	2.10(16)	2.63(11)
		1.77(7)	*2.04(7)*	*2.62(8)*	*2.64(10)*	*1.34(9)*	*1.83(7)*	*2.06(7)*	*2.46(7)*
	340/330**	-	-	1.95(8)	-	-	-	1.77(9)**	-
		-	-	*2.15(6)*	-	-	-	*1.50(8)***	-
	450	0.88(40)	0.74(31)	0.83(31)	0.97(29)	0.99(11)	-	0.77(14)	0.56(19)
		0.59(16)	*0.64(16)*	*0.58(34)*	*0.69(22)*	*0.80(13)*	-	*0.68(14)*	*0.81(13)*
a (Å)	10*/20	5.81423(16)	5.81357(2)*	5.81137(2)	5.80958(4)	5.80901(4)	5.80941(4)*	5.80784(4)	5.80732(10)
		5.81254(4)	*5.81189(6)**	*5.80975(4)*	*5.80800(4)*	*5.80827(8)*	*5.80896(6)**	*5.80749(6)*	*5.80594(6)*
	70	-	-	5.81187(4)	-	-	-	5.80856(6)	-
		-	-	*5.81040(4)*	-	-	-	*5.80810(6)*	-
	200	5.81926(2)	-	5.81619(2)	5.81434(4)	5.81367(2)	-	5.81215(2)	5.81139(10)
		5.81965(4)	-	*5.81665(4)*	*5.81462(4)*	*5.81498(8)*	-	*5.81392(6)*	*5.81228(6)*
	300	5.83136(2)	5.83217(2)	5.82350(2)	5.82534(2)	5.82437(2)	5.82253(2)	5.82261(4)	5.82144(12)
		5.82977(4)	*5.82903(4)*	*5.82437(4)*	*5.82385(4)*	*5.82384(4)*	*5.82395(4)*	*5.82242(4)*	*5.82062(4)*
	340/330**	-	-	5.82867(4)	-	-	-	5.82400(2)**	-
		-	-	*5.82878(4)*	-	-	-	*5.82454(4)***	-
	450	5.83899(4)	5.83940(4)	5.83725(4)	5.83363(2)	5.83221(2)	-	5.83158(2)	5.83024(8)
		5.83969(4)	*5.83958(4)*	*5.83743(4)*	*5.83459(4)*	*5.83412(4)*	-	*5.83293(4)*	*5.83097(4)*

Table 4.2 Magnetic moments and lattice constants for $Ni_2MnAl_{0.5}Ga_{0.5}$ and Ni_2MnAl samples in a variety of annealing states and at various temperatures obtained from Rietveld refinement of neutron powder diffraction data measured with two wavelengths bands $cw = 1.333$ Å and cw = 2.665 Å (italic font). All values refer to the $L2_1$ unit cell.

the spin spiral structure reported by Ziebeck and Webster (1975) evidenced by satellite reflections could not be observed in the here presented measurements. Instead, for the primarily B2-ordered, as-quenched state, a purely AFM structure was found. Comparing the data presented in this chapter obtained at POWGEN to the sample set reported in Chapter 5 which also includes an independently prepared Ni_2MnAl sample shows excellent agreement. The data set presented in Chapter 5 was measured at the SPODI diffractometer at the FRM II, Germany and the magnetic moment on Mn in the AFM structure was refined as 3.73 μ_B/f.u. Also in the SPODI measurements, no magnetic satellite peaks and hence no signs for a spin spiral structure were found. For $Ni_2MnAl_{0.5}Ga_{0.5}$, no neutron diffraction studies have been reported yet in the pertinent literature and consequently, with respect to the refined magnetic moments, no comparison to literature values can be given. However, as pointed out above, both $Ni_2MnAl_{0.5}Ga_{0.5}$ and Ni_2MnAl show quite identical magnetic structures.

Comparing the lattice constants of $Ni_2MnAl_{0.5}Ga_{0.5}$ and Ni_2MnAl shows at all temperatures higher values for $Ni_2MnAl_{0.5}Ga_{0.5}$, resulting from a larger atomic size of Ga in comparison to Al. The decrease in lattice constant with increased $L2_1$ order briefly discussed above is observed in both compounds at all temperatures. The magnetic transition however seems to have no visible effect on the lattice constant. Comparing absolute values of the lattice constant to previously published neutron diffraction and X-ray diffraction results shows excellent agreement. Ishikawa et al. (2008) report room temperature lattice constants for $Ni_2MnAl_{0.5}Ga_{0.5}$ in various annealing conditions and gives a lattice constant for the B2-ordered, as-quenched state of 5.830 Å and for the most progressed $L2_1$ ordered state of 5.820 Å. In the present investigation, averaged over both wavelengths bands, at 300 K, 5.830(5) Å for the as-quenched state and 5.825(2) Å for the 10 d at 623 K annealed state are found. For Ni_2MnAl, Ziebeck and Webster (1975) report a lattice constant of 5.822 Å at room temperature in the as-quenched condition and Acet et al. (2002) state a lattice parameter of 5.818 Å. In the present study, at 300 K, lattice constants between 5.824(4) Å and 5.821(4) Å are observed, depending on the annealing condition. The independent Ni_2MnAl sample measured at SPODI as presented in Chapter 5 showed a refined lattice constant at 300 K of 5.825(4) Å in the B2-ordered state. Considering presumably slightly different compositions and states of order in the different samples, the conformity of the stated values is excellent.

Further, it is of interest to study explicitly the temperature dependence of the magnetic moments. As given in Tab. 4.2, several isothermal measurements have been performed for the various annealing conditions between 20 K and 450 K. For $Ni_2MnAl_{0.5}Ga_{0.5}$ and Ni_2MnAl in an intermediate annealing state, these temperature dependent diffractograms are depicted in Fig. 4.7. Shown are measurements with *cw* = 2.665 Å. As can be seen, with temperature, the magnetic intensity gradually decreases and is completely vanished at 450 K.

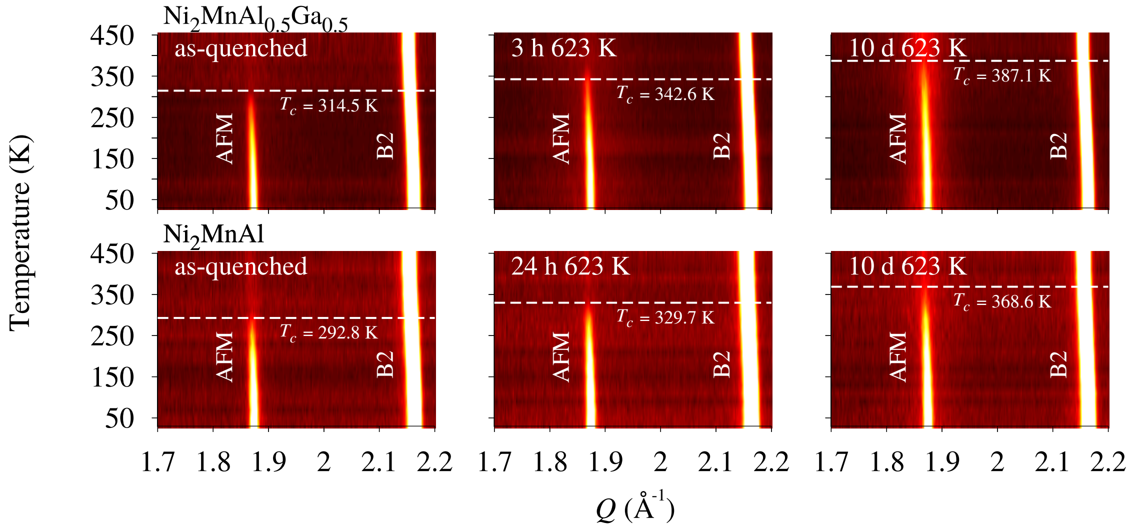

Fig. 4.9 Waterfall plots for Ni$_2$MnAl$_{0.5}$Ga$_{0.5}$ (top) and Ni$_2$MnAl (bottom) in different annealing conditions. The data was measured partially on cooling and heating using a *cw* of 1.333 Å. The white dashed lines indicate the T_c value retrieved from DSC measurements as given in Tab. 4.1.

Besides the isothermal measurements, continuous in-situ measurements have been performed for both systems in 3 different annealing states each, on cooling and heating. The retrieved data was afterwards sliced, yielding averaged diffractograms every 20 K between 30 K and 450 K. As previously discussed, the magnetic transition temperature is a reliable indicator for the state of order present in the sample and hence, despite similar Mn magnetic moments at 20 K, the decrease of the magnetic moment with temperature should be different for different annealing conditions. Fig. 4.9 shows waterfall plots for Ni$_2$MnAl$_{0.5}$Ga$_{0.5}$ and Ni$_2$MnAl in various annealing states. Evidently, the increase in T_c already observed in the DSC measurements (see Fig. 4.4 and Tab. 4.1) is also observed in the neutron diffraction data. Furthermore, with increased annealing time, for both systems the increased diffuse background is observed stemming from the L2$_1$ order with a pronounced APD structure. Despite the qualitative agreement between the DSC and neutron data, clearly the determination of T_c from a broad calorimetric signal is error-prone and quantitative discrepancies to the more accurate neutron diffraction data are observed.

The temperature dependent diffractograms can also be analyzed quantitatively. In the studied temperature range, evidently the nuclear scattering is, with the exception of the temperature dependent contribution of the Debye-Waller factor, constant. In order to extract the magnetic intensity, the purely nuclear signal at 450 K was subtracted from the diffractograms at lower temperatures. In this respect, the peak shift due to the temperature dependent lattice constant needs to be considered which was done using the refined values from the isothermal

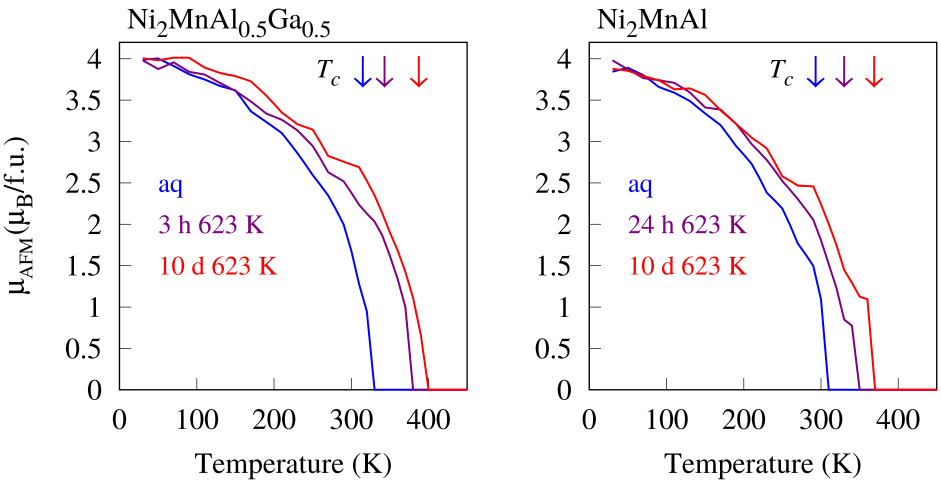

Fig. 4.10 Quantitative analysis of the AFM Mn moment as a a function of temperature for 3 different annealing states in $Ni_2MnAl_{0.5}Ga_{0.5}$ and Ni_2MnAl samples. The colored arrows indicate the T_c values obtained from DSC measurements.

measurements. After nuclear background subtraction, the intensity of the first magnetic peak was determined via numerical integration. Finally, the obtained intensities were corrected for the temperature dependent Debye-Waller factors obtained from the Rietveld refinement of the isothermal diffractograms. The obtained corrected intensity values were then normalized to match the refined magnetic moment at 20 K. Fig. 4.10 depicts the temperature dependent Mn magnetic moment in the AFM structure. In the paramagnetic state with the clear absence of a sharp magnetic superstructure peaks, the magnetic intensity was manually set to zero. Due to the μ^2 dependency of the magnetic intensity and a imperfect background description, in Rietveld refinement (see Tab. 4.2) always a small magnetic moment is retrieved also in the paramagnetic state which is an artifact of the refinement process rather than a meaningful result. Fig. 4.10 clearly shows the increased T_c values with increased annealing time that were already qualitatively observed in the waterfall plots. Also, the second order nature of the magnetic phase transition is nicely revealed.

To conclude, the here presented neutron diffraction results strongly suggest the existence of the postulated magnetic APD coupling. Evidently, a sharp magnetic superstructure is found in all states of order/APD sizes at low temperatures. This magnetic structure is found to be quasi constant in intensity throughout all annealing stages which perfectly confirms the predictions made in the introductory part of this chapter for the postulated scenario of an AFM coupling of structural APDs. At the same time, the magnetic transition temperature shows a clearly temperature-dependent behavior demonstrating, besides the emerging nuclear superstructure, the increased degree of $L2_1$ order evoked by low-temperature annealing.

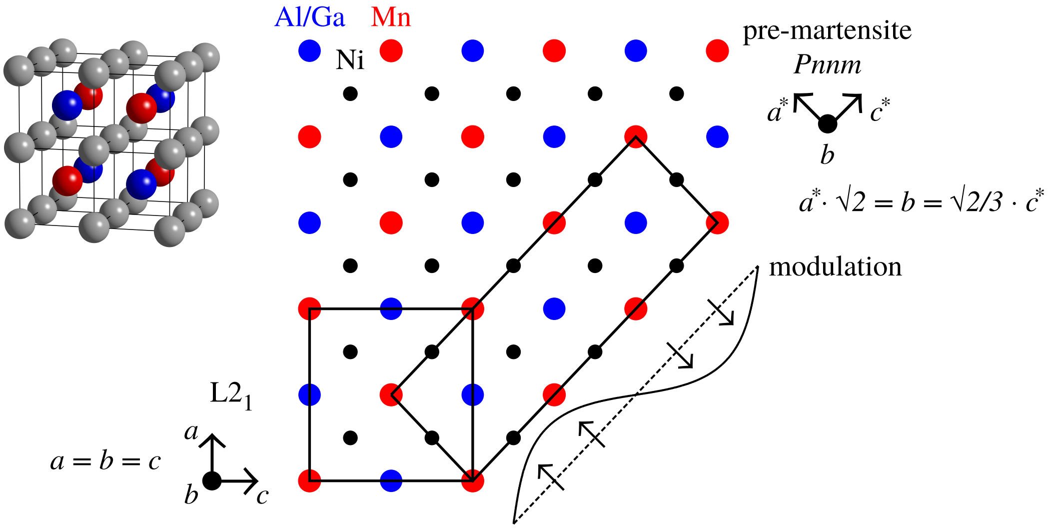

Fig. 4.11 Pre-martensite phase as originally described by Brown et al. (2002). Depicted is a 2D projection of the lattice together with the cubic L2$_1$ unit cell and the orthorhombic pre-martensite unit cell.

Overall, the presented results are an unambiguous proof for the existence of magnetic APD coupling in Ni$_2$MnZ Heusler alloys.

4.3.2 Pre-martensitic transition in Ni$_2$MnAl$_{0.5}$Ga$_{0.5}$

As first observed by Zheludev et al. (1995) with neutron diffraction experiments, the martensitic transition in the prototypical ferromagnetic shape memory compound Ni$_2$MnGa is preceded by a so-called pre-martensitic precursor phase that is stable between 220 K and 260 K. Brown et al. (2002) proposed an orthorhombic structure for this pre-martensite phase with space group Pnnm. It can be understood as a modulation of the $\{110\}$-planes of the L2$_1$ austenite structure as schematically depicted in Fig. 4.11. As can be seen in the figure, the pre-martensite is a 3-modulated structure with the modulation occurring in x direction of the orthorhombic unit cell while the displacement amplitudes of the different elements within a displaced plane are a degree of freedom. The lattice constants of the orthorhombic unit cell have been fixed in the description by Brown et al. (2002) to certain ratios of the cubic lattice parameter. Specifically, the lattice parameter b in y-direction is the same for the cubic and the orthorhombic structure while the lattice parameter a^* of the orthorhombic structure in x-direction is a factor of $\sqrt{2}$ smaller than b and the lattice parameter c^* of the orthorhombic structure in z-direction is a factor of $3/\sqrt{2}$ larger than b. It should be noted that in principle, in the orthorhombic structure the lattice constants are independent from each other and fixing

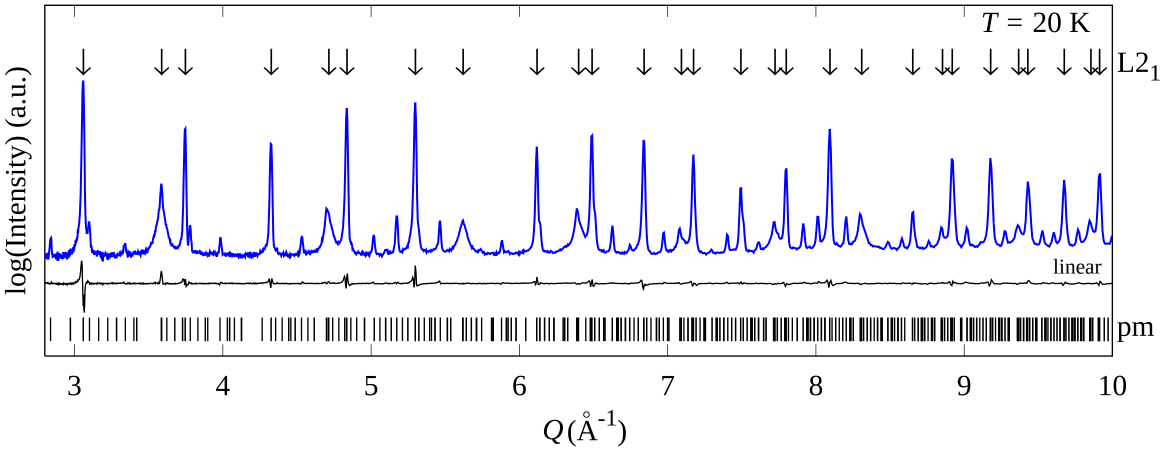

Fig. 4.12 Neutron diffractogram for a 10 d at 623 K annealed $Ni_2MnAl_{0.5}Ga_{0.5}$ sample at 20 K on a logarithmic scale. The black line below the diffractogram shows the (linear) residual of the Rietveld-refined diffractogram. The arrows above the measured data shows the position of the L2$_1$ peaks, the lines below the data indicate the peak positions of the pre-martensite (pm) Pnnm structure.

them to certain ratios already implies a certain restriction. Recently, the structural model by Brown et al. (2002) has been questioned and an incommensurate 4D superspace group has been proposed by Singh et al. (2013) in order to describe the structure more accurately. Yet, the resolution of the experiment presented in this thesis is insufficient for contributing to this debate and the orthorhombic structure is by any means a satisfactory approximation to treat the presented data.

In $Ni_2MnAl_{0.5}Ga_{0.5}$, the alloy system investigated in this chapter for studying the magnetic coupling of APDs, up to this point no pre-martensitic or martensitic transition has been reported. Employing bulk measurements, Ishikawa et al. (2008) observed a pre-martensitic transition only for the Ga rich side of the $Ni_2MnAl_xGa_{1-x}$ system. In the following, it is demonstrated by means of neutron diffraction, that also in $Ni_2MnAl_{0.5}Ga_{0.5}$, the L2$_1$ structure transforms at lower temperatures into a pre-martensitic structure that can well be described using the model by Brown et al. (2002). Furthermore, it is demonstrated that the pre-martensite is stable to at least 20 K and no transition to a martensite phase is observed. In Ni_2MnAl, in comparison to $Ni_2MnAl_{0.5}Ga_{0.5}$, no pre-martensitic transition is observed.

In the first part of this chapter, the structural and magnetic models used for Rietveld refinement did not consider the transition to a pre-martensite phase. Yet, evidently, the results of the refinements as depicted in Fig. 4.5 are satisfying and on a first glance the presence of a pre-martensite phase is hardly noticeable. The reason for this is the low intensity of the

Atomic position				Occupation	$Ni_2MnAl_{0.5}Ga_{0.5}$ (20 K)			Ni_2MnGa (230 K)		
					x	y	z	x	y	z
2a	0	0	0	Mn	0	0	0	0	0	0
4g	x	0	z	Mn	0.028(2)	0	1/3	0.013(2)*	0	1/3
			z					0.01590**		
2b	0	1/2	0	Al/Ga	0	1/2	0	0	1/2	0
4g	x	0	z	Al/Ga	0.027(1)	1/2	1/3	0.0015(9)*	1/2	1/3
								0.01970**		
4f	1/2	1/4	0	Ni	1/2	1/4	0	1/2	1/4	0
8h	x	y	z	Ni	0.5291(2)	1/4	1/3	0.4930(3)*	1/4	1/3
								0.52126**		

Table 4.3 Atomic positions and refined displacements for $Ni_2MnAl_{0.5}Ga_{0.5}$ at 20 K and for Ni_2MnGa at 230 K as given by Brown et al. (2002)* and Singh et al. (2013)**. All values refer to the space group Pnnm. Lattice constants of the orthorhombic unit cell are $b = a^* \cdot \sqrt{2} = c^* \cdot \sqrt{2}/3$ with b being the cubic L2_1 lattice constant.

superstructure peaks stemming from the described modulation of the $\{110\}$-planes that leaves the structural and magnetic peaks of the parent phase in a first approximation undisturbed.

Fig. 4.12 shows the neutron powder diffractogram of the $Ni_2MnAl_{0.5}Ga_{0.5}$ sample in the 10 d at 623 K annealed condition at 20 K on a logarithmic y-scale in order to amplify low-intensity regions. In this depiction, it is evident that besides the strong austenite peaks, additional low-intensity peaks are present that cannot be described with the L2_1 structure. Refining the structure with the model by Brown et al. (2002) yields excellent results. Specifically, the black line below the diffractogram shows the residual of the Rietveld refinement on a linear scale. As done by Brown et al. (2002), the ratio of lattice constants was fixed in the refinement process and the modulations were restricted to the x-direction. By this approach, the refined values can well be compared to the values reported by Brown et al. (2002) for Ni_2MnGa.

Tab. 4.3 lists the atomic positions in the orthorhombic unit cell for the pre-martensite phase in Ni_2MnGa together with the site occupancies as obtained by Brown et al. (2002) from neutron diffraction and by Singh et al. (2013) using high resolution X-ray diffraction. Additionally, the same values for $Ni_2MnAl_{0.5}Ga_{0.5}$ as refined in this study are listed. As can be seen, the displacements for $Ni_2MnAl_{0.5}Ga_{0.5}$ at low temperatures are higher than the displacements stated for Ni_2MnGa. Surprisingly, the discrepancies between the two cited studies on Ni_2MnGa are large. Yet, overall, the refined values for $Ni_2MnAl_{0.5}Ga_{0.5}$ seem plausible and agree especially well with the values for Ni_2MnGa reported by Singh et al. (2013). Specifically, in this study, similar displacements for all constituents with values

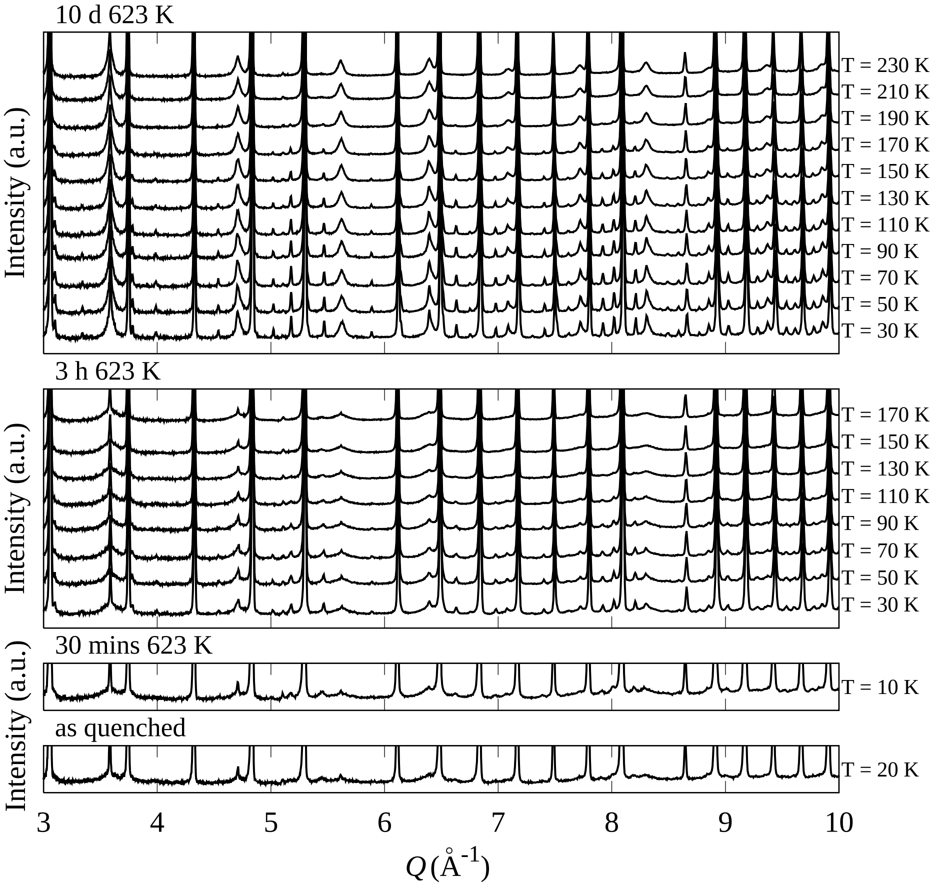

Fig. 4.13 Temperature dependent neutron diffraction patterns of $Ni_2MnAl_{0.5}Ga_{0.5}$ in 4 annealing conditions showing the emergence of the pre-martensite phase with decreasing temperature. Measurements for the top two panels were performed on cooling using a *cw* of 1.333 Å. The lower two panels show isothermal measurements at 10/20 K.

of $0.028a^*$, $0.027a^*$ and $0.0291a^*$ for Mn, Al/Ga and Ni, respectively are found. Finally, the results leave no doubt that the observed pre-martensitic structure in $Ni_2MnAl_{0.5}Ga_{0.5}$ is qualitatively the same as in Ni_2MnGa.

Furthermore, it is interesting to study the effects of the change in nuclear structure, i.e. the increasing degree of $L2_1$ order and the increasing APD size, on the emergence of the pre-martensite phase. Fig. 4.13 shows temperature dependent neutron diffraction patterns for $Ni_2MnAl_{0.5}Ga_{0.5}$ in the 3 h and 10 d at 623 K annealed conditions measured continuously on cooling using a *cw* of 1.333 Å together with the isothermal diffractograms at 10/20 K of the as-quenched and 0.5 h annealed samples. Clearly, the emergence of a pre-martensite phase with decreasing temperature is observed in the 3 h and 10 d annealed samples. Also the 0.5 h annealed sample shows very weak pre-martensitic peaks at 10 K. In the as-quenched sample however, no pre-martensite phase is observed. While all samples annealed at 623 K show the pre-martensite phase at low temperatures, the intensity of the peaks in the 10 d at 623 K annealed sample is significantly stronger than in the 3 h and the 0.5 h annealed samples. Also, the transition temperature to the pre-martensite phase is highest in the 10 d annealed sample where it is observed at approximately 190–210 K. In the 3 h annealed sample the transition is found at significantly lower temperatures of approximately 130-150 K. Since for the 0.5 h annealed sample only the 10 K measurement exists, no statement can be made about the transition temperature, yet, comparing the peak intensity to the 3 h annealed sample indicates that the transition temperature will be significantly lower in the 0.5 h annealed sample.

The presented results demonstrate for the first time the influence of the degree of order and the microstructure of the austenite phase on the pre-martensite phase. Specifically, it is found that the as-quenched B2-ordered sample (presumably with initial $L2_1$ short-range order) shows no pre-martensitic transition while with increased $L2_1$ order, the stability of the pre-martensite phase increases. The observation that already the 0.5 h and 3 h annealed samples show an increased tendency to develop the pre-martensite phase at low temperatures indicates that already the adjustment of short-range order, even under the presence of a high density of APBs, influences the pre-martensitic transition. At the same time, the significantly stronger pre-martensite peaks and the higher transition temperature of the 10 d with respect to the 3 h annealed sample indicates that even when the short-range order is in saturation (note, that both the 3 h and 10 d annealed samples show similar T_c and η_{L2_1} values) and primarily the APDs grow in size, the pre-martensite further gains stability. Hence, both processes, i.e. the adjustment of (short-range) $L2_1$ order and the growth of the APD structure seem to impact the structural austenite-pre-martensite transition while the exact mechanisms of this transition are subject of further investigations.

4.4 Conclusions

The results presented in this chapter make a strong case for the existence of a coupling of magnetic and structural domains in Ni_2MnZ compounds. Specifically, it was demonstrated that an AFM-like coupling of the Mn atoms in neighboring APDs exists over a wide range of APD dimensions. These findings have profound implications for the entire family of Ni_2MnZ alloys as commonly cherished for their excellent ferromagnetic shape memory and magnetocaloric properties. In fact, for practical purposes, it is not the short-range chemical structure but the mesoscale microstructure of these alloys that determines their functionality such as the magnetic properties. However, so far, when tuning the properties of these alloys, mainly the degree of order and the alloys' composition have been taken into consideration. The additional complexity of the microstructure leaves room for further optimization, especially considering that the understanding of the exact mechanisms of the interplay of the microstructure and the functionality (e.g. the magnetocaloric effect) is still lacking. It should be noted that nowadays much information about functional mechanisms is drawn from theoretical studies based on DFT calculations which are often restricted to ordered structures and atomic cells with a small number of atoms. Hence, the sensitization for the importance of the microstructure could trigger new research activities that will help to use the full potential of microstructure engineering for improving the functionality of Ni_2MnZ Heusler materials.

Experimentally, it will be interesting to compare the powder diffraction results to small angle neutron scattering measurements. As pointed out in the first part of this chapter, the observed AFM coupling of APDs does not only yield sharp magnetic superstructure peaks but also the presence of a magnetic small angle neutron scattering (SANS) signal is expected. First of all, this postulation should be tested given that the existence of a magnetic SANS signal that can be traced back to the size of the APD structure would be the ultimate proof that the presented model is correct. Next, SANS could be used to study the domain coupling in bulk samples as a function of APD size, magnetic field and temperature as it would be required to examine the exact mechanisms of the coupling and its interplay with an external field. Given the higher flux and the easier data evaluation with respect to powder diffraction, a much larger parameter space could be probed in the same time avoiding the problem of handling powder samples in magnetic fields. The retrieved results could finally be used in combination with magnetic simulations as e.g. presented in Chapter 2 to reveal the mechanisms of the magnetic coupling across APDs in Ni_2MnZ compounds.

Furthermore, with the presented discovery of $Ni_2MnAl_{0.5}Ga_{0.5}$ showing a surprising stability of the pre-martensite phase that is at the same time highly dependent on the degree of order in the austenite parent phase, a pathway for a better understanding of the mechanisms leading to a martensitic transition in Ni_2MnZ compounds is opened. Specifically, the order dependency presented in this thesis needs to be investigated theoretically by means of DFT calculations.

Chapter 5

Magnetic structure of B2-ordered $Ni_{2\text{-}x}Co_xMnAl$ compounds

5.1 Introduction

In the previous chapters, the primary topic was the adjustment of $L2_1$ order in Ni_2MnZ Heusler compounds on different length scales, its influence on the magnetic properties of these materials as well as the kinetic evolution of the ordering process. Specifically, the interdependency of the state of order in the sample and the bulk magnetization was established in Chapter 2. It was demonstrated that B2-ordered samples show perfect antiferromagnetic (AFM) properties while with increased $L2_1$ order, peculiar magnetic properties develop that adopt an increased ferromagnetic (FM) character. This behavior was ascribed to a magnetic coupling between adjacent structural APD which could be supported by neutron diffraction results presented in Chapter 4. As already discussed in the theoretical part of Chapter 2, the AFM-like coupling of adjacent antiphase domains (APDs) is a question of the ratio between the AFM and the FM exchange interactions J_1 and J_2 as given in the magnetic Hamiltonian of the system (2.1).

In perfect analogy to the coupling across antiphase boundaries (APBs), also in fully disordered B2 Ni_2MnZ compounds, the magnetic properties are crucially determined by the ratio of the competing AFM and FM exchange interactions. Specifically, B2-ordered Ni_2MnAl, with a weak Ni-Mn FM coupling, shows perfect AFM properties (Acet et al., 2002; Ziebeck and Webster, 1975), while B2-ordered Co_2MnAl, with a stronger Co-Mn FM coupling, shows perfect FM properties (Umetsu et al., 2008). Consequently, as a function of the Ni/Co ratio, a transition between the AFM and the FM structure is observed (Okubo et al., 2011). The relevant composition range for the transition can be confined between

$Ni_{50}Mn_{25}Al_{25}$ and $Ni_{40}Co_{10}Mn_{25}Al_{25}$. In the original study by Okubo et al. (2011), a clear distinction was made between apparently AFM compounds showing a cusp in the $M(T)$ curves together with a low bulk magnetization and FM compounds that show prototypical FM magnetization curves with large bulk magnetizations.

In this chapter, the $Ni_{50-x}Co_xMn_{25}Al_{25}$ system is revisited by making use of the possibility to adjust perfect B2 order over a large compositional range. Based on the bulk magnetization measurements previously reported by Okubo et al. (2011), neutron powder diffraction measurements are performed in order to study the exact mechanism of the peculiar AFM-FM transition as function of x. The AFM moment of the unit cell, confined to the Mn atoms, is conveniently retrieved from neutron diffraction while the FM moments in the unit cell provide a relatively weak contrast in neutron diffraction and are hence determined via bulk magnetization measurements performed by SQUID magnetometry. Based on the findings, a model for the magnetic structure of B2-ordered $(Ni/Co)_2MnZ$ compounds as a function of the FM exchange interaction strength between Ni/Co and Mn is developed.

For reasons of consistency, in the following the unit cell for all compounds refers to the formula unit X_2YZ in analogy to the $L2_1$-ordered Heusler compounds, even though the unit cell of B2 compounds in principle would be denoted as $XY_{0.5}Z_{0.5}$. Furthermore, in order to describe the alloys' compositions intuitively, the subscripts are written in at. %.

5.2 Sample preparation

As discussed in Chapter 1, cast rods have partially been obtained from the group of Ryosuke Kainuma at Tohoku University, Japan and some of the original sample materials are hence identical to the previous study by Okubo et al. (2011). In this respect, only the $Ni_{50}Mn_{25}Al_{25}$ compound has been freshly prepared for this study as this composition was not comprised in the set of samples by Okubo et al. (2011). Even though samples have been partially provided by the Kainuma group, the crucial steps of the sample preparation were performed by the author of this thesis and will be elucidated in the following given their direct implications for the diffraction results.

In order to provide high quality powder samples for neutron diffraction, the cast rods have to undergo a series of preparation steps. First, due to the casting process, the as-cast rods tend to show segregation which is removed via long time high-temperature solution annealing treatments in the bulk state. Specifically, samples have been solution-annealed for 48 h at 1273 K in quartz ampules in high purity Ar atmosphere with subsequent quenching in iced water. Due to the relatively large sample size of the as-cast rods and the high solution annealing temperature, the amount of quenched-in excess vacancies in the material after quenching is high and presumably spatially inhomogeneous. In order to obtain ideally B2-ordered samples, the solution-annealed rods were subject to a second annealing treatment approximately 50 K above the B2-L2_1 transition temperature followed by quenching in iced water. The annealing temperatures for all compositions are given in Tab. 5.1.

After having adjusted a state of homogeneous B2 order with a presumably low defect density, the rods have been manually crushed and ground to powders with grain diameters $< 125\,\mu$m. For every composition, powder samples with masses between 2.5 and 7.5 g were prepared. Due to the ductility of the material, grinding tends to introduce significant mechanical stresses and strains into the samples, leading to pronouncedly broadened peaks in diffraction experiments. To release the stresses and strains, the powder samples were recovery annealed for 4 h at the last applied annealing temperature as specified in Tab. 5.1. Special care was taken to avoid oxidization of the powder samples. For this purpose, the powder samples have been encapsulated in quartz ampules under high purity Ar atmosphere. Based on X-ray diffraction, a pronounced peak sharpening was observed as a consequence of the recovery annealing treatment. After recovery annealing, all powder samples were suitable for neutron diffraction experiments with the restriction that the explicit introduction of a strain model was necessary to successfully refine the diffraction patterns in Rietveld refinement. To show the conformity of the powder samples with the previously reported bulk samples by Okubo et al. (2011), magnetization measurements have been performed on the powder sample using a SQUID magnetometer. Magnetization measurements for this chapter have been performed in collaboration with Matthias Opel at the Walther-Meißner-Institute for Low Temperature Research of the Bavarian Academy of Sciences and Humanities, Germany.

5.3 Results

5.3.1 Bulk Magnetization measurements

Fig. 5.1 shows bulk magnetization measurements of $\mathrm{Ni}_{50-x}\mathrm{Co}_x\mathrm{Mn}_{25}\mathrm{Al}_{25}$ powder samples for various compositions. Fig. 5.1a depicts $M(T)$ measurements – the upper part of the figure shows all studied compositions while the lower part zooms in on the compositions with a low bulk magnetization. As previously reported by Okubo et al. (2011), the transition from predominantly AFM properties in $\mathrm{Ni}_{50}\mathrm{Mn}_{25}\mathrm{Al}_{25}$ to ideally FM properties in compounds with ≥ 10 at. % Co is revealed also in the powder samples. Additionally, the previously discussed cusp (see Chapter 2), characteristic for AFM order and AFM coupled APD structures, is clearly visible in the $M(T)$ curves up to Co compositions of 5 at. %. Fig. 5.1b shows the temperature derivative of the $M(T)$ curves given in Fig. 5.1a. The existence of an AFM-like

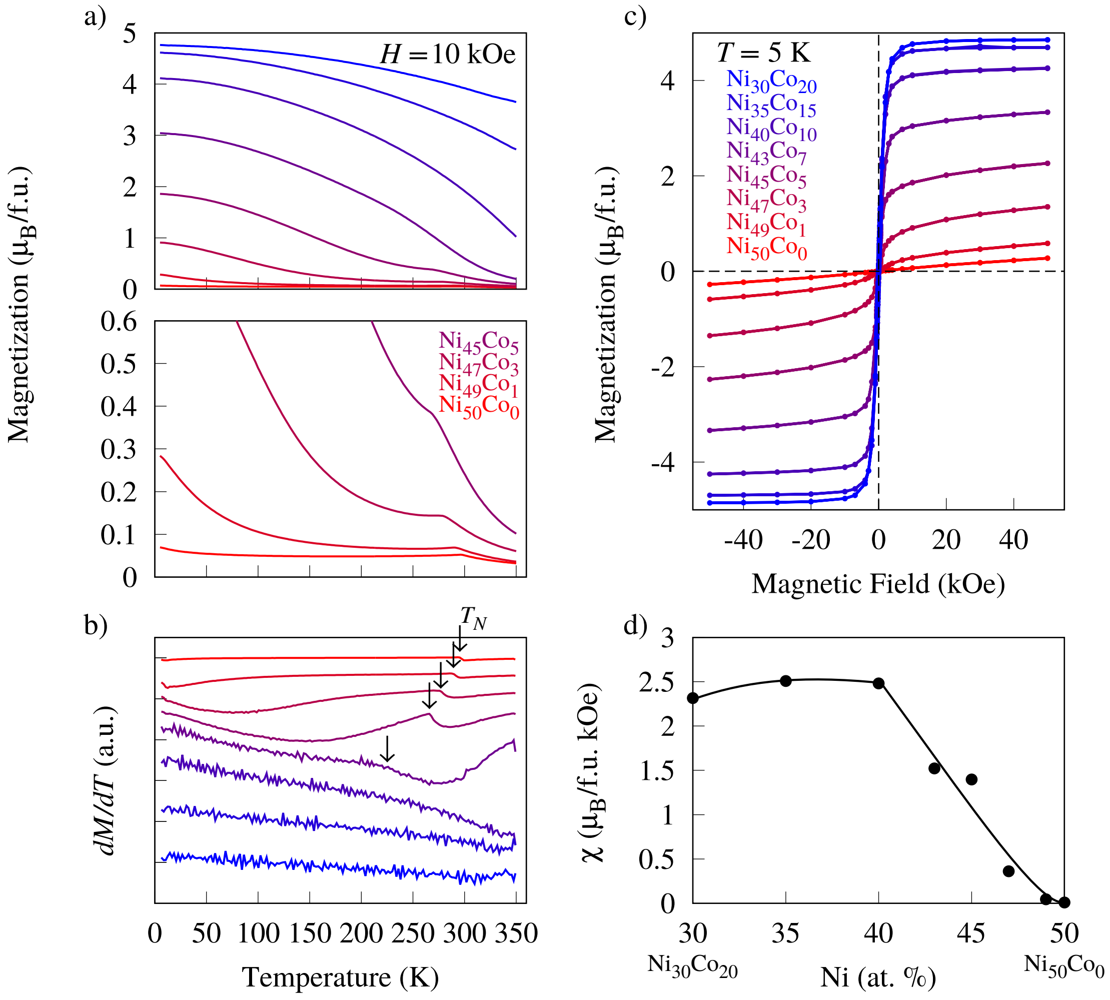

Fig. 5.1 Bulk magnetization measurements of $Ni_{50-x}Co_xMn_{25}Al_{25}$ samples obtained using SQUID magnetometry. a) $M(T)$ measurements under an external field of 10 kOe, b) temperature derivative of the bulk magnetization dM/dT, c) $M(H)$ measurements at 5 K and d) DC susceptibility χ at zero field and 5 K as a function of the alloy composition

magnetic structure is revealed in a characteristic cusp that is observed in all compositions with a Co content of ≤ 7 at. % Co.

In analogy to Fig. 5.1a, Fig. 5.1c shows $M(H)$ measurements at 5 K for various compositions, revealing an increased spontaneous magnetization M_s with increased Co content. M_s values were determined via linearly fitting the high field region of the $M(H)$ curves and calculating the y-axis intercept. The obtained M_s values together with the Néel temperatures T_N as shown in Fig. 5.1b are tabulated in Tab. 5.1. As depicted in Fig. 5.1d, with increased Co content, also the DC susceptibility at zero field χ increases while it is approximately

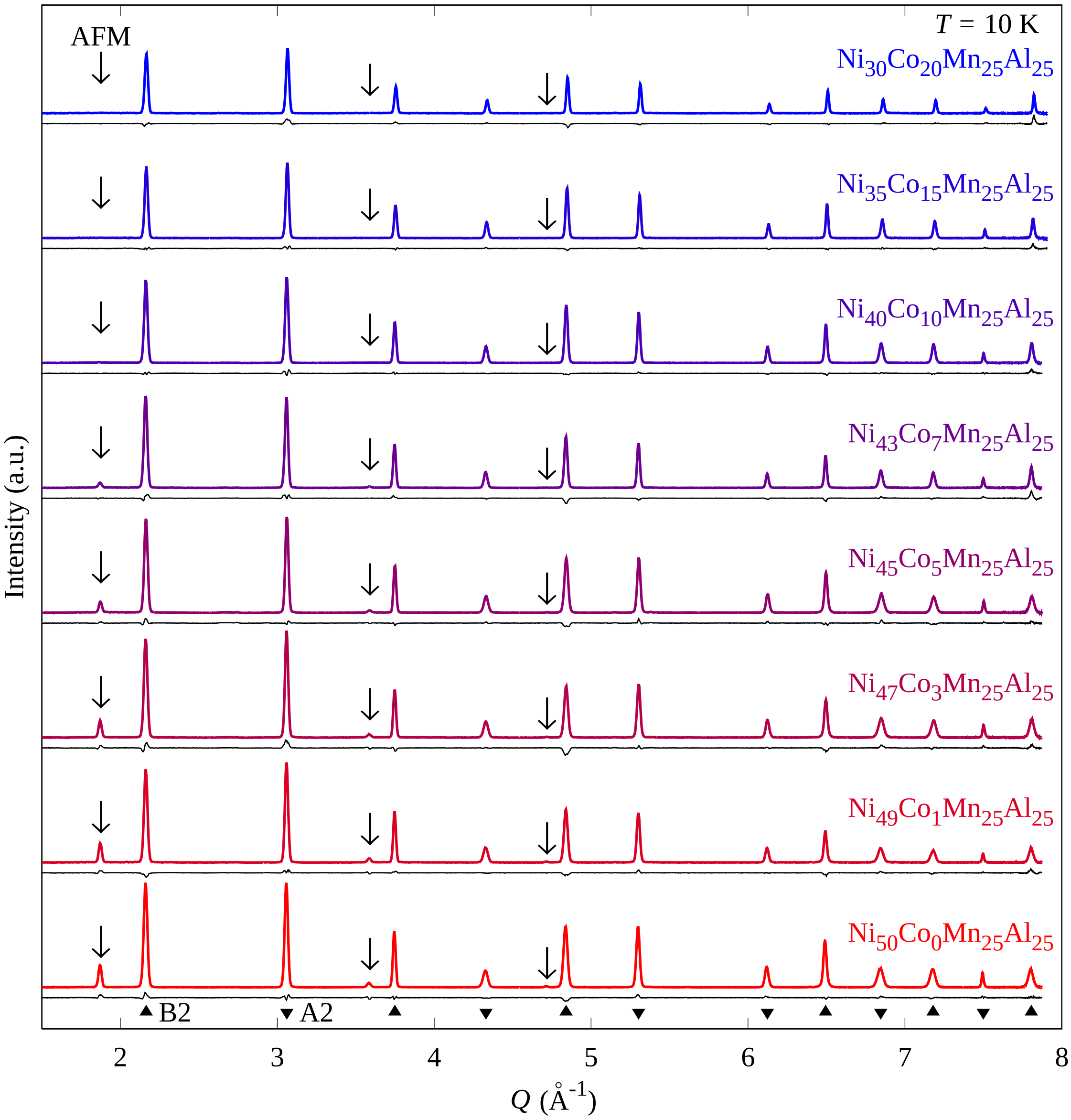

Fig. 5.2 Neutron powder diffraction measurements of $Ni_{50-x}Co_xMn_{25}Al_{25}$ samples at 10 K. The triangles at the bottom of the figure indicate the theoretical peak positions of the nuclear peaks, the arrows indicate the magnetic peaks corresponding to the AFM spin structure. The colored lines represent the measured intensity and the black lines below the diffractograms show the corresponding residues.

constant at Co contents ≥ 10 at. %. The results as presented are in good conformity to the results previously reported by Okubo et al. (2011) for bulk samples.

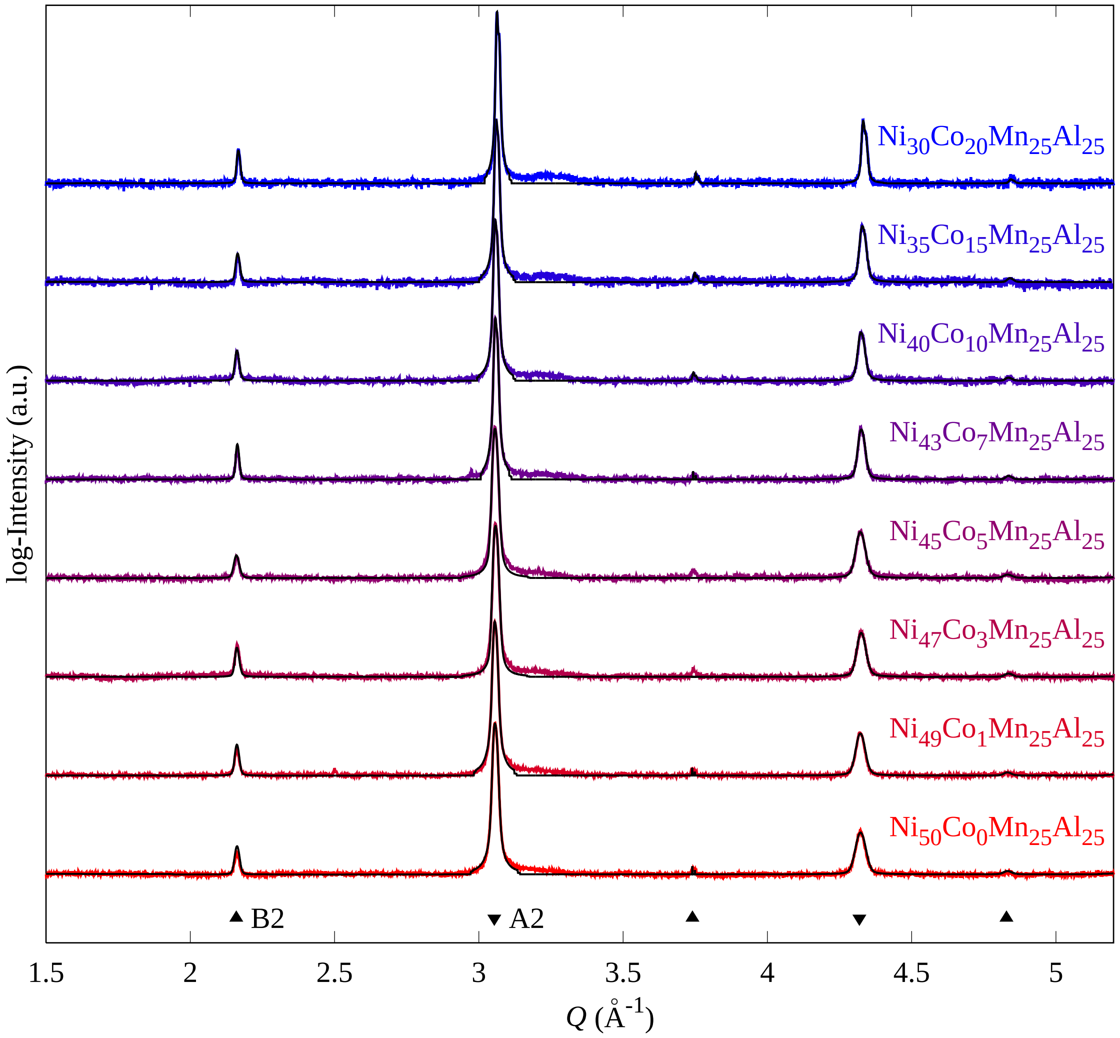

Fig. 5.3 X-ray powder diffraction measurements of $Ni_{50-x}Co_xMn_{25}Al_{25}$ samples at 295 K. The triangles at the bottom of the figure indicate the theoretical peak positions.

5.3.2 Neutron powder diffraction measurements

In order to study the transition from the AFM to the FM structure directly, temperature dependent neutron powder diffraction measurements have been performed at the SPODI high resolution powder diffractometer at the FRM II, Germany. Fig. 5.2 shows neutron diffractograms recorded at 10 K for a series of compositions x of the $Ni_{50-x}Co_xMn_{25}Al_{25}$ system. In the figure, the colored lines represent the measured intensities and the black lines below the diffractograms show the corresponding residues of the Rietveld refinement discussed below. As function of Co content, a number of qualitative features are observed. Evidently, a magnetic superstructure is found at the positions indicated by the black arrows above the diffractograms that is strongly pronounced for $Ni_{50}Mn_{25}Al_{25}$ and vanishes gradually as a function of the Co content. Due to their magnetic nature, the superstructure peaks decay quickly with increasing Q. In contrast, the intensity of the nuclear peaks, whose positions are indicated below the diffractograms, decays much slower with Q. Due to the position of the magnetic superstructure peaks, it is clear that these peaks result from an AFM spin structure. The magnetic peaks are located at exactly those Q values that would also correspond to a nuclear $L2_1$ superstructure. Considering the B2 structure with Ni/Co on the 1a and Mn/Al on the 1b Wyckoff position together with an AFM alignment of the Mn moments, this structure yields a magnetic unit cell resembling the nuclear $L2_1$ unit cell with basically Ni/Co on the 8c, Al/Mn-up on the 4a and Al/Mn-down on the 4b Wyckoff position. Note that the diffractograms are depicted normalized to the refined scale factors, meaning that the intensity of the magnetic peaks can quantitatively be compared in the figure among the different diffractograms over the entire compositional range. Clearly, the last composition showing a magnetic superstructure is $Ni_{43}Co_7Mn_{25}Al_{25}$ while the superstructure is absent in $Ni_{40}Co_{10}Mn_{25}Al_{25}$ and all samples with higher Co content. Further, it is observed that as an overall trend the lattice constant decreases as a function of Co content meaning that the effective size of Co is smaller than the size of Ni. Additionally, it is apparent that with increasing Co content the peaks increase in sharpness, resulting from higher recovery annealing temperatures and consequently lower residual strains of samples with higher structural transition temperatures (see Tab. 5.1).

The neutron diffraction measurements have been complemented by room temperature X-ray diffraction measurements in order to clearly separate nuclear from magnetic features. Fig. 5.3 presents the measured X-ray diffractograms (colored lines) for a series of compositions on a logarithmic y-scale together with the Rietveld refined diffractograms assuming a B2 structure with the nominal compositions (black lines). Clearly, the Rietveld refined curves describe the measured data excellently. The clear absence of $L2_1$ superstructure peaks indicates that indeed the samples are all perfectly B2-ordered.

In order to refine the neutron diffractograms, especially considering a relatively complex magnetic structure consisting presumably of AFM and FM components together with a disordered nuclear structure, it is necessary to confine the large parameter space by making some educated assumptions and introducing a model for the magnetic structure:

- First, it is assumed that indeed the nuclear structure is a B2 structure with Ni/Co strictly occupying the 1a site and Mn/Al strictly occupying the 1b site. Considering previous studies of X_2MnAl compounds as well as the absence of $L2_1$ superstructure peaks both in neutron and X-ray diffraction for all compounds justifies this initial assumption.

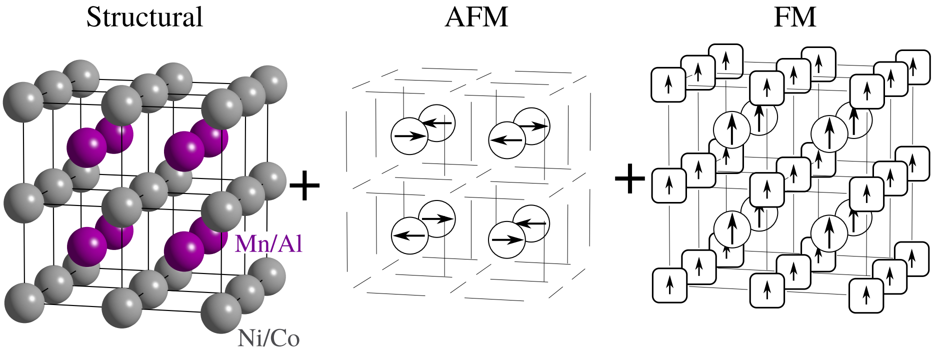

Fig. 5.4 Structural and magnetic models used for Rietveld refinement of the $Ni_{50-x}Co_xMn_{25}Al_{25}$ samples. The left panel shows the B2 structure, while the middle panel depicts the AFM spin structure and the right panel visualizes the FM spin structure.

- Next, based on WDS measurements presented in in Chapter 1, the samples' composition is fixed to the nominal composition.

- For the magnetic structure, it is assumed that the magnetic moment on Mn can be described in a Heisenberg picture, meaning that the length of the Mn spin stays constant as a function of composition. Considering the experimental observation of a gradually decreasing AFM moment with increasing Co content, this leads to the magnetic model that the Mn magnetic moments in intermediate compositions would be canted, which can be translated via a simple vector decomposition in a FM and AFM component of the Mn moment.

- Based on previous studies by Galanakis and Şaşıoğlu (2011) as well as the above presented magnetization measurements, it is assumed that $Ni_{50}Mn_{25}Al_{25}$ is entirely AFM with no FM component of the Mn spin. Hence, $Ni_{50}Mn_{25}Al_{25}$ is used to determine the length of the Mn spin. For all other compositions, the FM contribution can be calculated based on the refined AFM Mn moment.

- Furthermore, it is assumed that the FM moment on Ni is induced by the surrounding Mn moments as introduced in Chapter 2. In the completely FM structure, it takes on a value of approximately 0.3 μ_B/f.u. following the density functional theory (DFT) calculations reported by Galanakis and Şaşıoğlu (2011).

- Finally, it is assumed that the magnetic moment on Co is constant with a value of approximately 1.0 μ_B/f.u. as calculated by Kanomata et al. (2009) for the chemically similar but entirely FM and $L2_1$-ordered $Ni_{50-x}Co_xMn_{25}Ga_{25}$ system.

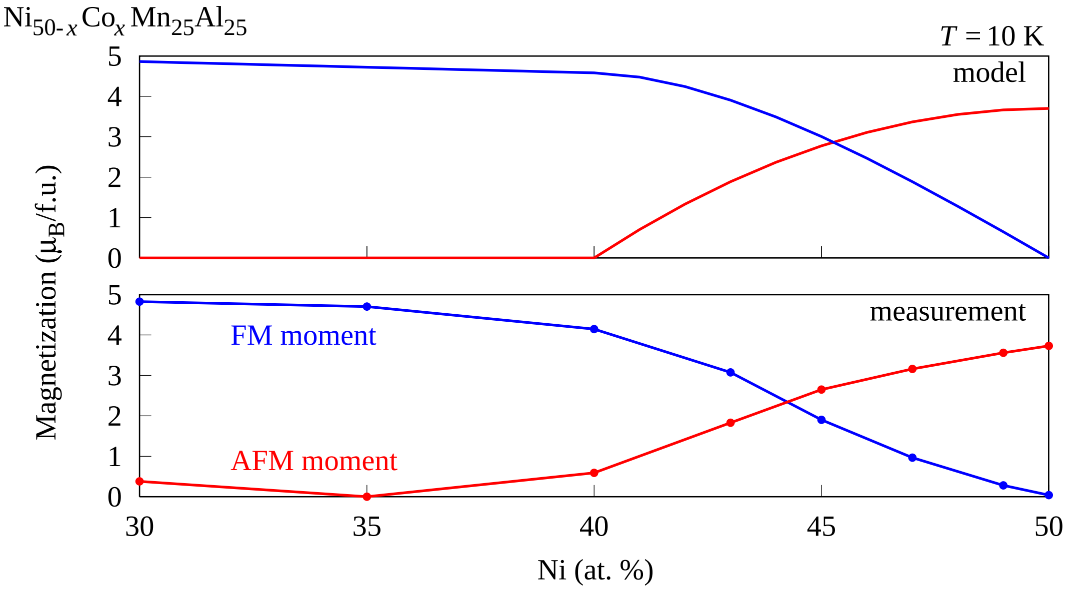

Fig. 5.5 Experimental observation of the AFM and FM moments of the unit cell (bottom) together with the comparison to the theoretical model (top).

Rietveld refinement has been performed using the FullProf suite (Rodriguez-Carvajal, 1990, 1993; Rodriguez-Carvajal and Roisnel, 1998). For every composition, the respective AFM moment was refined. With the obtained AFM moment, based on the above stated assumptions, the FM Mn and Ni/Co moments were calculated and the FM structure was manually incorporated iteratively during the refinement process. Fig. 5.4 visualizes the nuclear and magnetic phases considered in the refinement process. On the left hand side, the nuclear structure model is shown, specifically a B2 structure with Ni/Co on one sublattice (Wyckoff site 1a) and Mn/Al on the other sublattice (Wyckoff site 1b). The middle and right panel show models for the magnetic structure. Specifically, in the middle, the AFM component of the Mn moments and on the right the FM structure with a FM component of the Mn moment and a mean-field FM moment on Ni/Co is depicted.

As can be seen in Fig. 5.2 and Fig. 5.3, employing Rietveld refinement based on the presented nuclear and magnetic model, the diffractograms can excellently be described. Tab. 5.1 summarizes the results of the refinement, specifically, it tabulates the refined AFM moment on Mn as well as the lattice constants at 5 K and 300 K as obtained from neutron diffraction measurements and at 295 K as obtained by X-ray diffraction measurements. Note that the intensity contribution of the FM phase is quite weak and accounts for less than 20 % of the peak intensity even for the peak with the strongest FM signature in the extreme case of an ideally FM sample. For all other peaks and in all other compositions, especially the ones with an AFM contribution, the intensity of the FM contribution is much weaker and

Alloy	temperature recovery annealing	refined Mn AFM moment (μ_B/f.u.)	calculated Mn FM moment (μ_B/f.u.)	calculated $(Ni/Co)_2$ FM moment (μ_B/f.u.)	spontaneous magnetization M_s (μ_B/f.u.)	T_N (K)	a (Å) (300 K) *(295 K)*	a (Å) (10 K)
$Ni_{50}Co_0$	823 K	3.73(2)	0	0	0.04	295.3	2.91377(3) *2.9098(1)*	2.90436(1)
$Ni_{49}Co_1$	823 K	3.56(3)	1.11	0.21	0.28	289.0	2.91169(3) *2.9101(2)*	2.90335(2)
$Ni_{47}Co_3$	823 K	3.16(4)	2.00	0.42	0.97	276.8	2.90969(4) *2.9072(2)*	2.90176(2)
$Ni_{45}Co_5$	823 K	2.62(4)	2.65	0.58	1.90	265.8	2.90904(3) *2.9085(3)*	2.90157(2)
$Ni_{43}Co_7$	873 K	1.83(5)	3.25	0.72	3.08	225.0	2.90964(4) *2.9074(1)*	2.90257(2)
$Ni_{40}Co_{10}$	873 K	0.59(8)	3.68	0.87	4.15	-	2.90805(3) *2.9068(1)*	2.90168(1)
$Ni_{35}Co_{15}$	873 K	0.00(34)	3.73	1.02	4.70	-	2.90469(3) *2.9035(2)*	2.89858(1)
$Ni_{30}Co_{20}$	923 K	0.480(15)	3.73	1.16	4.83	-	2.90248(5) *2.9007(1)*	2.89628(2)

Table 5.1 Magnetic properties of $Ni_{50-x}Co_xMn_{25}Al_{25}$ compounds as retrieved from neutron powder diffraction and bulk magnetization measurements. AFM moments of the unit cell were obtained via Rietveld refinement of samples measured at 10 K. From the refined AFM moments, FM Mn and $(Ni/Co)_2$ moments were calculated as described in the text and iteratively included in the refinement process. Néel temperatures T_N and FM moments of the unit cell were obtained from $M(T)$ and $M(H)$ SQUID measurements. Lattice constants were obtained from Rietveld refinement of neutron diffraction data and X-ray diffraction data (italic font).

the refinement of the FM moments is challenging. Consequently, the description of the FM contribution has little influence on the quality of the refinement. For this reason, the FM moment was manually set in the refinement process instead of leaving it a free parameter.

The AFM Mn moment σ_{AFM} and spontaneous bulk magnetization values M_s measured by neutron diffraction and magnetization measurements, respectively, are in the following compared to the above stated model that the Mn moment is Heisenberg-like and canted. In this respect, the bulk magnetization values are taken as the experimentally determined FM moments of the unit cell.

Fig. 5.5 shows the experimental results for the AFM and FM moments of the unit cell (lower panel) as well as the phenomenological description of the composition dependent AFM moments and the calculated FM moments applying the introduced model (upper panel). Specifically, the FM moments are calculated via

$$\sigma_{\text{FM}} = \sqrt{\sigma_{\text{Mn}}^2 - \sigma_{\text{AFM}}^2} + \sigma_{\text{Ni}} \cdot \frac{\sqrt{\sigma_{\text{Ni}}^2 - \sigma_{\text{AFM}}^2}}{\sigma_{\text{Ni}}} \cdot \frac{50 - x}{50} + \sigma_{\text{Co}} \cdot \frac{x}{50} \tag{5.1}$$

where σ_{Mn} is the overall Mn moment determined as $3.73\,\mu_{\text{B}}$/f.u., σ_{AFM} is the experimentally determined AFM Mn moment, σ_{Ni} is the maximal Ni moment in the fully FM structure assumed as $0.3\,\mu_{\text{B}}$/f.u., σ_{Co} is the Co moment with a value of $1.0\,\mu_{\text{B}}$/f.u. x denotes the Co content in at. % as given in the sum formula $\text{Ni}_{50-x}\text{Co}_x\text{Mn}_{25}\text{Al}_{25}$. In general, the model closely resembles the experimentally observed features. However, there are some deficiencies at low Co contents where due to the square root dependence, small deviations of the experimentally observed AFM moment lead to a fast increase in the calculated FM moment that is not observed in the experiment. Apart from this, the model of canted Mn moments that are collinear AFM in $\text{Ni}_{50}\text{Mn}_{25}\text{Al}_{25}$ and gradually turn with increased Co content to a FM alignment describes the experimentally observed situation convincingly.

With the here presented interpretation of canted Mn moments as function of Co composition, a new interpretation for magnetic properties in B2-ordered NiMn-based Heusler compounds is provided. In the pertinent literature, the magnetic properties of these compounds were either described as AFM or FM while variations e.g. in the FM properties were mainly ascribed to changes of the magnetic moments on the different lattice sites. As Kanomata et al. (2009) demonstrate for the related L2_1-ordered $\text{Ni}_{50-x}\text{Co}_x\text{Mn}_{25}\text{Ga}_{25}$ system, these changes indeed exist. For instance, it is found that $\text{Ni}_{50-x}\text{Co}_x\text{Mn}_{25}\text{Ga}_{25}$ compounds on the Co-rich side of the phase diagram follow the so-called Generalized Slater Pauling (GSP) rule while the spontaneous magnetization diverges from the GSP rule on the Ni-rich side. In this respect, Kanomata et al. (2009) demonstrated via DFT calculations that the magnetic moments of Mn, Ni and Co change as a function of composition. Yet, small changes in

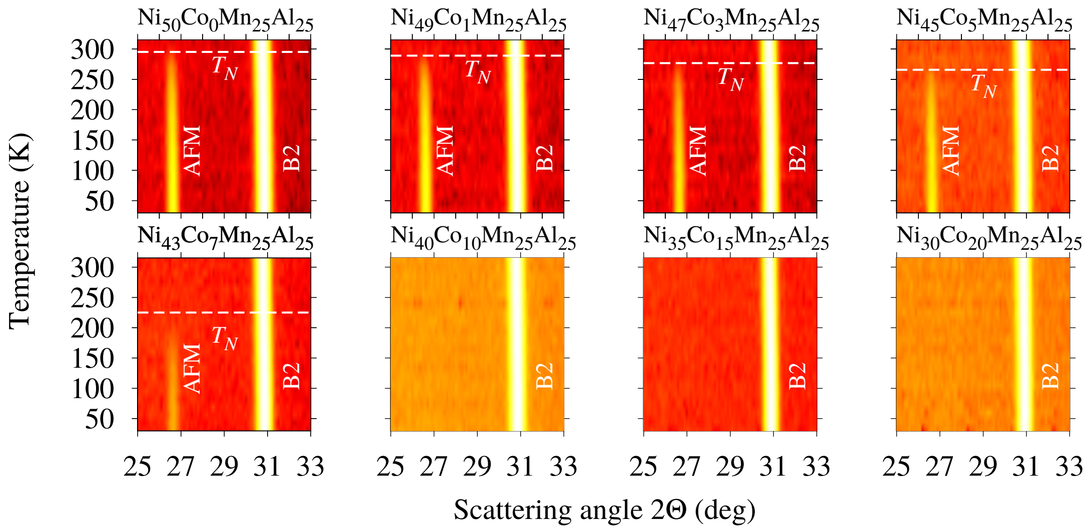

Fig. 5.6 Waterfall plot of the temperature dependent neutron diffraction patterns covering a scattering angle 2Θ from 25 to 33°. Two Bragg peaks are visible, the first one belonging to the AFM structure and the second one being a structural peak originating from to the B2 contrast between lattice site 1a and 1b. The white dashed lines represent the Néel temperatures T_N as determined from $M(T)$ measurements.

the size of the magnetic moment fail to explain the transition from AFM to FM properties in the here investigated $Ni_{50-x}Co_xMn_{25}Al_{25}$ compounds. In fact, transferring the findings by Kanomata et al. (2009) to $Ni_{50-x}Co_xMn_{25}Al_{25}$ compounds, only minor changes of the magnetic moments due to changes in the electronic structure are expected for the studied composition range. The magnitude of these compositional variations in the magnetic moments are expected to be in the order of 10 %. Hence, even though presumably superimposed with the canting of the Mn moments, it is the non-collinear magnetic structure that predominantly explains the magnetic properties of B2-ordered $(Ni/Co)_2MnAl$ Heusler compounds. However, certainly, the deviations between the presented FM moments calculated with the introduced model and the experimentally observed M_s values can at least partially be explained by these changes in the size of the magnetic moments which are explicitly not accounted for by the introduced model.

Temperature dependent neutron diffraction

In the following, temperature dependent neutron diffraction measurements of a series of $Ni_{50-x}Co_xMn_{25}Al_{25}$ compounds are presented. Specifically, neutron diffraction patterns have been recorded at temperatures between 15 K and 315 K with a step width of 15 K. The results are shown in Fig. 5.6 as 2D waterfall plots for scattering angles 2Θ between 25

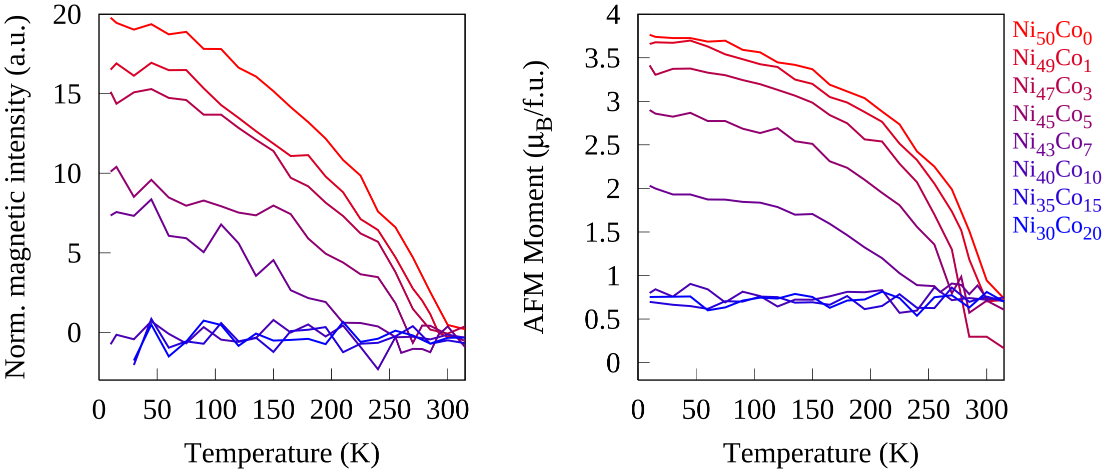

Fig. 5.7 Temperature dependent AFM magnetic intensity (a) and refined AFM moment (b) as obtained from Rietveld refinement for various compositions x in $Ni_{50-x}Co_xMn_{25}Al_{25}$.

and 33°, comprising the first magnetic peak belonging to the AFM structure and the first (predominantly) nuclear peak belonging to the B2 peak family resulting from the diffraction contrast between the Wyckoff 1a and 1b site. Clearly, a decrease of the magnetic intensity is observed as function of temperature while the nuclear peak, as reference, stays relatively constant in intensity. From the plots, the Néel temperature T_N for the AFM structures can be determined. As depicted by the white dashed lines, T_N values retrieved from neutron diffraction agree well with the T_N values estimated from the cusp in the $M(T)$ curves as presented in Fig. 5.1a–b. Interestingly, as previously reported by Okubo et al. (2011) and also discussed in the beginning of this chapter, T_N decreases as a function of Co content. This is especially pronounced close to the compositional transition between the canted AFM-like magnetic structure and the collinear FM structure. Specifically, $Ni_{43}Co_7Mn_{25}Al_{25}$ shows a T_N of 225 K – around 70 K lower than T_N in $Ni_{50}Mn_{25}Al_{25}$. Note that in bulk magnetization measurements, the AFM contribution in compounds with mainly FM properties is hardly visible while neutron diffraction still excellently resolves the AFM spin structure. Compounds with $\geq$ 10 at. % Co show perfectly FM properties and no AFM superstructure is visible in the diffraction patterns. Hence, these compositions correspond to a collinear FM spin structure with Curie temperatures T_C outside the probed temperature range. These findings are in good agreement with the results reported by Okubo et al. (2011) where T_C was stated as approximately 340 K, 430 K and 530 K for $Ni_{40}Co_{10}Mn_{25}Al_{25}$, $Ni_{35}Co_{15}Mn_{25}Al_{25}$ and $Ni_{30}Co_{20}Mn_{25}Al_{25}$, respectively.

Additionally, all temperature dependent diffraction patterns have been Rietveld-refined as described above. The background has been modeled with a 6^{th} order polynomial. From the refinements, temperature dependent lattice constants and AFM moments have been retrieved.

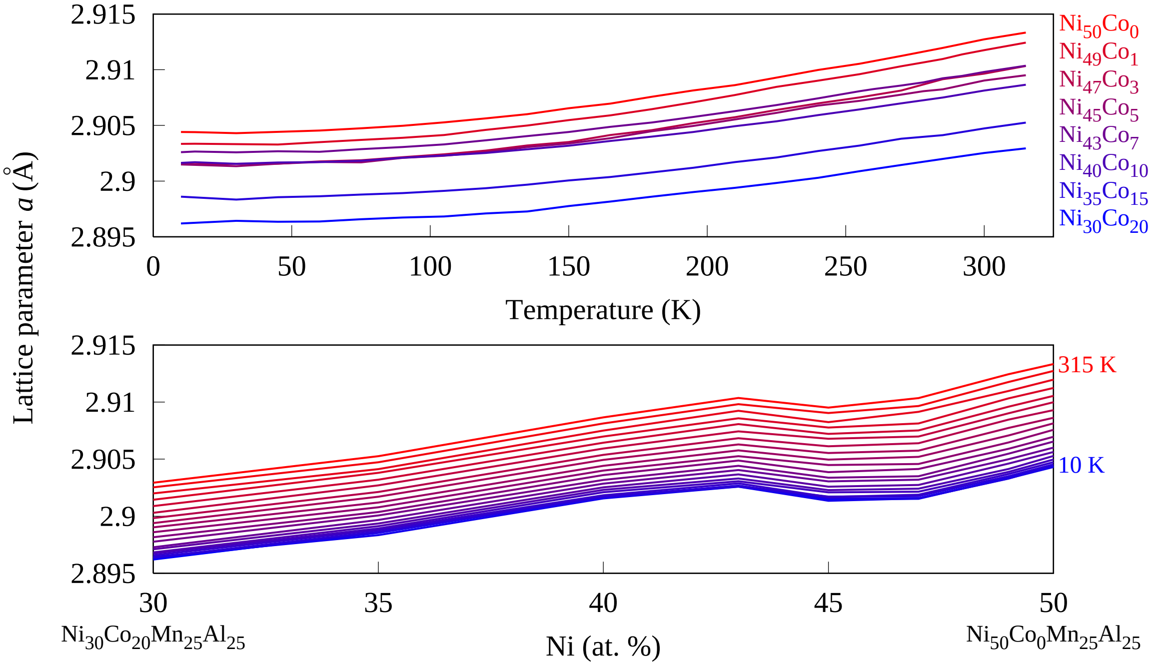

Fig. 5.8 Temperature dependent lattice constant a for various compositions (a) and composition dependent lattice constant for various temperatures (b) recovering the transition from the AFM to the FM structure with increasing Co content.

Fig. 5.7 shows in the left panel the temperature dependent AFM peak intensity as obtained via subtracting the background and integrating over the first two magnetic peaks belonging to the AFM structure. In the right panel, the refined AFM moment on Mn is depicted. Note, the moment has a square root dependency of the intensity. Hence, a refined magnetic moment of 0.5 μ_B/f.u. corresponds to approximately a factor of 60 lower scattering intensity than the maximal AFM moment of 3.73 μ_B/f.u.. As a result, the magnetic moment in the refinement does not actually go to zero but remains also for the FM compositions at approximately 0.6-0.8 μ_B/f.u. which is explained by an imperfect background description and the resulting refinement of a very small magnetic intensity into the background intensity, even if no AFM peak is in fact present. Besides this, the transition temperatures as already qualitatively observed in Fig. 5.6 are nicely revealed in the quantitative analysis.

Fig. 5.8 depicts the temperature and composition dependent lattice parameters a determined by neutron powder diffraction. In the upper panel of Fig. 5.8, the lattice parameters for all 8 investigated compositions are shown as a function of temperature from 10 K to 315 K. As can be seen, the thermal expansion is similar in all compounds. The transition from the AFM phase to the paramagnetic phase is not visible in the lattice constant. Note that the retrieved lattice constants are in good agreement with the lattice constants reported

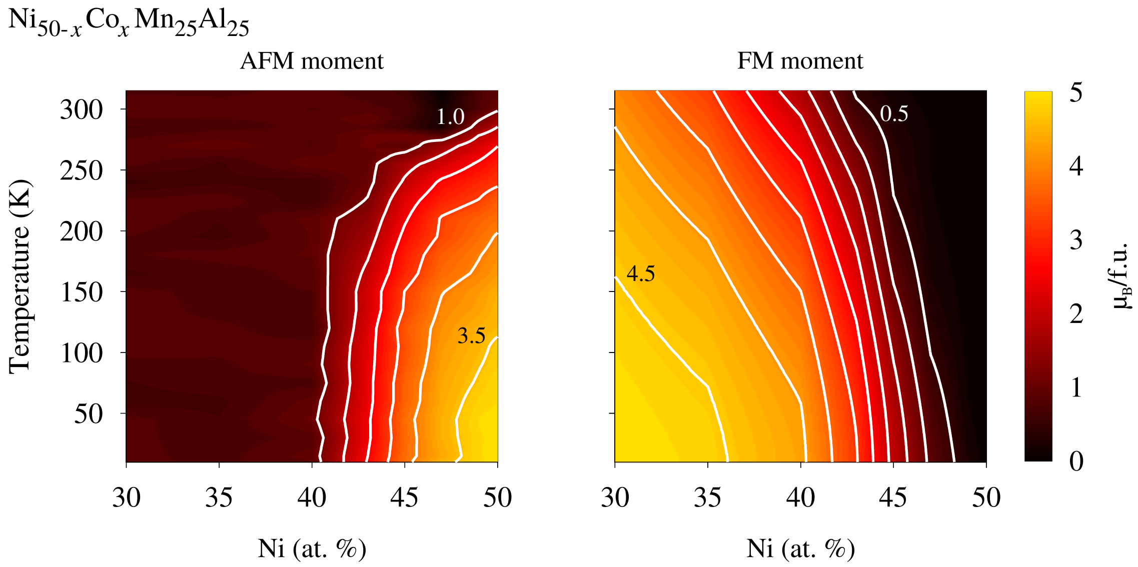

Fig. 5.9 AFM (left) and FM (right) magnetic moment as a function of composition and temperature. Contour lines are drawn in steps of 0.5 μ_B/f.u.

in the pertinent literature. Specifically, Buschow and van Engen (1981); Okubo et al. (2011); Ziebeck and Webster (1975) find lattice parameters for Ni_2MnAl at room temperature of approximately 2.912 Å, 2.912 Å and 2.911 Å, respectively. For Co_2MnAl, Buschow and van Engen (1981); Umetsu et al. (2008) report a lattice constant at room temperature for a B2-ordered compound of 2.875 Å and 2.878 Å which confirms the general trend of a decreasing lattice constant with increasing Co content. Additionally, Okubo et al. (2011) report composition dependent lattice constants in good conformity to the here presented results.

In contrast to the temperature dependent behavior, the dependency of the lattice constant from the alloy composition is less trivial. The lower panel of Fig. 5.8 shows the determined lattice parameters as a function of Ni content at all measured temperatures. Evidently, the transition from the AFM to the FM spin structure influences the lattice parameter. Surprisingly, this is the case at all temperatures, also above T_N where the samples with low Co content are already in a paramagnetic state. Referring to Fig. 5.1a, it is visible that the T_C of the purely FM compounds is significantly above the maximal temperatures reached during the neutron diffraction experiments, meaning that even at the highest temperatures, the compounds with high Co contents are FM. Consequently, it is concluded that the FM spin alignment expands the lattice which acts against the general trend of the Co substitution decreasing the lattice parameter. Hence, with an increasingly FM structure with increasing

Co content, an expansion of the lattice is observed before, for Co contents larger than 7 at. %, the overall trend of a decreasing lattice parameter is followed again.

Finally, the analysis presented in Fig. 5.5 can be extended to a temperature dependent description of the AFM and FM moments of the unit cell. In this respect, the temperature dependent AFM moments as retrieved from neutron powder diffraction as well as the composition dependent $M(T)$ curves were interpolated with respect to temperature and composition. The results are depicted in Fig. 5.9. As can be seen, first of all, the model of canted Mn moments is further supported by the 2D analysis. The AFM structure at low Co contents transforms gradually into a FM structure at high Co contents while the overall FM moment of the unit cell comprises the FM component of the Mn moments and the FM moment on Ni/Co. Consequently, the maximal FM moment (at high Co contents) is approximately 1 μ_B/f.u. higher than the maximal AFM moment (at low Co contents). Furthermore, the decreasing T_N with increasing Co content discussed before is clearly observed in the the 2D analysis.

5.4 Conclusions

The results presented in this chapter reveal that the overall magnetic properties of B2-ordered Ni_2MnZ Heusler compounds with partial Co substitution for Ni are primarily determined by a non-collinear arrangement of the Mn magnetic moments. This can be expressed by an effective FM and AFM contribution of the Mn moment. The exact magnetic structure, i.e. the angle between Mn spins can conveniently be tailored via the Ni/Co ratio and hence the strength of the FM exchange interaction in the system.

Fig. 5.10 shows a schematic drawing of the magnetic structure as function of Co content. On the left hand side, the purely AFM structure is depicted as it is observed in $Ni_{50}Mn_{25}Al_{25}$. Due to induced magnetic moments on Ni, the Ni/Co lattice is not carrying a magnetic moment. With increasing Co content, the Mn magnetic moments start canting (middle panel) and develop a FM component. At the same time, due to the FM component of the Mn spins, a magnetic moment is induced on Ni and also the presence of Co, with a constant magnetic moment, additionally increases the magnetic moment on the Ni/Co lattice. Finally, when the Mn moments have turned completely to a collinear FM arrangement, as depicted in the right panel of the figure, the moment on the Ni/Co lattice is large with Ni carrying a moment of around 0.3 μ_B/f.u. and Co carrying a moment of approximately 1.0 μ_B/f.u.

As an outlook, the here presented investigation can easily be transferred to partially $L2_1$-ordered $(Ni/Co)_2MnZ$ compounds, which would be a perfect model system to study the magnetic coupling across APB (similar to Chapter 4) as function of the FM interaction in the

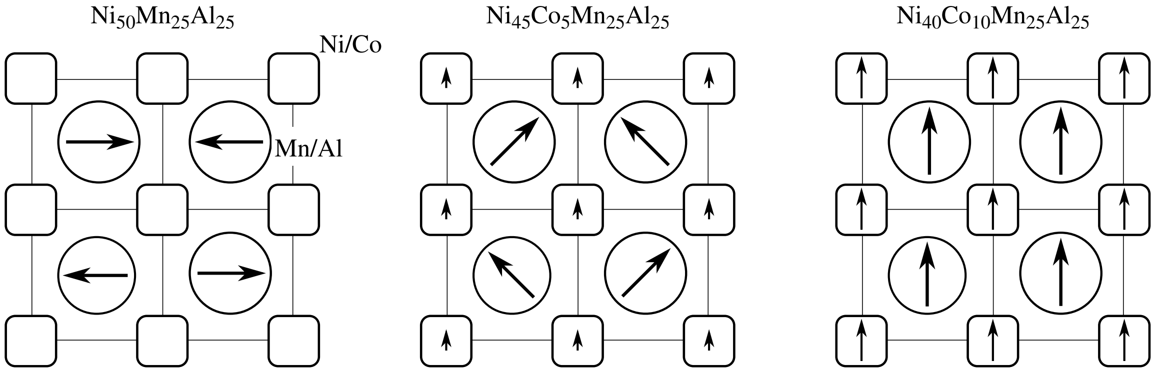

Fig. 5.10 Schematic drawing of the spin structure in $Ni_{50-x}Co_xMn_{25}Al_{25}$ as function of the Co content, starting on the left with $Ni_{50}Mn_{25}Al_{25}$. The spin structure is a 2D representation of the 3D unit cell. The depiction is to be understood as a front view of the magnetic unit cell.

system. Even though being more complicated with respect to the local chemical structure, there is a good indication that the overall features observed for the B2-ordered compounds will be transferable to the magnetic coupling of APD. Yet, clearly, the compositional range where the transition from AFM coupling across APBs to an ideally FM arrangement occurs might be different from the transition observed between the AFM and FM structure in the B2-ordered compounds.

Chapter 6

Ordering tendencies and electronic properties in quaternary Heusler derivatives

This chapter is a textual citation of the recently published first author paper by the author of this thesis (Neibecker et al., 2017) in the peer-reviewed journal Physical Review B of the American Physical Society (APS). All text and figures are taken from this publication, only the citation style and the layout has been adjusted to fit the style of this thesis. In the following, a summary of the work is given, highlighting the individual contribution of the author of this thesis to the publication.

The cited publication reports on phase stabilities and ordering tendencies in the quaternary full-Heusler compounds NiCoMnAl and NiCoMnGa employing experimental methods such as in-situ neutron powder diffraction, calorimetric measurements and magnetization measurements as well as theoretical methods such as density functional theory (DFT) calculations. Both NiCoMnAl and NiCoMnGa have been proposed to adopt half-metallic properties in their fully ordered Y structure (Alijani et al., 2011b; Halder et al., 2015), yet, the actual ordering tendencies in both systems have never been systematically investigated. The presented results reveal a strong tendency for $L2_1$ order in NiCoMnGa with disorder on the Ni-Co sublattice and order on the Mn-Ga sublattice while NiCoMnAl was observed to have a B2 ordering tendency with a pronounced disorder on both the Ni-Co and the Mn-Al sublattices in all experimentally feasible heat treatment conditions. Furthermore, it was found that the inherently disordered NiCoMnAl compound is very sensitive to low temperature annealing treatments, resulting in the formation of incipient order as evidenced by an increase of the magnetic transition temperature. NiCoMnGa in contrast shows a very high degree of $L2_1$ order already after quenching and consequently, hardly any response to low temperature annealing treatments was observed. DFT calculations were used to study the thermodynamic phase stabilities of both compounds as well as the order-dependent electronic density of states. A near half-metallic pseudo-gap was found for NiCoMnGa and NiCoMnAl in the fully ordered Y structure while the pseudo-gap was absent in all disordered structures. Further, the Y structure was observed to be unstable with respect to a fully ordered tetragonal structure with alternating Ni-Co layers. Consequently, this tetragonal structure was proposed as the new ground state structure for both compounds.

The author of this thesis is accountable for all experiments presented and discussed in the cited publication. Specifically, the author prepared all samples and conducted the neutron diffraction, calorimetric and magnetization measurements. Furthermore, the author of this thesis is the primary author of the publication, meaning that he composed the structure of the document, primarily wrote the *Introduction* section, the *Macroscopic properties* section, the *Neutron diffraction* section, the *Conclusions* and the experimental parts of the *Supporting Information*. DFT calculations were performed by Markus Gruner from the University of Duisburg-Essen, Germany who also primarily wrote the *First-principles calculations* section of the publication as well as the computational parts of the *Supporting information*.

6.1 Introduction

6.1.1 Motivation and Scope

The class of Heusler alloys, with the ternary system Cu_2MnAl as the prototypical representative (see Heusler, 1903), hosts a variety of systems displaying intriguing properties (for a recent review see Graf et al., 2011). For instance, the latent structural instability in the magnetic Ni_2Mn-based compounds gives rise to significant magnetic shape memory (Sozinov et al., 2002) and magnetocaloric (Krenke et al., 2005) effects. On the other hand, they can also display attractive properties that are directly related to their electronic configuration, with the technique of spintronics, which relies on the detection and manipulation of spin currents, as an example. In a magnetic tunnel junction for instance, the achievable tunneling magnetoresistive effect and thereby the miniaturization of components depends on the spin polarization of the conduction electrons in the electrodes (Jullière, 1975). As a consequence, half-metallic materials, which have a 100% spin polarization due to a band gap at the Fermi level in one spin channel, are highly sought after and currently the focus of both theoretical and experimental investigations.

While the first half-metal identified by theoretical calculations in 1983 by de Groot et al. (1983) was the half-Heusler compound NiMnSb of $C1_b$ structure, also in full-Heusler alloys with $L2_1$ structure half-metallic properties have been predicted (Fujii et al., 1990; Ishida et al., 1982) and experimentally observed (Jourdan et al., 2014). Recently, also a large number of quaternary Heusler derivatives, among them NiCoMnAl (Halder et al., 2015) and NiCoMnGa (Alijani et al., 2011b), have been suggested by *ab initio* calculations to be half-metals in their fully ordered Y structure (Özdoğan et al., 2013). Half-metallic properties in the $Ni_{2-x}Co_xMnAl$ (Okubo et al., 2011) and $Ni_{2-x}Co_xMnGa$ (Kanomata et al., 2009) systems have additionally been proposed for the Co-rich side of the respective phase diagrams on the basis of magnetization measurements via the Generalized Slater-Pauling rule. It is obvious that the degree of chemical order will have direct consequences for the half-metallic properties of these systems. However, the connection between atomic order, segregation and functional properties has also been established for the magnetocaloric and metamagnetic shape memory effects, (Barandiaran et al., 2013; Recarte et al., 2012; Singh et al., 2011), ferroic glasses (Monroe et al., 2015) and the recently reported shell-ferromagnetism in off-stoichiometric Heusler compounds (Çakır et al., 2016).

In assessing the application potential of a given material following from its electronic structure, theoretical and experimental investigations have contrasting characteristics: in *ab initio* calculations, the distribution of electronic charge is the fundamental quantity that is considered, which depends in principle only on the positions of the ions and their atomic numbers. From this, properties like total energies, magnetic moments and forces on the ions are derived, and different structures can be compared in terms of their total energies. Chemical disorder can be handled very efficiently in terms of the coherent potential approximation (see, for a recent review, Ruban and Abrikosov, 2008), which, however, does not provide an easy way to account for ionic relaxations. Explicit calculations of disordered structures with randomly distributed atoms in larger super-cells are much more involved and numerically intensive. Thus, for practical reasons often an ordered configuration is assumed to be representative. On the other hand, in experiments the appropriate state of order as determines the application potential can be realized easily, while the determination of aspects of the electronic structure is often quite hard, which especially applies for the spin polarization. Thus, it seems indicated to combine the respective strengths of experiment and theory, which is what we set out to do in this paper. Specifically, in the systems of NiCoMnAl and NiCoMnGa we study the degrees of equilibrium long-range order and the associated order/disorder phase transitions by *in situ* neutron diffraction, and the kinetics of order relaxation during isothermal annealing by way of its effect on magnetization and Curie temperature. Further, we perform *ab initio* calculations on different ordered and disordered structures to determine the associated electronic structures as well as ordering energies. As we will show, these calculations imply that among the realistic candidates only the hitherto assumed Y ordering displays a large spin polarization, but does not correspond to the actual ground state. In addition, the associated ordering energies are small, which explains the experimentally observed stability of disorder among Ni and Co.

6.1.2 States of order in quaternary Heusler derivatives

To facilitate the discussion of the different ordered quaternary structures and their relations later in this article, we enumerate here the structures, define the nomenclature and summarize the pertinent knowledge on their ternary parent compounds.

Heusler alloys in the strict sense of the word are ternary systems of composition X_2YZ displaying $L2_1$ order, which is defined by the space group 225 ($Fm\bar{3}m$) with inequivalent occupations of the Wyckoff positions 4a, 4b and 8c. Typically, X is a late transition metal occupying preferentially 8c, while an early transition metal Y and a main-group metal Z occupy the other two sites (Graf et al., 2011), with Cu_2MnAl as the prototypical representative.

Ni_2MnGa conforms to above definition and displays a stable $L2_1$ phase at intermediate temperatures.[1] Around 1053 K it shows a second-order disordering transition to the B2 (CsCl) structure (Sánchez-Alarcos et al., 2007), corresponding to a mixing of Mn and Ga, that is, it acquires space group 221 ($Pm\bar{3}m$) with Wyckoff position 1a occupied preferentially by Ni, while Mn and Ga share position 1b. This partial disordering can be understood by the observation that B2 order, i.e., the distinction between Ni on the one hand and Mn and Ga on the other hand, is stabilized by nearest-neighbor interactions on the common bcc lattice, while the ordering between Mn and Ga corresponding to full $L2_1$ order can only be effected by the presumably weaker next-nearest-neighbor interactions. Indeed, in Ni_2MnAl only the B2 state or at the most very weak $L2_1$ order can experimentally be observed (Acet et al., 2002). In both systems the B2 state is stable up to the melting point, that is, there is no transition to the fully disordered bcc state. In the Co-based systems, the situation is remarkably similar, with well-developed $L2_1$ order in Co_2MnGa and only B2 order in Co_2MnAl (Webster, 1971).

It seems probable, and is indeed corroborated by our experimental observations to be reported below, that the behavior of the quaternary systems NiCoMnGa and NiCoMnAl can be traced back to their ternary parent compounds. The most plausible candidates of ordered structures following this reasoning are illustrated in Fig. 6.1. Given that both Ni- and Co-based ternary parents display the B2 structure at high temperatures, it is natural to assume this to be also the case for NiCoMnZ, with site 1a shared by Ni and Co and site 1b

---

[1] We neglect here the martensitic transitions below room temperature.

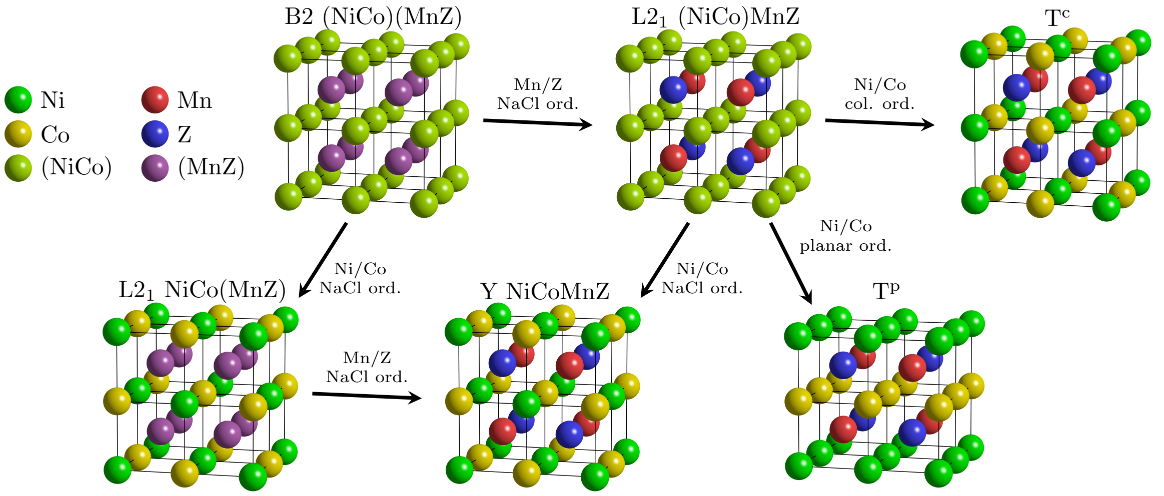

Fig. 6.1 Illustration of the ordered structures of NiCoMnZ considered here. Starting with B2 (NiCo)(MnZ), NaCl-type ordering on either sublattice leads to L2$_1$ structure of (NiCo)MnZ or NiCo(MnZ) type, and ordering on both sublattices to the Y structure. Those four structures have cubic symmetry. Ordering of the Ni and Co atoms in L2$_1$ (NiCo)MnZ into alternating columns or planes gives the tetragonal T^c and T^p structures, respectively.

by Mn and Z. We will denote this as (NiCo)(MnZ), where the parentheses denote mixing between the enclosed elements.[2]

As temperature is decreased, transitions to states of higher order can appear. For the Mn-Z sublattice, a NaCl-like ordering of Mn and Z is most likely by analogy with the ternary parents. Assuming the same kind of interaction favoring unlike pairs also between Ni and Co, the realized structures depend on the relative strengths: for dominating Mn–Z interactions, the B2 phase would transform to an L2$_1$ structure of type (NiCo)MnZ, where Ni and Co are randomly distributed over the 8c sites, and in the converse case to L2$_1$ NiCo(MnZ) with Mn and Z on 8c. In either case, the ordering of the other sublattice at some lower temperature would transform the system to the so-called Y structure (Bacon and Plant, 1971; Pauly et al., 1968) of prototype LiMgPdSn (Eberz et al., 1980) with space group 216 ($F\bar{4}3m$) and Wyckoff positions 4a, 4b, 4c, and 4d being occupied by Ni, Co, Mn and Z, respectively.

However, as the kind of chemical interaction within the Ni-Co sublattice is as yet unknown, also other possibilities have to be considered. In principle, there is an unlimited number of superstructures on the L2$_1$ (NiCo)MnZ structure, corresponding to different Ni/Co orderings. In particular, apart from the above-mentioned cubic Y structure (with NaCl-type Ni/Co ordering) there are two other totally ordered structures with four inequivalent sublattices, making them appear *a priori* equally likely to be realized as the Y structure.

---

[2] We do not consider the other two B2 possibilities (NiMn)(CoZ) and (NiZ)(CoMn).

These are tetragonal structures characterized by either alternating columns or planes of Ni and Co atoms, which we denote by T^c and T^p. Specifically, the T^c structure has space group 131 ($P4_2/mmc$), with Ni on Wyckoff position 2e, Co on 2f, Mn 2c, and Z on 2d, while T^p has space group 129 (P4/nmm) with Ni on 2a and Co on 2b, while Mn and Z reside on two inequivalent 2c positions, with prototype ZrCuSiAs (Johnson and Jeitschko, 1974). Note that the Ni/Co ordering in these three fully-ordered structures can equally be understood as alternating planes in different crystallographic orientations, with T^p corresponding to $(1, 0, 0)$ planes, T^c to $(1, 1, 0)$, and Y to $(1, 1, 1)$ planes. Finally, of course the possibility of phase separation into $L2_1$ Ni_2MnZ and Co_2MnZ has to be considered.

6.2 Macroscopic properties

6.2.1 Sample preparation and thermal treatments

Nominally stoichiometric NiCoMnAl and NiCoMnGa alloys have been prepared by induction melting and casting of high-purity elements under argon atmosphere. After casting, the samples have been subjected to a solution-annealing treatment at 1273 K followed by quenching in room-temperature water. In this state, the samples have been checked for their actual composition using wavelength-dispersive X-ray spectroscopy (WDS). For each alloy, eight independent positions have been measured. The average over the retrieved values are given in Table 6.1, showing satisfactory agreement with the nominal compositions. Additionally, sample homogeneity was confirmed by microstructure observation using backscattered electrons.

In order to track the ordering processes of the alloys upon low-temperatures isothermal aging, samples have been annealed at 623 K for different times t_{ann} and water-quenched. Thus, for both systems we consider four states, corresponding to the as-quenched state and after annealings for 6 h, 24 h, and 72 h, respectively. Previous results (Neibecker et al., 2014) have proven this low-temperature annealing protocol to be successful for increasing the achievable state of order in structurally similar alloys of the Ni_2MnAl system.

at. %(±0.5%)	Ni	Co	Mn	Ga	Al
NiCoMnGa	25.6	23.4	26.1	25.0	-
NiCoMnAl	25.1	25.5	25.7	-	23.8

Table 6.1 Composition as determined by WDS.

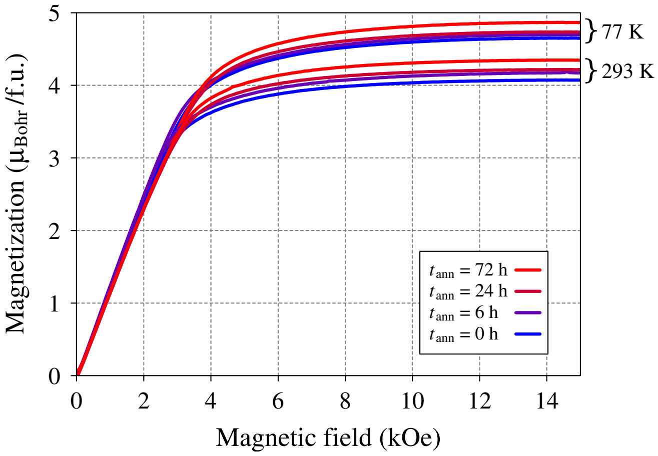

Fig. 6.2 Field-dependent magnetization of NiCoMnAl in different annealing conditions measured at 293 K and 77 K.

6.2.2 Magnetization measurements

Magnetization measurements corresponding to the different annealing conditions were performed, specifically the Curie temperatures T_{C} and spontaneous magnetization values M_{S} have been determined. Temperature-dependent magnetization measurements were carried out in a TOEI Vibrating Sample Magnetometer (VSM) applying an external magnetic field of 500 Oe in a temperature range from room temperature to 693 K. The spontaneous magnetization for NiCoMnGa has been determined with a Superconducting Quantum Interference Device (SQUID) based Quantum Design MPMS system at 6 K employing external magnetic fields up to 7 T. Since for the ductile NiCoMnAl alloy sample preparation turned out to have an effect on sample properties, presumably due to introduced mechanical stresses, in this alloy system temperature-dependent magnetization measurements have been performed by VSM on samples of larger size in an external field of 1.5 T.

Figure 6.2 shows field-dependent magnetization curves ($M(H)$) of NiCoMnAl in four different annealing conditions measured at 293 K and 77 K. The spontaneous magnetization M_{S} has been retrieved via constructing Arrott plots. Additionally, $M(T)$ curves of NiCoMnAl in the four annealing conditions at an external magnetic field of 15 kOe that were used to extrapolate the 0 K value of the spontaneous magnetization M_{S} are given in the Supplementary Information, along with the corresponding measurements for NiCoMnGa. The obtained values are given in Table 6.2. As expected, the spontaneous magnetization increases with decreasing measurement temperature. Further, specifically NiCoMnAl shows a significant increase in M_{S} with annealing from 4.68 μ_{B}/f.u. in the as-quenched state to 4.89 μ_{B}/f.u. after annealing for 72 h. Clearly, at higher measurement temperatures the difference in M_{S} after annealing is even larger due to lower magnetic transition temperatures in the shorter annealed samples. The values obtained for M_{S} are in good agreement with two previous studies, where M_{S} in the B2 ordered state was reported as 4.66 μ_{B}/f.u. (Halder et al., 2015) and 4.90 μ_{B}/f.u.

	t_{ann}	T_{C} (K)		M_{S} (μ_{Bohr}/f.u.)		
		up	down	6 K*		293 K*
NiCoMnGa	0 h	636.0	633.9	4.47		4.11
	6 h	635.4	632.3	4.58		4.14
	24 h	637.1	633.4	4.46		4.18
	72 h	638.2	632.9	4.53		4.17
		up	down	0 K†	77 K	293 K
NiCoMnAl	0 h	572.1	583.3	4.68	4.61	3.98
	6 h	586.8	590.2	4.72	4.66	4.08
	24 h	593.2	593.8	4.75	4.72	4.15
	72 h	602.9	599.2	4.89	4.86	4.30

Table 6.2 Magnetic properties of NiCoMnAl and NiCoMnGa in different annealing conditions. Unless otherwise noted, values have been measured by VSM, while those indicated by * have been measured by SQUID and those indicated by † have been extrapolated from the VSM $M(T)$ measurements reported in the Supplementary Information.

(Okubo et al., 2011) On the other hand, in NiCoMnGa no convincing increase in M_{S} with annealing is visible, with the values of M_{S} scattering around 4.15 and 4.50 μ_{B}/f.u. at 293 K and 6 K, respectively. These values again show good agreement to previous studies with M_{S} being stated as 4.67 μ_{B}/f.u. at a temperature of 5 K (Kanomata et al., 2009).

Figure 6.3 shows the corresponding temperature-dependent magnetization measurements ($M(T)$) of NiCoMnGa and NiCoMnAl under an external field of 500 Oe. In the following discussion, we define the apparent magnetic transition temperature as the locus of the maximal slope of the $M(T)$ curves for consistence with the pertinent previous experimental works (Okubo et al., 2011), which at small external fields is a good proxy for the actual Curie temperature. Note that at these small fields, the absolute values of the low-temperature magnetizations are affected by demagnetization effects and thus by the specific shapes of the different samples, which leads particularly for the brittle NiCoMnGa to unsystematic variations. Further, the apparently temperature-independent magnetization at low temperatures is due to the increasing local magnetization being compensated by decreasing ferromagnetic domain sizes due to the demagnetizing field and has been observed also by other groups in related materials (Singh et al., 2016).

In NiCoMnAl, the magnetic transition temperature increases from 572.1 K to 602.9 K with annealing of the samples, reflecting a corresponding increase of L2_1 order. The specific transition temperatures are given in Table 6.2. This compares satisfactorily with the value of 570 K determined by Okubo et al. (2011) for samples quenched from the B2 region. An important point to note is that, in order to probe the high Curie temperatures in these systems,

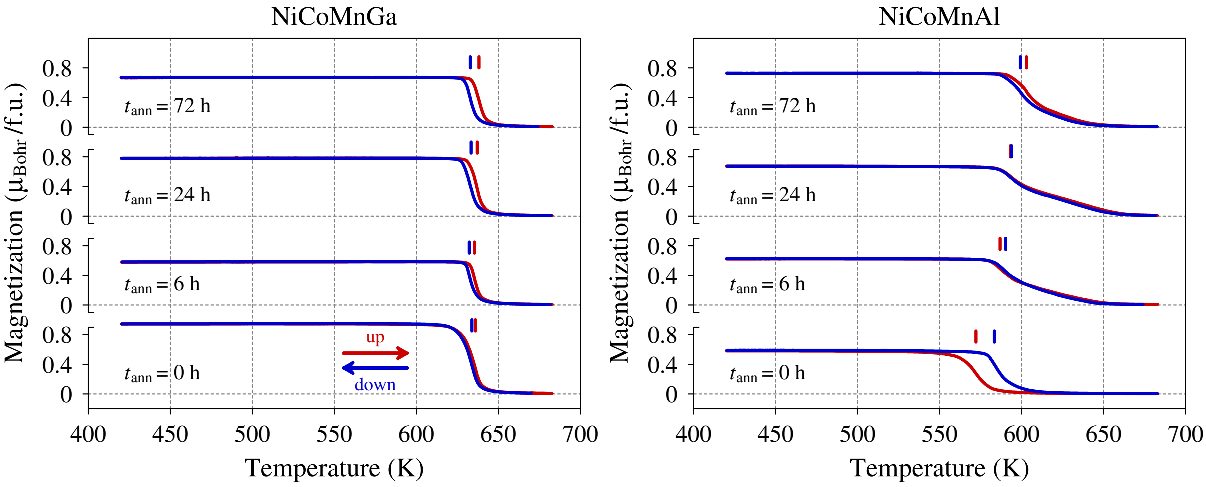

Fig. 6.3 Temperature-dependent magnetization of NiCoMnGa and NiCoMnAl in different annealing conditions at an external magnetic field of 500 Oe. Depicted in red and blue are the heating and cooling curves, while the markers represent the magnetic transition temperatures determined as given in the text.

during the measurements the sample is subjected to temperatures where the ordering kinetics become appreciable. Specifically, with ordering kinetics at 623 K on the order of hours, the Curie temperatures below 600 K measured on heating at a rate of 2 K/min can safely be assumed to correspond to the degree of order imposed by the isothermal annealing treatments. However, at the maximum temperature of 683 K the degree of order will relax during the measurement towards the corresponding equilibrium value, leading to an increase of order for the as-quenched state and a decrease when starting from a high degree of order. This difference between heating and cooling curves is well discernible.

NiCoMnGa shows a magnetic transition from the ferromagnetic to the paramagnetic state between 636.0 K and 638.2 K. Since the degree of $L2_1$ order in NiCoMnGa is high in all annealing conditions, annealing has a much smaller effect on T_C than in NiCoMnAl. The determined transition temperatures are given in Table 6.2. Apparently, still a small increase of order with annealing exists in this alloy system. We attribute the constant offset of about 3.5 K between heating and cooling to effects of thermal inertia.

6.2.3 Differential scanning calorimetry

Differential Scanning Calorimetry (DSC) has been employed to analyze both alloys with respect to magnetic and structural phase transitions on a Netzsch DSC 404 C Pegasus. All

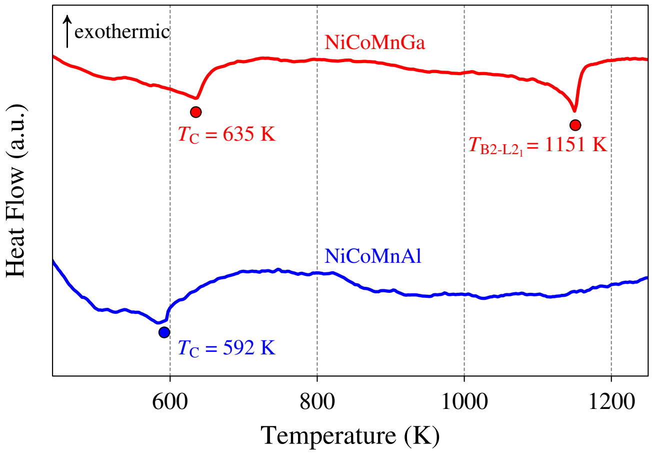

Fig. 6.4 DSC measurements of annealed NiCoMnGa and NiCoMnAl. DSC curves have been recorded on heating with a rate of 10 K/min.

measurements have been performed at a heating rate of 10 K/min over a temperature range from 300 K to 1273 K. Figure 6.4 shows DSC results for the NiCoMnGa and NiCoMnAl alloys that have been subject to solution annealing at 1273 K, quenching to room temperature, followed by a low-temperature annealing at 623 K applied with the intention to adjust a large degree of $L2_1$ order. Taking into account different ordering kinetics, the NiCoMnGa alloy was annealed for 24 h, while the NiCoMnAl alloy was annealed for 72 h.

Both alloys show a clear magnetic transition from the ferromagnetic to the paramagnetic state at 592 K and 635 K for NiCoMnAl and NiCoMnGa, respectively. This is in good agreement with magnetization measurements (Table 6.2), justifying our approach of defining the Curie temperatures via the position of maximal slope in the magnetization under constant field. NiCoMnGa shows additionally an order-disorder phase transition at higher temperatures that can be assigned according to our neutron diffraction measurements (Sec. 6.3) to the transition from the $L2_1$-(NiCo)MnGa to the B2-(NiCo)(MnGa) structure, which is in accordance with the behavior of the structurally similar Ni_2MnGa compound (Sánchez-Alarcos et al., 2007) and with previous results from Kanomata et al. (2009). The phase transition temperature was determined as 1151 K, a value in excellent agreement to the 1152 K reported in Kanomata et al. (2009). In contrast, NiCoMnAl does not show any further apparent peaks in the calorimetric signal besides the magnetic transition.

6.3 Neutron diffraction

Neutron diffraction measurements have been performed at the SPODI (Hoelzel et al., 2015) high-resolution neutron powder diffractometer at the Heinz Maier-Leibnitz Zentrum (MLZ) in Garching, Germany. Polycrystalline samples were measured continuously on heating and cooling between room temperature and 1273 K, employing rates of approximately 2 K/min

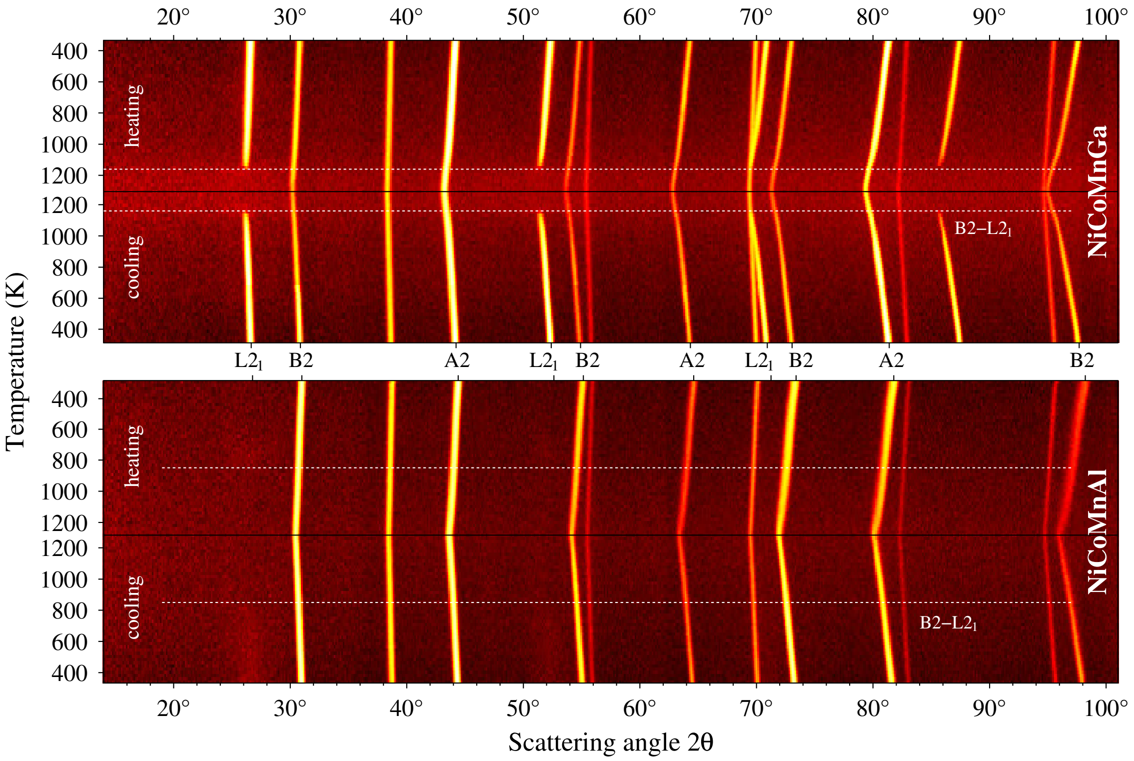

Fig. 6.5 Waterfall plots of the temperature-dependent neutron powder diffraction patterns of NiCoMnGa (above) and NiCoMnAl (below) on heating and cooling with rates of approximately 2 K/min. Before the measurement, samples were solution annealed at 1273 K and quenched in room temperature water. The unlabeled peaks with pronouncedly lower thermal expansion are due to the Nb sample cans.

and a recording frequency of approximately one pattern per 15 minutes. Measurements have been done using Nb sample cans and employing a neutron wavelength of 1.54827 Å. Temperature-dependent lattice constants, peak widths and structure factors corresponding to the different degrees of long-range order have been refined. Additionally, for the depiction of the waterfall plots, data treatment as described in Hoelzel et al. (2012) has been applied.

Figure 6.5 shows waterfall plots of the neutron diffraction patterns of NiCoMnGa/Al upon heating and cooling on a logarithmic pseudocolor scale. All reflection families, namely $L2_1$, B2 and A2, are labeled in the figure. Their presence corresponds to the symmetry breaking into inequivalent sublattices as discussed in Sec. 6.1, and their strength indicates the quantitative degree of long-range order. The A2 peaks are not influenced by any disorder in the system, since here all lattice sites contribute in phase. The presence of the B2 peak family indicates different average scattering lengths on the Ni-Co and the Mn-Z sublattices. Finally, $L2_1$ peaks are due to a further symmetry breaking between either the 4a and 4b and/or 4c and 4d sublattices. Note that such a qualitative reasoning cannot distinguish whether the system has the Y structure or one of the two possible $L2_1$ structures, which can only be decided by a quantitative analysis (as will be done below). Similar as for the A2 peak family, the intensity of the B2 peak family is not influenced by the degree of $L2_1$ order.

In the waterfall depiction, the evolution of peak positions and (in qualitative terms) peak intensities with temperature can be followed nicely. Initially, the samples correspond to the state quenched from 1273 K. Already in this state, NiCoMnGa exhibits $L2_1$ order as evidenced by the presence of the corresponding diffraction peaks. Upon heating, the thermal expansion of the lattice leads to a gradual shifting of the peak positions to smaller scattering angles. At approximately 1160 K, a disordering phase transition from the $L2_1$ phase to the B2 phase is observed. This is reversed on cooling at practically the same temperature, which shows that at these high temperatures the equilibrium states of order are followed closely. The observed value of 1160 K is in good agreement to the 1151 K determined by calorimetry.

In contrast to NiCoMnGa, NiCoMnAl is found to have a B2 state in the as-quenched condition with no $L2_1$ reflections visible. On cooling, the peaks are slightly narrower than on heating, indicating the release of internal stresses in the sample remaining from quenching. Interestingly, upon slowly cooling the sample down from 1273 K, at approximately 850 K very diffuse maxima appear at the positions where $L2_1$ reflections would be expected. Indeed, also during heating a very faint additional intensity can be discerned in the corresponding regions as soon as temperatures sufficient to facilitate a relaxation of order via diffusion are reached. Arguably, the diffuse intensity observed is the manifestation of $L2_1$ short-range order or incipient $L2_1$ long-range order with very small anti-phase domains. Such anti-phase domains have previously been observed in $Ni_2MnAl_{0.5}Ga_{0.5}$ alloys (Ishikawa et al., 2008; Umetsu et al., 2011), where the phase transition temperature implies ordering kinetics on experimentally accessible time scales. The absence of well-defined $L2_1$ order as well as the pronouncedly lower B2-$L2_1$ transition temperature in NiCoMnAl compared to the NiCoMnGa alloy is consistent with the behavior observed in the related Ni_2MnAl and Ni_2MnGa compounds where transition temperatures of, respectively, 775 K (Kainuma et al., 2000) and 1053 K (Sánchez-Alarcos et al., 2007) have been reported.

While confirming a state of B2 order, in neutron diffraction no magnetic superstructure peaks are observed. Thus, in contrast to Ni_2MnAl, where Ziebeck and Webster (Ziebeck and Webster, 1975) discovered a helical magnetic structure manifesting itself in form of antiferromagnetic superstructure reflections and satellite peaks at the (200) and (220) reflections, NiCoMnAl is entirely ferromagnetic even under B2 order. This goes along with $M(H)$ measurements (Sec. 6.2) showing prototypical ferromagnetic properties. In contrast, for Ni_2MnAl antiferromagnetic properties have been reported (Acet et al., 2002). Presumably, the drastic difference in magnetic structure results from strong ferromagnetic interactions in

Fig. 6.6 Middle panel: Temperature-dependent lattice constants of NiCoMnGa and NiCoMnAl on heating and cooling starting with samples quenched from 1273 K. Upper and lower panels depict the temperature-dependent thermal expansion coefficients $\alpha = \frac{1}{a}\frac{\mathrm{d}a}{\mathrm{d}T}$.

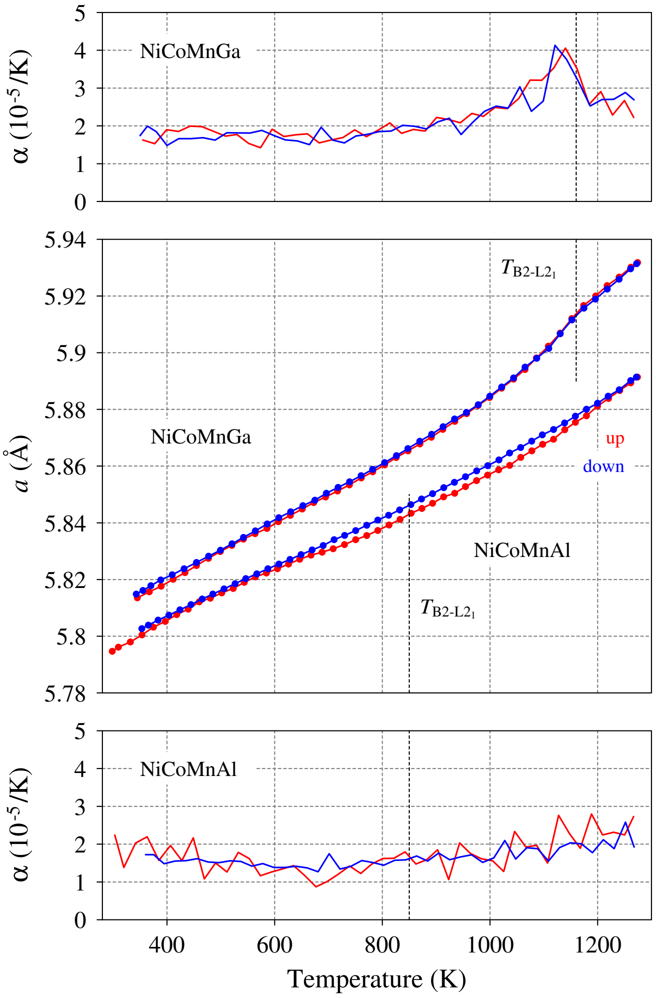

the system introduced by Co, overcoming the antiparallel coupling between neighboring Mn atoms.

Figure 6.6 shows the temperature-dependent lattice constants retrieved from fitting the in-situ neutron diffraction data as well as the corresponding temperature-dependent thermal expansion coefficients. At 340 K, the lattice constant of approximately 5.81 Å in as quenched NiCoMnGa is only slightly larger than the one of NiCoMnAl with approximately 5.80 Å, while the thermal expansion is similar in both alloys with a value of approximately $2\times 10^{-5}\,\mathrm{K}^{-1}$. In the case of NiCoMnGa, the heating and cooling curves coincide, indicating little effect of the applied quenching treatment. The B2-L2_1 transition is clearly mirrored in the lattice constant, with a maximum in the thermal expansion coefficient below 1160 K, in agreement with the calorimetric transition temperature and the vanishing of L2_1 intensities in neutron diffraction.

In the case of NiCoMnAl, the B2–L2_1 ordering transition is neither visible directly in the lattice constant nor in the thermal expansion coefficient. However, this system

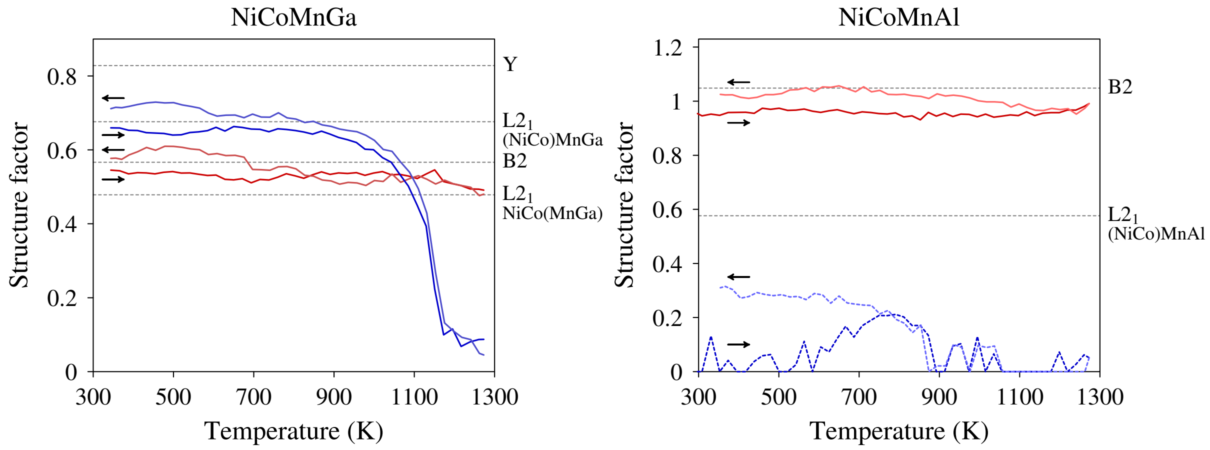

Fig. 6.7 Structure factors of the B2 (red) and L2$_1$ (blue) peak families as function of temperature on heating and cooling as determined by in-situ neutron diffraction for both systems. Theoretical values for different ordered structures are given as horizontal lines.

displays another striking effect with the divergence of the lattice constants on heating and cooling at intermediate temperatures. The absence of an analogous effect in the determined Nb lattice constants proves that this deviation is real as opposed to, e.g., an error in the determination of the sample temperature. We interpret it to be due to a superposition of a lattice expansion due to quenched-in disorder with a lattice contraction due to a quenched-in vacancy supersaturation. On heating, around 650 K ordering kinetics become active, leading to a relaxation of the lattice expansion, while only at temperatures above 1100 K vacancies become mobile enough to equilibrate their concentrations at vacancy sinks such as surfaces or grain boundaries. Thus, in this interpretation the agreement in the lattice constants of the slow-cooled and quenched states at low temperatures is just a coincidence.

Figures 6.7 show the temperature-dependent structure factors of NiCoMnGa and NiCoMnAl, i.e., essentially the square root of the ratio of the B2 and L2$_1$ intensities to the A2 peak families after taking into account Lorentz and Debye-Waller factors and multiplicities. In the case of NiCoMnGa, the second-order B2–L2$_1$ transition at 1160 K is clearly visible. Additionally, comparing the theoretical structure factors for different kinds of disorder as given in the figure to the experimental values implies the observed L2$_1$ intensity to be due to solely Mn/Ga order as opposed to Y ordering or only Ni/Co ordering. Note that the reason for the L2$_1$ structure factor's failure to go to zero above the transition lies in the residual diffuse intensity due to short-range order, which contributes to the apparent L2$_1$ peak intensities because of their finite experimental widths.

For NiCoMnAl, the diffuse intensity at the L2_1 positions was modeled by increased peak widths compared to the A2 and B2 peaks due to finite-length correlations. The structure factor obtained in this way is indicated in Fig. 6.7. The different behavior on heating and cooling implies quenched-in disorder in the initial state, with a convergence towards the equilibrium value starting around 600 K in parallel with the decrease in the lattice constant discussed above. Also on slow cooling, the determined structure factor stays well below the value corresponding to full (NiCo)MnAl L2_1 order, which however may also be due to the kinetically limited finite correlation lengths of order.

Interestingly, also the B2 structure factors in NiCoMnAl and NiCoMnGa are higher on cooling than on heating, while they decrease only by minute amounts with temperature. We are confident in these qualitative conclusions even though quantitative interpretations of the data have to be treated with qualification, considering the limited number of crystallite grains fulfilling the Bragg condition that defines the statistical precision.

Regarding the realized crystal structures, the neutron diffraction results can be summarized as proving the exclusive existence of partially disordered cubic phases with B2 at high temperatures and L2_1 (NiCo)MnZ at low temperatures, where the latter is only at the brink between short-range ordering and small anti-phase domains for Z = Al. In contrast, tetragonal ordering would be expected to lead to peak splittings due to the symmetry breaking as well as additional superstructure peaks, with lowest-order reflections comparable in intensity to the B2 peaks around $2\theta = 15°$ and $2\theta = 22°$ for T^p and T^c, respectively, which however are not detectable. On the other hand, phase separation into Ni- and Co-rich ternary Heusler phases should lead to a peak splitting on the order of 1% according to the respective lattice constants (Acet et al., 2002; Sánchez-Alarcos et al., 2007; Webster, 1971). Also for this effect, there is no indication, with the slowly-cooled samples showing narrower rather than wider peaks.

6.4 First-principles calculations

Computational details

We performed *ab initio* calculations for the structures proposed in Sect. 6.1.2. Specifically, we computed ordering energies and electronic densities of states (DOS) by plane-wave density functional theory as implemented in VASP (Vienna Ab-initio Simulation Package) (Kresse and Furthmüller, 1996), and magnetic interactions in the Liechtenstein approach (Liechstenstein et al., 1987) as implemented by Ebert et al. (2011) in their Korringa-Kohn-Rostoker Green's function code (SPR-KKR).

In the VASP calculations, the disordered structures were realized by 432 atom supercells (corresponding to 6×6×6 bcc cells) with random occupations, taking advantage of the

Fig. 6.8 Comparison of the total energies of the various structures of ferromagnetic NiCoMnAl and NiCoMnGa obtained from density functional theory. The inner levels (blue) refer to fully relaxed structures (positions and lattice constants), whereas in the outer columns (red) only the lattice constants were relaxed and the ions remain on the ideal (symmetric) positions with bcc coordination. The energies are specified relative to a mixture of the ferromagnetic ground state structures of ternary ferromagnetic Co_2MnZ and Ni_2MnZ. Thus negative energies denote structures which are inherently stable against demixing, whereas the others require to be stabilized by mixing entropy.

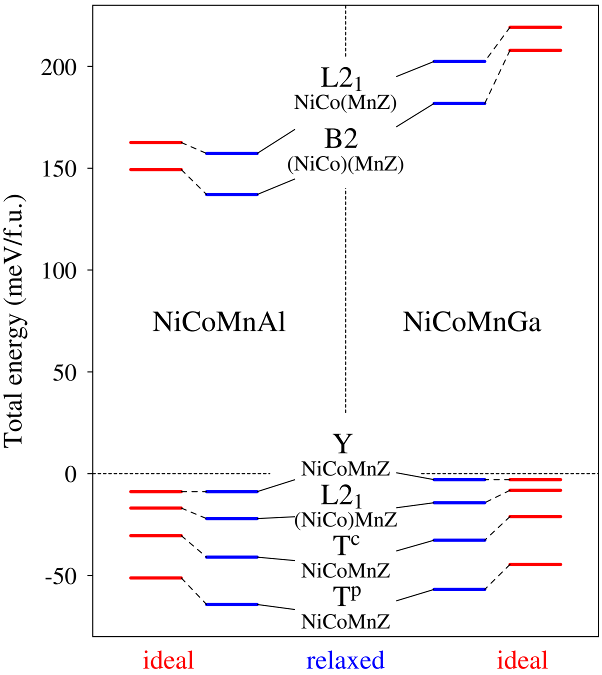

efficient parallelization in VASP for massively parallel computer hardware. Here, the wavefunctions of the valence electrons are described by a plane wave basis set, with the projector augmented wave approach taking care of the interaction with the core electrons (Kresse and Joubert, 1999). Exchange and correlation was treated in the generalized gradient approximation using the formulation of Perdew, Burke and Ernzerhof (Perdew et al., 1996). We converged unit cell dimensions and atomic positions by a conjugate gradient scheme until forces and pressures reached values around 3 meV/Å and 1 kbar, respectively. For the structural relaxations of the disordered systems, we used a $2\times2\times2$ Monkhorst-Pack k-mesh with the 432 atom supercells in combination with Methfessel-Paxton (Methfessel and Paxton, 1989) Fermi surface smearing (σ =0.1 eV), while total energies and densities of states were calculated by the tetrahedron method with Blöchl corrections (Blöchl et al., 1994) using a $4\times4\times4$ k-mesh. A $17\times17\times17$ k-mesh was employed for the ordered structures represented in a cubic 16 atom unit cell. Additional details on the numerical parameters are given in the Supplementary Information. In all our calculations we allowed for a spontaneous spin polarization, always resulting in stable ferromagnetism.

In the SPR-KKR calculations, the ferromagnetic ground state was chosen as reference and disorder was treated analytically in the framework of the coherent potential approximation. The electronic density of states obtained for the different disordered structures agreed very well with the results obtained from the plane wave calculations, which corroborates our explicit supercell-based description.

The results of our total-energy calculations are shown in Fig. 6.8 and given in Tab. 6.3. In addition to the quaternary systems, we also computed the ternary full Heusler systems for use as reference energies, specifically cubic $L2_1$ Co_2MnAl, Ni_2MnAl, and Co_2MnGa, as well as tetragonal $L1_0$ Ni_2MnGa, according to the martensitic transition occurring in the latter case. The energy differences are always specified with respect to the four-atom Heusler formula unit in the fully relaxed states. As expected for isoelectronic systems, the energy differences of the different phases behave similar in NiCoMnAl and NiCoMnGa. In both cases, we observe a significant gain in energy by ordering the main group element Z and Mn. As one would expect, the B2 phase is among the least favorable ones in terms of total energy, and thus its observed thermodynamic stability at high temperatures is due to its large configurational entropy. The fully disordered bcc phases turned out to be significantly higher in energy, at 1.00 eV/f.u. for NiCoMnGa and 1.07 eV/f.u. for NiCoMnAl (both without relaxation), and are therefore not included in Fig. 6.8.

In contrast, the fully ordered Y structure, which has previously been proposed as a new candidate for a half metal, appears significantly more stable, not only against B2 disorder but also against decomposition into the ternary phases. However, a surprising result of our calculations is that NaCl-type ordering of Ni and Co is always disfavored compared to random disorder: this pertains both to $L2_1$ NiCo(MnZ), which is about 20 meV higher in energy than B2 (NiCo)(MnZ), as well as the energetical gain of about 12 meV when Y NiCoMnZ is disordered to $L2_1$ (NiCo)MnZ. Thus, considering only structural thermodynamics, the Y structure will not be thermodynamically stable at any temperature, as it has both higher internal energy as well as lower configurational entropy compared to $L2_1$ (NiCo)MnZ.

However, the partially disordered $L2_1$ structure should not be the ground state. Indeed, in both NiCoMnAl and NiCoMnGa the two tetragonal structures with a four-atom unit cell T^p and T^c have lower energies than all structures considered up to now. Thus, our calculations identify T^p with the alternation of Ni and Co $(1,0,0)$ planes as the ground state structure. We are confident that, at least among the superstructures on the bcc lattice, there should be no structures with significantly lower energies, as the NaCl-type Mn/Z order with its large energy gain seems quite stable, while any Ni/Co order different from the three kinds considered here would need to rely on quite long-range interactions.

We observe that the relaxation procedure yields a considerable energy gain for the disordered structures. An analysis of the corresponding atomic displacements is given in the Supplementary Information, evidencing an expansion of $\langle 1,0,0\rangle$-coordinated pairs made up of equal atoms due to Pauli repulsion as common characteristic of the relaxations. Specifically for Mn/Z disorder, the mean bond lengths show an asymmetry, reflecting the larger size of the Z atom, particularly in the case for $Z = Ga$. The relaxation energies of the disordered

	Structure		a_0	c_0	V_0	E_{form}	$\Delta E_{\mathrm{relax}}$	M_{S}	μ_{Mn}	μ_{Ni}	μ_{Co}
			(Å)	(Å)	(Å^3)	(meV/f.u.)		(μ_{B}/f.u.)	(μ_{B}/at.)		
NiCoMnAl	L2$_1$	NiCo (MnAl)	5.736		188.7	157	6	4.89	3.24	0.59	1.11
	B2	(NiCo)(MnAl)	5.728		187.9	137	12	4.59	3.15	0.46	1.07
	Y	NiCo MnAl	5.733		188.4	−9	-	4.93	3.19	0.62	1.19
	L2$_1$	(NiCo) MnAl	5.723		187.4	−22	5	4.60	3.10	0.51	1.10
	T$^{\mathrm{c}}$		5.662	5.839	187.2	−41	11	4.58	3.10	0.49	1.11
	T$^{\mathrm{p}}$		5.752	5.648	186.9	−64	13	4.43	3.05	0.40	1.11
NiCoMnGa	L2$_1$	NiCo (MnGa)	5.759		191.0	202	17	4.95	3.27	0.57	1.14
	B2	(NiCo)(MnGa)	5.750		190.1	182	26	4.68	3.19	0.45	1.09
	Y	NiCo MnGa	5.748		189.9	−3	-	4.97	3.23	0.60	1.18
	L2$_1$	(NiCo) MnGa	5.738		188.9	−14	6	4.66	3.15	0.49	1.10
	T$^{\mathrm{c}}$		5.671	5.871	188.8	−33	12	4.61	3.14	0.46	1.09
	T$^{\mathrm{p}}$		5.772	5.658	188.5	−57	12	4.48	3.10	0.36	1.10

Table 6.3 Overview of the DFT results: Lattice constants and cell volumina, total energies of formation relative to the respective ternary Heusler compounds as discussed in the text, energy gain due to relaxation (resulting from disorder as well as tetragonal distortion), magnetic moments per formula unit NiCoMnZ and element-resolved moments for the various relaxed structures. For a better comparison, the lattice parameters a_0 and c_0 as well as V_0 refer in all cases to the 16 atom cubic cell instead of the respective primitive cell.

structures as given in Tab. 6.3 can be satisfactorily reproduced by assuming independent contributions of 6 meV due Ni/Co disorder, 6 meV due Mn/Al disorder, and 18 meV due Mn/Ga disorder, with the prominence of the latter value again due to the larger size of Ga.

Due to the tetragonal arrangement of the Ni and Co atoms in T^p and T^c, the cubic symmetry is reduced to tetragonal, which is reflected also in the lattice parameters. Specifically, as reported in Tab. 6.3, c, the lattice constant along the fourfold tetragonal axis, is 3–4% larger than a for the T^c structure, while it is about 2% smaller for T^p. Indeed, this behavior is expected due to above-reported tendency of $\langle 1, 0, 0 \rangle$-coordinated equal elements in $L2_1$ (NiCo)MnZ to be pushed apart due to Pauli repulsion, while Ni–Co pairs are contracted. Further, the Wyckoff positions 2c in space group 129, which are occupied by Mn and Z in the T^p structure, have an internal degree of freedom z corresponding to a translation along the tetragonal axis. For NiCoMnAl, the parameters are $z_{\text{Mn}} = -0.2556$ and $z_{\text{Al}} = 0.2512$, and for NiCoMnGa $z_{\text{Mn}} = -0.2555$ and $z_{\text{Ga}} = 0.2511$, being practically the same in both compounds. With Ni in 2a at $z = 0$ and Co in 2b at $z = 1/2$, this means that Mn and Z are slightly shifted away from the Ni planes. Again, this is mirrored in the increased bond lengths of $\langle 1/2, 1/2, 1/2 \rangle$-coordinated Ni-Mn and Ni–Z pairs compared to Co–Mn and Co–Z pairs under disorder as given in the Supplementary Information. Thus, with these small tetragonal distortions and deviations of the internal degrees of freedom from the ideal values, it is clearly appropriate to consider also the tetragonal phases as superstructures on the bcc lattice.

While the tetragonal distortions as mentioned above are on the order of a few percent, the differences in the unit cell volumes between the cubic and the tetragonal structures is much smaller. Indeed, we observe that there is a nearly perfect monotonic decrease of unit cell volume with internal energy of the structures: while the volume contraction with Mn/Z ordering by values of about 0.2% for NiCoMnAl and 0.6% for NiCoMnGa was expected, and also the bigger effect in the latter case can be rationalized by the larger Ga atoms, NaCl-type Ni/Co order, which was already found to be energetically unfavorable, leads to a lattice expansion by about 0.5% in both systems. In contrast, the energy gains with T^c and T^p are reflected in a corresponding volume contraction.

Our theoretical results explain the experimental observations: as reported above, experimentally NiCoMnGa displays the B2 phase at high temperatures with a well-defined ordering transition to the $L2_1$ (NiCo)MnGa phase at lower temperatures, while for NiCoMnAl the transition temperature is reduced and only barely kinetically accessible. This is reproduced by our calculations, with $L2_1$ (NiCo)MnZ being the lowest-energy cubic phase, while B2 can be stabilized by entropy, with indeed a larger energy gain and thus a higher expected transition temperature for Z = Ga. Ni/Co ordering always increases the internal energy and decreases configurational entropy, thus $L2_1$ NiCo(MnZ) and Y NiCoMnZ are predicted not to be existing. Also, as the energy cost of disordering B2 to A2 is about five times larger than the gain of ordering to $L2_1$ (NiCo)MnZ, with the latter happening around 1000 K, we do not expect a transition to A2 in the stability range of the solid.

On the other hand, also the $L2_1$ (NiCo)MnZ phase is only stabilized by entropy, and thus should transform at some temperature to T^p. With an argumentation as above, where the B2–$L2_1$ and the $L2_1$–T^p transitions have the same entropy difference, but the latter's energy difference of 42 meV is about a factor of 4–5 lower, we predict a transition temperature around 250 K (see the Supplementary Information for a more detailed discussion of these issues). As already the B2–$L2_1$ transition in NiCoMnAl at around 850 K is only barely progressing, a bulk transition to T^p is therefore not to be expected on accessible timescales.

Extrapolating the lattice constants measured on cooling to T=0 K gives 5.785 Å for NiCoMnGa and 5.773 Å for NiCoMnAl. The deviation of about 0.05 Å to the calculated values for $L2_1$ (NiCo)MnZ is quite satisfactory, corresponding to a relative error of 0.9%. Of course, the difference in lattice constants between the two alloys should be predicted even much more accurately, giving 0.012 Å to be compared to the value of 0.011 Å determined experimentally. Further, the predicted contraction at the B2–$L2_1$ transition in NiCoMnGa of 0.012 Å agrees perfectly with the experimental value as obtained by integrating the excess thermal expansion coefficient between 1000 and 1200 K, while in NiCoMnAl the contraction with ordering is estimated as 0.003 Å by the differences in the heating and cooling curves evaluated at 600 K and 900 K to be compared with the predicted value of 0.005 Å. This small discrepancy implies that the experimental lattice constant of NiCoMnAl at low temperatures on cooling is increased compared to the theoretical predictions, which is consistent with a reduced degree of $L2_1$ long-range order in NiCoMnAl due to kinetical reasons.

Magnetism

From the non-integer values of the total magnetic moment per formula unit listed in Tab. 6.3, one can already conclude that neither of the structures yields the desired half-metallic properties. For the fully ordered Y structure, our calculated values for M_S are slightly lower than the values of 5.0 μ_B/f.u. (Halder et al., 2015) and 5.07 μ_B/f.u. (Alijani et al., 2011b) previously reported for NiCoMnAl and NiCoMnGa, and the integer moment of 5 μ_B, which follows from the generalized Slater-Pauling rule $M_\mathrm{S} = Z_\mathrm{v} - 24$ for half-metallic full-Heusler compounds (Galanakis et al., 2002) with $Z_\mathrm{v} = 29$ valence electrons per unit cell. The calculated M_S is even smaller for the other structures. Experimentally, we measured values between 4.47 and 4.58 μ_B/f.u. for $L2_1$ (NiCo)MnGa, while for Z = Al an increase from 4.68 μ_B/f.u. in the as quenched state to 4.89 μ_B/f.u. after the longest annealing was observed.

Thus, it seems that the dependence of M_S on the state of order in the intermediate states is more complicated than the situation captured by our calculation of the respective extremes, corresponding to a decrease from perfect Mn/Z disorder in the B2 case to perfect order in the $\mathrm{L2_1}$ case.

The values in Tab. 6.3 imply that the magnetic moment per formula unit M_S depends primarily on the order on the Ni/Co sublattice, with values around 4.95 μ_B/f.u. for NaCl-type order, 4.60 μ_B/f.u. for columnar order or disorder, and 4.45 μ_B/f.u. for planar order. The equilibrium unit cell volume V_0 grows with increasing M_S, with an additional lattice expansion in the cases of Mn/Z disorder.

The induced Ni moments show the largest variation between the different structures, in absolute and relative numbers. The Co moments follow the behavior of the Ni moments with a smaller variation. This is a consequence of the hybridization of Co and Ni in the minority spin density of states, which is responsible for the formation of a gap-like feature at E_F as discussed in detail in the next section. The Mn moments appear well localized with values slightly above 3.1 μ_B/f.u. and vary only by a tenth of a Bohr magneton.

The ferromagnetic ground state of the compounds arises from the strong ferromagnetic coupling between nearest-neighbor Mn–Ni (coupling constant approximately 7 meV) and, in particular, Mn–Co (coupling constant approximately 11.7 meV) pairs. On the other hand, Mn pairs in $\langle 1, 0, 0 \rangle$ coordination, which randomly occur in the B2 case, exhibit large frustrated antiferromagnetic coupling (coupling constant approximately -8 meV). This behavior is well known from ternary stoichiometric and off-stoichiometric Mn-based Heusler systems (Buchelnikov et al., 2008; Comtesse et al., 2014; Şaşıoğlu et al., 2004, 2008, 2005; Entel et al., 2014; Kurtulus et al., 2005; Rusz et al., 2006; Sokolovskiy et al., 2012). A more detailed account of the coupling constants for NiCoMnZ is given in the Supplementary Information. Thus for the low-energy structures, which do not exhibit Mn pairs with negative coupling constant, we expect the magnetic ordering temperature T_C to be significantly higher than in the B2 case. This agrees nicely with the significant increase under annealing observed for NiCoMnAl, while NiCoMnGa is already $\mathrm{L2_1}$-ordered in the as quenched state and thus has still a higher transition temperature.

Electronic Structure

The shape of the electronic density of states (DOS) of ternary $\mathrm{L2_1}$ Heusler compounds of the type $\mathrm{X_2YZ}$, including the appearance of a half-metallic gap, has been explained convincingly by Galanakis et al. (2002, 2006) in terms of a molecular orbital picture. First, we consider the formation of molecular orbitals on the simple cubic sublattice occupied by atoms of type X. Here, the d_{xy}, d_{yz} and d_{zx} orbitals hybridize forming a pair of $t_{2\mathrm{g}}$ and $t_{1\mathrm{u}}$ molecular orbitals,

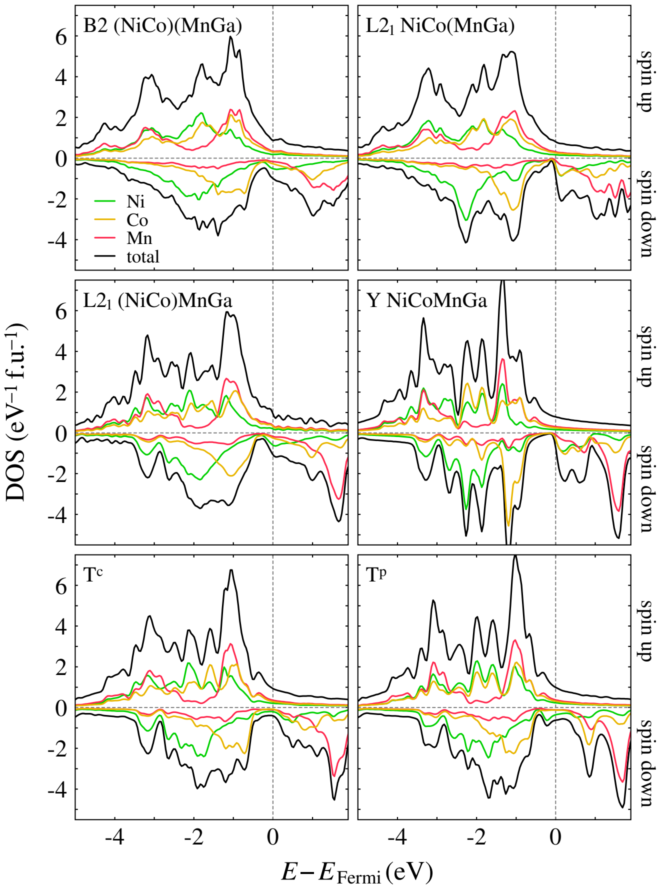

Fig. 6.9 Spin-polarized electronic density of states (DOS) in ferromagnetic NiCoMnGa for the distinct ordered structures.

while the $d_{x^2-y^2}$ and the $d_{3z^2-r^2}$ states form e_g and e_u molecular orbitals. The molecular orbitals of t_{2g} and e_g symmetry can hybridize with the respective orbitals of the nearest neighbor on the Y-position (in the present case Mn), splitting up in pairs of bonding and anti-bonding hybrid orbitals. However, due to their symmetry, no partner for hybridization is available for the t_{1u} and e_u orbitals, which therefore remain sharp. Accordingly, these orbitals are dubbed "non-bonding".

If the band filling is adjusted such that the Fermi level is located between the t_{1u} and e_u states in one spin channel, the compound can become half-metallic. This is for instance the case for Co_2MnGe with $Z_v = 29$, which has according to the generalized Slater–Pauling rule $M_S = 5\,\mu_B$ (Galanakis et al., 2002; Picozzi et al., 2002). If additional valence electrons are made available, also the e_u states may become occupied. This is the case for Ni_2MnGa and Ni_2MnAl ($Z_v = 30$), which do not possess half-metallic properties. Here, the Ni-e_u states form a sharp peak just below the Fermi energy and gives rise to a band-Jahn-Teller mechanism leading to a martensitic transformation and modulated phases arising from strong electron-phonon coupling due to nesting features of the Fermi surface (Brown et al., 1999; Bungaro et al., 2003; Haynes et al., 2012; Lee et al., 2002; Opeil et al., 2008; Zayak et al., 2003). Consequently, the magnetic moments of these compounds are significantly smaller. First principles calculations report values of 3.97 – 4.22 μ_B/f.u. (Ayuela et al., 1999; Galanakis et al., 2002; Godlevsky and Rabe, 2001) and 4.02 – 4.22 μ_B/f.u. (Ayuela et al., 2002, 1999; Şaşıoğlu et al., 2004; Fujii et al., 1989; Godlevsky and Rabe, 2001; Gruner et al., 2008) for Ni_2MnAl and Ni_2MnGa, respectively.

Figure 6.9 shows the total and element-resolved electronic densities of states (DOS) of NiCoMnGa for the most relevant structures, which have the same valence electron concentration as the half metal Co_2MnGe (NiCoMnAl shows an analogous picture and can be found in the Supplementary Information). Here, the perfectly alternating NaCl-type order of the elements on the Ni-Co sublattice in the Y-structure enforces a complete hybridization of the Ni- and Co-states, since the atoms find only $\langle 1,0,0\rangle$ neighbors of the other species. This becomes apparent from the pertinent illustration, as essentially the same features are present in the partial density of states of both elements. The magnitude of a specific peak may, however, be larger for one or the other species. This can be understood from the concept of covalent magnetism (Mohn, 2003; Schwarz et al., 1984; Williams et al., 1981) which has been applied to Heusler alloys recently (Dannenberg et al., 2010). The molecular orbitals are occupied by each species with a weight scaling inversely with the energy difference to the constituting atomic levels. In the minority spin channel, the bonding molecular orbitals are dominated by Ni-states, while the non-bonding $t_{1\mathrm{u}}$ states around -1 eV and the anti-bonding orbitals above E_F are dominated by the Co-states. The non-bonding e_u orbitals directly above E_F are equally shared by Co and Ni states.

As expected, with decreasing order the features of the DOS smear out and become less sharp. Specifically the pseudo-gap at the Fermi level in one spin channel, which corresponds to the near half-metallic behavior suggested first by Entel et al. (2010), and subsequently by Alijani et al. (2011b), Singh et al. (2012) and Halder et al. (2015), is in particular sensitive to ordering on the Ni-Co sublattice, and only encountered for the NaCl-type ordering of the fully ordered Y and the partially ordered $L2_1$ NiCo(MnZ) structures.

In fact, the minority spin gap is not complete. A close inspection of the band structure (see Supplementary Information) of Y NiCoMnGa/Al clearly shows several bands crossing the Fermi level. Since this occurs in the immediate vicinity of the Γ point, the weight of the respective states in the Brillouin zone is small and a gap-like feature appears in the DOS. Thus, in this configuration the compound should be classified as a half-semimetal rather than a half-metal. Nearly perfect gaps are observed if Z is a group IV element with a half-filled sp-shell. In our case, the missing electron of the main group element has to be compensated by the additional valence electron from one of the transition metals. These are only available on parts of the X-sites, which can lead to a distribution of sp-states between the sharp $t_{1\mathrm{u}}$ and e_{u} states of the transition metals below and above E_{F}.

In all other structures, the Ni-Co sublattice contains neighboring pairs of the same element. In this case, the respective d-orbitals can hybridize independently at different levels. As a consequence, the $t_{1\mathrm{u}}$ and e_{u} molecular orbitals split up. This is best seen in the DOS of the T^{p} structure. Here, the Ni-dominated part of the former e_{u} peak moves to below the Fermi level (where we expect it in $\mathrm{Ni_2MnGa/Al}$), which creates considerable DOS right at E_{F} and fully destroys the half-metallic character. An analogous argument can be applied to the cubic $\mathrm{L2_1}$ (NiCo)MnZ and B2 structures with disorder on the Ni-Co sublattice. The disorder on the Mn-Z sublattice in the B2 phase causes only minor changes in the electronic structure and manifests mainly in a larger band width of the valence states and the disappearance of a pronounced peak at -3.2 eV in the minority channel, which originates from the hybridization between the Ni-Co and Mn-Z sublattice. In contrast, the distribution of the Ni and Co states near the Fermi level, which are decisive for the functional properties of this compound family, is not significantly changed compared to the $\mathrm{L2_1}$ case.

6.5 Conclusions

Employing in-situ neutron diffraction, magnetic measurements and calorimetry, we studied the ordering tendencies in the quaternary Heusler derivatives NiCoMnAl and NiCoMnGa. NiCoMnGa was found to display an $\mathrm{L2_1}$ (NiCo)MnGa structure with strong Mn/Ga order and no to minor Ni/Co ordering tendencies, where the degree of order achieved upon slow cooling was higher than in quenched samples. The B2–$\mathrm{L2_1}$ second-order phase transition was observed at 1160 K. NiCoMnAl after quenching was found to adopt the B2 structure, while on slow cooling from high temperatures broadened $\mathrm{L2_1}$ reflections were observed to emerge at temperatures below 850 K in neutron diffractometry. Yet, kinetics at these temperatures are so slow that the adjustment of large degrees of $\mathrm{L2_1}$ order in this compound is kinetically hindered. Still, low-temperature annealing treatments at 623 K in samples quenched from 1273 K showed a strong effect on the magnetic transition temperatures, proving that this parameter probes sensitively the state of order in the sample.

Density functional theory reproduces the experimentally observed trends of the order-dependent magnetic behavior and of the ordering tendencies between the two systems. Our calculations reveal that the fully ordered Y structure with $\mathrm{F\overline{4}3m}$ symmetry is thermodynamically not accessible, since the partially disordered $\mathrm{L2_1}$ phase is lower in energy. Instead, we propose as the ground state a tetragonal structure with a planar arrangement of Ni and Co. This structure is stable against decomposition into the ternary Heusler compounds, but we expect the energetic advantage to be too small to compensate for the larger entropy of the $L2_1$ phase at reasonable annealing conditions. However, the fabrication of this structure by layered epitaxial growth on appropriately matching substrates, which favor the slight tetragonal distortion, could be possible. From the electronic density of states and band structure, we could conclude that neither of the structures is half-metallic in the strict definition. This specifically pertains also to the hypothetical Y structure, which exhibits several bands crossing the Fermi level close to the Γ point in the minority spin channel, and is thus a half-semimetal.

Since the first quaternary Heusler derivatives adopting the Y structure have been proposed to possess half-metallic properties (Dai et al., 2009), the interest in these materials has developed rapidly with numerous publications dealing with the topic (Al-zyadi et al., 2015; Alijani et al., 2011a,b; Bainsla et al., 2014; Berri et al., 2014; Elahmar et al., 2015; Enamullah et al., 2016, 2015; Entel et al., 2010; Feng et al., 2015; Gao et al., 2013, 2015; Gökoğlu, 2012; Halder et al., 2015; Mukadam et al., 2016; Özdoğan et al., 2013; Singh et al., 2012; Wei et al., 2015; Xiong et al., 2014; Zhang et al., 2014). Density-functional theory calculations have been used to identify promising systems among the NiCo- (Al-zyadi et al., 2015; Alijani et al., 2011b; Entel et al., 2010; Gökoğlu, 2012; Halder et al., 2015; Singh et al., 2012; Wei et al., 2015), NiFe- (Alijani et al., 2011b; Mukadam et al., 2016; Wei et al., 2015) and CoFe-based (Alijani et al., 2011a; Bainsla et al., 2014; Berri et al., 2014; Dai et al., 2009; Elahmar et al., 2015; Enamullah et al., 2016, 2015; Feng et al., 2015; Gao et al., 2013, 2015; Özdoğan et al., 2013; Xiong et al., 2014; Zhang et al., 2014) compounds. However, in most cases the phase stability of the Y structure is tested, if at all, only against stacking order variations of this Y structure (see, for instance Alijani et al., 2011a; Dai et al., 2009) but rarely against disorder (Enamullah et al., 2016) or other states of order. Simultaneously, experimental investigations as a rule either point towards disordered structures (Alijani et al., 2011a; Bainsla et al., 2014; Enamullah et al., 2015; Halder et al., 2015; Mukadam et al., 2016) or, specifically for the case of X-ray diffraction on ordering between transition metal elements, cannot decide these issues (Alijani et al., 2011a,b; Enamullah et al., 2015).

Based on our findings, we conclude that at least in the NiCo-based, but probably also in the NiFe- and CoFe-based alloys, the stability of the Y structure is doubtful and, even if it was thermodynamically stable, might still not be kinetically accessible in most quaternary Heusler derivatives. Indeed, preliminary first-principles results show that also for the NiFeMnGa and CoFeMnGa alloys, the tetragonal T^p order is lower in energy than the Y structure by 62 meV/f.u and 80 meV/f.u., respectively, comparable to the values reported here. This underlines that a detailed analysis of phase stabilities in those systems that have been identified as promising half-metals, especially with respect to the tetragonal structures and/or

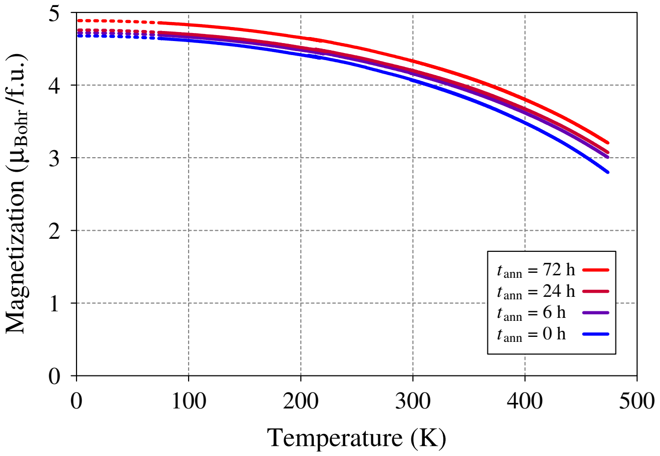

Fig. 6.10 $M(T)$ measurements of NiCoMnAl in four annealing conditions at an external magnetic field of 15 kOe down to 77 K. Second-order polynomial extrapolations to zero temperature are indicated by the dashed lines.

$L2_1$ type disorder, is essential in order to evaluate their actual potential. More generally, the comparatively small energetical differences between the various possible types of order along with small disordering energies specifically with respect to the late transition metal constituents as obtained here suggest that in these quaternary Heusler derivatives disorder could be the norm rather than the exception in physical reality. Thus, our findings imply that for computationally predicting the potential of a given system for applications, the assumed ground state has first to be tested against other plausible candidates, and second, that only with a comparatively large energy gain compared to disordered structures (0.2 eV for the B2–$L2_1$ transition in NiCoMnGa as considered here) the ordered phase can be assumed with some certainty to be actually realizable.

6.6 Supporting Information

6.6.1 Magnetization measurements

Figure 6.10 shows $M(T)$ measurements of NiCoMnAl in four annealing conditions (as quenched from 1273 K, as well as after additional annealing treatments at 623 K for 6 h, 24 h and 72 h). The increase of magnetization with annealing agrees with the $M(H)$ measurements given in Fig. 6.2 of the main text. As indicated in Fig. 6.10, these temperature-dependent measurements have been used to extrapolate to the zero-temperature magnetization values given in Tab. 6.2 in the main text.

Figure 6.11 shows $M(H)$ for NiCoMnGa in the four annealing conditions as obtained by SQUID magnetometry at 6 K and 293 K, analogous to the corresponding VSM measurements for NiCoMnAl given in Fig. 6.2 of the main text. The spontaneous magnetization M_S was

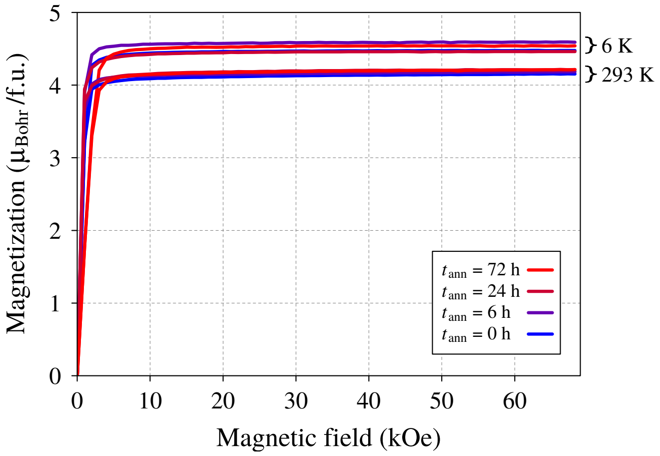

Fig. 6.11 $M(H)$ measurements of NiCoMnGa in four annealing conditions at 6 K and 293 K that were used to determine the spontaneous magnetization M_{S}. The retrieved values for M_{S} are given in Tab. 6.2 of the main text.

determined via fitting the linear part of the magnetization curve and identifying the y-axis intercept. The retrieved values are given in Tab. 6.2 of the main text.

6.6.2 Computational details

Electronic structure, energetic order and mixing energy have been calculated from first-principles in the framework of density functional theory. For the structural optimization of large supercells, we employed the Vienna Ab-initio Simulation Package (VASP) (Kresse and Furthmüller, 1996) for massively parallel computer hardware, which describes the wavefunctions of the valence electrons using a plane wave basis set in combination with the projector augmented wave (PAW) approach (Kresse and Joubert, 1999) to take care of the interaction with the core electrons. We used the standard potentials supplied with the code, treating the $3p^6 3d^6 4s^1$ states for Mn explicitly as valence states in the potential from Aug. 2007, $3s^2 3p^6 3d^8 4s^1$ for Co (Jul. 2007), $3p^6 3d^9 4s^1$ for Ni (Sep. 2000), $3d^{10} 4s^2 4p^1$ for Ga (Sep. 2000), and $3s^2 3p^1$ for Al (Jan. 2001). We used a plane-wave energy cutoff of $\mathrm{E}_{\mathrm{cut}} =$ 400 eV.

6.6.3 Phase stabilities

In order to estimate the transition temperature to the fully ordered T^p structure, we calculated the temperature-dependent free energy for both systems in all structures. The results are given in Fig. 6.12. Here, the free energy is calculated as $F = U - TS$, with the internal energy U being the total energy per unit cell from DFT calculations as presented in Fig. 6.8 of the main text and the entropy given by the mixing entropy per unit cell in a Bragg-Williams picture of 0 for the fully ordered structures, $2k_{\mathrm{B}}\log(2)$ for the L2_1 structures and $4k_{\mathrm{B}}\log(2)$ for the B2 structure. In this approximation we neglect any spatial correlations as well as contributions

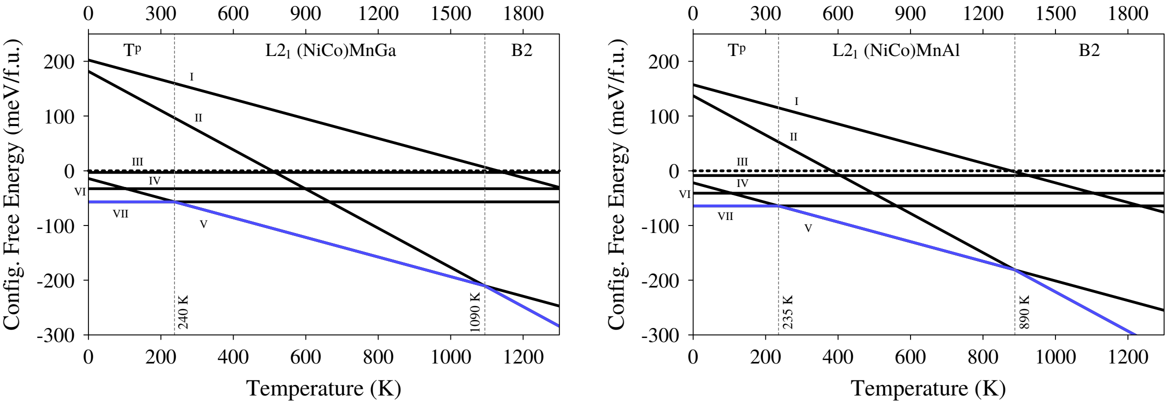

Fig. 6.12 Depiction of the configurational Free Energy as a function of temperature for NiCoMnGa (left) and NiCoMnAl (right). The upper horizontal axis refers to the nominal temperature, while the lower axis refers to a scaled temperature to reproduce the experimentally obtained B2-L2_1 phase transition temperatures of the compounds. The blue line indicates the stable phase at any temperature. Phases I to VII correspond to the L2_1 NiCo(MnZ) state, B2, the demixed 1/2 Ni_2MnGa + 1/2 Co_2MnGa state, Y, L2_1 (NiCo)MnZ, the tetragonal T^c and the tetragonal T^p phases, respectively.

to the free energy differences such as zero point energies, vibrational entropy, magnetic and electronic entropy. Employing this model, the transition temperatures retrieved for the B2–L2_1 transition are 1330 K and 1641 K for NiCoMnAl and NiCoMnGa, respectively, values considerably larger than the experimentally observed 850 K and 1160 K. This over-estimation of the critical temperature in the Bragg-Williams model is well known and accepted (Fisher, 1967). In a first approximation we assume this discrepancy to be a constant factor, thus the observed ratio between experimental and theoretical B2–L2_1 transition temperatures of about 2/3 leads us to correspondingly scaled-down estimated L2_1–T^p transition temperatures around 235 K and 240 K for NiCoMnAl and NiCoMnGa, respectively.

6.6.4 Electronic Structure

NiCoMnAl and NiCoMnGa have been discussed as promising candidates for half-metallic behavior. Even though the minority channel densities of states of both systems in the Y structure as shown in Fig. 6.13 display an apparent gap at E_F, an inspection of the minority spin band structure of NiCoMnGa in Fig. 6.14 reveals that there is no true gap. In contrast, five bands, all with predominantly d character are present around the Fermi level, with two of them actually crossing it. As in the molecular-orbital model of Galanakis *et al.* for Co_2MnGa (Galanakis et al., 2002, 2006), these bands are of e_u and $t_{1\mathrm{u}}$ character, and specifically away from Γ the two e_u bands are slightly above E_F, while the three $t_{1\mathrm{u}}$ bands are quite flat around

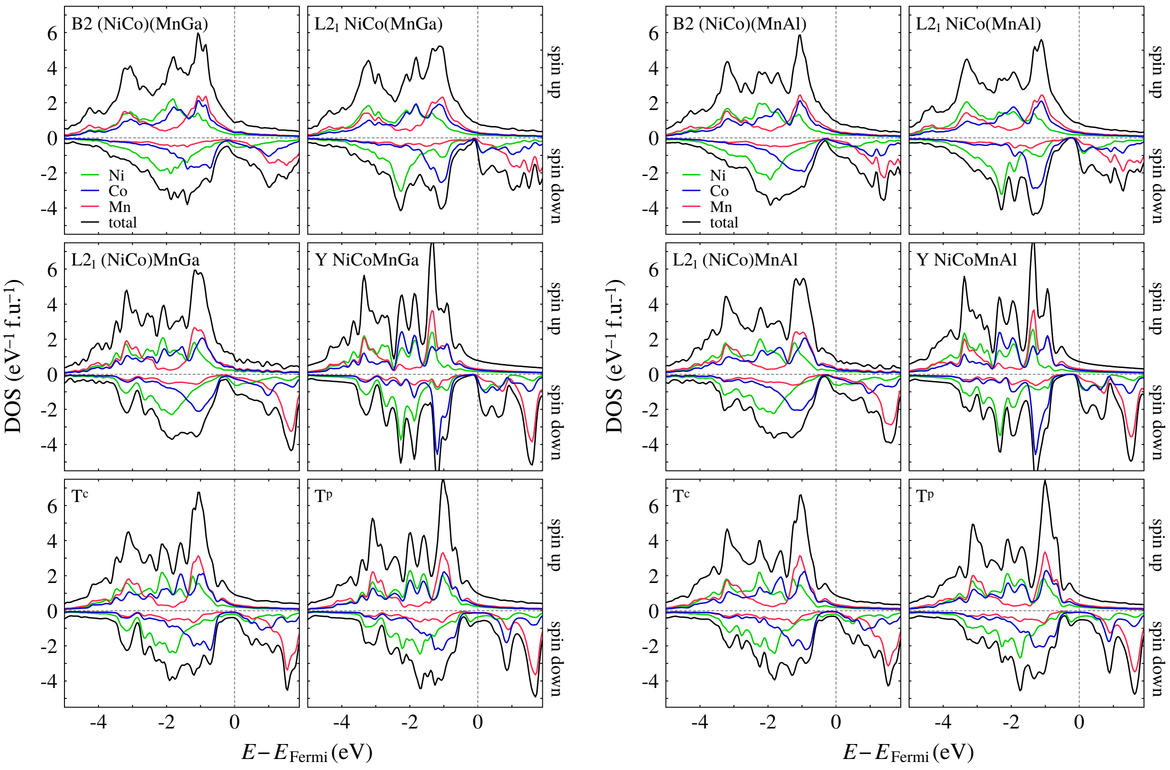

Fig. 6.13 Spin-polarized electronic density of states (DOS) in ferromagnetic NiCoMnGa (left) and NiCoMnAl (right) for the distinct ordered structures as outlined in the main text. The plot for NiCoMnGa from the main text is reproduced here to ease comparison with the NiCoMnAl case, albeit with a different color coding to agree with the element-resolved dispersions in Fig. 6.14.

-1 eV and thus lead to a sharp peak in the DOS. Element-wise, the e_{u} bands have a shared Ni-Co character, while the $t_{1\mathrm{u}}$ bands are predominantly due to Co, being paralleled by the corresponding Ni bands an additional 1 eV lower.

The apparent gap below E_{F} now results from all five bands being gathered closely around E_{F} at the Γ point and splitting up as one moves away from Γ. Specifically the $t_{1\mathrm{u}}$ bands decrease significantly in energy, while one band of dominatingly e_{u} character closely follows the Fermi level along some high-symmetry directions. However, as is visible for instance along the Γ–L-line, over most of the Brillouin zone this band is above E_{F}, limiting the conductivity in the minority spin channel. Thus, we classify NiCoMnGa in the Y structure as a half-semimetal, with an analogous situation in NiCoMnAl (dispersions not shown here).

In Fig. 6.13, the densities of states of NiCoMnAl are shown alongside those for NiCoMnGa, which have already been discussed in the main part. Obviously, the qualitative situation is equal, with specifically Ni/Co disorder as well as tetragonal order closing the

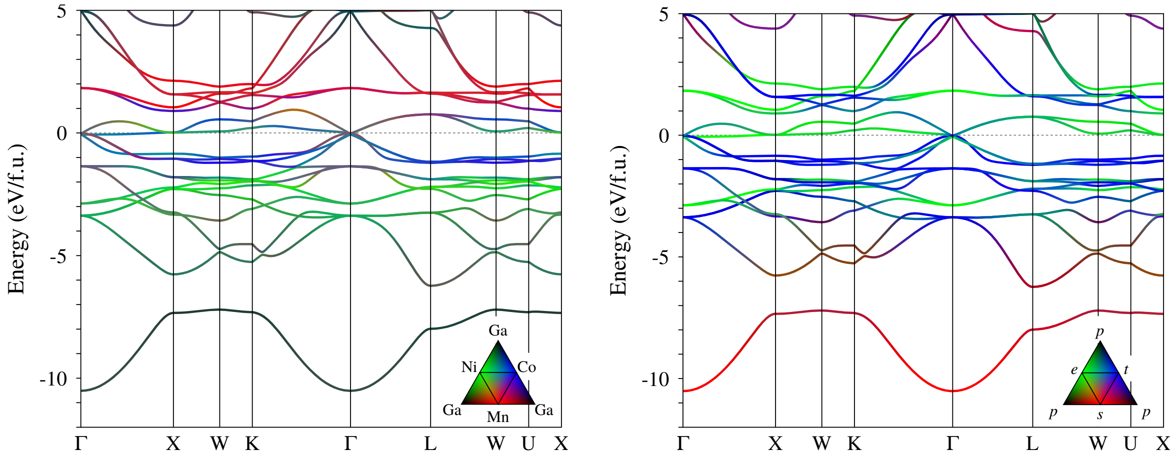

Fig. 6.14 Minority spin band structure of NiCoMnGa in the Y phase. The left panel resolves the elemental character of the states, with green for Ni, blue for Co, red for Mn and black for Ga, while the right panel shows the orbital character, with red for s character, black for p, blue for the d orbitals transforming according to the $T_{2\mathrm{g}}$ and $T_{1\mathrm{u}}$ representations, i.e., those made up of d_{xy}, d_{yz}, and d_{zx}, and finally green for those transforming according to the E_{g} and E_{u} representations, i.e., $d_{x^2-y^2}$ and $d_{3z^2-r^2}$.

pseudo-gap. Interestingly, in NiCoMnAl the pseudo-gap seems slightly more stable with respect to disorder than in NiCoMnGa.

6.6.5 Atomic relaxations in disordered structures

Table 6.4 reports the statistical parameters of the static atomic displacements due to chemical disorder as obtained from analyzing the relaxed configurations computed by DFT. Generally, equal atoms appear to repel each other due to Pauli repulsion, with both the Ni–Co and Mn–Z distances being smaller than the distances between equal atoms. The asymmetry in the Mn/Z-case suggests that in these compounds the Z element should be considered effectively larger than Mn, which is even more pronounced for Z = Ga. This is also reflected in the widths of the distributions of all distances under Mn/Z-disorder, being significantly larger in the Ga case.

Co–Co distances are larger than Ni–Ni distances, which would imply Co being larger than Ni. On the other hand, Co–Z and Co–Mn distances are smaller than the respective values for Ni, showing that the effects of Ni/Co-disorder are beyond such a simple picture of atomic sizes. Also the effect on the widths of the distributions is smaller than for Mn/Z-disorder, presumably due to the larger chemical similarity between Ni and Co.

In the light of this discussion, the slight tetragonal distortions of the $\mathrm{T^p}$ and $\mathrm{T^c}$ structures can be motivated: $\mathrm{T^p}$ is characterized by a planar arrangement of Ni and Co, so the in-plane

Fig. 6.15 Magnitude of magnetic exchange interactions between nearest Mn–Ni, Mn–Co and Mn–Mn pairs in ferromagnetic B2 NiCoMnAl and NiCoMnGa as a function of the lattice constant. Interactions at a larger separation and those involving other pairs of atoms are significantly smaller and thus not shown.

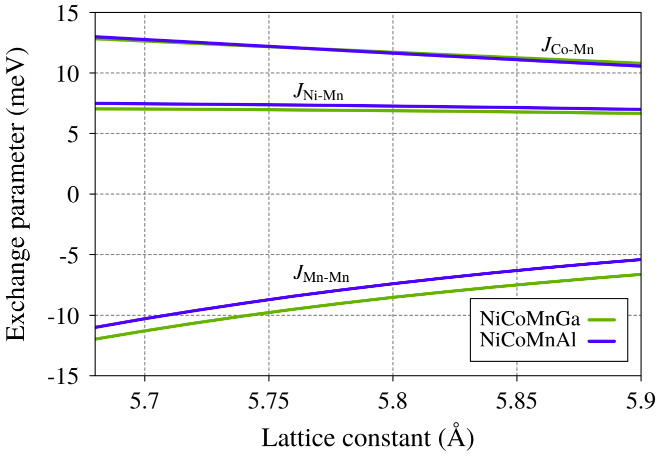

lattice constant a is expanded due to Ni–Ni and Co–Co repulsion, and consequently c being perpendicular to the planes is contracted. For $\mathrm{T^c}$, the converse argument applies, leading to expansion along the columns. Interestingly, the internal degree of freedom in the $\mathrm{T^p}$ structure, corresponding to Mn and Z being shifted away from the Ni planes and towards the Co planes is also already disclosed in the disordered structures, where the Co–Mn and Co–Z distances are always smaller than the respective values for Ni.

6.6.6 Exchange Couplings

Figure 6.15 shows the main coupling constants in NiCoMnAl and NiCoMnGa as a function of the lattice constant for the disordered B2 case, computed in the KKR-CPA framework with the Liechtenstein approach (Liechstenstein et al., 1987). While $\langle 1/2, 1/2, 1/2\rangle$-coordinated Mn–Co and Mn–Ni pairs show a strong ferromagnetic interaction, $\langle 1, 0, 0\rangle$-coordinated Mn–Mn pairs show a strong frustrated antiferromagnetic interaction. With increasing lattice constant, the absolute values of the ferromagnetic Mn–Co and the antiferromagnetic Mn–Mn exchange interactions decrease, while the ferromagnetic Mn–Ni interaction is less affected by changes in the lattice constant. As discussed in the main text, the lattice contraction with ordering is on the order of 0.01 Å. Such differences modify the Mn–Mn interaction by about 0.3 eV, and the other interactions even less. Thus, these effects are minute compared to the vanishing of Mn–Mn frustration under Mn/Z-ordering, and therefore the latter are responsible for the marked concomitant increase in T_C specifically for NiCoMnAl.

Another point to note is that the weaker antiferromagnetic Mn–Mn coupling for NiCoMnAl suggests actually higher T_C for NiCoMnAl than for NiCoMnGa. Even though this is partly compensated by the lower lattice constants, the opposite finding in the experiment again underlines the conclusion of lower degrees of Mn/Z-order in NiCoMnAl.

	NiCoMnGa			NiCoMnAl		
	B2 (NiCo)(MnZ)	L2$_1$ (NiCo)MnZ	L2$_1$ NiCo(MnZ)	B2 (NiCo)(MnZ)	L2$_1$ (NiCo)MnZ	L2$_1$ NiCo(MnZ)
Ni–Ni	1.0029±0.0140	1.0011±0.0045		1.0014±0.0087	1.0003±0.0042	
Ni–Co	0.9962±0.0126	0.9980±0.0031	1.0001±0.0110	0.9974±0.0074	0.9983±0.0028	1.0000±0.0064
Co–Co	1.0057±0.0123	1.0032±0.0027		1.0043±0.0078	1.0033±0.0026	
Mn–Mn	1.0022±0.0094		1.0019±0.0051	1.0033±0.0083		1.0031±0.0037
Mn–Z	0.9894±0.0136	1.0000±0.0078	0.9904±0.0093	0.9937±0.0105	1.0000±0.0081	0.9944±0.0047
Z–Z	1.0212±0.0133		1.0192±0.0112	1.0105±0.0080		1.0090±0.0055
Ni–Mn	1.0042±0.0077	1.0037±0.0041	1.0011±0.0054	1.0036±0.0051	1.0039±0.0042	1.0014±0.0031
Co–Mn	0.9959±0.0074	0.9964±0.0047	1.0004±0.0060	0.9958±0.0052	0.9962±0.0047	1.0000±0.0032
Ni–Z	1.0041±0.0114	1.0022±0.0035	0.9992±0.0106	1.0031±0.0063	1.0025±0.0036	0.9986±0.0048
Co–Z	0.9953±0.0111	0.9979±0.0029	0.9999±0.0104	0.9967±0.0065	0.9976±0.0030	1.0001±0.0054

Table 6.4 Atomic relaxations in relative atomic distances as obtained from DFT calculations, given as mean value and standard deviation (the estimated statistical errors are much smaller). The first three rows refer to closest pairs on the Ni/Co sublattice, the middle rows to pairs on the Mn/Z sublattice (that is, both with $\langle 1,0,0\rangle$ coordination), and the last four to inter-sublattice pairs (having $\langle 1/2,1/2,1/2\rangle$ coordination).

Chapter 7

Half- to Full-Heusler transition in $Ni_{2\text{-}x}$MnSb compounds

7.1 Introduction

The $Ni_{2-x}MnSb$ system comprises materials with many interesting properties and consequently applications. Specifically, in the vicinity of the full-Heusler structure Ni_2MnSb, ferromagnetic shape memory alloys are found (see for instance Chatterjee et al., 2008). At the same time, the half-Heusler compound NiMnSb is the prototypical half-metal (de Groot et al., 1983; Hanssen et al., 1990), making it an interesting material for spintronics applications.

As in most Heusler alloys, atomic order plays a crucial role in the goal of achieving optimal functionality in $Ni_{2-x}MnSb$ alloys. For example, NiMnSb, although predicted to be 100 % spin polarized at the Fermi surface, shows in real-world spintronics components a much lower spin polarization of only about 58 %, as evidenced by Soulen et al. (1998). This discrepancy has been ascribed, besides potential chemical segregation and electronic structure changes at the interfaces, to atomic disorder and deviations from the ideal structure (Orgassa et al., 1999).

While Ni_2MnSb is found to adopt the full-Heusler $L2_1$ structure (Castelliz, 1955), NiMnSb was demonstrated to show the half-Heusler $C1_b$ structure (Webster, 1968). Interestingly, this $C1_b$ structure, characterized by the $F\bar{4}3m$ space group and an inequivalent occupancy of the 4a, 4b, 4c and 4d Wyckoff positions by Ni, structural vacancies, Mn and Sb, respectively, is stable for a wide range of x on the Ni lean side of the $Ni_{2-x}MnSb$ phase diagram as evidenced by Nagasako et al. (2015); Webster and Mankikar (1984). Note that the $C1_b$ structure has the same space group as the Y structure discussed in Chapter 6 with the difference that one of the four sublattices is empty. As function of x as well as for a

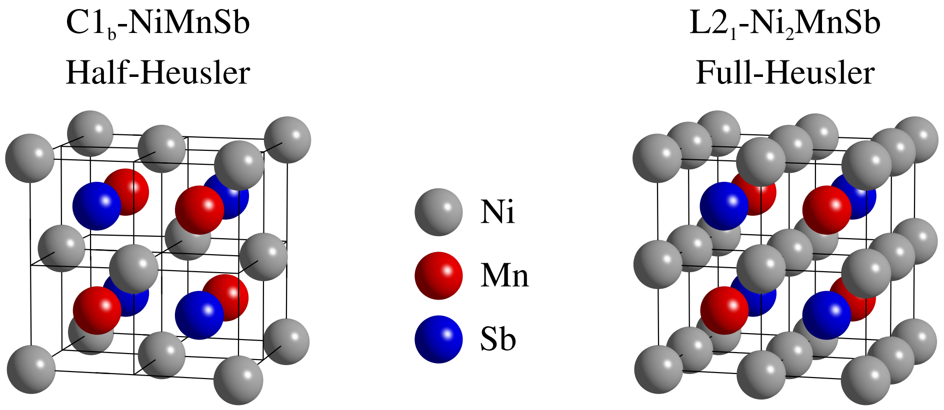

Fig. 7.1 Depiction of the half-Heusler $C1_b$ (left) and full-Heusler $L2_1$ (right) structures. While NiMnSb and Ni_2MnSb are illustrated as prototypical representatives of the crystal structures, clearly any $C1_b$ structure can transfer into a $L2_1$ structure via accommodating the Ni atoms equally on the 4a and 4b Wyckoff sites.

given x as a function of temperature, a transition from the $C1_b$ structure to the full-Heusler $L2_1$ structure with space group $Fm\bar{3}m$ is observed. For a depiction of the $C1_b$ and $L2_1$ crystal structures please refer to Fig. 7.1. The most detailed phase diagram available for the $Ni_{2-x}MnSb$ system was recently established by Nagasako et al. (2015) via Differential Scanning Calorimetry (DSC) together with High-Resolution Scanning Transmission Electron Microscopy (HRSTEM). Furthermore, an earlier work by Webster and Mankikar (1984) provides ex-situ neutron diffraction results for various compositions x at a selected temperature proving the stability of the $C1_b$ phase in the system. Yet, these published investigations do not resolve the microscopic origin of the $C1_b$-$L2_1$ phase transition.

Presumably, for $Ni_{2-x}MnSb$ compounds in the high temperature $L2_1$ phase, the Ni deficiency is accommodated via the structural vacancies being equally distributed on both Ni sublattices. Then, when lowering the temperature, a transition to a case where one Ni sublattice is hosting more vacancies than the other occurs. This corresponds to a symmetry breaking and hence a phase transition from the $L2_1$ to the $C1_b$ phase. However, this mechanism has never been confirmed. It is also thinkable that the Ni deficiency in the $L2_1$ phase is accommodated by antisites and/or the annihilation of structural vacancies. The temperature dependent, complex interplay of structural vacancies and antisite disorder at the $C1_b$-$L2_1$ transition can only be revealed by in-situ scattering experiments where such information is directly contained in the peak area of the superstructure reflections.

7.2 Sample Preparation

In order to study the nature of the $C1_b$-$L2_1$ transition in the $Ni_{2-x}MnSb$ system, a series of polycrystalline bulk samples with differing Ni composition has been prepared via induction melting of high purity elements. Specifically, 5 samples with x = 0.25, 0.4, 0.5, 0.75 and 0.95 have been cast. Subsequent to casting, the samples were solution annealed for 3 days at 1173 K, a heat treatment previously reported to be effective by Nagasako et al. (2015) in order to homogenize the samples. After solution annealing, samples were water quenched. The sample composition was measured in the solution annealed samples as tabulated in Chapter 1 showing an excellent agreement to the nominal sample compositions. From the quenched bulk ingots, samples for DSC and magnetization measurements have been cut using a low speed diamond saw. The remaining sample material was crushed and ground to fine powders with a grain size $< 125\,\mu$m. Due to the brittleness of the material, additional strain-release/recovery heat treatments of the powders were not necessary, given that no strain related peak broadening was observed in X-ray diffraction after powder preparation.

7.3 Results

The experimental work carried out on the $Ni_{2-x}MnSb$ samples can be divided into two parts. First, a pre-characterization of the samples mostly via bulk measurements partially reproducing and partially exceeding the state of the art knowledge about this material system was performed and second, an in-situ neutron diffraction study was carried out at the 3T2 neutron powder diffractometer at the Laboratoire Léon Brillouin in Saclay, France. These measurements were complemented by room temperature X-ray powder diffraction as well as room temperature high resolution neutron powder diffraction measurements at the SPODI diffractometer at the FRM II in Garching, Germany.

7.3.1 Structural and magnetic properties

In order to evaluate the quality of the produced $Ni_{2-x}MnSb$ samples, DSC measurements have been performed over a wide temperature range from room temperature to 1500 K in order to determine the Curie temperatures T_C of the compounds as well as the $C1_b$-$L2_1$ transition temperatures and the melting temperatures T_m. Fig. 7.2 shows these DSC measurements in the stated temperature range for all 5 compositions. T_C has been determined via fitting the left and right part of the calorimetric signal as described in Chapter 1 while the values for the $C1_b$-$L2_1$ transition were determined following the definition by Nagasako et al. (2015) where the maximum of the calorimetric peak was taken as the transition temperature.

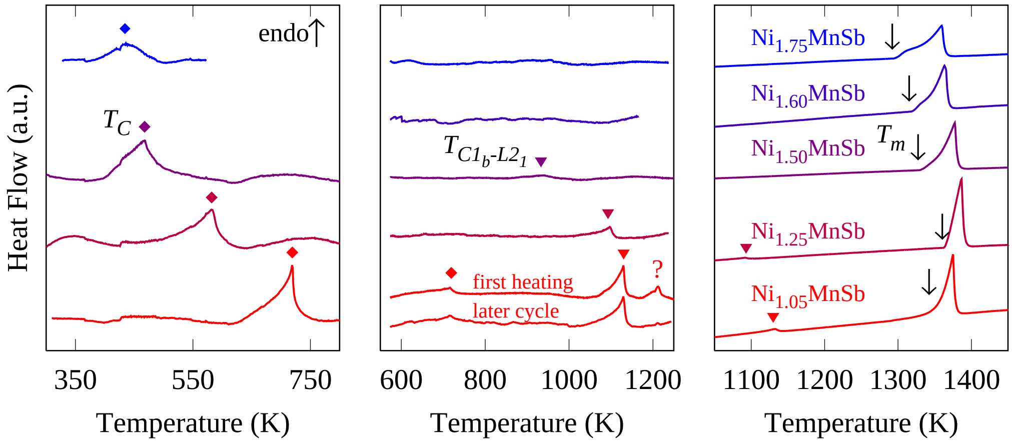

Fig. 7.2 High and low temperature DSC measurements for a series of compositions from the $Ni_{2-x}MnSb$ system showing magnetic and structural phase transitions. The curves were recorded on heating employing a heating ramp of 10 K/min. Specifically, depending on the composition, a ferromagnetic-paramagnetic transition with a characteristic Curie temperature T_C, a $C1_b$-$L2_1$ transition and melting of the samples is observed. The low temperature DSC curves (left panel) were recorded as part of the B.Sc. thesis by Hollender (2016) under the supervision of the author of this thesis.

Note, that usually in diffusion controlled phase transitions, the maximum of the calorimetric peak is dependent on kinetic effects and thus, rather the onset of the peak should be used as reliable definition of the transition temperature. However, due to the low peak intensity, the determination of the peak onset is difficult in this case, especially for samples with high Ni content, and hence, the peak maximum was used as the transition temperature. For the melting peak, the peak onset is better defined and was used as the value for the melting temperature.

Fig. 7.3 summarizes the transition temperatures obtained from the calorimetric measurements together with the available literature data by Nagasako et al. (2015); Webster and Mankikar (1984). Additionally shown are the transition temperatures retrieved from in-situ neutron diffraction as presented in the following section. Evidently, the determined values are in very good agreement to the literature data while clearly, the transition temperatures determined by neutron diffraction are systematically lower than the ones determined by DSC. This discrepancy is most likely the result of the definition of the transition temperature via the peak maximum instead of the onset temperature. To the author's knowledge, there are no literature reports on the melting temperatures in this system. However, the exact determination of the melting temperatures was necessary in order to establish a safe measurement protocol for in-situ neutron diffraction not risking to melt the samples in the furnace.

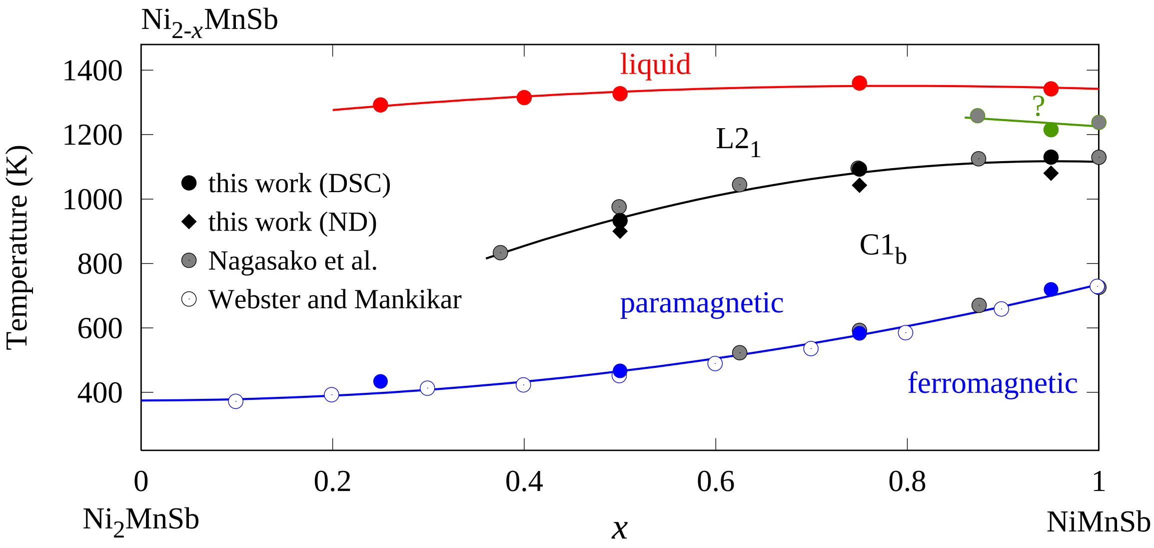

Fig. 7.3 Phase diagram of the pseudo-binary $Ni_{2-x}MnSb$ system showing data from this thesis, as well as literature data by Webster and Mankikar (1984) and Nagasako et al. (2015).

Furthermore, the presented experiments reproduce the existence of an undefined calorimetric peak in the DSC measurements of the $Ni_{1.05}MnSb$ sample previously pointed out by Nagasako et al. (2015). Interestingly, it appears that its intensity is decreased after several heating and cooling cycles as shown in Fig. 7.2. Yet, also in-situ neutron diffraction (reported below) was not able to reveal the nature of this peak since it finds no correspondence in the peak intensities of the diffraction patterns as demonstrated in Fig. 7.8.

As an overall tendency, it is observed that the magnetic transition temperature as well as the $C1_b$-$L2_1$ transition temperature decrease with increasing Ni content. The last composition showing a $C1_b$-$L2_1$ transition in the experiments conducted in this thesis is $Ni_{1.50}MnSb$ while Nagasako et al. (2015) report to observe a transition also for $Ni_{1.625}MnSb$. For samples with higher Ni content it is not entirely clear whether no transition occurs (i.e. already the quenched samples are $L2_1$ ordered) or whether the signal associated with the transition is too small to be detected. In contrast to the $C1_b$-$L2_1$ transition temperature and the magnetic transition temperature, the melting temperature T_m is relatively constant as a function of x.

In order to pre-characterize the samples and as a complement to neutron diffraction, room temperature X-ray diffraction measurements have been performed on the powder samples. The results are shown in Fig. 7.4 for four compositions. The patterns have been Rietveld-refined using the FullProf suite (Rodriguez-Carvajal, 1990, 1993; Rodriguez-Carvajal and Roisnel, 1998; Roisnel and Rodriguez-Carvajal, 2000). As can be seen, the refined curves (black lines) show excellent agreement to the measured data (colored lines). Assuming fully ordered Mn and Sb sublattices and fixing the composition, the distribution of Ni and

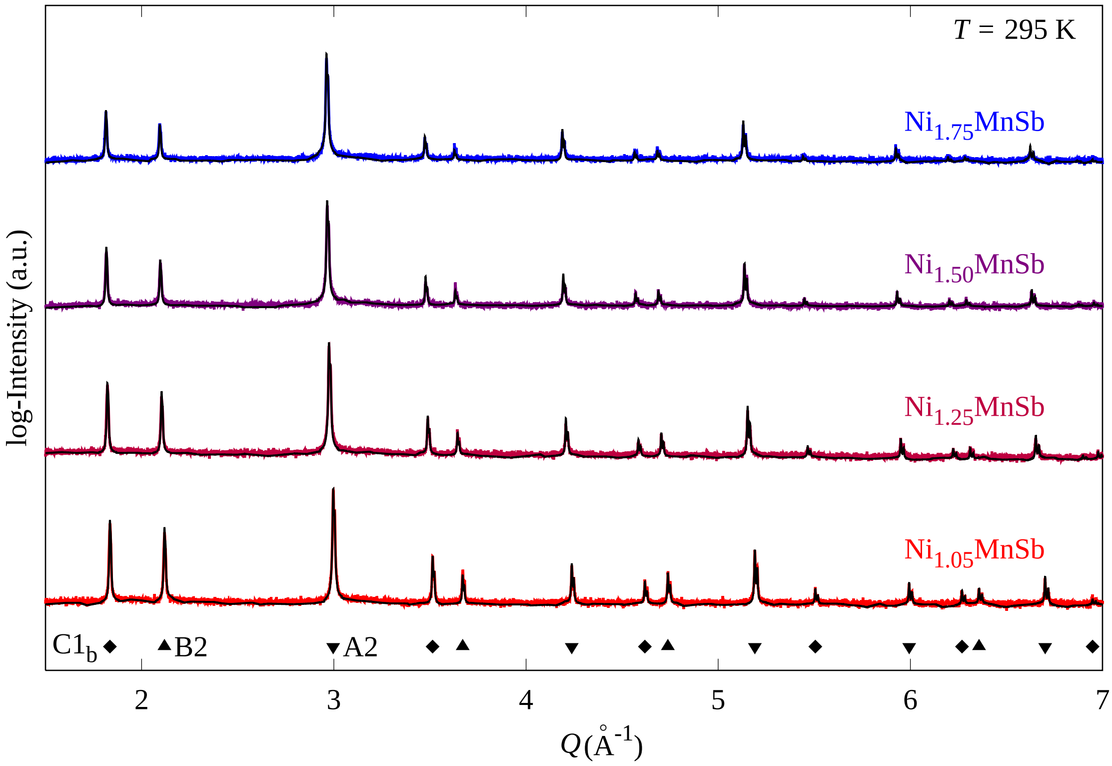

Fig. 7.4 XRD diffractograms of $Ni_{2-x}MnSb$ samples on a logarithmic intensity scale showing the measured data (colored curves) and the Rietveld-refined diffractograms (black curves). The patterns have been recorded at room temperature using Cu-K_α radiation. Samples have been quenched from 1173 K. Peak families are indicated below the diffractograms.

Compound	rel. Ni occ. (4a)	rel. Ni occ. (4b)	lattice parameter a (Å)
$Ni_{1.05}MnSb$	1.077(8)	-0.027(8)	5.93015(5)
$Ni_{1.25}MnSb$	1.074(10)	0.176(10)	5.97334(6)
$Ni_{1.50}MnSb$	1.125(12)	0.375(12)	5.99265(7)
$Ni_{1.75}MnSb$	1.097(20)	0.653(20)	5.99962(3)

Table 7.1 Refined relative site occupancies of Ni and lattice parameters for room temperature X-ray diffractograms of a series of $Ni_{2-x}MnSb$ samples quenched from 1173 K.

vacancies on the 4a and 4b sites has been determined in the refinement process. The refined occupancies together with the determined lattice parameters are given in Tab. 7.1.

Clearly, for all compositions the retrieved nuclear structure is $C1_b$ since Rietveld refinement reveals, besides the full order of Mn and Sb on the 4c and 4d sites, also a fully ordered 4a and 4b site, evidenced by a refined relative occupancy > 1 on the 4a site and hence a maximally depleted 4b site. The deviations from 1 certainly arise from slightly diverging sample compositions and/or types of disorder not accounted for by the employed structural

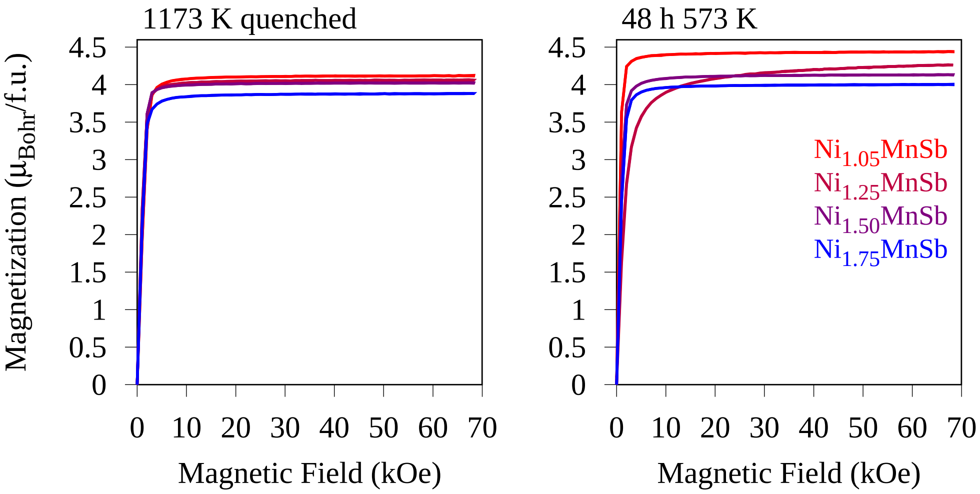

Fig. 7.5 $M(H)$ SQUID measurements at 6 K of $Ni_{2-x}MnSb$ samples in two different annealing conditions, i.e. 1173 K-quenched (left panel) and 48 h annealed at 573 K (right panel).

model. Yet, the overall great conformity of the refined and measured diffractograms in combination with the previously reported evidence for the $C1_b$ structure draws a clear picture of the room temperature nuclear structure of the compounds. Note that the observed perfect $C1_b$ order is to some extent surprising considering that the samples have been quenched from the $L2_1$ regime at 1173 K. Yet, apparently, kinetics are so fast that no disorder can be quenched-in.

Further, it is observed that the lattice parameter increases from NiMnSb towards Ni_2MnSb, a fact previously pointed out by Webster and Mankikar (1984). Comparing the lattice parameters obtained in this investigation with the ones stated by Webster and Mankikar (1984) shows excellent agreement with deviations between 0.03 % and 0.14 %. In their recent neutron single crystal diffraction study, Brown et al. (2010) report a slightly lower lattice parameter for stoichiometric NiMnSb of 5.909 Å, but, given different thermal treatments of the samples, all reported lattice parameters are in reasonable agreement to the here presented data set.

Finally, to conclude the bulk characterization of the samples, low temperature SQUID magnetization measurements have been performed. Fig. 7.5 shows $M(H)$ curves for four compositions in two annealing conditions each. In the left panel, $M(H)$ curves for 1173 K-quenched samples are shown while the right panel portrays $M(H)$ curves for 1173 K-quenched plus 48 h at 573 K annealed samples. The spontaneous magnetization M_s was obtained via linearly fitting the linear part of the $M(H)$ curve and determining the y-axis intercept. The obtained values are tabulated in Tab. 7.2.

Compound	M_s - 1173 K quenched (μ_B/f.u.)	M_s - 48 h 573 K (μ_B/f.u.)
$Ni_{1.05}MnSb$	4.11	4.44
$Ni_{1.25}MnSb$	4.03	4.23
$Ni_{1.50}MnSb$	4.03	4.15
$Ni_{1.75}MnSb$	3.88	3.98

Table 7.2 Magnetic moments per formula unit at 6 K as obtained from SQUID measurements for a series of $Ni_{2-x}MnSb$ samples quenched from 1173 K and quenched plus additionally annealed for 48 h at 573 K.

The data shows an increasing M_s with decreasing Ni content. Webster and Mankikar (1984) report a maximum of M_s = 4.3 μ_B/f.u. for x = 0.45 while M_s decreases towards high and low Ni contents. This observation is not reproduced by the here presented measurements. Instead, a systematic decrease of M_s is observed from NiMnSb to Ni_2MnSb for both sample families. For NiMnSb, according to the Generalized Slater Pauling (GSP) rule for half-Heusler half-metals (see Galanakis et al., 2006), a magnetization of 4.0 μ_B/f.u. is expected which was experimentally confirmed by Webster and Mankikar (1984). The here reported M_s of 4.11 μ_B/f.u. for the $Ni_{1.05}MnSb$ compound is in accordance to the work by Webster and Mankikar (1984) slightly larger than the value for NiMnSb. Specifically, Webster and Mankikar (1984) report M_s values of 4.04 μ_B/f.u. and 4.07 μ_B/f.u. for NiMnSb and $Ni_{1.1}MnSb$, respectively, in good agreement to the value of the 1173 K-quenched sample reported here. Interestingly, in the here presented study, the annealed samples show systematically higher M_s values than the as-quenched samples. This is rather surprising, given that the previously presented X-ray diffraction results show an ideal $C1_b$ order already after quenching. Hence, low temperature annealing in the $C1_b$ stable regime should in principle not affect the nuclear structure. However, clearly, it is possible that slight quenched-in Mn-Sb disorder that goes unnoticed in the diffraction experiments leads to the observed increase of magnetization. Another possible explanation emerges from the in-situ neutron diffraction results presented in the following section. Here, a lattice relaxation in the temperature range between 573 K and 873 K was observed for most samples that finds no correspondence in the structure factors. It could be this lattice contraction which changes the electronic structure in a way that increases the magnetic moment on Mn and/or Ni. However, the reason of the decrease of the lattice parameter is up to this point unclear.

7.3.2 Neutron powder diffraction

In order to clarify the mechanism of the $C1_b$-$L2_1$ phase transition, in-situ neutron powder diffraction experiments have been performed at the 3T2 spectrometer at the Laboratoire Léon

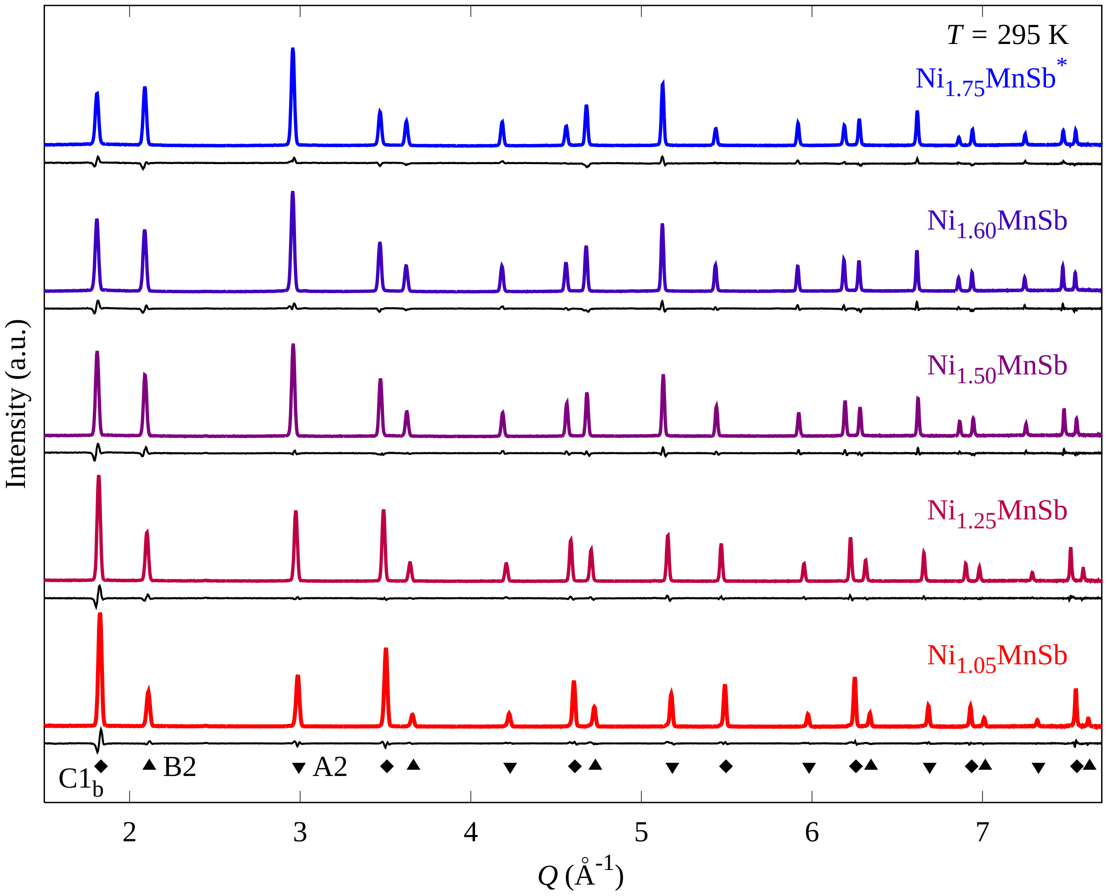

Fig. 7.6 Neutron diffractograms of $Ni_{2-x}MnSb$ samples showing the measured data (colored curves) and the residues of the Rietveld refinement (black curves). The patterns have been recorded at room temperature at the SPODI diffractometer. Samples have been furnace cooled from high temperatures, except of $Ni_{1.75}MnSb$ (marked with *) which has been quenched from 1173 K. Peak families are indicated below the diffractograms.

Brillouin in Saclay, France. After the in-situ measurements, additionally, room temperature high resolution diffractograms have been recorded for all samples at the SPODI diffractometer at the FRM II in Garching, Germany in order to provide an optimal data set for quantitative analysis and Rietveld refinement. First, these room temperature diffractograms and some structural considerations are presented, while subsequently, the analysis is extended to the temperature dependent in-situ measurements.

Fig. 7.6 shows the room temperature neutron diffraction patterns for 5 compositions of the $Ni_{2-x}MnSb$ system. The curves are normalized in a way that the intensity of the fundamental A2 peaks of the diffractograms have intensities resembling the calculated structure factors. From Ni_2MnSb to NiMnSb, the A2 structure factor per formula unit increases which is

Compound	rel. Ni occ. (4a)	rel. Ni occ. (4b)	lattice parameter a (Å)	Mn magn. moment (μ_{Bohr}/f.u.)	Ni magn. moment (μ_{Bohr}/f.u.)
$Ni_{1.05}MnSb$	0.981(3)	0.069(3)	5.94690(2)	4.04(11)	0.03(07)
$Ni_{1.25}MnSb$	1.011(2)	0.239(2)	5.97013(2)	4.04(12)	-0.02(5)
$Ni_{1.50}MnSb$	1.060(3)	0.440(3)	6.00095(2)	3.46(14)	0.264*
$Ni_{1.60}MnSb$	1.079(4)	0.521(4)	6.00709(2)	2.81(17)	0.264*
$Ni_{1.75}MnSb$	1.073(7)	0.677(7)	6.00523(4)	2.61(24)	0.264*

Table 7.3 Refined relative site occupancies of Ni, lattice parameters and magnetic moments for room temperature neutron diffractograms of a series of $Ni_{2-x}MnSb$ samples slow cooled from high temperatures. Note, the $Ni_{1.75}MnSb$ sample was quenched from 1173 K instead of slow furnace cooling. * indicates that the labeled magnetic moments were set to the value of 0.264 μ_B/f.u. in the refinement applying the limits outlined in the text.

visible in the increasing A2 peak intensities. From the presented curves, it is evident that the relative intensity of the $C1_b/L2_1$ peak family decreases strongly with increasing Ni content while, at the same time, the relative B2 intensity increases slightly. According to Fig. 7.3, all compositions are at room temperature in the ferromagnetic regime. This means that besides the nuclear structure also a magnetic structure needs to be taken into consideration in order to achieve satisfying refinement results. Concerning this matter, referring to the magnetization measurements presented above and also to literature reports by Brown et al. (2010) and Galanakis et al. (2006), a collinear ferromagnetic structure was considered. Tab. 7.3 shows the refined values of the Ni sublattice occupancies, the lattice parameter and the refined magnetic moment on Ni and Mn for all compositions. Note that in order to enforce realistic magnetic structures, the small magnetic moment on Ni has been limited to at maximum the theoretically calculated value of 0.264 μ_B/f.u. (Galanakis et al., 2006).

Evidently, the refined site occupancies from room temperature neutron diffraction suggest a fully $C1_b$ ordered structure, in line with the values retrieved from X-ray diffraction presented above. This is especially noticeable given that the neutron samples, with the exception of $Ni_{1.75}MnSb$, were in a different heat treatment condition than the X-ray samples. Specifically, the X-ray samples and the $Ni_{1.75}MnSb$ neutron diffraction sample were quenched from 1173 K while the remaining neutron diffraction samples were slowly furnace cooled from high temperatures. However, since already the as-quenched samples show a fully ordered structure, the same is of course expected for the slow cooled samples.

Comparing the lattice parameters between the X-ray and neutron diffraction measurements shows slight deviations of at maximum 0.28 %. These deviation are due to the different heat treatment condition of the neutron and X-ray samples as discussed in detail below. The

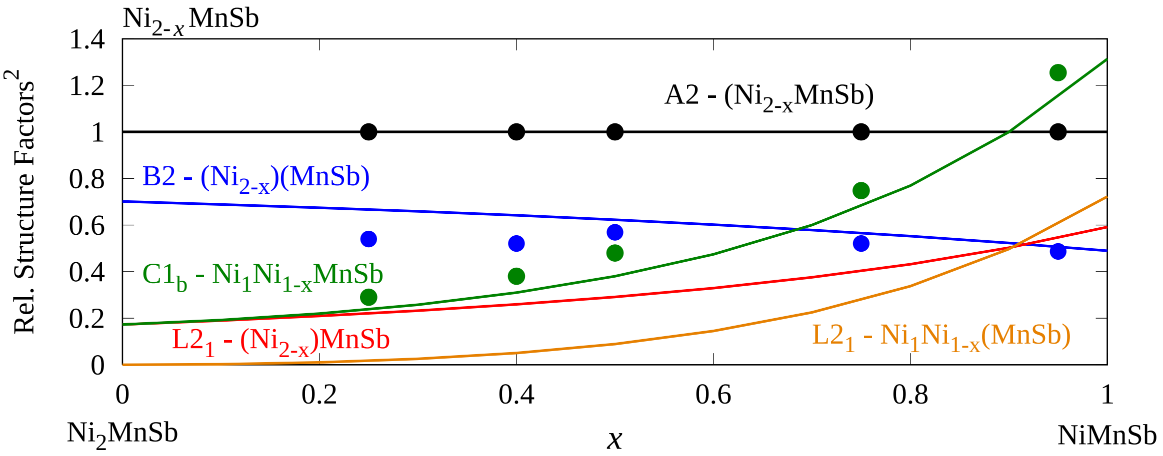

Fig. 7.7 Experimentally obtained relative absolute squared structure factors (circles) for the A2, B2 and C1_b/L2_1 peak families for 5 compositions of the $Ni_{2-x}MnSb$ system together with the calculated absolute squared structure factors under various types of disorder (lines). As introduced before, brackets indicate a state of disorder between the constituents.

increase of the lattice parameter with increasing Ni content is clearly revealed in the neutron diffraction results. The refinement of the magnetic structure with the model outlined above yields a decreasing Mn magnetic moment at room temperature with increasing Ni content. Clearly, the reason for this is partially the decreasing low temperature magnetic moment of the unit cell with increasing Ni content as revealed by the presented magnetization measurements. However, additionally, the decreasing magnetic transition temperature towards higher Ni contents and consequently the lower homologous temperature explains the decrease of the Mn magnetic moment. Due to the low value of the Ni magnetic moment, its refinement is less reliable. In fact, for high Ni contents, the refinements yielded unphysically large Ni moments. Yet, presumably, these large moments are rather a compensation of deficiencies of the nuclear model with respect to the low Q peaks. Hence, it is reasonable to restrict the Ni moment to physically reasonable values as outlined above.

Besides the results from Rietveld refinement, it is the intention to present a more basic evaluation of the neutron diffraction data that does not rely on certain structural models. Specifically, the structure factors of the peak families, i.e. A2, B2 and C1_b/L2_1, can be directly extracted from the peak intensities of the diffractograms. Concerning this matter, the peak intensities as retrieved via fitting individual peaks or integrating over them have to be corrected for their individual multiplicities, the Lorentz factor and the Debye-Waller factor. After this correction, the peak intensities for all peaks should, with respect to their intensity, be divided into 3 groups while the relative intensity of these groups is given directly by the relative absolute squared structure factors. In Fig. 7.7 the measured absolute squared structure factors of the A2, B2 and $\mathrm{C1_b/L2_1}$ peak families relative to the A2 peak family are depicted together with the calculated relative absolute squared structure factors of the A2-(Ni_{2-x}MnSb), B2-(Ni_{2-x})(MnSb), $\mathrm{L2_1}$-(Ni_{2-x})MnSb, $\mathrm{L2_1}$-$\mathrm{Ni_1Ni}_{1-x}$(MnSb) and $\mathrm{C1_b}$-$\mathrm{Ni_1Ni}_{1-x}$MnSb structures. The bracket notation here follows the scheme introduced in Chapter 6 where the constituents inside the brackets are mixed. This means for example that in an A2-(Ni_{2-x}MnSb) structure, all elements occupy the lattice positions randomly, or, for the A2 peaks, that all lattice sites contribute in phase to the peak intensity and are consequently independent from the state of order. The structure factor for the A2 peak family is calculated as

$$F_N^{\mathrm{A2}} = b_{4a} + b_{4b} + b_{4c} + b_{4d} \tag{7.1}$$

For the B2 family the structure factor is calculated as

$$F_N^{\mathrm{B2}} = b_{4a} + b_{4b} - b_{4c} - b_{4d} \tag{7.2}$$

and the expression for the structure factor of the $\mathrm{C1_b/L2_1}$ family is

$$F_N^{\mathrm{C1_b/L2_1}} = b_{4a} - b_{4b} + \mathrm{i}b_{4c} - \mathrm{i}b_{4d} \tag{7.3}$$

In these expressions, b stands for the average coherent neutron scattering length on the indicated lattice site.

Comparing the measured data with the calculated absolute squared structure factors shows that indeed the half-Heusler $\mathrm{C1_b}$ structure as introduced above is the most plausible structural model for the investigated samples. Specifically, it is evident that the data points for the $\mathrm{C1_b}$ structure factors follow the calculated $\mathrm{C1_b}$ values rather than the $\mathrm{L2_1}$ values. However, interestingly, it seems that the B2 peak intensity is systematically to low and the $\mathrm{C1_b}$ intensity is systematically to high with respect to the calculated values. This could for instance be the result of different kinds of disorder not considered here, e.g. a state of mixing between Mn and vacancies. In other words, if a Mn on a 4c site is exchanged for a vacancy on the 4b site, this would have exactly the described effect, i.e. a decrease in the B2 peak intensity and an increase in the $\mathrm{C1_b/L2_1}$ intensity. Yet, there are multiple possibilities for lattice site disorder evoking the described effect that will be discussed in the detail below. Also plausible are of course slight deviations from the perfect stoichiometry.

In order to reveal the temperature dependent phase stabilities in the system, in-situ neutron diffraction measurements have been performed for four Ni_{2-x}MnSb compositions at temperatures between 300 K and 1173 K at the 3T2 diffractometer. For $\mathrm{Ni_{1.05}}$MnSb, $\mathrm{Ni_{1.25}}$MnSb and $\mathrm{Ni_{1.50}}$MnSb, heating and cooling curves are presented while $\mathrm{Ni_{1.60}}$MnSb was only measured

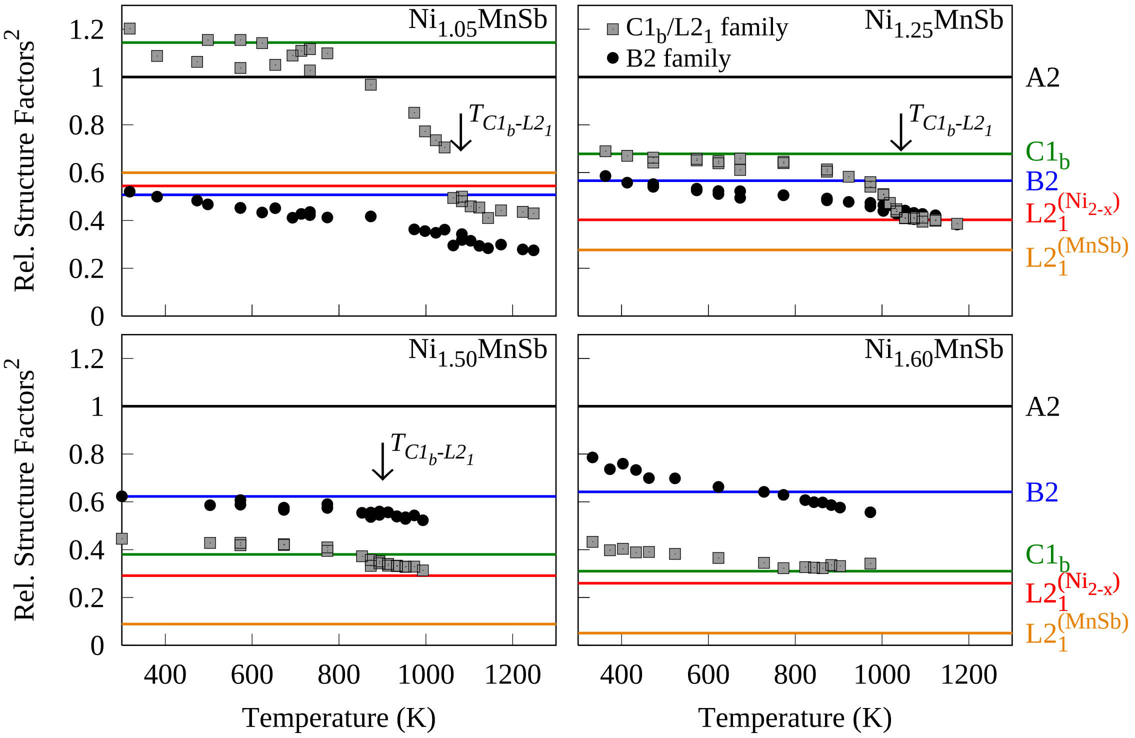

Fig. 7.8 Relative absolute squared structure factors for the B2 and $C1_b/L2_1$ peak families as function of temperature as obtained by in-situ neutron diffraction measurements for four compositions of the $Ni_{2-x}MnSb$ system. The colored lines indicate the calculated structure factors for various types of disorder. Note, plotted is the absolute square of the B2 and $C1_b/L2_1$ structure factors relative to the absolute squared A2 structure factor.

on heating. Due to relatively long acquisition times, it was not possible to measure the samples continuously upon heating/cooling. Instead, isothermal measurements have been performed at various temperatures. From the diffractograms, temperature dependent absolute squared structure factors have been extracted which are shown in Fig. 7.8. Also for the 3T2 data, this was done again by fitting the diffraction patterns and extracting the individual peak intensities. In order to retrieve the absolute squared structure factors, these peak intensities were corrected for the Lorentz factor, the multiplicities and the Debye-Waller factor. Due to partial shielding from the high-temperature furnace, the peak intensities as obtained at 3T2 were additionally subject to an unphysical decay of peak intensities towards large Q values. In order to obtain correction factors for this effect, after the 3T2 in-situ measurements, all samples have been remeasured at the SPODI diffractometer, the results of which were presented above in Fig. 7.6. With these correction factors, the LLB data could be analyzed quantitatively as presented in Fig. 7.8. It can be seen that for all samples, the low-temperature absolute squared structure factors on heating and cooling resemble the calculated absolute squared structure factors for the $C1_b$ structure with full order on the 4a/4b sites as well as on the 4c/4d sites. For the $Ni_{1.60}MnSb$ sample, both the B2 and $C1_b/L2_1$ intensity are slightly larger than expected for the $C1_b$ structure, yet this can clearly be an effect of a slightly diverging composition. In $Ni_{1.05}MnSb$, the $C1_b$ structure factor at low temperatures for the heating curve is slightly higher than for the cooling curve. Besides that, heating and cooling curves show no significant differences for the measured samples.

Upon heating, two overall effects are observed. First, the samples undergo a second order transition from the $C1_b$ to a $L2_1$-type structure visible in the $C1_b/L2_1$ intensity decreasing as a function of temperature. This transition is most pronounced in $Ni_{1.05}MnSb$ while both the difference in intensity between the two phases as well as the transition temperature decrease with increasing Ni content. While for $Ni_{1.50}MnSb$, still a clear transition is observed, for $Ni_{1.60}MnSb$, the peak intensity of the $C1_b/L2_1$ family seems to decrease rather continuously with temperature.

As expected, the structure factor analysis suggests that the observed transition is between a fully ordered $C1_b$ and a $L2_1$ structure with Ni/vacancy disorder on the 4a and 4b sites, if only considering the $C1_b/L2_1$ peak family. This also explains the smaller effect with respect to the decrease of $C1_b$ peak intensities with increasing Ni content since simply the structure factor difference of the $C1_b$ and $L2_1$ phase diminishes. Considering the B2 peak family however, it is clear that the ordering process has to be more complex than the simple picture of a mixing of Ni and vacancies on the 4a and 4b sites. Evidently, the squared structure factor of the B2 family decreases with temperature. Yet, an ordering process exclusively on the 4a/4b sites with Ni as well as Mn/Sb strictly remaining on their sublattices would leave the B2 intensity unaltered. Hence, a decreasing B2 intensity directly translates into an intermixing between the Mn/Sb and the Ni sublattices. The exact mechanism of this intermixing cannot be deduced solely from the data presented here. In fact, due to the large number of possible kinds of disorder it might not at all be possible to solve this question by experimental means only. Rather, comprehensive density function theory (DFT) calculations of defect energies might be necessary in order to reveal a likely mechanism that can then be tested against the experimental evidence. Nonetheless, at this point one possible and to the author's understanding realistic mechanism in line with the experimental observation will be outlined.

A peculiar feature of the ideally empty sublattice in half-Heusler compounds is the possibility of thermal vacancy annihilation. This would imply that the constituents rearrange on the lattice sites, reducing the overall number of unit cells. Alling et al. (2006) calculated defect energies for the related stoichiometric NiMnSb compound by means of DFT. Taking into consideration these reported defect energies, the most plausible scenario for vacancy annihilation in NiMnSb is the following: In order to reduce the amount of structural vacancies, the atoms of entire unit cells need to be rearranged onto the structural vacancy sites. Hence, for dissipating an entire unit cell, 1 Ni, 1 Mn and 1 Sb atom need to be redistributed. An energetically cheap and straightforward way to do so is first to move 1 Sb atom onto a Mn site. Now 2 Mn atoms and 1 Ni atom need to be redistributed which hence move to vacancy sites. According to Alling et al. (2006) the energy of this process is 2.67 eV and it creates 4 defects. Energetically even more favorable is to move Mn on Ni sites and Ni on vacancy sites. A process with an activation energy of 2.63 eV would be to move 1 Sb atom onto a Mn site, 1 Mn atom on a vacancy site, 1 Mn atom onto a Ni site and 2 Ni atoms onto vacancy sites which creates 5 defects. An even cheaper mechanism is to move 1 Sb atom onto a Mn site, 2 Mn atoms onto a Ni site and 3 Ni atoms onto vacancy sites which has an energy of 2.59 eV while creating 6 defects. Clearly, due to the higher entropy and lower energy, the 6 defects mechanism is the most likely process for vacancy annihilation in stoichiometric NiMnSb which can however change for off-stoichiometric compounds with higher Ni contents. Even though, due to interaction effects, the defect energies reported by Alling et al. (2006) are not necessarily suited for an extrapolation towards extremely high defect densities, the presented considerations give a good understanding of realistically occurring mechanisms. In the case of the high temperature $L2_1$-type structure where Ni and vacancies are in a first approximation randomly occupying their sublattices, similar calculations as for the $C1_b$ case would be needed in order to make justified statements about defect energies and annihilation mechanisms. Nonetheless, it is plausible to assume that vacancy annihilation occurs in line with the above presented $C1_b$ mechanisms via Sb migrating onto the Mn lattice, Mn migrating to the Ni/vacancy lattices while on these lattices the Ni content increases and the vacancy content decreases. This would lead to a situation where the high temperature $L2_1$ phase shows a random occupancy of Ni, Mn and vacancies on the 4a and 4b site while the 4c and 4d sites still show Mn/Sb order which is however necessarily partially reduced due to the unequal Mn and Sb composition on the sublattices. The result of this vacancy annihilation would be a decreased B2 and $L2_1$ intensity which is overall consistent with the experimental observations.

Finally, Fig. 7.9 shows temperature dependent lattice parameters as obtained from in-situ measurements at 3T2. While overall, the lattice parameters obtained from neutron diffraction at SPODI and X-ray diffraction show good conformity to the lattice parameters observed at 3T2, the temperature dependent lattice parameter curve shows interesting features. Upon heating, in all samples a lattice parameter contraction is observed at intermediate temperatures that is compensated again at higher temperatures. Especially pronounced is this contraction

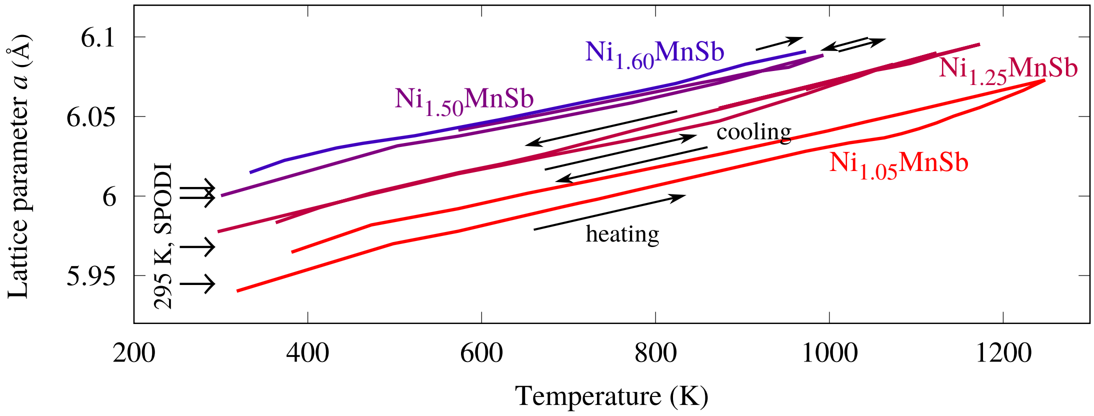

Fig. 7.9 Temperature dependent lattice parameters for four compositions of the $Ni_{2-x}MnSb$ system as obtained from in-situ neutron diffraction. On the left hand side, the lattice parameters obtained from reference measurements at SPODI are indicated.

in $Ni_{1.05}MnSb$ and $Ni_{1.25}MnSb$ where it is observed at approximately 1100 K and 800 K, respectively. In the samples with higher Ni content, the effect is less pronounced or the contraction at least seems to be extended over a larger temperature range. Upon cooling, this lattice contraction is not observed. For $Ni_{1.05}MnSb$, lattice parameters upon cooling are significantly larger than upon heating while for all other samples, the lattice parameters upon cooling coincide again with the ones upon heating at low temperatures. Putting effort into confirming this behavior, i.e. heating and cooling samples several times and jumping in between temperatures, it became clear that the lattice parameter contraction is presumably an effect of quenching/sample preparation. After the first heating, all points measured on subsequent heating and cooling cycles perfectly coincided. Interestingly, the structure factors show no apparent effect related to the lattice parameter contraction. With respect to the relevant temperature range, the contraction seems to be unrelated to both the magnetic and structural phase transitions in the system. A possible scenario would be the annihilation of quenched-in excess vacancies upon initial heating. Yet, such a process would result in a lattice expansion rather than a lattice contraction. Hence, also a relation to quenched-in vacancies seems not likely. At the structural transition, if a simple disordering process of Ni and constitutional vacancies on the 4a and 4b site would occur, a lattice expansion would be expected upon heating that would be reversible upon cooling. Nonetheless, especially upon cooling, the lattice parameter shows no signs of the phase transition. This unexpected observation is a good indication for a more complex ordering process as indicated above. However, from the presented data set, no clear conclusion can be drawn concerning this matter.

7.4 Conclusions

In the scope of this chapter, the $C1_b$ half-Heusler to the $L2_1$ full-Heusler phase transition in the $Ni_{2-x}MnSb$ was investigated as function of composition and temperature. Reproducing initially phase transition temperatures and room temperature structure reports from the pertinent literature, the main focus of this chapter is an in-situ neutron diffraction study of the mentioned phase transition. Confirming a $C1_b$-ordered structure of all studied compositions at room temperature, both in a quenched and furnace-cooled heat treatment condition, there is compelling evidence that the phase transition from the $C1_b$ to a $L2_1$-type structure is more complex than previously assumed. The simple picture of a disordering reaction on the 4a and 4b Wyckoff sites cannot explain the observed experimental features. Specifically, a reduction of the B2 structure factor is observed upon heating, indicating an intermixing of Ni and Mn/Sb. Without unambiguous evidence, it was conjectured that this observation could be related to an annihilation process of structural vacancies at elevated temperatures that goes along with an effective decrease of the numbers of unit cells. Presumably, in such a process, Mn migrates onto the Ni lattice, while emerging Mn vacancies are filled up by Sb. Such a mechanism would be overall in line with the experimental observations, yet, there is no conclusive evidence for the correctness of this model and even if correct, the exact site occupancies in the high temperature $L2_1$-type structure remain unsolved.

Finding conclusive evidence for the proposed mechanism of vacancy annihilation would require comprehensive theoretical investigations of this issue with determining the energetic cost of various types of disorder by DFT calculations. Having identified realistic mechanisms, these mechanisms could then be tested against the experimental observations in order to evaluate their likeliness. Besides that, it would be of interest to remeasure selected samples at a high flux instrument during continuous heating and cooling in order to obtain a higher temperature resolution both for the structure factors and the lattice parameters. Furthermore, additional in-situ X-ray diffraction measurements would give complementary information that together with the neutron diffraction results would facilitate a more accurate description of the phase transition. Within the scope of this thesis, in-situ X-ray diffraction experiments have been attempted using a vacuum heating stage for a conventional laboratory based X-ray diffractometer operating under a vacuum of 10^{-5} mbar. However, due to a large oxidation tendency of the samples and small penetration depths for X-rays, sample oxidation was despite the vacuum conditions so severe that only oxide peaks were present in the diffractogram when the phase transition temperature was reached. Consequently, a set-up for X-ray diffraction would be needed that allows at best for a sealing of the powder samples under inert atmosphere during the measurements.

Summary and outlook

In this thesis, the influence of the state of atomic order on the magnetic, electronic and structural properties of NiMn-based Heusler alloys was comprehensively studied using a variety of experimental methods such as neutron diffraction, X-ray diffraction, electron diffraction, calorimetry and magnetization measurements as well as employing computational methods such as Monte Carlo (MC) simulations and Density Functional Theory (DFT) calculations (provided by collaboration partners). In the following, the main outcomes of this thesis are summarized and interesting further research pathways are outlined.

Chapter 2 was dedicated to the investigation of order dependent magnetic properties in Ni_2MnZ full-Heusler alloys. Specifically, the model alloy $Ni_2MnAl_{0.5}Ga_{0.5}$ as well as stoichiometric and off-stoichiometric Ni_2MnAl compounds were studied. It was conjectured that, starting with a B2 ordered sample, $L2_1$ order emerges in a simple picture first via short range/local order formation with the initial presence of a high density of antiphase boundaries (APBs). Further in the ordering process, the local order saturates close to the equilibrium value and mainly the antiphase domain (APD) structure grows. Both processes, short-range order formation and APD growth, are manifestations of the same effect, yet, happen on fundamentally different time scales. In principle, the non-equilibrium process of order formation is described by a static correlation function of the lattice site occupancies. This correlation function decays above the B2-$L2_1$ phase transition temperature at large distances to the random value while it decays to a non-random value below the transition temperature. This non-random value is the degree of long-range order which is again a function of temperature. The state of order is realized starting from a disordered configuration via short range interaction potentials. Hence, the order starts, as described above, to emerge from small scales. The correlation function over small distances is consequently what is referred to above as short-range order while the correlation function over longer distances is what is referred to as APD size. Furthermore, it was demonstrated via comprehensive magnetization measurements and MC simulations employing a Heisenberg model that the magneto-structural interactions in Ni_2MnZ compounds directly couple the magnetic properties to the local but also mesoscale nuclear structure. First, it was shown experimentally that the short-range order formation and the antiphase domain growth are predominantly responsible for different magnetic properties, i.e. the magnetic transition temperature and the bulk magnetization/D.C. susceptibility, respectively. Hence, probing both properties as a function of annealing time yields a distinct evolution pathway in the 2D parameter space composed of them. Second, it was demonstrated via MC simulations that magnetic domains inherently coincide with structural APDs. While within a structural domain, due to lattice site occupancies, ferromagnetic interactions prevail, across APBs, via a nearest-neighbor (NN) antiferromagnetic (AFM) Mn-Mn interaction, AFM interactions dominate. As a consequence, entire $L2_1$ APDs behave magnetically as super spins and are coupled to each other in an AFM fashion. The employed magneto-structural model, taking into account a simple well-accepted magnetic Hamiltonian for the system as well as simulated atomic configurations, perfectly reproduces the experimental magnetization results. This good descriptive power of the model is a strong indication for its correctness.

After having established in Chapter 2 the relation between the magnetic transition temperature and the short-range order on the one hand as well as the bulk magnetization/D.C. susceptibility and the APD structure on the other hand, Chapter 3 was concerned with the kinetics of the $L2_1$ ordering process starting with B2-ordered samples. Specifically, the mentioned magnetic properties were used to follow the evolution of the ordering process. Based on these measurements, a simple Arrhenius-type description for the kinetics of the ordering process was developed and so-called time temperature transformation (TTT) diagrams were created. These diagrams offer a detailed manual on adjusting a certain combination of magnetic properties via the appropriate annealing treatment. Furthermore, activation energies for the ordering process were determined. In total, 3 systems were considered, i.e. $Ni_2MnAl_{0.5}Ga_{0.5}$, Ni_2MnAl and off-stoichiometric $Ni_2Mn_{1.12}Al_{0.88}$ where activation energies of 1.52-1.55 eV, 1.65 eV and 1.65 eV were found for high-temperature quenched samples, respectively. For $Ni_2Mn_{1.12}Al_{0.88}$ it was further demonstrated that the ordering process relies heavily on quenched-in excess vacancies. Concerning this matter, the activation energy of the ordering process was determined in slow cooled samples with little to no quenched-in excess vacancies and an activation energy of 2.3-2.5 eV was found. Finally, by quenching samples from different quenching temperatures and following the ordering process upon isothermal annealing at a constant annealing temperature, the activation energy for vacancy formation in $Ni_2Mn_{1.12}Al_{0.88}$ was determined as 1.0 eV. As expected, this value corresponds roughly to the difference of the activation energies for the ordering process in slowly cooled and high-temperature quenched samples given that vacancy formation is not necessary under the presence of quenched-in excess vacancies.

In Chapter 4, after having made a case for the influence of the APD structure on the magnetic properties in Chapter 2 and having analyzed the kinetics of this process in Chapter 3, the topic of magneto-structural coupling in Ni_2MnZ compounds was revisited employing temperature-dependent neutron powder diffraction measurements. Concerning this matter, the implications of magnetically coupled APDs for the neutron diffraction patterns were derived. It was demonstrated that a small-scale APD structure with AFM coupling of entire magnetic domains leads to broad nuclear $L2_1$ superstructure peaks as well as sharp magnetic superstructure peaks at the same position in reciprocal space. These predictions were compared to neutron diffraction patterns where exactly such a phenomenon was observed. Initially, in the AFM ordered B2 structure, only sharp magnetic superstructure peaks were found. With increased $L2_1$ order, broad nuclear superstructure peaks emerged while however the magnetic superstructure stayed constant despite the high degree of local $L2_1$ order. These observations were further demonstrated to be perfectly consistent to the model of magnetically coupled structural $L2_1$ APDs as presented in Chapter 2.

Besides the AFM coupling of APDs, the neutron diffraction results presented in Chapter 4 revealed the strong dependence of martensitic phase transitions from the atomic order in the austenite parent phase. In $Ni_2MnAl_{0.5}Ga_{0.5}$, for the first time, a transition to a pre-martensitic phase similar to the one found in Ni_2MnGa compounds was observed that proved to be stable down to at least 10 K. Interestingly, both the intensity of the pre-martensite superstructure peaks as well as the pre-martensite transition temperature increased as a function of $L2_1$ order in the austenite phase. While no pre-martensitic transition was found in 1073 K-quenched, B2-ordered samples, the pre-martensite phase was found in 623 K-annealed samples showing a transition temperature of 130-150 K in 3 h annealed samples and a transition temperature of 190-210 K in 10 d annealed samples.

The results as presented in the first 3 chapters of this thesis leave room for further research pathways. For instance, it would be interesting to study the observed magnetically coupled structural $L2_1$ APDs by Small Angle Neutron Scattering (SANS). In SANS, in case of AFM coupled antiphase domains, a clear magnetic signature is expected. Hence, temperature dependent SANS measurements would ideally complement the neutron powder diffraction measurements presented in this thesis. With the higher neutron flux and faster acquisition times, tracking the APD coupling as function of temperature and external magnetic field would be feasible and insights into the exact nature of the coupling could be won. Especially, it would be interesting to investigate the magnetization distribution within an APD by manipulating the magnetization direction and bulk magnetization via an external magnetic field. Further, it would be interesting to study the kinetic pathway of APD growth in-situ as a function of time in neutron powder diffraction. This procedure was employed in this thesis for selected states of order, yet, a continuous measurement would allow for a much better resolution of the short-range order and APD size as a function of annealing temperature and annealing time. The results could then be compared to MC simulations of the ordering process in order to gain information on its exact pathway.

While Chapters 2-4 were concerned with order dependent magnetic properties, Chapter 5 was concerned with compositional influences on the magnetic structure of B2-ordered Heusler compounds. Specifically, the magnetic structure of $\mathrm{Ni}_{2-x}\mathrm{Co}_x\mathrm{MnAl}$ alloys with a B2 nuclear structure was studied as function of x. Interestingly, leaving the degree of order untouched, the substitution of Co for Ni drastically changes the magnetic properties. For instance, $\mathrm{Ni_2MnAl}$ shows in a B2 structure AFM properties while NiCoMnAl is perfectly FM. Between these extremes, a magnetic transition from an antiparallel spin alignment to a parallel one has necessarily to occur. The reason for the observed composition effect is founded in Co having a much stronger FM exchange interaction strength than Ni. Studying the magnetic structure as function of the FM interaction strength was the main topic of Chapter 5. For this purpose, a series of alloys with varying Ni/Co ratios was prepared and bulk magnetization measurements as well as temperature dependent neutron powder diffraction measurements were performed. The results revealed an increasing bulk magnetization as function of the Co content while simultaneously the AFM superstructure peak in neutron diffraction decreased in intensity. With Mn carrying the major magnetic moment in this system, this observation was explained by a canting of the Mn spins as function of the FM interaction strength. At Co contents > 7 at. % no AFM component was observed anymore in neutron diffraction and the samples showed perfect FM properties.

Having provided strong evidence for spin canting in the $\mathrm{Ni}_{2-x}\mathrm{Co}_x\mathrm{MnAl}$ system in this thesis, it would be of interest to study the exact spin structure in $\mathrm{Ni}_{2-x}\mathrm{Co}_x\mathrm{MnAl}$ single crystals with approximately 3-5 at. % Co. Here, a pronounced canted spin structure is expected which could presumably be resolvable using polarized neutron diffraction. Yet, it should be kept in mind that the B2 structure in these compounds is characterized by disorder of Mn and Al as well as Ni and Co on their respective sublattices which naturally leads to an inhomogeneous nuclear structure and consequently spin structure throughout the sample. Hence, the situation is to distinguish from neutron diffraction studies of magnetic structures in fully ordered compounds. Still, a deeper insight into the magnetic structure and the question of spin canting could be gained from such experiments. Furthermore, for $\mathrm{Ni_2MnAl}$, so-called induced Ni moments have been proposed by DFT calculations. This means that the magnetic moment on Ni is induced via the vector sum of its NN Mn spins. In order to confirm this postulation and also to study the effect of Co addition on the Ni moment, X-ray Magnetic Circular Dichroism (XMCD) measurement would be of interest. The insights to be gained would help to improve the understanding of the magnetic structure of Ni_2MnZ compounds in general.

Having been mainly concerned with magnetic properties in Chapters 2-5, Chapter 6 investigated the effect of the atomic state of order on the electronic properties of NiCoMnAl and NiCoMnGa full-Heusler compounds. Both compounds have been predicted to show potentially half-metallic properties in their fully ordered Y structure and are thus conjectured to be interesting materials for spintronics applications. Using in-situ neutron diffraction, the nuclear structure of both compounds was investigated and, similar to Ni_2MnAl and Ni_2MnGa, a B2 ordering tendency in NiCoMnAl was found while NiCoMnGa was observed to adopt a $L2_1$ structure with order on the Mn-Ga sublattices and a phase transition to the B2 structure at 1160 K. Interestingly, slow cooling or low temperature annealing proved to be successful in adjusting incipient $L2_1$ order in NiCoMnAl. Yet, neither in NiCoMnGa nor in NiCoMnAl, signs for Ni-Co ordering were found. With NiCoMnGa being essentially always $L2_1$-ordered in all annealing conditions, annealing treatments showed little effect on the magnetic properties such as the magnetic transition temperature. However, in NiCoMnAl where the state of order can be manipulated by annealing treatments, a drastic increase in the magnetic transition temperature was observed as function of annealing time in the $L2_1$ stable regime. DFT calculations were conducted in order to investigate phase stabilities and to reveal the order dependent electronic structure. It was found that a pseudo-gap emerges in the minority spin channel of the electronic density of states that is dependent on a fully Y-ordered structure and vanishes with Ni-Co disorder. Concerning this matter, it was furthermore demonstrated that the Y structure is thermodynamically unstable compared to a tetragonal structure with alternating Ni and Co layers. Due to kinetic limitations at the predicted transition temperatures, this ground state structure is however inaccessible in bulk samples under realistic experimental conditions.

Finally, in Chapter 7, the comprehensive study of atomic ordering in full-Heusler Ni_2MnZ alloys was extended to half-Heusler compounds, specifically the $Ni_{2-x}MnSb$ system. First, magnetic and structural phase transition temperatures were determined by calorimetric measurements. Next, the magnetic properties of a series of compounds were studied by SQUID magnetometry for different annealing conditions. Interestingly, an increase in spontaneous magnetization was observed upon low temperature annealing with respect to 1173 K-quenched samples. Furthermore, as a function of composition, i.e. the Ni content, as well as temperature, the nuclear structure of 1073 K-quenched $Ni_{2-x}MnSb$ compounds was studied by means of in-situ neutron diffraction and room temperature X-ray diffraction. It was found that all studied compounds with compositions between $Ni_{1.05}MnSb$ and $Ni_{1.75}MnSb$ show $C1_b$ order with a fully Ni-occupied Wyckoff 4a site and an only partially Ni-occupied

4b site. As a function of temperature, in compounds with Ni contents $\leq$ $Ni_{1.50}MnSb$, a transition to a $L2_1$ structure was observed with transition temperatures between 900 K and 1080 K for $Ni_{1.50}MnSb$ and $Ni_{1.05}MnSb$, respectively. This $L2_1$ structure, being in a first approximation characterized by Ni and structural vacancies randomly occupying the 4a and 4b sites, proved however to be more complicated than presently believed. In fact, the peak intensities of B2 family peaks in the neutron diffractograms were observed to decrease as a function of temperature. This observation indicates a state of mixing between the Ni/vacancy and Mn/Sb sublattices not accounted for by the simple picture of Ni/vacancy mixing. Instead, based on defect energies reported in the pertinent literature, it was conjectured that vacancies annihilate as a function of temperature effectively leading to Mn migrating onto the Ni/vacancy sublattices. Yet, due to its complexity and the amount of potential kinds of disorder, purely based on the neutron diffraction results, a specification of the exact mechanism proved to be difficult.

Referring to the results presented in Chapter 7, it would be interesting to complement the neutron diffraction results with in-situ X-ray diffraction. This was attempted in the scope of this thesis, yet strong oxidation and low X-ray penetration depths made it impossible to observe the $C1_b$-$L2_1$ transition despite the use of proper vacuum sample chambers. However, it might be possible to investigate this ordering process by X-ray diffraction employing a set-up making use of sample holders sealed in inert atmosphere. Due to different elemental contrast in X-ray diffraction, these measurements could, together with the neutron diffraction results, help to identify the exact site occupancies as function of temperature. Additionally, in order to identify the most realistic mechanisms of vacancy annihilation, DFT calculations of a variety of disordered structures would be beneficial. The results of such calculations could then be compared to the experimental evidence in order to identify the most plausible mechanism for the $C1_b$-$L2_1$ phase transition.

List of publications, conference presentations and patent applications

Articles in peer-reviewed journals

- Ordering tendencies and electronic properties in quaternary Heusler derivatives
  P. Neibecker, M. E. Gruner, X. Xu, R. Kainuma, W. Petry, R. Pentcheva, and M. Leitner, Phys. Rev. B. 96, 165131 (2017)
- $L1_2$ ordering and δ' precipitation in Al-Cu-Li
  P. Neibecker, M. Leitner, M. Kushaim, T. Boll, D. Anjum, T. Al-Kassab, F. Haider, Sci. Rep. 7, 3254 (2017)
- Increasing the achievable state of order in Ni-based Heusler alloys via quenched-in vacancies
  P. Neibecker, M. Leitner, G. Benka, W. Petry, Appl. Phys. Lett. 105, 261904 (2014)

Presentations on conferences, summer schools and workshops

- The influence of the anti-phase domain structure on the magnetic properties in $Ni_2MnAl_{0.5}Ga_{0.5}$
  P. Neibecker, X. Xu, W. Petry, R. Kainuma, M. Leitner, DPG Spring Meeting, Dresden, Germany (2017)
- Ordering Tendencies and Electronic Properties in Full-Heusler NiCoMnAl and NiCoMnGa Alloys
  P. Neibecker, M. Gruner, O. Doltoko, X. Xu, R.Y. Umetsu, R. Kainuma, W. Petry, M. Leitner, 5^{th} International Conference on Ferromagnetic Shape Memory Alloys, Sendai, Japan (2016)
- Temperature dependence and linewidths of Al phonon dispersions
  P. Neibecker, J. Neuhaus, M. Leitner, K. Hradil, W. Petry, A. Glensk, B. Grabowski, T.

Hickel, J. Neugebauer, 35th Symposium on Dynamical Properties of Solids, Freising, Germany (2015)

- Ordering kinetics in Ni-Mn based ferromagnetic shape memory Heusler alloys
  P. Neibecker, M. Leitner, G. Benka, W. Petry, Summer School, TRR 80 program of the German Research Foundation (DFG), Frauenwörth, Germany (2015)

- Increasing the achievable state of order in Ni-Mn-based Heusler alloys
  P. Neibecker, M. Leitner, G. Benka, W. Petry, 20th International Conference on Magnetism, Barcelona, Spain (2015)

- Magnetism of disordered Heusler alloys
  M. Leitner, P. Neibecker, W. Petry, 20th International Conference on Magnetism, Barcelona, Spain (2015)

- Ordering kinetics in Ni-Mn based ferromagnetic shape memory alloys
  P. Neibecker, M. Leitner, G. Benka, W. Petry, DPG Spring Meeting, Berlin, Germany (2015)

Poster presentations on conferences and workshops

- Atomic order effects on the electronic properties in NiCoMnGa and NiCoMnAl Heusler alloys
  P. Neibecker, M. Leitner, M. Gruner, O. Dolotko, W. Petry, Retreat Meeting, TRR 80 program of the German Research Foundation (DFG), Freising, Germany (2016)

Patent applications

- Verfahren und Vorrichtung zum Herstellen eines dreidimensionalen Objekts, EP3059074 (2015)

References

Acet, M., Duman, E., Wassermann, E. F., Mañosa, L., and Planes, A. (2002). Coexisting ferro- and antiferromagnetism in Ni_2MnAl Heusler alloys. *J. Appl. Phys.*, **92**(7):3867–3871.

Al-zyadi, J. M. K., Gao, G. Y., and Yao, K.-L. (2015). Theoretical investigation of the electronic structures and magnetic properties of the bulk and surface (001) of the quaternary Heusler alloy NiCoMnGa. *J. Magn. Magn. Mater.*, **378**:1–6.

Alijani, V., Ouardi, S., Fecher, G. H., Winterlik, J., Naghavi, S. S., Kozina, X., Stryganyuk, G., Felser, C., Ikenaga, E., Yamashita, Y., Ueda, S., and Kobayashi, K. (2011a). Electronic, structural, and magnetic properties of the half-metallic ferromagnetic quaternary Heusler compounds CoFeMnZ ($Z =$ Al, Ga, Si, Ge). *Phys. Rev. B*, **84**:224416.

Alijani, V., Winterlik, J., Fecher, G. H., Naghavi, S. S., and Felser, C. (2011b). Quaternary half-metallic Heusler ferromagnets for spintronics applications. *Phys. Rev. B*, **83**:184428.

Alling, B., Shallcross, S., and Abrikosov, I. A. (2006). Role of stoichiometric and nonstoichiometric defects on the magnetic properties of the half-metallic ferromagnet NiMnSb. *Phys. Rev. B*, **73**:064418.

Ayuela, A., Enkovaara, J., and Nieminen, R. M. (2002). Ab initio study of tetragonal variants in Ni_2MnGa alloy. *J. Phys.: Condens. Matter*, **14**(21):5325–5336.

Ayuela, A., Enkovaara, J., Ullakko, K., and Nieminen, R. M. (1999). Structural properties of magnetic Heusler alloys. *J. Phys.: Condens. Matter*, **11**(8):2017–2026.

Bacon, G. E. and Plant, J. S. (1971). Chemical ordering in Heusler alloys with the general formula A_2BC or ABC. *J. Phys. F: Met. Phys.*, **1**(4):524–532.

Bainsla, L., Suresh, K. G., Nigam, A. K., Manivel Raja, M., Varaprasad, B. S. D. C. S., Takahashi, Y. K., and Hono, K. (2014). High spin polarization in CoFeMnGe equiatomic quaternary Heusler alloy. *J. Appl. Phys.*, **116**(20):203902.

Barandiaran, J. M., Chernenko., V. A., Cesari, E., Salas, D., Gutierrez, J., and Lazpitza, P. (2013). Magnetic field and atomic order effect on the martensitic transformation of a metamagnetic alloy. *J. Phys.: Condens. Matter*, **25**:484005.

Berri, S., Maouche, D., Ibrir, M., and Zerarga, F. (2014). A first-principle study of half-metallic ferrimagnetism in the CoFeTiSb quaternary Heusler compound. *J. Magn. Magn. Mater.*, **354**:65–69.

Blöchl, P. E., Jepsen, O., and Andersen, O. K. (1994). Improved tetrahedron method for Brillouin-zone integrations. *Phys. Rev. B*, **49**:16223.

Brown, P. J. (2003). *Neutron Data Booklet: Magnetic form factors*. Old City Publishing.

Brown, P. J., Bargawi, A. Y., Crangle, J., Neumann, K.-U., and Ziebeck, K. R. A. (1999). Direct observation of a band Jahn-Teller effect in the martensitic phase transition of Ni_2MnGa. *J. Phys.: Condens. Matter*, **11**:4715–4722.

Brown, P. J., Crangle, J., Kanomata, T., Matsumoto, M., Neumann, K. U., Ouladdiaf, B., and Ziebeck, K. R. A. (2002). The crystal structure and phase transitions of the magnetic shape memory compound Ni_2MnGa. *J. Phys.: Condens. Matter*, **14**(43):10159–10171.

Brown, P. J., Gandy, A. P., Kainuma, R., Kanomata, T., Miyamoto, T., Nagasako, M., Neumann, K. U., Sheikh, A., and Ziebeck, K. R. A. (2010). Atomic order and magnetization distribution in the half metallic and nearly half metallic $C1_b$ compounds NiMnSb and PdMnSb. *J. Phys.: Condens. Matter*, **22**(20):206004.

Buchelnikov, V. D., Entel, P., Taskaev, S. V., Sokolovskiy, V. V., Hucht, A., Ogura, M., Akai, H., Gruner, M. E., and Nayak, S. K. (2008). Monte Carlo study of the influence of antiferromagnetic exchange interactions on the phase transitions of ferromagnetic Ni-Mn-X alloys ($X = \mathrm{In, Sn, Sb}$). *Phys. Rev. B*, **78**:184427.

Bungaro, C., Rabe, K. M., and Dal Corso, A. (2003). First-principles study of lattice instabilities in ferromagnetic Ni_2MnGa. *Phys. Rev. B*, **68**:134104.

Buschow, K. H. J. and van Engen, P. G. (1981). Magnetic and magneto-optical properties of heusler alloys based on aluminium and gallium. *J. Magn. Magn. Mater.*, **25**(1):90–96.

Caglioti, G., Paoletti, A., and Ricci, F. P. (1958). Choice of collimators for a crystal spectrometer for neutron diffraction. *Nucl. Instrum. Methods*, **3**(4):223–228.

Castelliz, L. (1955). Beitrag zum Ferromagnetismus von Legierungen der Übergangsmetalle mit Elementen der B-Gruppe. *Z. Metallkd.*, **46**:198–203.

Çakır, A., Acet, M., and Farle, M. (2016). Shell-ferromagnetism of nano-Heuslers generated by segregation under magnetic field. *Sci. Rep.*, **6**:28931.

Chatterjee, S., Giri, S., Majumdar, S., and De, S. (2008). Magnetic after-effect in Ni-Mn-Sb Heusler alloy. *J. Magn. Magn. Mater.*, **320**(5):617–621.

Comtesse, D., Gruner, M. E., Ogura, M., Sokolovskiy, V. V., Buchelnikov, V. D., Grünebohm, A., Arróyave, R., Singh, N., Gottschall, T., Gutfleisch, O., Chernenko, V. A., Albertini, F., Fähler, S., and Entel, P. (2014). First-principles calculation of the instability leading to giant inverse magnetocaloric effects. *Phys. Rev. B*, **89**:184403.

Şaşıoğlu, E., Sandratskii, L. M., and Bruno, P. (2004). First-principles calculation of the intersublattice exchange interactions and Curie temperatures of the full Heusler alloys $\mathrm{Ni_2Mn}X$ $(X = \mathrm{Ga, In, Sn, Sb})$. *Phys. Rev. B*, **70**:024427.

Şaşıoğlu, E., Sandratskii, L. M., and Bruno, P. (2008). Role of conduction electrons in mediating exchange interactions in Mn-based Heusler alloys. *Phys. Rev. B*, **77**:064417.

Şaşıoğlu, E., Sandratskii, L. M., Bruno, P., and Galanakis, I. (2005). Exchange interactions and temperature dependence of magnetization in half-metallic Heusler alloys. *Phys. Rev. B*, **72**:184415.

Dai, X., Liu, G., Fecher, G. H., Felser, C., Li, Y., and Liu, H. (2009). New quarternary half metallic material CoFeMnSi. *J. Appl. Phys.*, **105**(7):07E901.

Dannenberg, A., Siewert, M., Gruner, M. E., Wuttig, M., and Entel, P. (2010). Competing structural ordering tendencies in Heusler-type alloys with high Curie temperatures: $Fe_2CoGa_{1-x}Zn_x$ studied by first-principles calculations. *Phys. Rev. B*, **82**:214421.

Davenport, E. S. and Bain, E. C. (1930). Transformation of Austenite at Constant Subcritical Temperatures. *Trans. AIME*, **90**:117–144.

de Groot, R. A., Mueller, F. M., van Engen, P. G., and Buschow, K. H. J. (1983). New Class of Materials: Half-Metallic Ferromagnets. *Phys. Rev. Lett.*, **50**:2024–2027.

Ebert, H., Ködderitzsch, D., and Minár, J. (2011). Calculating condensed matter properties using the KKR-Green's function method — recent developments and applications. *Rep. Prog. Phys.*, **74**(9):096501.

Eberz, U., Seelentag, W., and Schuster, H. (1980). Coloured Ternary and Quaternary Zintl-Phases. *Z. Naturforsch. B*, **35**:1341–1343.

Elahmar, M. H., Rached, H., Rached, D., Khenata, R., Murtaza, R., Bin Omran, S., and Ahmed, W. K. (2015). Structural, mechanical, electronic and magnetic properties of a new series of quaternary Heusler alloys CoFeMnZ (Z=Si, As, Sb): A first-principle study. *J. Magn. Magn. Mater.*, **393**:165–174.

Enamullah, Johnson, D. D., Suresh, K. G., and Alam, A. (2016). Half-metallic Co-based quaternary Heusler alloys for spintronics: Defect- and pressure-induced transitions and properties. *Phys. Rev. B*, **94**:184102.

Enamullah, Venkateswara, Y., Gupta, S., Varma, M. R., Singh, P., Suresh, K. G., and Alam, A. (2015). Electronic structure, magnetism, and antisite disorder in CoFeCrGe and CoMnCrAl quaternary Heusler alloys. *Phys. Rev. B*, **92**:224413.

Entel, P., Buchelnikov, V. D., Khovailo, V. V., Zayak, A. T., Adeagbo, W. A., Gruner, M. E., Herper, H. C., and Wassermann, E. F. (2006). Modelling the phase diagram of magnetic shape memory Heusler alloys. *J. Phys. D: Appl. Phys.*, **39**(5):865–889.

Entel, P., Gruner, M. E., Comtesse, D., Sokolovskiy, V. V., and Buchelnikov, V. (2014). Interacting magnetic cluster-spin glasses and strain glasses in Ni-Mn based Heusler structured intermetallics. *phys. stat. sol. (b)*, **251**(10):2135–2148.

Entel, P., Gruner, M. E., Dannenberg, A., Siewert, M., Nayak, S. K., Herper, H. C., and Buchelnikov, V. D. (2010). Fundamental aspects of magnetic shape memory alloys: Insights from ab initio and Monte Carlo studies. *Mater. Sci. Forum*, **635**:3–12.

Erdélyi, G., Mehrer, H., Imre, A. W., Lograsso, T. A., and Schlagel, D. L. (2007). Self-diffusion in Ni_2MnGa. *Intermetallics*, **15**(8):1078–1083.

Feder, R. and Cahn, R. W. (1960). Kinetics of ordering in Fe_3Al. *Phil. Mag. A*, **5**(52):343–353.

Feng, Y., Chen, H., Yuan, H., Zhou, Y., and Chen, X. (2015). The effect of disorder on electronic and magnetic properties of quaternary Heusler alloy CoFeMnSi with LiMgPbSb-type structure. *J. Magn. Magn. Mater.*, **378**:7–15.

Fisher, M. E. (1967). The theory of equilibrium critical phenomena. *Rep. Prog. Phys.*, **30**(2):615–730.

Foner, S. (1956). Vibrating sample magnetometer. *Rev. Sci. Instrum.*, **27**(7):548–548.

Foner, S. (1959). Versatile and sensitive vibrating-sample magnetometer. *Rev. Sci. Instrum.*, **30**(7):548–557.

Fujii, S., Ishida, S., and Asano, S. (1989). Electronic Structure and Lattice Transformation in Ni_2MnGa and Co_2NbSn. *J. Phys. Soc. Japan*, **58**(10):3657–3665.

Fujii, S., Sugimura, S., Ishida, S., and Asano, S. (1990). Hyperfine fields and electronic structures of the Heusler alloys Co_2MnX (X=Al, Ga, Si, Ge, Sn). *J. Phys.: Condens. Matter*, **2**(43):8583–8589.

Fujita, A., Fukamichi, K., Gejima, F., Kainuma, R., and Ishida, K. (2000). Magnetic properties and large magnetic-field-induced strains in off-stoichiometric Ni-Mn-Al Heusler alloys. *Appl. Phys. Lett.*, **77**(19):3054–3056.

Fultz, B. and Howe, J. M. (2012). *Transmission Electron Microscopy and Diffractometry of Materials*. Springer Science & Business Media.

Galanakis, I., Dederichs, P. H., and Papanikolaou, N. (2002). Slater-Pauling behavior and origin of the half-metallicity of the full-Heusler alloys. *Phys. Rev. B*, **66**:174429.

Galanakis, I., Mavropoulos, P., and Dederichs, P. H. (2006). Electronic structure and Slater-Pauling behaviour in half-metallic Heusler alloys calculated from first principles. *J. Phys. D: Appl. Phys.*, **39**(5):765–775.

Galanakis, I. and Şaşıoğlu, E. (2011). Structural-induced antiferromagnetism in Mn-based full Heusler alloys: The case of Ni_2MnAl. *Appl. Phys. Lett.*, **98**(10):102514.

Gao, G. Y., Hu, L., Yao, K. L., Luo, B., and Liu, N. (2013). Large half-metallic gaps in the quaternary Heusler alloys CoFeCrZ (Z = Al, Si, Ga, Ge): A first-principles study. *J. Alloys Comp.*, **551**:539–543.

Gao, Q., Li, L., Lei, G., Deng, J.-B., and Hu, X.-R. (2015). A first-principle study on the properties of a new series of quaternary Heusler alloys CoFeScZ (Z=P, As, Sb). *J. Magn. Magn. Mater.*, **379**:288–293.

Gejima, F., Sutou, Y., Kainuma, R., and Ishida, K. (1999). Magnetic Transformation of Ni_2AlMn Heusler-Type Shape Memory Alloys. *Met. Mat. Trans. A*, **30**(10):2721–2723.

Godlevsky, V. V. and Rabe, K. M. (2001). Soft tetragonal distortions in ferromagnetic Ni_2MnGa and related materials from first principles. *Phys. Rev. B*, **63**:134407.

Gökoğlu, G. (2012). Ab initio electronic structure of NiCoCrGa half-metallic quaternary Heusler compound. *Solid State Sci.*, **14**(9):1273–1276.

Graf, T., Felser, C., and Parkin, S. S. P. (2011). Simple rules for the understanding of Heusler compounds. *Prog. Solid State Chem.*, **39**(1):1–50.

Gruner, M. E., Adeagbo, W. A., Zayak, A. T., Hucht, A., Buschmann, S., and Entel, P. (2008). Influence of magnetism on the structural stability of cubic $L2_1$ Ni_2MnGa. *Eur. Phys. J. Special Topics*, **158**(1):193–198.

Hahn, T., editor (2005). *International Tables for Crystallography*, volume A. Springer-Verlag.

Halder, M., Mukadam, M. D., Suresh, K. G., and Yusuf, S. M. (2015). Electronic, structural, and magnetic properties of the quaternary Heusler alloy NiCoMnZ (Z=Al, Ge, and Sn) . *J. Magn. Magn. Mater.*, **377**:220–225.

Hanssen, K. E. H. M., Mijnarends, P. E., Rabou, L. P. L. M., and Buschow, K. H. J. (1990). Positron-annihilation study of the half-metallic ferromagnet NiMnSb: Experiment. *Phys. Rev. B*, **42**:1533–1540.

Haynes, T. D., Watts, R. J., Laverock, J., Major, Z., Alam, M. A., Taylor, J. W., Duffy, J. A., and Dugdale, S. B. (2012). Positron annihilation study of the Fermi surface of Ni_2MnGa. *New J. Phys.*, **14**:035020.

Heusler, F. (1903). Über magnetische Manganlegierungen. *Verh. DPG*, **5**:219.

Heusler, F. (1904). Über Manganbronze und über die Synthese magnetisierbarer Legierungen aus unmagnetischen Metallen. *Angew. Chem.*, **17**(9):260–264.

Heusler, F., Starck, W., and Haupt, E. (1903). Magnetisch-chemische Studien. *Verh. DPG*, **5**:220–223.

Hoelzel, M., Senyshyn, A., and Dolotko, O. (2015). Spodi: High resolution powder diffractometer. *J. Large-Scale Res. Facil.*, **1**:A5.

Hoelzel, M., Senyshyn, A., Juenke, N., Boysen, H., Schmahl, W., and Fuess, H. (2012). High-resolution neutron powder diffractometer SPODI at research reactor FRM II. *Nucl. Instrum. Methods A*, **667**:32–37.

Höhne, G., Hemminger, W. F., and Flammersheim, H.-J. (2013). *Differential scanning calorimetry*. Springer Science & Business Media.

Hollender, L. (2016). The $C1_b$-$L2_1$ Transition in the $Ni_{2-x}MnSb$ System. B.Sc. thesis, Technische Universität München.

Hu, F.-X., Shen, B.-G., and Sun, J.-R. (2000). Magnetic entropy change in $Ni_{51.5}Mn_{22.7}Ga_{25.8}$ alloy. *Appl. Phys. Lett.*, **76**(23):3460–3462.

Huq, A., Hodges, J. P., Gourdon, O., and Heroux, L. (2011). Powgen: A third-generation high-resolution high-throughput powder diffraction instrument at the Spallation Neutron Source. *Z. Kristallogr. Proc.*, **1**:127–135.

Ishida, S., Akazawa, S., Kubo, Y., and Ishida, J. (1982). Band theory of Co_2MnSn, Co_2TiSn and Co_2TiAl. *J. Phys. F: Met. Phys.*, **12**(6):1111–1122.

Ishikawa, H., Umetsu, R. Y., Kobayashi, K., Fujita, A., Kainuma, R., and Ishida, K. (2008). Atomic ordering and magnetic properties in $Ni_2Mn(Ga_xAl_{1-x})$ Heusler alloys. *Acta Mater.*, **56**(17):4789–4797.

James, R. D. and Wuttig, M. (1998). Magnetostriction of martensite. *Phil. Mag. A*, **77**(5):1273–1299.

Jiles, D. (2015). *Introduction to Magnetism and Magnetic Materials*. CRC press.

John, C. and Alex, I. B. (2004). *The SQUID Handbook Vol. 1 Fundamentals and Technology of SQUIDs and SQUID Systems*. Wiley-VCH Verlag GmbH & Co. KGaA.

Johnson, V. and Jeitschko, W. (1974). ZrCuSiAs: A “filled” PbFCl type. *J. Solid State Chem.*, **11**(2):161–166.

Jourdan, M., Minár, J., Braun, J., Kronenberg, A., Chadov, S., Balke, B., Gloskovskii, A., Kolbe, M., Elmers, H. J., Schönhense, G., Ebert, H., Felser, C., and Kläui, M. (2014). Direct observation of half-metallicity in the Heusler compound Co_2MnSi. *Nat. Commun.*, **5**:3974.

Jullière, M. (1975). Tunneling between ferromagnetic films. *Phys. Lett. A*, **54**(3):225–226.

Kainuma, R., Gejima, F., Sutou, Y., Ohnuma, I., and Ishida, K. (2000). Ordering, martensitic and ferromagnetic transformations in Ni-Al-Mn Heusler shape memory alloys. *Mat. Trans. JIM*, **41**(8):943–949.

Kanomata, T., Kitsunai, Y., Sano, K., Furutani, Y., Nishihara, H., Umetsu, R. Y., Kainuma, R., Miura, Y., and Shirai, M. (2009). Magnetic properties of quaternary Heusler alloys $Ni_{2-x}Co_xMnGa$. *Phys. Rev. B*, **80**:214402.

Kim, Y. J., Busch, R., Johnson, W. L., Rulison, A. J., and Rhim, W. K. (1996). Experimental determination of a time–temperature–transformation diagram of the undercooled $Zr_{41.2}Ti_{13.8}Cu_{12.5}Ni_{10.0}Be_{22.5}$ alloy using the containerless electrostatic levitation processing technique. *Appl. Phys. Lett.*, **68**(8):1057–1059.

Krauth, W. (2006). *Statistical Mechanics: Algorithms and Computations*, volume 13. Oxford University Press.

Kreissl, M., Neumann, K.-U., Stephens, T., and Ziebeck, K. R. A. (2003). The influence of atomic order on the magnetic and structural properties of the ferromagnetic shape memory compound Ni_2MnGa. *J. Phys.: Condens. Matter*, **15**(22):3831–3839.

Krenke, T., Duman, E., Acet, M., Wassermann, E. F., Moya, X., Mañosa, L., and Planes, A. (2005). Inverse magnetocaloric effect in ferromagnetic Ni-Mn-Sn alloys. *Nature Mater.*, **4**(6):450–454.

Kresse, G. and Furthmüller, J. (1996). Efficient Iterative Schemes for Ab Initio Total-Energy Calculations Using a Plane-Wave Basis Set. *Phys. Rev. B*, **54**:11169.

Kresse, G. and Joubert, D. (1999). From Ultrasoft Pseudopotentials to the Projector Augmented-Wave Method. *Phys. Rev. B*, **59**:1758.

Kurtulus, Y., Dronskowski, R., Samolyuk, G. D., and Antropov, V. P. (2005). Electronic structure and magnetic exchange coupling in ferromagnetic full heusler alloys. *Phys. Rev. B*, **71**:014425.

Lapworth, A. J. and Jakubovics, J. P. (1974). Effect of antiphase boundaries on the magnetic properties of Cu-Mn-Al Heusler alloys. *Phil. Mag.*, **29**(2):253–273.

Lawley, A. and Cahn, R. W. (1961). A high temperature X-ray study of ordering in iron-aluminium alloys. *J. Phys. Chem. Solids*, **20**(3):204–221.

Lee, Y., Rhee, J. Y., and Harmon, B. N. (2002). Generalized susceptibility of the magnetic shape-memory alloy Ni_2MnGa. *Phys. Rev. B*, **66**:054424.

Ležaić, M., Mavropoulos, P., Bihlmayer, G., and Blügel, S. (2013). Exchange interactions and local-moment fluctuation corrections in ferromagnets at finite temperatures based on noncollinear density-functional calculations. *Phys. Rev. B*, **88**:134403.

Leitner, M. (2015). Thermodynamics of point defects and diffusion mechanisms in B2-ordered compounds. arXiv:1503.03798 [cond-mat.mtrl-sci].

Liechstenstein, A. I., Katsnelson, M. I., Antropov, V. P., and Gubanov, V. A. (1987). Local spin density functional approach to the theory of exchange interactions in ferromagnetic metals and alloys. *J. Magn. Magn. Mater.*, **67**:65–74.

Likhachev, A. A. and Ullakko, K. (2000). Magnetic-field-controlled twin boundaries motion and giant magneto-mechanical effects in Ni-Mn-Ga shape memory alloy. *Phys. Lett. A*, **275**(1):142–151.

Liu, J., Gottschall, T., Skokov, K. P., Moore, J. D., and Gutfleisch, O. (2012). Giant magnetocaloric effect driven by structural transitions. *Nature Mater.*, **11**(7):620–626.

Martynov, V. V. and Kokorin, V. V. (1992). The crystal structure of thermally-and stress-induced martensites in Ni_2MnGa single crystals. *J. Phys. III France*, **2**(5):739–749.

Mañosa, L., Planes, A., Acet, M., Duman, E., and Wassermann, E. F. (2004). Magnetic shape memory in Ni-Mn-Ga and Ni-Mn-Al. *J. Magn. Magn. Mater.*, **272-276, Part 3**:2090–2092.

Mehaddene, T., Neuhaus, J., Petry, W., Hradil, K., Bourges, P., and Hiess, A. (2008). Interplay of structural instability and lattice dynamics in Ni_2MnAl. *Phys. Rev. B*, **78**(9):104110.

Mehrer, H. (1996). Diffusion in Intermetallics. *Mat. Trans. JIM*, **37**(6):1259–1280.

Merida, D., García, J. A., Sánchez-Alarcos, V., Pérez-Landazábal, J. I., Recarte, V., and Plazaola, F. (2014). Vacancy dynamic in Ni-Mn-Ga ferromagnetic shape memory alloys. *Appl. Phys. Lett.*, **104**(23):231905.

Merida, D., García, J. A., Sánchez-Alarcos, V., Pérez-Landazábal, J. I., Recarte, V., and Plazaola, F. (2015). Characterisation and modelling of vacancy dynamics in Ni-Mn-Ga ferromagnetic shape memory alloys. *J. Alloys Comp.*, **639**:180–186.

Methfessel, M. and Paxton, A. T. (1989). High-precision sampling for Brillouin-zone integration in metals. *Phys. Rev. B*, **40**:3616.

Metropolis, N., Rosenbluth, A. W., Rosenbluth, M. N., Teller, A. H., and Teller, E. (1953). Equation of state calculations by fast computing machines. *J. Chem. Phys.*, **21**(6):1087–1092.

Mohn, P. (2003). *Magnetism in the Solid State*, volume 134 of *Springer Series in Solid-State Sciences*. Springer-Verlag, Berlin, Heidelberg.

Monroe, J. A., Raymond, J. E., Xu, X., Nagasako, N., Kainuma, R., Chumlyakov, Y. I., Arroyave, R., and Karaman, I. (2015). Multiple ferroic glasses via ordering. *Acta Mater.*, **101**:107–115.

Mukadam, M. D., Roy, S., Meena, S. S., Bhatt, P., and Yusuf, S. M. (2016). Quantification of site disorder and its role on spin polarization in the nearly half-metallic Heusler alloy NiFeMnSn. *Phys. Rev. B*, **94**:214423.

Murakami, Y. (1985). Kinetics of order-disorder transformations in the heusler $AuAgZn_2$ alloy. *Acta Metall.*, **33**(2):167–174.

Murakami, Y., Watanabe, Y., and Kachi, S. (1980a). An X-ray Study of the Heusler-type Ordering in $AuAgZn_2$ Alloy. *Mat. Trans. JIM*, **21**(11):708–713.

Murakami, Y., Watanabe, Y., and Kachi, S. (1980b). Kinetics of the Heusler-type Ordering in $AuAgZn_2$ Alloy. *Mat. Trans. JIM*, **21**(11):714–720.

Murakami, Y., Yanagisawa, K., Niitsu, K., Park, H. S., Matsuda, T., Kainuma, R., Shindo, D., and Tonomura, A. (2013). Determination of magnetic flux density at the nanometer-scale antiphase boundary in Heusler alloy $Ni_{50}Mn_{25}Al_{12.5}Ga_{12.5}$. *Acta Mater.*, **61**(6):2095–2101.

Murakami, Y., Yano, T., Umetsu, R. Y., Kainuma, R., and Shindo, D. (2011). Suppression of ferromagnetism within antiphase boundaries in $Ni_{50}Mn_{25}Al_{12.5}Ga_{12.5}$ alloy. *Scripta Mater.*, **65**(10):895–898.

Murray, S. J., Marioni, M., Allen, S. M., O'Handley, R. C., and Lograsso, T. A. (2000). 6 % magnetic-field-induced strain by twin-boundary motion in ferromagnetic Ni-Mn-Ga. *Appl. Phys. Lett.*, **77**(6):886–888.

Nagasako, M., Taguchi, Y., Miyamoto, T., Kanomata, T., Ziebeck, K. R. A., and Kainuma, R. (2015). Order-disorder transition of vacancies from the full- to the half-Heusler structure in $Ni_{2-x}MnSb$ alloys. *Intermetallics*, **61**:38–41.

Neibecker, P., Gruner, M. E., Xu, X., Kainuma, R., Petry, W., Pentcheva, R., and Leitner, M. (2017). Ordering tendencies and electronic properties in quaternary Heusler derivatives. *Phys. Rev. B*, **96**:165131.

Neibecker, P., Leitner, M., Benka, G., and Petry, W. (2014). Increasing the achievable state of order in Ni-based Heusler alloys via quenched-in vacancies. *Appl. Phys. Lett.*, **105**(26):261904.

Niitsu, K., Minakuchi, K., Xu, X., Nagasako, M., Ohnuma, I., Tanigaki, T., Murakami, Y., Shindo, D., and Kainuma, R. (2017). Atomic-resolution evaluation of microsegregation and degree of atomic order at antiphase boundaries in $Ni_{50}Mn_{20}In_{30}$ Heusler alloy. *Acta Mater.*, **122**:166–177.

Oki, K., Hasaka, M., and Eguchi, T. (1973). An X-ray Diffraction Study of Kinetic Behaviors of Ordering in Fe_3Al Alloy. *Mat. Trans. JIM*, **14**(1):8–14.

Okubo, A., Xu, X., Umetsu, R. Y., Kanomata, T., Ishida, K., and Kainuma, R. (2011). Magnetic properties of $Co_{50-x}Ni_xMn_{25}Al_{25}$ alloys with B2 structure. *J. Appl. Phys.*, **109**(7):07B114.

Opeil, C. P., Mihaila, B., Schulze, R. K., Mañosa, L., Planes, A., Hults, W. L., Fisher, R. A., Riseborough, P. S., Littlewood, P. B., Smith, J. L., and Lashley, J. C. (2008). Combined experimental and theoretical investigation of the premartensitic transition in Ni_2MnGa. *Phys. Rev. Lett.*, **100**:165703.

Orgassa, D., Fujiwara, H., Schulthess, T. C., and Butler, W. H. (1999). First-principles calculation of the effect of atomic disorder on the electronic structure of the half-metallic ferromagnet NiMnSb. *Phys. Rev. B*, **60**:13237–13240.

Özdoğan, K., Şaşıoğlu, E., and Galanakis, I. (2013). Slater-Pauling behavior in LiMgPdSn-type multifunctional quaternary Heusler materials: Half-metallicity, spin-gapless and magnetic semiconductors. *J. Appl. Phys.*, **113**(19):193903.

Park, H. S., Murakami, Y., Yanagisawa, K., Matsuda, T., Kainuma, R., Shindo, D., and Tonomura, A. (2012). Electron Holography Studies on Narrow Magnetic Domain Walls Observed in a Heusler Alloy $Ni_{50}Mn_{25}Al_{12.5}Ga_{12.5}$. *Adv. Funct. Mater.*, **22**(16):3434–3437.

Pauly, H., Weiss, A., and Witte, H. (1968). *Z. Metallkd.*, **59**:47–57.

Perdew, J. P., Burke, K., and Ernzerhof, M. (1996). Generalized gradient approximation made simple. *Phys. Rev. Lett.*, **77**:3865–3868.

Picozzi, S., Continenza, A., and Freeman, A. J. (2002). Co_2MnX (X=Si, Ge, Sn) Heusler compounds: An ab initio study of their structural, electronic, and magnetic properties at zero and elevated pressure. *Phys. Rev. B*, **66**:094421.

Pons, J., Chernenko, V. A., Santamarta, R., and Cesari, E. (2000). Crystal structure of martensitic phases in Ni-Mn-Ga shape memory alloys. *Acta Mater.*, **48**(12):3027–3038.

Recarte, V., Pérez-Landazábal, J. I., and Sánchez-Alarcos, V. (2012). Dependence of the relative stability between austenite and martensite phases on the atomic order in a Ni-Mn-In metamagnetic shape memory alloy. *J. Alloys Comp.*, **536**:S308–S311.

Ricolleau, C., Loiseau, A., Ducastelle, F., and Caudron, R. (1992). Logarithmic divergence of the antiphase boundary width in Cu-Pd(17%). *Phys. Rev. Lett.*, **68**(24):3591–3594.

Rietveld, H. M. (1969). A profile refinement method for nuclear and magnetic structures. *J. Appl. Cryst.*, **2**(2):65–71.

Rodriguez-Carvajal, J. (1990). FULLPROF: a program for Rietveld refinement and pattern matching analysis. In *Satellite meeting on powder diffraction of the XV congress of the IUCr*, page 127. Toulouse, France.

Rodriguez-Carvajal, J. (1993). Recent Advances in Magnetic Structure Determination by Neutron Powder Diffraction. *Physica B*, **192**(1–2):55–69.

Rodriguez-Carvajal, J. and Roisnel, T. (1998). FullProf. 98 and WinPLOTR: New Windows 95/NT Applications for Diffraction. Commission for Powder Diffraction, International Union of Crystallography. *Newsletter*, **20**:35–36.

Roisnel, T. and Rodriguez-Carvajal, J. (2000). WinPLOTR: a Windows tool for powder diffraction patterns analysis. In *Proceedings of the Seventh European Powder Diffraction Conference (EPDIC 7)*, pages 118–123.

Ruban, A. V. and Abrikosov, I. A. (2008). Configurational thermodynamics of alloys from first principles: Effective cluster interactions. *Rep. Prog. Phys.*, **71**(4):046501.

Rusz, J., Bergqvist, L., Kudrnovský, J., and Turek, I. (2006). Exchange interactions and Curie temperatures in Ni_{2-x}MnSb alloys: First-principles study. *Phys. Rev. B*, **73**:214412.

Sánchez-Alarcos, V., Pérez-Landazábal, J. I., Gómez-Polo, C., and Recarte, V. (2008). Influence of the atomic order on the magnetic characteristics of a Ni-Mn-Ga ferromagnetic shape memory alloy. *J. Magn. Magn. Mater.*, **320**(14):e160–e163.

Sánchez-Alarcos, V., Pérez-Landazábal, J. I., Recarte, V., Rodríguez-Velamazán, J. A., and Chernenko, V. A. (2010). Effect of atomic order on the martensitic and magnetic transformations in Ni-Mn-Ga ferromagnetic shape memory alloys. *J. Phys.: Condens. Matter*, **22**(16):166001.

Sánchez-Alarcos, V., Recarte, V., Pérez-Landazábal, J. I., and Cuello, G. J. (2007). Correlation between atomic order and the characteristics of the structural and magnetic transformations in Ni-Mn-Ga shape memory alloys. *Acta Mater.*, **55**(11):3883–3889.

Schmid, F. and Binder, K. (1992). Monte Carlo investigation of interface roughening in a bcc-based binary alloy. *Phys. Rev. B*, **46**:13565–13570.

Schwarz, K., Mohn, P., Blaha, P., and Kübler, J. (1984). Electronic and magnetic structure of BCC Fe-Co alloys from band theory. *J. Phys. F: Met. Phys.*, **14**(11):2659–2671.

Seguí, C. (2014). Effects of the interplay between atomic and magnetic order on the properties of metamagnetic Ni-Co-Mn-Ga shape memory alloys. *J. Appl. Phys.*, **115**(11):113903.

Seguí, C. and Cesari, E. (2011). Effect of ageing on the structural and magnetic transformations and the related entropy change in a Ni-Co-Mn-Ga ferromagnetic shape memory alloy. *Intermetallics*, **19**(5):721–725.

Seguí, C. and Cesari, E. (2012). Composition and atomic order effects on the structural and magnetic transformations in ferromagnetic Ni-Co-Mn-Ga shape memory alloys. *J. Appl. Phys.*, **111**(4):043914.

Seguí, C., Pons, J., and Cesari, E. (2007). Effect of atomic ordering on the phase transformations in Ni-Mn-Ga shape memory alloys. *Acta Mater.*, **55**(5):1649–1655.

Simon, E., Vida, J. G., Khmelevskyi, S., and Szunyogh, L. (2015). Magnetism of ordered and disordered Ni_2MnAl full Heusler compounds. *Phys. Rev. B*, **92**:054438.

Singh, M., Saini, H. S., and Kashyap, M. K. (2012). Mn-disorder effect on Magnetism and Half Metallicity of NiCoMnGa Qarternary Heusler Alloy. *Adv. Mater. Res.*, **585**:270–273.

Singh, N., Dogan, E., Karaman, I., and Arróyave, R. (2011). Effect of configurational order on the magnetic characteristics of Co-Ni-Ga ferromagnetic shape memory alloys. *Phys. Rev. B*, **84**(18):184201.

Singh, S., Caron, L., D'Souza, S. W., Fichtner, T., Porcari, G., Fabbrici, S., Shekhar, C., Chadov, S., Solzi, M., and Felser, C. (2016). Large Magnetization and Reversible Magnetocaloric Effect at the Second-Order Magnetic Transition in Heusler Materials. *Adv. Mater.*, **28**(17):3321–3325.

Singh, S., Nayak, J., Rai, A., Rajput, P., Hill, A. H., Barman, S. R., and Pandey, D. (2013). (3 + 1) D superspace description of the incommensurate modulation in the premartensite phase of $\mathrm{Ni_2MnGa}$: a high resolution synchrotron x-ray powder diffraction study. *J. Phys.: Condens. Matter*, **25**(21):212203.

Sokolovskiy, V. V., Buchelnikov, V. D., Zagrebin, M. A., Entel, P., Sahoo, S., and Ogura, M. (2012). First-principles investigation of chemical and structural disorder in magnetic $\mathrm{Ni_2Mn_{1+x}Sn_{1-x}}$ Heusler alloys. *Phys. Rev. B*, **86**:134418.

Soulen, R. J., Byers, J. M., Osofsky, M. S., Nadgorny, B., Ambrose, T., Cheng, S. F., Broussard, P. R., Tanaka, C. T., Nowak, J., Moodera, J. S., Barry, A., and Coey, J. M. D. (1998). Measuring the Spin Polarization of a Metal with a Superconducting Point Contact. *Science*, **282**(5386):85–88.

Sozinov, A., Likhachev, A. A., Lanska, N., and Ullakko, K. (2002). Giant magnetic-field-induced strain in NiMnGa seven-layered martensitic phase. *Appl. Phys. Lett.*, **80**(10):1746–1748.

Squires, G. L. (2012). *Introduction to the theory of thermal neutron scattering*. Cambridge University Press.

Ullakko, K., Huang, J. K., Kantner, C., O'Handley, R. C., and Kokorin, V. V. (1996). Large magnetic field induced strains in $\mathrm{Ni_2MnGa}$ single crystals. *Appl. Phys. Lett.*, **69**(13):1966–1968.

Umetsu, R. Y., Ishikawa, H., Kobayashi, K., Fujita, A., Ishida, K., and Kainuma, R. (2011). Effects of the antiferromagnetic anti-phase domain boundary on the magnetization processes in $\mathrm{Ni_2Mn(Ga_{0.5}Al_{0.5})}$ Heusler alloy. *Scripta Mater.*, **65**(1):41–44.

Umetsu, R. Y., Kobayashi, K., Fujita, A., Kainuma, R., and Ishida, K. (2008). Magnetic properties and stability of $L2_1$ and B2 phases in the $\mathrm{Co_2MnAl}$ Heusler alloy. *J. Appl. Phys.*, **103**(7):07D718.

Venkateswaran, S. P., Nuhfer, N. T., and De Graef, M. (2007). Anti-phase boundaries and magnetic domain structures in $\mathrm{Ni_2MnGa}$-type Heusler alloys. *Acta Mater.*, **55**(8):2621–2636.

Von Dreele, R. B., Jorgensen, J. D., and Windsor, C. G. (1982). Rietveld refinement with spallation neutron powder diffraction data. *J. Appl. Cryst.*, **15**(6):581–589.

Webster, P. J. (1968). PhD thesis, Sheffield University.

Webster, P. J. (1971). Magnetic and chemical order in Heusler alloys containing cobalt and manganese. *J. Phys. Chem. Solids*, **32**(6):1221–1231.

Webster, P. J. and Mankikar, R. M. (1984). Chemical order and magnetic properties of the Ni_{2-x}MnSb system. *J. Magn. Magn. Mater.*, **42**(3):300–308.

Webster, P. J. and Ziebeck, K. R. A. (1988). Landolt-Bornstein, New Series Group III, Vol. 19C, Ed. HRJ Wijin.

Webster, P. J., Ziebeck, K. R. A., Town, S. L., and Peak, M. S. (1984). Magnetic order and phase transformation in $\mathrm{Ni_2MnGa}$. *Phil. Mag. B*, **49**(3):295–310.

Wei, X.-P., Zhang, Y.-L., Chu, Y.-D., Sun, X.-W., Sun, T., Guo, P., and Deng, J.-B. (2015). Electronic, magnetic and Fermi properties investigates on quaternary Heusler NiCoCrAl, NiCoCrGa and NiFeCrGa. *J. Phys. Chem. Solids*, **82**:28–35.

Wever, H. (1992). Intermetallic compounds. In *Defect and Diffusion Forum*, volume 83, pages 55–72. Trans Tech Publ.

Williams, A. R., Zeller, R., Moruzzi, V. L., Gelatt, C. D. J., and Kübler, J. (1981). Covalent magnetism: An alternative to the Stoner model. *J. Appl. Phys.*, **52**(3):2067–2069.

Willis, B. T. M. and Carlile, C. J. (2009). *Experimental neutron scattering*, volume 30. Oxford University Press.

Wolff, U. (1989). Comparison between cluster Monte Carlo algorithms in the Ising model. *Phys. Lett. B*, **228**(3):379–382.

Xiong, L., Yi, L., and Gao, G. Y. (2014). Search for half-metallic magnets with large half-metallic gaps in the quaternary Heusler alloys CoFeTiZ and CoFeVZ (Z=Al, Ga, Si, Ge, As, Sb). *J. Magn. Magn. Mater.*, **360**:98–103.

Yano, T., Murakami, Y., Kainuma, R., and Shindo, D. (2007). Interaction between magnetic domain walls and antiphase boundaries in $\mathrm{Ni_2Mn(Al,Ga)}$ studied by electron holography and Lorentz microscopy. *Mat. Trans. JIM*, **48**(10):2636–2641.

Zayak, A. T., Entel, P., Enkovaara, J., Ayuela, A., and Nieminen, R. M. (2003). A first-principles investigation of phonon softenings and lattice instabilities in the shape-memory system $\mathrm{Ni_2MnGa}$. *Phys. Rev. B*, **68**:132402.

Zhang, Y. J., Liu, Z. H., Li, G. T., Ma, X. Q., and Liu, G. D. (2014). Magnetism, band gap and stability of half-metallic property for the quaternary Heusler alloys CoFeTiZ (Z = Si, Ge, Sn). *J. Alloys Comp.*, **616**:449–453.

Zheludev, A., Shapiro, S. M., Wochner, P., Schwartz, A., Wall, M., and Tanner, L. E. (1995). Phonon anomaly, central peak, and microstructures in $\mathrm{Ni_2MnGa}$. *Phys. Rev. B*, **51**:11310–11314.

Ziebeck, K. R. A. and Webster, P. J. (1975). Helical magnetic order in $\mathrm{Ni_2MnAl}$. *J. Phys. F: Met. Phys.*, **5**(9):1756–1766.

Zijlstra, H. and Haanstra, H. B. (1966). Evidence by Lorentz microscopy for magnetically active stacking faults in MnAl alloy. *J. Appl. Phys.*, **37**(7):2853–2856.